STUDY OF THE ISSUES OF COMPUTATIONAL AEROTHERMODYNAMICS USING A RIEMANN SOLVER

A proposal submitted in partial fulfillment of the
requirements for the degree of
Doctor of Philosophy in Engineering

By

SEAN JAMES HENDERSON
B.S.M.E., Wright State University, 2001
M.S.M.E., Wright State University, 2003

2007
Wright State University
Dayton, Ohio 45435-0001

WRIGHT STATE UNIVERSITY
SCHOOL OF GRADUATE STUDIES

December 14, 2007

I HEREBY RECOMMEND THAT THE THESIS PREPARED UNDER MY SUPERVISION BY Sean J. Henderson ENTITLED Study of the Issues of Computational Aerothermodynamics Using a Riemann Solver BE ACCEPTED IN PARTIAL FULFILLMENT OF THE REQUIREMENTS FOR THE DEGREE OF Doctor of Philosophy in Engineering.

James Menart, Ph. D.
Dissertation Director

Ramana Grandhi, Ph. D.
Director, Engineering Ph.D. Program

Joseph F. Thomas, Jr., Ph.D
Dean, School of Graduate Studies

Committee on
Final Examination

James Menart, Ph. D., Wright State University

Mitch Wolff, Ph. D., Wright State University

Joseph Shang, Ph. D., Wright State University

Raymond Maple, Ph. D., Air Force Institute of Technology

James Miller, Ph. D., Air Force Research Laboratory

ABSTRACT

Henderson, Sean James. Ph.D. Department of Mechanical and Materials Engineering, Wright State University, 2008. Study of the Issues of Computational Aerothermodynamics Using a Riemann Solver.

This work is part of a project to more accurately model hypersonic flow. A number of issues in hypersonic flow are addressed.

The first issue addressed is that of air properties at increased temperatures. In particular the thermodynamic and transport properties of chemical equilibrium air are found for temperatures up to 30,000 K for a pressure range from 1x10^{-4} to 100 atm. This work provides properties at slightly higher temperatures for the lower pressure region than can be found in the literature. This work also covers adding equilibrium air chemistry to the computational fluid dynamics computer code known as AVUS.

The second issue addressed is commonly referred to as the carbuncle phenomenon. The carbuncle phenomenon is a numerical instability that affects the capturing of strong shocks when using a Riemann solver with low numerical dissipation. The carbuncle phenomenon manifests itself in the inability to compute uniform flow conditions downstream of a normal or nearly normal shock. Prior work has been done in this area to accurately capture strong shocks; and great progress has been made in reducing the effects of the carbuncle phenomenon. Even with these improvements the heat transfer profiles in the stagnation region still show some distortion from small upstream perturbations convected downstream to the wall. It has been determined that the grid quality in the region of the shock is a major factor in the inability of Riemann solvers to accurately capture the flow in the stagnation region. For this reason this work performs a grid study and makes recommendations as to what types of structured grids should be used to accurately capture strong shocks and predict

heat transfer profiles at the body surface. This grid study shows that some types of grids suffer more than others from the carbuncle problem. The reason for this is the numerical dissipation that is introduced from the numerical routine. This work shows that grid aspect ratio and the alignment of the grid to the flow can be used to reduce the effects of the carbuncle phenomenon. This work also shows that another mechanism for the carbuncle phenomenon is the alignment of the grids with the shock. The heat transfer profile cannot be properly captured if the grid is not aligned well with the shock.

The third issue addressed in this work is the domain of applicability of the perfect gas model, the equilibrium air model, the nonequilibrium air model, and the thermo-chemical nonequilibrium air model. A computational study is carried out using AVUS to determine the regions of applicability of these air models for a blunt body at various velocities and altitudes. This type of altitude-velocity plot has already been produced by previous researchers, but the dividing lines between the different gas models were found using residence times. This work looks at temperature and heat transfer profiles for a blunt body in a high speed air flow to determine the dividing lines between the regions of applicability of the different air models. Unlike the previous work, this work provides specific error values for using a given model in a certain flight regime. It is found that the dividing lines between chemical equilibrium and chemical nonequilibrium have two dips in the curve that were not shown by previous researchers. These dips correspond to regions where O_2 and N_2 strongly dissociate.

Table of Contents

List of Figures

List of Tables

Nomenclature

a_i	moles of i element in the gas mixture
A_j	surface area of cell face $FF(j)$
$\mathbf{A}$	Jacobian matrix of $\partial\mathbf{F}/\partial\mathbf{U}$
AR	aspect ratio (length of cell face normal to shock/length of cell face perpendicular to shock)
$AVUS$	Air Vehicles Unstructured Solver
c	speed of sound, m/s
C_{cfl}	CFL condition
C_f	skin friction
C_h	coefficient of heat transfer
$C_P^\circ(T)$	molar specific heat at constant pressure of a chemical species, $J/mol\text{-}K$
C_P	specific heat at constant pressure, $J/kg\text{-}K$
$C_\mathcal{V}$	specific heat at constant volume, $J/kg\text{-}K$
CFD	Computational Fluid Dynamics
e	specific internal energy, J/kg
E	total thermal energy per unit volume, J/m^3
EQ	chemical equilibrium air
$\mathbf{F}(\mathbf{U})$	vector of fluxes for j faces
$FF(j)$	cell face j of computational cell
g_m	degeneracy of m^{th} electronic energy level

g_j°	molar Gibb's free energy of individual chemical species, J/mol
$\mathbf{G}(\mathbf{U})$	vector of fluxes for i faces
$h^\circ(T)$	molar enthalpy of a chemical species, J/mol
h	specific enthalpy, J/kg
h_c	convective heat transfer coefficient, W/m^2-K
$\triangle h_f^\circ(T)$	enthalpy of formation, J/mol
H	total enthalpy per unit volume, J/m^3
I	ionization energy required to form an ion, J
I_s	computational cell s
$IVBP$	Initial Value Boundary Problem
k	thermal conductivity, W/m-K or from $k-\omega$ turbulence model
k_b	Boltzmann constant = 1.38x10^{-23} J/K
$K^{(i)}$	right eigenvector of Jacobian matrix $\mathbf{A}$
Kn	Knudsen number
L	characteristic length
M	Mach number
$\mathcal{M}$	molecular weight, kg/mol
$\mathcal{M}_o$	molecular weight of undissociated gas, kg/mol
n	distance normal to wall
$\hat{n}_i$	outward unit normal vector of cell face i
n_{ij}	number of element i in a species j particle
Nu	Nusselt number
$\mathcal{N}_i$	moles of species i
$\mathcal{N}_{tot}$	total moles of gas mixture
NE	number of elements

NS	number of species
P	pressure, Pa
PF	perfect gas
Pr	Prandtl number
q	heat flux, W or velocity component normal to cell face
$q^{'}$	heat flux per unit area, W/m^2
Q	molecular partition function
R	specific gas constant, $J/kg\text{-}K$
R_o	specific gas constant of undissociated air = 286.99 $J/kg\text{-}K$
$\Re$	universal gas constant = 8314 $J/mol\text{-}K$
Re	Reynolds number
$s^{\circ}(T)$	molar entropy of a chemical species, $J/mol\text{-}K$
s	entropy, $J/kg\text{-}K$
S_c	Sackur-Tetrode constant = 1.164856
S_L	left wave speed, m/s
S_M	middle wave speed, m/s
S_{max}^n	maximum wave speed in domain at time t^n, m/s
S_R	right wave speed, m/s
t	time, s
T	temperature, K
T_{res}	thermal reservoir temperature, K
u	x-component of velocity, m/s
$\mathbf{U}$	vector of conserved variables
v	y-component of velocity, m/s
V	velocity, m/s

$\|V_s\|$	volume of computational cell I_s
$\mathcal{V}$	volume, m^3
X	mole fractions
Z	ratio of molecular weights
$\mathcal{Z}$	neutral atom or molecule

Greek

α_i	wave stength of Jacobian matrix $\mathbf{A}$
$\overrightarrow{\nabla}$	gradient operator
η	ratio of densities across shock (ρ_2/ρ_1)
γ	ratio of specific heats (C_p/C_v)
γ_s	isentropic exponent
$\overline{\gamma}$	ratio of enthalpy over internal energy
ϵ_m	energy of the m^{th} electronic energy level, J
η	ratio of densities across shock (ρ_1/ρ_2)
λ	mean free path
λ_i	element potential of element i or eigenvalue of Jacobian matrix $\mathbf{A}$
Λ	diagonal matrix containing eigenvalues of $\mathbf{A}$
μ	dynamic viscosity, $kg/s\text{-}m$
ρ	mass density, kg/m^3
τ	shear stress, N/m^2
ω	from $k-\omega$ turbulence model

Subscript/Superscript

1	property upstream of shock

2	property downstream of shock
eq	equilibrium
fr	frozen
HLL	HLL scheme variable
$HLLC$	HLLC scheme variable
L	left state
m	gas mixture
n	degree of ionization
o	stagnation property
r	rotational
R	right state
Roe	Roe's scheme variable
t	tangential
w	wall
x	component of vector in x-direction
y	component of vector in y-direction
z	component of vector in z-direction
$*$	starred state
∞	freestream condition
$\hat{}$	Roe-average value
$+$	variable associated with forward traveling component of $\mathbf{F}$
$-$	variable associated with backward traveling component of $\mathbf{F}$

ACKNOWLEDGEMENTS

There are several people without whom this thesis would have not been possible. I would like to thank my friends and family for their encouragement and support throughout my college career. I would also like to thank my wife, Jenny for her love and unwavering support throughout my graduate education, particularly toward the end. Her presence was a source of strength and inspiration for me to complete this dissertation, which I am eternally grateful.

I would like to thank Dr. James Menart for guiding me though my Master's and Ph.D. program. Without his assistance, this experience would not have been as enjoyable as it was. I owe him a great debt of gratitude, and am grateful for the chance to work with him.

I would also like to thank Dr. Joseph Shang, Dr. Mitch Wolff, Dr. James Miller, and Dr. Raymond Maple for taking time to serve on my defense committee and guiding me throughout my research and academic endeavors. I would also like to thank William Strang for his assistance on help on modifying the AVUS code.

Financial support from the Dayton Area Graduate Studies Institute, Air Force Research Labs Air Vehicle Directorate, and Wright State University is acknowledged.

1

Research Objectives, Background and Theory

Hypersonic flows are dominated by certain physical phenomena that do not exist or are negligible in supersonic flows. The dividing line between supersonic and hypersonic flows is not as clearly defined as the dividing line between subsonic and supersonic flows, but a gradual transition occurs where certain physical phenomena become more important as the Mach number is increased.

Hayes and Probstein (1959) in their textbook "*Hypersonic Flow Theory*" labeled hypersonic flow as a new category of flows that behave fundamentally different from supersonic flows. To justify creating a new flow category, separate from supersonic flows, the authors state:

> *Within recent years, the development of aircraft and guided missiles has brought a number of new aerodynamic problems into prominence. Most of the problems arise because of extremely high flight velocities, and are characteristically different from problems which arise in supersonic flight. The term hypersonic is used to distinguish flow fields, phenomena, and problems appearing at flight speeds much greater than the speed of sound from their counterparts appearing at flight speeds which are moderately supersonic. The appearance of new characteristic features in hypersonic flow fields justifies the use of a new term, different from*

the well established term supersonic.

1.1 Research Objectives

This work is part of a project to more accurately model hypersonic flow. A number of issues in hypersonic flow are addressed. To accomplish this goal the CFD code Air Vehicles Unstructured Solver (AVUS, formerly designated Cobalt_{60} [Strang et al. 1999]) was used. Since the AVUS code was used extensively in the work, a brief overview of the codes capabilities are given.

The AVUS program is capable of solving the Euler/Navier-Stokes equations for any three-dimensional geometry. The foundation of the AVUS program consist of various approximate Riemann solvers that are first-order accurate in space and time. Second-order accuracy in space is obtained by using van Leer's MUSCL scheme [van Leer 1979], which uses a piecewise linear data reconstruction to compute the fluxes at the faces of the cells. First and second-order temporal accuracy are implemented into the code using a point implicit scheme as implemented by Tomaro et al (1997). Second order accurate viscous fluxes are employed. The AVUS program is capable of modeling turbulence using the one-equation [Spalart and Allmaras 1992; Spalart et al. 1997] and two equation [Wilcox 1998; Menter 1993] models. AVUS is a very robust and general computer program for solving gas flow problems for any type of geometry. The capabilities of AVUS are many and a detailed explanation of the perfect gas version of this code can be found in the article by Strang et al. (1999).

The version of the AVUS code used in this study is capable of carrying out calculations for both a calorically perfect gas and for chemical equilibrium air. The thermodynamic and transport properties were added to the AVUS code for chemical equilibrium air by using the Tannehill curve fits [Srinivasan et al. 1987a; 1987b]. The Tannehill curve fits include the species O_2, N_2, N, O, NO, O+, N+, NO^+, and e^- in their analysis. More details of the chemical equilibrium version of AVUS will be discussed in Chapter 4.

The other version of AVUS used in this work is capable of carrying out calculations in chemical nonequilibrium air in both thermal equilibrium and thermal nonequilibrium [Hudson et al. 2005]. The nonequilibrium version of AVUS has a generalized model for finite-rate chemistry and is able to model the thermal nonequilibrium effects of the chemical reactions through Park's T-T_v model. The species included in the nonequilibrium air model are O_2, N_2, N, O, NO, O_2^+, N_2^+, O^+, N^+, NO^+, and e^-.

The final section of Chapter 1 will cover the revelant background and theory that is required for the topics covered in this dissertation. Chapter 2 is a literature survey of the previous work that has been done on the carbuncle phenomenon.

Chapter 3 covers the work of finding the thermodynamic properties of chemical equilibrium air for temperatures up to 30,000 K and for a pressure range of $1x10^{-4}$ to 100 atm. These thermodynamic properties were originally planned to be used by the AVUS program to calculate the thermodynamic properties of chemical equilibrium air. The equilibrium composition and thermodynamic properties of air were determined using the CANTERA program, which uses the element potential method [Reynolds 1986] to find the equilibrium composition. There were 22 species of interest in this work, N_2, O_2, Ar,O, N, NO, N_2^+, O_2^+, NO^+, N^+, N^{+2},N^{+3}, O^+, O^{+2}, O^{+3}, Ar^+, Ar^{+2},Ar^{+3}, N^-, O^-, O_2^- and e^-. Once the equilibrium composition and thermodynamic properties of the individual species present in the gas are found, the thermodynamic properties of the gas mixture can be found using gas mixture rules. The chemical equilibrium composition and thermodynamic properties are presented for a wide range of temperatures and pressures. To verify the results the chemical equilibrium composition and thermodynamic property results of this work were compared to the results of various researchers.

It was decided later in this project to use the "Tannehill curve fits" of Srinivasan et al. (1987a and 1987b) to calculate the thermodynamic and transport properties of equilibrium air to be used by the AVUS code. The reason for this decision was that the Tannehill curve fits required much less computational time than using the the CANTERA program, but both methods gave approximatly

the same results. The use of the CANTERA program, however, would allow greater flexibility by allowing other compositions of air, such as adding hydrocarbons or having oxygen rich or lean air.

Chapter 4 covers the procedure of adding equilibrium air chemistry to AVUS. This was done by using the Tannehill curve fits. This is an important step because it validates that Tannehill curve fits have been correctly coupled to the AVUS code. The capability of AVUS to handle chemical equilibrium air is needed for the work done in Chapter 5. To verify that the equilibrium air chemistry part of the AVUS code is working properly, the results were compared to the results of several researchers for several body geometries in hypersonic flows. The body geometries specifically used are a blunt body in inviscid hypersonic flow, a flat plate in laminar supersonic and hypersonic flows and a wedge and cone with a 10° half angle in a hypersonic laminar flow.

In chapter 5 a computational study is carried out using AVUS to determine the regions of applicability of the perfect gas model, equilibrium air model, chemical nonequilibrium air model and the thermo-chemical nonequilibrium air model for blunt bodies at various velocities and altitudes. This type of altitude-velocity plot has already been produced by previous researchers [Gupta et al. 1990; Hansen 1959], but the dividing lines between the different gas models were found using residence time. For this work the temperature, pressure, and heat transfer from the AVUS CFD code are compared from each gas model to determine the dividing lines. These results are unique to the field and should be useful to future investigators. Unlike the previous work, this work provides specific error values for using a given model in a certain flight regime. It was found that the dividing lines between chemical equilibrium and chemical nonequilibrium have two dips in the curve that were not shown by previous researchers. These dips correspond to regions where O_2 and N_2 strongly dissociate.

For Chapter 6 a grid study was performed on blunt bodies to see what grid resolution and placement is required to accurately capture strong shocks and the heat transfer profiles at the surface of a blunt body. It is the carbuncle phenomenon that is causing difficulties in capturing the strong shocks and heat transfer profiles at the surface of blunt bodies. The carbuncle phenomenon is a

numerical instability that affects the capturing of strong shocks when a low dissipation flux function is used in determining the fluxes passing through the cell faces. The carbuncle phenomenon manifests itself in the inability of the simulation to compute uniform flow downstream of a normal or nearly normal shock. The carbuncle phenomenon is best illustrated by a distorted bow shock upstream of a blunt body in a hypersonic flow.

Prior work has been done to more accurately capture strong shocks and great progress has been made in reducing the effects of the carbuncle phenomenon. Even with these improvements, the heat transfer profile in the stagnation region still shows some distortion from small upstream perturbations being convected downstream to the wall. It is known that grid quality in the region of the shock is a factor in the inability of the Riemann solver to accurately capture the flow field in the stagnation region. For this reason a grid study was performed to give recommendations on what types of structured grids should be used to accurately capture strong shocks and accurately predict the heat transfer profiles at the body surface. This work provides recommendations on grid design that minimize the carbuncle problem.

The results for the grid study on the carbuncle phenomenon were first performed using Quirk's case. Quirk's case consists of a single shock traveling down a straight duct. Quirk's case is commonly used to study the carbuncle phenomenon instead of blunt bodies, due to its simpler geometry. From the grid study it was found that increasing the aspect ratio of the computational cells near the shock is the most important factor that reduces the magnitude of the carbuncle phenomenon.

This grid study on blunt bodies shows that some grids suffer more than others from the carbuncle problem. The reason for this is the numerical dissipation that is introduced from the numerical routine. This work shows that grid aspect ratio and the alignment of the grid to the flow can be used to reduce the effects of the carbuncle phenomenon. This work also shows that another mechanism for the carbuncle phenomenon is the alignment of the grids with the shock. The heat transfer profile cannot be properly captured if the grid is not aligned well with the shock.

1.2 Relevant Background and Theory

The rest of this chapter will cover some background and theory of the topics covered in this dissertation. The first section will discuss the differences between the perfect gas, chemical equilibrium air, and chemical nonequilibrium air. This section will also cover the different flight regimes associated with high temperature effects an aircraft can experience flying at different altitudes and velocities. This discussion ties into Chapter 5 which covers computationally determining the the flight regimes of a blunt body using CFD. The next section will go over the relevant theory used in determining the equilibrium composition of chemical equilibrium air discussed in Chapter 3. The final section will go over some of the basic features of Riemann solvers. This is an important discussion since the choice of the approximate Riemann solvers used in a CFD code can effect the accuracy of the results. The formulation of several approximate Riemann solvers is discussed in this chapter. In particular it is important to understand how accurately the various approximate Riemann solvers capture the contact wave. This discussion aids in the understanding of the discussion of the carbuncle phenomenon in Chapters 2 and 6.

1.2.1 High Temperature Effects

In order to accurately determine the hydrodynamic and thermal characteristics of the flow field around an aircraft moving at hypersonic speeds it is imperative that the thermodynamic and transport properties account for the gas composition that has a changing chemical make up. At low Mach numbers the ideal gas properties for air can be used with good accuracy, where the chemical makeup of the air is essentially 79% diatomic nitrogen and 21% percent diatomic oxygen. For higher speed flows the air starts to disassociate and ionize due to higher temperatures. This causes the composition of the air to change, which can have a large effect on the properties of the gaseous medium. This in turn will affect the thermal and hydrodynamic flow fields predicted by the CFD simulation. Basically there are three continuum gas models that can be used to obtain the required

air properties for high speed flow. These three models are the perfect gas model, the equilibrium air model, and the nonequilibrium air model.

1.2.1.1 Energy Storage Modes of Atoms and Molecules

To better understand the differences in the perfect gas model, equilibrium air model, and nonequilibrium air model a brief description of the energy storage modes of atoms and molecules is given. Gas mixtures are composed primarily of atoms and molecules. Each of the atoms/molecules are bound together by various intermolecular forces. Statistical mechanics shows that molecules have four modes of energy storage. The modes of energy storage are sometimes referred to in the literature as degrees of freedom. The first mode of energy storage is from the translational energy resulting from the translational motion of the center of mass of the molecule. A molecule also has a rotational energy storage mode since the molecules can rotate about their center of mass. The third energy storage mode of molecules is from the atoms of molecules vibrating with respect to an equilibrium location. This is termed the vibrational energy mode. The fourth energy mode is the electronic energy mode and due to the fact that the electrons of the atom/molecule orbit around the nucleus of the atom/molecule with each orbit having a particular electronic energy.

Results from quantum mechanics show that the above energies only exist at certain discrete values. The total energy stored in the molecule is the sum of the four energy modes mentioned above, namely the translational, rotational, vibrational and electronic energies. For monoatomic species the vibrational mode of energy storage does not exist and the rotational mode of energy storage is negligible. At room temperature the electronic energy states are generally in the ground state. The rotational energy modes of N_2, O_2, and NO are all easily excited so that the rotational energy modes are highly excited at room temperature. This means the contributions of the rotational modes at the fully excited state are relatively constant.

1.2.1.2 Perfect Gas Model

The perfect gas model assumes that the rotational, vibrational, and electronic energy models of the atom and molecules of the gas remain constant. With this assumption the perfect gas model asserts that the specific heats of the gas remain constant. The perfect gas model also assumes the ratio of the specific heats to be constant. Utilizing a perfect gas model affords some simplification in the flow calculations; but it must be remembered that this is an approximation and specific heat values can change drastically for high-speed flows because of the drastic temperature changes.

1.2.1.3 Chemical Equilibrium

The equilibrium gas model accounts for a varying air composition as the temperature and pressure of the air change. It also accounts for properties changing as the air temperature and pressure change. The primary assumption made with the equilibrium air model is that chemical reactions occur instantaneously. For extremely high speed flows this may not be a good assumption.

1.2.1.4 Chemical Nonequilibrium

When the speed of the air flow becomes extremely fast many chemical reactions do not have time to occur at a given location. With this increased speed of the air flow the gas passing through a shock will see a sudden increase in the pressure and temperature. The gas attempts to reach an equilibrium distribution of the chemical species through collisions as the gas moves downstream of the shock. If enough collisions do not occur in the shock for the gas to reach an equilibrium distribution, the gas will be in chemical nonequilibrium. The thermodynamic properties of a gas in chemical nonequilibrium are a function of the temperature, pressure, and the composition of the gas. The local composition of the gas is no longer a function of the local temperature and pressure. The local composition is a function of the rate of movement of each individual species and the rate of production/destruction of each species. This requires solving additional species continuity equations for each of the individual species present in the gas mixture.

The nonequilibrium air model is the most accurate physical model for obtaining properties of air in a high speed flow environment. The drawback of the nonequilibrium air model is that it increases the complexity of a CFD code and it increases the computational time required to run the CFD code. It also requires a larger amount of input data. For the nonequilibrium air model the species continuity equations must be solved, along with the Navier-Stokes equations. This is a very complex, time consuming computation.

1.2.1.5 Thermal Nonequilibrium

The rotational and vibrational states of the molecules are also excited by molecular and electron collisions. Like chemical equilibrium, a system in thermal equilibrium is assumed to have sufficient time for collisions to occur. This leads to the properties of the system being constant and independent of time at a fixed pressure and temperature. However, if enough collisions do not occur as the fluid element passes through the shock for the rotational and vibrational states of energy to reach an equilibrium distribution, the gas will be in thermal nonequilibrium. This leads to a region of thermal nonequilibrium immediately downstream of the shock.

Experimental data [Park 1990] reveals that the three neutral molecules in air (N_2, O_2, and NO) all have rotational energy modes that relax to an equilibrium distribution very rapidly, at about the same rate for all three species. For this reason the rotational energy modes can be accurately modeled as a single rotational temperature, T_r. It is also shown experimentally that the rotational energy modes require approximately the same number of collisions as is required for the translational energy mode to reach an equilibrium distribution. For this reason it is rather common to assume that the rotational and translational energy modes are in thermal equilibrium at the translational-rotational temperature of T.

The vibrational modes of energy storage are often modeled using a two-temperature model [Park 1989a; 1989b], where the vibrational population distributions of all the species can be characterized by a single vibrational temperature, T_v. This is due to the fact that at temperatures above 3000 K

the coupling between the various vibrational modes of the molecules is strong, thus forcing the vibrational temperatures of the three neutral molecules to be nearly identical. The two temperature model requires the solution of a single partial differential equation for the total vibrational energy of all the species. The vibrational population distribution of N_2, O_2, and NO requires a smaller number of collisions to reach an equilibrium distribution than is required for chemical equilibrium to occur. This is the reason that thermal nonequilibrium occurs at higher altitude and velocities than chemical equilibrium as shown in Figure 1.1.

1.2.1.6 Flight Regimes of Blunt Body in Flight

The high temperature effects discussed above can drastically change the fluid flow around a blunt body with the major differences between the calorically perfect gas model and the high temperature, reacting flow model being [Anderson 1989]:

1. The thermodynamic properties are different.

2. The transport properties (viscosity and thermal conductivity) are different. Also the additional transport mechanism of diffusion.

3. The heat transfer rates are usually a dominant aspect of high temperature applications.

4. The ratio of specific heats,γ, and a closed form analysis of the thermodynamic properties cannot be used.

5. If the temperature is high enough to cause ionization, the gas becomes a partially ionized plasma, which has a finite electrical conductivity. This means that the flow can be altered by applying an electric or magnetic field. This is the purpose of the area called magnetohydrodynamics (MHD).

6. If the gas temperature is high enough then energy transfer can occur from radiation to and from the gas. This can drastically affect the heat transfer at the wall.

For a blunt body at various flight velocities, different chemical reactions can occur behind the shock wave depending on the flight velocity and altitude. Figure 1.1 shows the chemical reactions that occur as a 30.5 cm blunt body increases its flight velocity. For flight velocities less that 1 km/s the gas can be assumed a calorically perfect gas with N_2 and O_2 being the only species present. The calorically perfect gas model assumes that the vibrational and electronic energy modes are in their ground states. This means that only changes in the translational and rotational energy modes are contributing to changes in the thermodynamic properties of the fluid. As the velocity of the blunt body is increased the vibrational mode of energy storage becomes important and the calorically perfect gas model is no longer valid. It is said the gas is vibrationally excited and the ratio of specific heats becomes a function of temperature. As the temperature is further increased the molecules start to dissociate and even ionize. These physical effects are the reason that a high-temperature gas deviates from a calorically perfect gas.

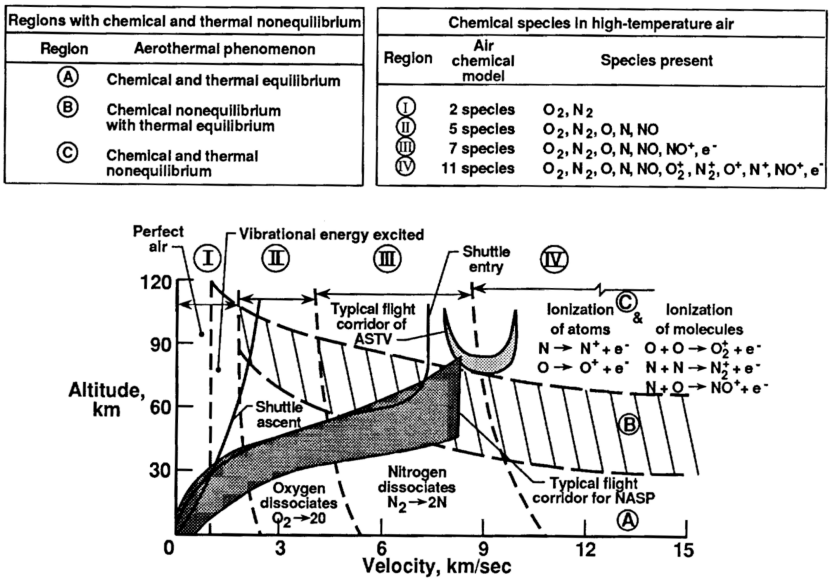

Figure 1.1: Flight stagnation region air chemistry of a 0.305 m radius sphere [Gupta et al. 1990].

Figure 1.1 shows that increasing the altitude of the blunt body can lead to chemical nonequilibrium since the density of air decreases with altitude. Therefore there are less molecular collisions

occurring so that the gas cannot reach an equilibrium distribution. Increasing the velocity of the flow can also lead to chemical nonequilibrium. This happens because the fluid particles pass through the shock more quickly and are not given enough time to reach an equilibrium distribution. This occurs because the shock is only a few mean free paths thick so the fluid element reaches an equilibrium distribution downstream of the shock. This leaves a region of chemical nonequilibrium immediately downstream of the shock.

1.2.2 Determining High Temperature Air Properties

This sections covers the relevant theory needed to calculate the thermodynamic properties of the chemical equilibrium air calculated in Chapter 3. The first section gives a general overview of the various methods that can be used to calculate the chemical composition of chemical equilibrium air. The procedure of determining the chemical composition of chemical equilibrium air using the element potential method is then discussed. The chemical composition of the chemical equilibrium air is calculated using the CANTERA program, which uses the element potential method. Once the thermodynamic properties of the individual species and chemical composition of the air is calculated the thermodynamic properties of the gas mixture can be calculated.

1.2.3 Overview of Methods to Calculate Equilibrium Air Compositions

There are several methods available for the determination of the equilibrium composition and thermodynamic properties of a high temperature gas. One method is the direct calculation of the composition and thermodynamic properties using either equilibrium constants, minimization of Gibbs free energy, or the element potential method. Another method is to use a tabulation of the equilibrium thermodynamic properties such as the tabulations for high temperature air given by Hillensrath and Klein (1965) . Another option is to use curve fits of the thermodynamic properties such as the curve fits Srinivasan et al. (1987a) and Gupta et al. (1991).

Tabulation or curve fits of the thermodynamic properties can only be used if they exist in the

literature for the gas of interest for the temperature and pressure range of interest. Several curve fits and tabulations exist for high-temperature air, but it is much more difficult to find tabulations and curve fits for other gases. The method of equilibrium constants or the element potential method can be used to find the equilibrium composition for any gas mixture as long as the fundamental input data required by the method for the individual species can be found.

In general, to solve for the equilibrium composition of a chemically reacting mixture using the method of equilibrium constants with NS species in the mixture and NE elements present requires solving NS simultaneous linear equations. Also the method of equilibrium constants requires NS independent chemical equations along with the associated equilibrium constant. For a more in depth discussions of how the method of equilibrium constants are used see Anderson (1989) and Vincenti and Kruger (1965). It should be noted that for gas mixtures with many species present the solution of NS simultaneous nonlinear equitation can be rather difficult and involve custom-designed algorithms [Anderson 1989]. The minimization of Gibbs free energy and element potential method are described in Section 2.4. It should be noted that both of these methods do not rely on knowledge of the chemical reactions that are occurring in the gas mixture.

The minimization of Gibbs free energy and element potential method both require knowledge of the thermodynamic properties of the individual species present in the gas mixture. There are two main methods that can be used to find the thermodynamic properties of the individual species. One of these methods is to use tabulations of the thermodynamic properties of the individual species. These tabulations are often presented as polynomial curve fits of the data over a range of temperatures as found in the ThermoBuild program by NASA Glenn[1] and are found in several references [Gupta et al. 1991; Gurivich et al. 1989]. The other option is to calculate the thermodynamic properties of the individual species using partition functions.

It should be noted that the results of the individual thermodynamic properties calculated by partition functions can vary significantly for higher temperatures depending on the types of models

[1]URL: http://cea.grc.nasa.gov [Cited June 2007].

used in calculating the partition function. For this reason it is better to use tabulations or curve fits of the thermodynamic properties of individual species if they already exist, since this data has already been compared to the results of other authors. For more information on determining the thermodynamic properties of individual species using partition functions the following references can be consulted [Vincenti and Kruger 1965; McBride and Gordon 1992; Gordon and McBride 1999; Capitelli et al. 2004].

Once the thermodynamic properties of the individual species are found the thermodynamic properties of the gas mixture can be found by using ideal gas mixture rules as discussed in many references [Anderson 1989; Gupta et al. 1991; Vincenti and Kruger 1965].

1.2.3.1 Determining the Equilibrium Composition

The following section will give a short description of how the element potential method is used for determining the equilibrium composition of an ideal gas mixture. For a more detailed derivation and explanation of usage of the element potential method a paper by Reynolds (1986) can be consulted. To aid in the discussion, the mole fractions and specific gas constant are defined as X_i and R respectively,

$$X_i = \frac{\mathcal{N}_i}{\sum_{i=1}^{NS} \mathcal{N}_i} \quad \text{and} \quad R = \sum_{i=1}^{NS} X_i \frac{\mathcal{R}}{\mathcal{M}_i} \tag{1.1}$$

where $\mathcal{M}_i$ is the molecular weight of chemical species i and $\mathcal{N}_i$ is the number of moles of species i in the gas mixture.

The element potential method and minimization of Gibbs free energy methods both are derived from a fundamental law, the second law of thermodynamics. The minimization of Gibbs free energy involves minimizing the Gibbs free energy of NS species with conservation of mass as a constraint. The element potential method involves the minimization of NE element potentials, λ_i, along with the conservation of mass as a constraint. In a gas mixture with a large number of species present there is a much smaller number of elements present, so the system of equations to be solved simultaneously

is much smaller for the element potential method.

The molar Gibbs free energy, g_j°, of chemical species j, can be obtained from h_j° and s_j° that are supplied as input data for each chemical species present in the gas mixture,

$$g_j^\circ = h_j^\circ - s_j^\circ T. \tag{1.2}$$

Conservation of mass can be written as an atomic population constraint,

$$\sum_{j=1}^{NS} n_{ij}\mathcal{N}_j = a_i \qquad i = 1, 2, \ldots, NE \tag{1.3}$$

where n_{ij} is the number of element i in a species j and a_i is the moles of element i present in the gas mixture.

The element potential is found by trying to minimize the Gibbs free energy by taking arbitrary variations of the Gibbs free energy of a chemical species. With some algebraic manipulation and the use of the conservation of mass constraint, the mole fractions can be expressed as a function of element potentials and Gibbs free energies. For every species we have

$$X_j = \exp\left(\frac{-g_j^\circ}{\Re\, T} + \sum_{i=1}^{NE} \lambda_i n_{ij}\right). \tag{1.4}$$

The element potential of the elements, λ_i, are actually Lagrange multipliers. The method of Lagrange multipliers is used to minimize the Gibbs free energy with the conservation of mass constraint.

Substituting the mole fractions determined in Equation 1.4 into the conservation of mass Equation 1.3, the element potentials are determined by

$$\sum_{j=1}^{NS} n_{ij}\mathcal{N}_{tot}X_j = \sum_{j=1}^{NS} n_{ij}\mathcal{N}_{tot} \exp\left(\frac{-g_j^\circ}{\Re\, T} + \sum_{i=1}^{NE} \lambda_i n_{ij}\right) = a_i \qquad i = 1, 2, \ldots, NE-1. \tag{1.5}$$

From the definition of mole fractions we have

$$\sum_{j=1}^{NS} X_j = \sum_{j=1}^{NS} \exp\left(\frac{-g_j^\circ}{\Re\, T} + \sum_{i=1}^{NE} \lambda_i n_{ij}\right) = 1. \tag{1.6}$$

With Equations 1.5 and 1.6 we have NE equations that must be solved simultaneously to determine the element potentials. Once the element potentials are determined the mole fractions can easily be found with Equation 1.4. With a good initial guess of the mole fractions of the dominant species in the gas mixture, a form of the Newton-Raphson method can be used to solve the system of equations.

1.2.3.2 Gas Mixture Property Determination

If the gas can be modeled as an ideal gas then the properties of the gas mixture can be calculated using algebraic relations. The three mixture properties are all on a per mass basis and are internal energy, e_m, enthalpy, h_m, and entropy, s_m, which are determined from

$$h_m = \sum_{i=1}^{NS} \frac{X_i\, h_i^\circ}{\mathcal{M}_i}, \tag{1.7}$$

$$e_m = h_m - RT, \tag{1.8}$$

$$s_m = \sum_{i=1}^{NS} \frac{X_i s_i^\circ}{\mathcal{M}_i} - R\sum_{i=1}^{NS} \ln(X_i) - R\ln\left(\frac{P}{P_\circ}\right) \tag{1.9}$$

where subscript m refers to the property value for the product mixture and P_o is the reference pressure of one atmosphere.

The total specific heat at constant pressure and the total specific heat at constant volume, which are a combination of the frozen and reactional contributions, can be determined from

$$C_{P,m} = \left.\frac{\partial h_m}{\partial T}\right|_P \qquad \text{and} \qquad C_{\mathcal{V},m} = \left.\frac{\partial e_m}{\partial T}\right|_{\mathcal{V}}. \tag{1.10}$$

For a gas in chemical equilibrium the ratio of enthalpy over internal energy, $\overline{\gamma}$, is often used in

CFD codes. It is defined as

$$\overline{\gamma} = \frac{h_m}{e_m} \tag{1.11}$$

where it should be noted that the mixture enthalpy and internal energy are taken at their absolute values and not from their reference states. With the use of $\overline{\gamma}$ the following relationship between pressure, density, and internal energy can be obtained,

$$P = (\overline{\gamma} - 1)\rho e. \tag{1.12}$$

Equation 1.12 is almost identical to the perfect gas relation for pressure, except that $\overline{\gamma}$ is replaced with the ratio of frozen specific heats for the perfect gas case. At lower temperatures $\overline{\gamma}$ converges to the ratio of specific heats.

The speed of sound is obtained from the definition as

$$c^2 = \left(\frac{\partial P}{\partial \rho}\right)_s. \tag{1.13}$$

For a frozen perfect gas mixture the equation for the frozen speed of sound is

$$c_{fr} = \sqrt{\gamma_{fr} RT} \tag{1.14}$$

with γ_{fr} being the ratio of the frozen specific heats and R is the specific gas constant of the undissociated gas.

There are several forms that allow the equilibrium speed of sound to be expressed as a function of the ratio of equilibrium specific heats, γ_{eq}, but the simplest expression is very similar to the frozen speed of sound using the isentropic exponent, γ_s. It can be shown that by using the isentropic exponent the equilibrium speed of sound can be cast in the following form [Bottin 2000; Gordon

1970],

$$c_{eq} = \sqrt{\gamma_s RT} \qquad \text{with} \qquad \gamma_s = \frac{\gamma_{eq}\rho}{P}\left(\frac{\partial P}{\partial \rho}\right)_T. \tag{1.15}$$

The equation of state for an equilibrium gas can be defined as

$$P = Z\rho RT \qquad \text{with} \qquad Z = \frac{\mathcal{M}_o}{\mathcal{M}} \tag{1.16}$$

and $\mathcal{M}_o$ represents the molecular weight of the undissociated gas and $\mathcal{M}$ is the average molecular weight of the equilibrium gas. It should be noted that the ratio of molecular weights is commonly referred to as the compressibility factor for high temperature gases. This can be a confusing terminology since the compressibility factor is also used for high pressure gases as a measure of the deviation of a gas from the ideal gas equation of state. The changes in the ratio of molecular weights is due to the dissociation and ionization of the gas species and not from compressible effects.

1.2.4 Brief Review of Riemann Solvers

The following discussion provides some of the basic features of Riemann solvers. The majority of the discussion is taken from Toro (1999) and Strang (2005) . Of main interest in this review is in how the various Riemann solvers handle the contact wave. If a Riemann solver exactly captures the contact wave then the scheme is vulnerable to the carbuncle phenomenon. If the Riemann solver does not exactly capture the contact wave the scheme is less vulnerable due to the carbuncle phenomenon. However, the scheme may not be able to properly capture boundary layers due to the excess dissipation from not properly capturing the contact wave.

The first part of this section describes the physics of the Riemann shocktube problem. Following this section the formulation of the one-dimensional Riemann solver is given due to its simple geometry and the natural extension of this formulation to multidimensional problems. The next section shows how the one-dimensional Riemann solver is extended to three-dimensions using generalized coordinates. A general overview of the properties of various approximate Riemann solvers is also

given. The final section goes into more detail on the Exact Riemann solver [Godunov 1959], Roe scheme [Roe 1981; Roe and Pike 1984], van Leer scheme [van Leer 1982], HLL scheme [Harten et al. 1983], HLLC scheme [Toro et al. 1994], HLLEM scheme [Einfeldt et al. 1991], and the HLL+ scheme [Park and Kwon 2003].

The solution of the Riemann problem is governed by the Euler equations so the assumption of inviscid flow is made. The Riemann solvers can be extended to viscous flows by adding terms that account for fluxes due to viscous forces and heat conduction at each face of the finite volume cell.

1.2.4.1 Riemann/Shocktube Problem

The shock-tube problem is a very interesting test case because the exact time-dependent solution is known and can be compared with the solution computed using numerical discretizations. The initial solution of the shock-tube problem is composed of two uniform states separated by a discontinuity which is usually located at the origin. This particular initial value problem is known as the Riemann problem. The Riemann problem is governed by the one-dimensional Euler equations and has the conservative formulation [Toro 1999]:

$$\frac{\partial \mathbf{U}}{\partial t} + \frac{\partial \mathbf{F}}{\partial x} = 0 \tag{1.17}$$

with

$$\mathbf{U} = \begin{pmatrix} \rho \\ \rho u \\ E \end{pmatrix} \qquad \mathbf{F} = \begin{pmatrix} \rho u \\ \rho u^2 + P \\ \rho u H \end{pmatrix} \tag{1.18}$$

where $\mathbf{U}$ is a vector of conserved variables, $\mathbf{F}$ is the vector of fluxes, E is the total energy per unit volume, and H is the total enthalpy per unit volume,

$$E = \rho(\frac{1}{2}u^2 + e) \tag{1.19}$$

$$H = E + P/\rho \tag{1.20}$$

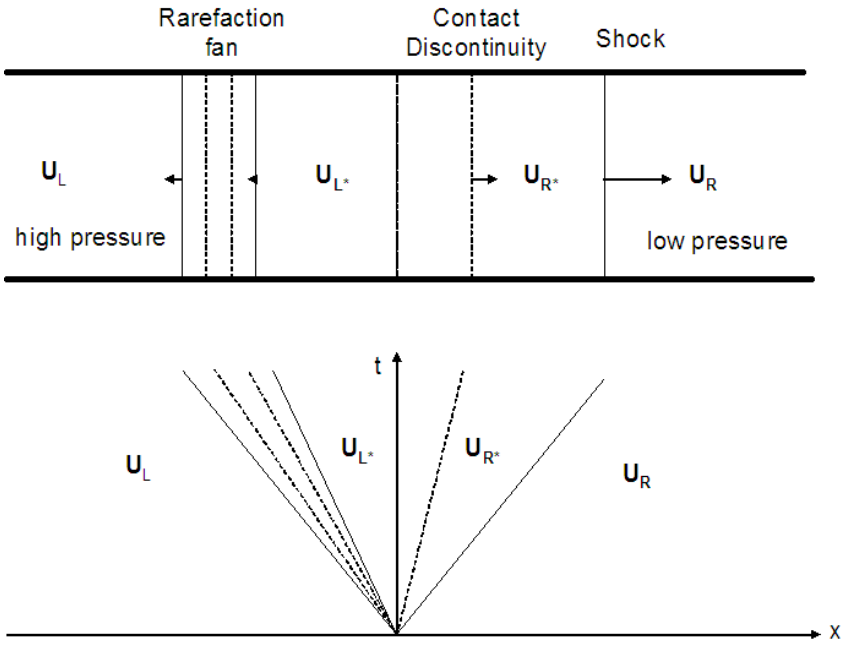

Figure 1.2: The shock tube with wave patterns for inviscid flow.

and P is the pressure

$$P = (\gamma - 1)\rho e \tag{1.21}$$

The initial conditions for this problem are:

$$\mathbf{U}(x,0) = \begin{cases} \mathbf{U}_L & \text{if} \quad x < 0 \\ \mathbf{U}_R & \text{if} \quad x > 0. \end{cases} \tag{1.22}$$

These initial conditions represent a tube where the left and the right regions are separated by a diaphragm, filled by the same gas, in two different physical states. If all the viscous effects are negligible along the tube walls, and assuming that the tube is infinitely long in order to avoid reflections at the tube ends, the exact solution of the full Euler equations can be obtained on the basis of a simple wave analysis. At the bursting of the diaphragm, the discontinuity between the two initial states breaks into leftward and rightward moving waves, which are separated by a contact wave as shown in Figure 1.2.

The three waves separate the x-t plane into four constant states. From left to right these are $\mathbf{U}_L$, $\mathbf{U}_{L*}$, $\mathbf{U}_{R*}$ and $\mathbf{U}_R$. The solution across each wave is called an elementary wave solution. With the ideal gas law assumed, the following three elementary wave patterns may appear: a rarefaction which has smooth changes, a contact discontinuity which has a discontinuity for ρ, but P and u are constant, and a shock which has a discontinuity for ρ, P and u.

Each wave pattern is composed of a contact discontinuity in the middle, and a shock or a rarefaction wave at the left and the right sides separating the uniform state solution. All the available combinations produce four wave patterns which are self-similar, that is they depend only on x/t.

Each of the elementary wave patterns has a distinct pattern of how the characteristics behave on both sides of the wave. A more detailed explanation of the types of eigenvalues and their associated characteristic fields may be found in Toro (1999). For shocks the characteristics run into the shock, they run parallel to the contact discontinuity and they diverge away from the rarefaction fan. The left and right waves are nonlinear waves and have an associated non-linear eigenvalue or wave speed as shown in Figure 1.3. The nonlinear waves that are present in an ideal gas are shock waves and rarefaction waves. The left wave has a wave speed of S_L and the right wave has a wave speed of S_R. It should be noted that the leftmost wave and the rightmost wave do not necessarily travel to the left or right, but are the wave patterns that are the furthest left or right from the initial discontinuity. Since the rarefaction wave is a continuous wave it has a wave speed at the head and tail of the wave. The contact discontinuity is the middle wave and has an associated wave speed of S_M as shown in Figure 1.3.

1.2.4.2 One-Dimensional Riemann Solver

The one-dimensional Riemann solver is first introduced due to its relative simplicity and the natural extension of the one-dimensional Riemann solver to multidimensional Riemann solvers. A basic assumption of Riemann solvers is that the data given at time $t = t^n$ has a piecewise linear distribution

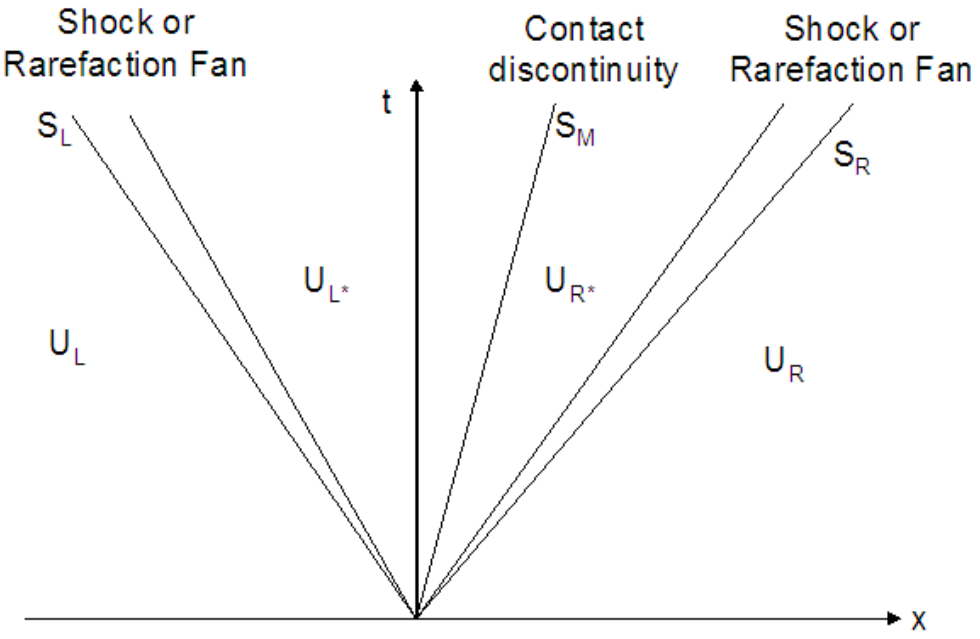

Figure 1.3: Structure of 3-wave Riemann fan.

as shown in Figure 1.4. The data at time t^n can be seen as a pair of constant states ($\mathbf{U}_i^n$,$\mathbf{U}_{i+1}^n$) separated by a discontinuity at the intercell boundary ($x_{i+\frac{1}{2}}$).

These pairs of constant states each consist of an Initial Value Boundary Problem that can be solved using the Riemann problem as described in the previous section, but using modified input data. Effectively this involves solving a local Riemann problem with the data $\mathbf{U}_i^n$ (left side) and $\mathbf{U}_{i+1}^n$ (right side) centered at the intercell boundary position of $x_i + \frac{1}{2}$. The correspondence between the global (x,t) and local ($\overline{x}, \overline{t}$) coordinate system is given by

$$\begin{aligned} \overline{x} = x - x_{i+\frac{1}{2}} \quad &, \quad \overline{t} = t - t^n, \\ x \in [x_i, x_{i+1}] \quad &, \quad t \in [t^n, t^{n+1}], \\ \overline{x} \in [-\tfrac{\triangle x}{2}, \tfrac{\triangle x}{2}] \quad &, \quad \overline{t} \in [0, \triangle t]. \end{aligned} \tag{1.23}$$

With a new frame of reference used for each Initial Value Problem the global solution of each pair of constant states can be given in a local coordinate system that was used in the previous section. The local Riemann problems at each intercell boundary can be advanced forward in time to find the

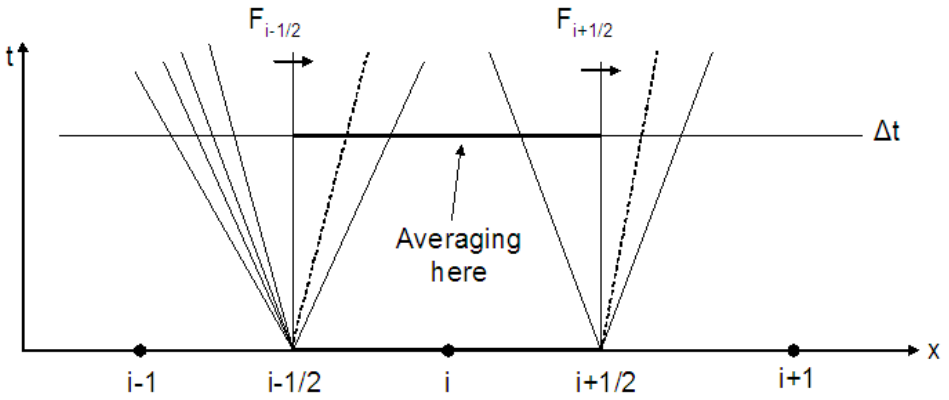

Figure 1.4: Godunov averaging of local solutions to Riemann problem within cell I_i at a fixed time $\triangle t$.

wave patterns that emerge from the initial discontinuity. Typical wave patterns that emerge from solving the two Riemann problems at the left and right faces of $\mathbf{U}_i$ are shown in Figure 1.4. The local Riemann problems are advanced forward for a time step $\triangle t$ that is sufficiently small to avoid wave interactions between the waves emerging from the intercell boundaries. For a one-dimensional problem with constant $\triangle x$ the time step required to avoid wave interactions is

$$\triangle t = \frac{\frac{1}{2} C_{cfl} \triangle x}{S^n_{max}} \tag{1.24}$$

where C_{cfl} is the CFL coefficient used by the Riemann solver. The S^n_{max} is the maximum wave velocity that is present throughout the entire computational domain at time t^n.

Once the solution is advanced forward in time the values in each cell are averaged to a new constant cell center value $\mathbf{U}^{n+1}_i$ at the time $t^{n+1} = t^n + \triangle t$ by the integrals

$$\mathbf{U}^{n+1}_i = \frac{1}{\triangle x} \int_{x_{i-\frac{1}{2}}}^{x_{i+\frac{1}{2}}} \mathbf{U}(x, t^{n+1}) dx \tag{1.25}$$

within each cell $I_i = [x_{i-\frac{1}{2}}, x_{i+\frac{1}{2}}]$. This averaging is often called Godunov averaging. The above scheme however is rather restrictive on the $\triangle t$ that can be used, and evaluating the integrals of Equation 1.25 can be rather involved. The averaging of the values of $\mathbf{U}^{n+1}_i$ can however be rewritten

in a conservative form where the new average value is a function of the fluxes passing through the intercell boundaries

$$\mathbf{U}_i^{n+1} = \mathbf{U}_i^n + \frac{\triangle t}{\triangle x}[\mathbf{F}_{i-\frac{1}{2}} - \mathbf{F}_{i+\frac{1}{2}}] \tag{1.26}$$

with $\mathbf{F}_{i-\frac{1}{2}}$ being the numerical flux that passes through the $x_{i-\frac{1}{2}}$ intercell boundary and $\mathbf{F}_{i+\frac{1}{2}}$ is the numerical flux that passes through the $x_{i+\frac{1}{2}}$ intercell boundary. The numerical fluxes can be evaluated using either the Exact Riemann solver or an approximate Riemann solver. More details of the HLLC, HLL, Roe, and van Leer schemes are given in the following subsections.

The time step $\triangle t$ to satisfy the conservative form is

$$\triangle t = \frac{C_{cfl}\triangle x}{S_{max}^n}. \tag{1.27}$$

The time step $\triangle t$ required for Equation 1.26 is less restrictive than the time step of Equation 1.25. The conservative form of finding the new average value $\mathbf{U}_i^{n+1}$ is the form that is used for practical computations.

The Godunov method is first-order accurate in space and can be extended to second-order accurate in space by using van Leer's MUSCL scheme [van Leer 1979]. The MUSCL scheme replaces the piecewise constant distribution by a piecewise linear reconstruction to evaluate the fluxes at the intercell faces.

1.2.4.3 Three-Dimensional Riemann Solver with Generalized Coordinates

The three-dimensional Riemann solvers are a natural extension of the one-dimensional Riemann solvers and use the same methods. Most Riemann solvers used for multidimensional problems use a one-dimensional Riemann solver for the fluxes at the cell interfaces and assume that the elementary wave speeds are nearly independent of the tangential component of properties to the cell interface. The basic idea of applying one-dimensional Riemann solvers to a multi-dimensional problem is to compute the fluxes through each cell face independently. For example, a two-dimensional oblique

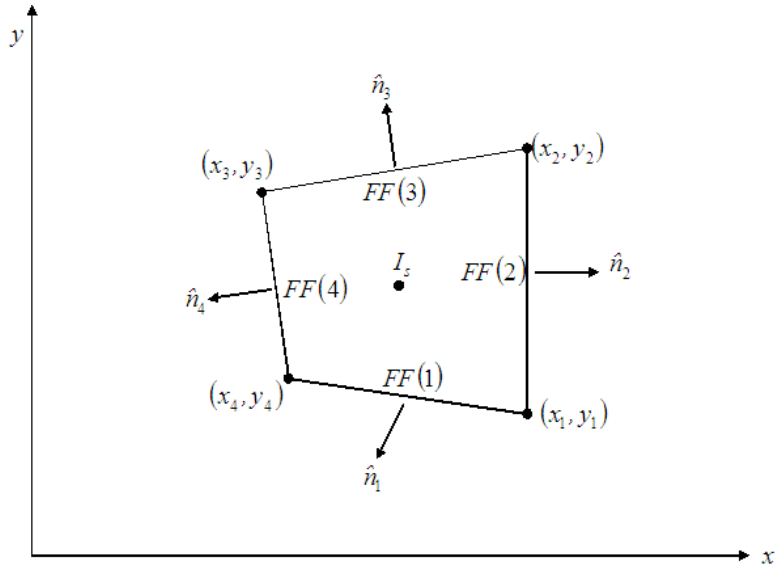

Figure 1.5: Typical 2D finite volume cell with corresponding intercell fluxes.

shock wave is computed using one-dimensional Riemann fluxes using a superposition of two normal shocks emanating from each face of the cell. This approach works remarkably well in practice for most cases, but can lead to smearing of the shock waves if they are not aligned with the mesh [Roe 1988]. The development of genuine multidimensional schemes is currently an area of intense research. This will reduce the smearing effect and also has the potential of curing the carbuncle phenomenon. The main disadvantage of current, genuine multidimensional Riemann solvers is the much greater computational time required and the complexity.

A typical two-dimensional finite volume cell with a general orientation of the intercell faces for a quadrilateral cell is shown in Figure 1.5. The computational cell (I_s) has four intercell faces labeled as $FF(1)$ - $FF(4)$ with corresponding outward unit normal vectors $\hat{n}_1$ - $\hat{n}_4$. Due to the properties of the Euler equations the intercell fluxes that pass through each cell face of the computation cell (I_s) can be evaluated separately for the augmented one-dimensional equation system for the Riemann problem governed by the Euler equations

$$\frac{\partial \hat{\mathbf{U}}}{\partial t} + \frac{\partial \hat{\mathbf{F}}_j}{\partial \hat{n}_j} = 0 \tag{1.28}$$

with

$$\hat{\mathbf{U}} = \begin{pmatrix} \rho \\ \rho u \\ \rho v \\ \rho v \\ E \end{pmatrix} \qquad \hat{\mathbf{F}}_j = \begin{pmatrix} \rho q \\ \rho q u + P n_{x,j} \\ \rho q v + P n_{y,j} \\ \rho q w + P n_{z,j} \\ \rho q H \end{pmatrix} \tag{1.29}$$

with

$$\begin{aligned} E &= \rho\left[\tfrac{1}{2}(u^2+v^2)+e\right] \\ H &= E + \tfrac{P}{\rho} \\ q &= u n_{x,j} + v n_{y,j} + w n_{z,j} \end{aligned} \tag{1.30}$$

where $\hat{\mathbf{U}}$ is the vector of conserved variables, $\hat{\mathbf{F}}_j$ is the vector of fluxes passing through cell face $FF(j)$, E is the total energy per unit volume, H is the total enthalpy per unit volume, and q is the velocity component normal to the cell face $FF(j)$

The initial conditions of the augmented one-dimensional Riemann problem are

$$\mathbf{U} = \begin{cases} \mathbf{U}_L^n & \text{if state interior to the computational cell } I_s \\ \mathbf{U}_R^n & \text{if state exterior to the computational cell } I_s \end{cases} \tag{1.31}$$

The cell average $\mathbf{U}_s^n$ is assigned to the center of the computational cell I_s as in the one-dimensional method and each of the cell faces correspond to a numerical flux. The cell average $\mathbf{U}_s^n$ in cell I_s at time $t = t^n$ is updated to $t = t + \triangle t$ by a single time step involving the flux contributions from each face of the cell:

$$\mathbf{U}_s^{n+1} = \mathbf{U}_s^n - \frac{\triangle t}{|V_s|} \sum_{j=1}^{4} A_j F_j \tag{1.32}$$

where $|V_s|$ is the volume of computational cell I_s, A_j is the surface area of cell face $FF(j)$, and F_j is the intercell flux passing through cell face $FF(j)$. For two dimensional problems the $|V_s|$ is the area of computational cell I_s and A_j is the length of cell face $FF(j)$.

The above three-dimensional formulation for generalized coordinates is a natural extension of the one-dimensional Riemann solver and is completely determined once the numerical fluxes are specified and the grid has been made. The solution of the augmented one-dimensional Riemann problem is solved using the same method that was described for the one-dimensional problem at each cell faces of the computation cell. The numerical fluxes for the intercell faces are also based on the solution of the one-dimensional Riemann problem. These are solved using the same methods as the one-dimensional problem. The main difference between the multi-dimensional Riemann problem and the one-dimensional Riemann problem is that the updating of cell average $\mathbf{U}_s^n$ involves fluxes from all the intercell faces and the time step $\triangle t$ is slightly more difficult to determine, due to multidimensional considerations. It should be mentioned that the cell average $\mathbf{U}_s^n$ in Equation 1.32 uses explicit Euler time integration while most Riemann solvers use more complicated time integration schemes, such as Runga-Kutta methods or implicit time integration due to stability issues. Larger time steps can be used with these methods.

1.2.5 Review of Several Riemann Flux Functions

To calculate the fluxes for a Riemann solver a profile of the properties across the Riemann fan must be selected. The profile of a component of $\mathbf{U}$ across the full Riemann fan might look something like that shown in Figure 1.6. Riemann solvers that recognize the three waves of the one-dimensional Euler equations are termed "three-wave Riemann methods".

Most flux solvers used in supersonic/hypersonic simulations are categorized as upwind schemes. Upwind schemes use the local flow speed and direction to determine how information is propagated between cells. Central difference schemes can draw flow information from outside the domain of dependance of a cell interface, which is not physically correct [Toro 1999]. This property of central difference schemes can cause them to generate noise or fail, and artificial dissipation terms must be added to stabilize the solution. Upwind schemes usually have a larger stability bound than central difference schemes and do not generally require artificial viscosity to maintain stability [Steger and

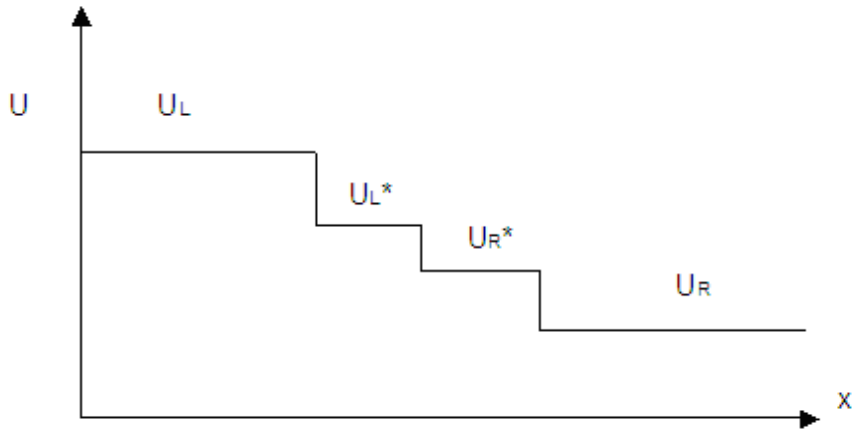

Figure 1.6: Component of **U** across a 3-wave Riemann fan.

Warming 1981].

Most upwind schemes can be classified as either Flux Difference Splitting (FDS) or Flux Vector Splitting (FVS). The first FDS scheme was proposed by Godunov for the Exact Riemann solver [Godunov 1959; Toro et al. 1994]. The Exact Riemann solver determines the interface fluxes from an exact solution of the Riemann problem using the left and right cell interface states as initial values. The solution of the Exact Riemann solver involves an iterative procedure that has a high computational cost. For this reason there are many approximate Riemann solvers that do not require an iterative procedure to find the solution to the Riemann problem. The HLLC scheme [Batten et al. 1997; Toro 1999; Toro et al. 1994] and Roe scheme [Roe 1981; Roe and Pike 1984] are examples of of approximate Riemann solvers that capture all three waves of the Riemann fan as shown in Figure 1.6. The HLL scheme is also a approximate Riemann solver, but the scheme is a two-wave Riemann method because it ignores the middle contact discontinuity in the derivation. This causes the HLL scheme to be very diffusive of contact surfaces, shear waves, and boundary layers. Figure 1.7 shows an example of a component of **U** across a two-wave Riemann fan.

Most approximate Riemann solvers, including the HLLC, Roe, and HLL schemes treat the continuous rarefaction waves as a discontinuous wave. The HLLC scheme treats rarefaction waves as

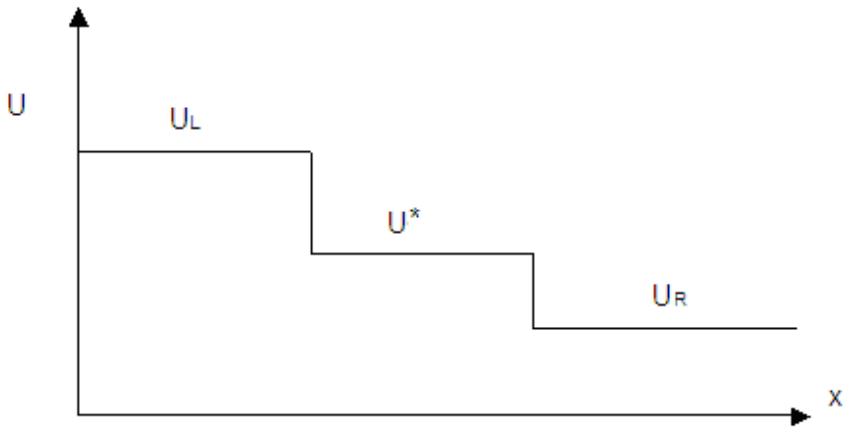

Figure 1.7: Component of **U** across a 2-wave Riemann fan.

two discontinuous waves, one at the head and one at the tail of the rarefaction wave. The HLLC scheme is often referred to as a four-wave Riemann method.

Treating the rarefaction wave as a discontinuous wave gives approximate Riemann solvers several advantages. First the profile of **U** across the Riemann fan becomes a series of constant states so that an analytical integration over x and t is possible. Second, the Rankine-Hugoniot jump conditions apply over the entire Riemann fan. The use of the Rankine-Hugoniot jump conditions give the Roe, HLL, and HLLC methods the ability to recognize discontinuous waves in the flow field.

FVS (Flux Vector Splitting) schemes differ from FDS (Flux Difference Splitting) schemes in that the interface fluxes are calculated as a combination of split forward and backward component flux vectors, that depend on the sign of associated eigenvalues. In general FVS schemes are simpler and faster than FDS schemes [van Leer 1982], the FVS schemes are well-suited for use with implicit techniques [Amaladas and Kamath 1998]. The main disadvantage of FVS schemes is their excessive dissipation which can diffuse contact surfaces [van Leer 1982], thicken shocks, and cause boundary layers to be inaccurately resolved [van Leer et al. 1987]. Part of this difficulty with FVS schemes is that they ignore the contact discontinuity in the formulation. FDS schemes can capture these flow features substantially more accurately and are less dissipative than FVS schemes [Amaladas

and Kamath 1998; van Leer et al. 1987]. In fact, no FVS scheme can exactly capture a stationary contact discontinuity [van Leer 1982].

To correctly satisfy the physics of fluid dynamics a good Riemann solver should satisfy positivity and not violate the Second Law of Thermodynamics (commonly called the entropy condition). Positivity preserving schemes correctly disallow the production of negative values of density, pressure, temperature, and species concentrations. This condition is particulary important to prevent code failures with colliding shocks, strong rarefactions and gases with multiple species present [Larrouturou 1991]. As well as satisfying positivity, a good flux function should not violate the Second Law of Thermodynamics. This is usually done by limiting the characteristic wave speeds so that nonphysical solutions, such as an expansion shock wave, cannot be introduced into the flow.

1.2.5.1 Exact Riemann Solver

Exact Riemann solvers are also called Godunov schemes. These solvers find the exact solution of the Riemann problem with the initial value problem defined by the left and right cell interface states. The Riemann problem is solved by considering the speed, direction, and strength of discrete pressure waves, shock waves, and contact waves emerging from the cell interface. Since the Exact Riemann solver exactly captures the contact wave, the scheme is susceptible to the carbuncle phenomenon.

There are a number of approaches to solving the exact Riemann problem [Gottlieb and Groth 1988]; however, all of them are iterative and are at least moderately computationally expensive. Furthermore, exact solutions become very expensive for non-polytropic gases and gases with generalized equations of state [Roe 1988]. For finite-volume schemes the details of the exact Riemann solution at the cell interfaces are lost during the averaging process that takes place to update the properties at the cell centers [Donat and Marquina 1996]. Due to this loss of information, exact Riemann solvers can be somewhat wasteful, but still produce accurate and usually well-behaved shock waves because of their physical basis [Quirk 1994].

1.2.5.2 Roe Scheme

Because the accuracy of exact Riemann solvers is wasted to a large extent, approximate solutions can be employed without significant degradation of the overall flow results. Roe's approach of solving a linearized Riemann problem is both cheap and popular. Unfortunately Roe's scheme [Roe 1981] admits entropy violating expansion shocks, and requires the addition of artificial dissipation to cure it (known as an entropy fix) [Roe 1988]. The Roe scheme also suffers from the carbuncle phenomenon, a nonphysical protuberance visible near the stagnation region of strong bow shocks.

Since the Roe scheme is currently the most widely used Riemann solver in the CFD community, all the assumptions and theory of the Roe scheme are not included in this work. References for the derivation of Roe's scheme for the three-dimensional setting with passively advected scalars are scant, so the basic relations of Roe's scheme in this setting are presented here [Strang 2005; Park and Kwon 2003]. The subscripts L and R denote values evaluated at the left and right states. The two passively advected scalars used are the k and ω of the two-equation $k-\omega$ turbulence model, however, the k and ω could be replaced with two other passively advected scalars.

The Roe flux for the one-dimensional Euler equation is

$$\mathbf{F}^{Roe} = \frac{1}{2}(\mathbf{F}_L + \mathbf{F}_R) - \frac{1}{2}\sum_{i=1}^{3} \hat{\alpha}_i |\hat{\lambda}_i| \hat{K}^{(i)} \tag{1.33}$$

where the multi-dimensional extension with passively advected scalars is

$$\mathbf{F}^{Roe} = \frac{1}{2}(\mathbf{F}_L + \mathbf{F}_R) - \frac{1}{2}\sum_{i=1}^{5} \hat{\alpha}_i |\hat{\lambda}_i| \hat{K}^{(i)} - \frac{1}{2}\hat{\rho}|\hat{\lambda}_2|\hat{C} \tag{1.34}$$

with $\hat{\lambda}_i$, $\hat{\alpha}_i$, and $\hat{K}^{(i)}$ being the eigenvalues, wave strengths, and right eigenvectors evaluated at the Roe-averaged state. The extra term on the right-hand side of the multidimensional equation arises from the requirement that

$$\mathbf{F}_R - \mathbf{F}_L = \sum_{i=1}^{5} \hat{\alpha}_i |\hat{\lambda}_i| \hat{K}^{(i)}. \tag{1.35}$$

The Roe-averaged variables used to find the Roe-average eigenvalues, wave strengths, and right-eigenvectors are given as

$$\begin{aligned}
\hat{g} &= \tfrac{\sqrt{\rho_R} g_R + \sqrt{\rho_L} g_L}{\sqrt{\rho_R} + \sqrt{\rho_L}} \quad \text{for} \quad g = u, v, w, h, k, \omega, \\
\hat{\rho} &= \sqrt{\rho_R \rho_L}, \\
\hat{c} &= [(\gamma - 1)\hat{h} - \hat{z}]^{\frac{1}{2}}, \\
\hat{z} &= \tfrac{1}{2}(\hat{u}^2 + \hat{v}^2 + \hat{w}^2).
\end{aligned} \tag{1.36}$$

The eigenvalues used in Roe's scheme are given as

$$\begin{aligned}
\hat{\lambda}_1 &= \hat{q} - \hat{c}, \\
\hat{\lambda}_2 &= \hat{q}, \\
\hat{\lambda}_3 &= \hat{q} + \hat{c}, \\
\hat{\lambda}_4 &= \hat{q}, \\
\hat{\lambda}_5 &= \hat{q}.
\end{aligned} \tag{1.37}$$

The wave strengths used in Roe's scheme are given as

$$\begin{aligned}
\hat{\alpha}_1 &= \tfrac{1}{2\hat{c}^2}[(P_R - P_L) - \hat{\rho}\hat{c}(q_R - q_L)], \\
\hat{\alpha}_2 &= (\rho_R - \rho_L) - \tfrac{1}{\hat{c}^2}(P_R - P_L), \\
\hat{\alpha}_3 &= \tfrac{1}{2\hat{c}^2}[(P_R - P_L) + \hat{\rho}\hat{c}(q_R - q_L)], \\
\hat{\alpha}_4 &= \hat{\rho}(k_R - k_L) + \hat{\alpha}_2(\hat{k} - 1), \\
\hat{\alpha}_5 &= \hat{\rho}(\omega_R - \omega_L) + \hat{\alpha}_2(\hat{\omega} - 1).
\end{aligned} \tag{1.38}$$

The right-eigenvectors used in Roe's scheme are given as

$$\begin{aligned}
\hat{K}^{(1)} &= [1, \quad \hat{u} - \hat{c}n_x, \quad \hat{v} - \hat{c}n_y, \quad \hat{w} - \hat{c}n_z, \quad \hat{H} - \hat{c}\hat{q}, \quad \hat{k}, \quad \hat{\omega}]^T \\
\hat{K}^{(2)} &= [1, \quad \hat{u}, \quad \hat{v}, \quad \hat{w}, \quad \hat{z}, \quad 1, \quad 1]^T, \\
\hat{K}^{(3)} &= [1, \quad \hat{u} + \hat{c}n_x, \quad \hat{v} + \hat{c}n_y, \quad \hat{w} + \hat{c}n_z, \quad \hat{H} + \hat{c}\hat{q}, \quad \hat{k}, \quad \hat{\omega}]^T, \\
\hat{K}^{(4)} &= [0, \quad 0, \quad 0, \quad 0, \quad 0, \quad 1, \quad 0]^T, \\
\hat{K}^{(5)} &= [0, \quad 0, \quad 0, \quad 0, \quad 0, \quad 0, \quad 1]^T.
\end{aligned} \tag{1.39}$$

The vector $\hat{C}$ used in Roe's scheme is

$$\begin{aligned}
\hat{C}_1 &= 0, \\
\hat{C}_2 &= (u_R - u_L) - (q_R - q_L)n_x, \\
\hat{C}_3 &= (v_R - v_L) - (q_R - q_L)n_y, \\
\hat{C}_4 &= (w_R - w_L) - (q_R - q_L)n_z, \\
\hat{C}_5 &= (u_R - u_L)\hat{u} + (v_R - v_L)\hat{v} + (w_R - w_L)\hat{w} - (q_R - q_L)\hat{q}, \\
\hat{C}_6 &= 0, \\
\hat{C}_7 &= 0.
\end{aligned} \tag{1.40}$$

The solution of Roe's scheme is a linearized Riemann problem solution that consists of discontinuous jumps across the waves only. This is a good approximation for contact and shock waves, but the size of the jump may not always be correctly approximated by using a linearized solution. Rarefaction waves are not discontinuous in nature and actually have a continuous change from the head to the tail. Quite clearly, approximating the rarefaction wave as a discontinuous wave is not exact. In practice approximating the rarefaction wave as a discontinuity works rather well, unless the rarefaction wave is strong enough to create a near vacuum state or a sonic point exists in the Riemann fan. In both of these cases the Roe scheme can fail without corrections.

If the rarefaction wave is strong enough to create a near vacuum state the Roe scheme can predict a negative density or internal energy which is nonphysical. A scheme that predicts negative

densities or internal energies is not "positively conservative" [Einfeldt et al. 1991]. The reason for this failure with Roe's scheme is that the Roe-average eigenvalue associated with the rarefaction wave is approximated to a small magnitude. This causes the Roe scheme to miss important information that is inside the rarefaction wave, causing the method to fail. To correct this problem a modification to the non-linear eigenvalues suggested by Einfeldt et al. (1991) is often used

$$|\lambda_1^{PC}| = \min[|\hat{\lambda}_1|, (q_L - c_L)] \quad \text{and} \quad |\lambda_3^{PC}| = min[|\hat{\lambda}_3|, (q_R + c_R)]. \tag{1.41}$$

The second failing of the Roe scheme is in predicting a sonic point across a rarefaction wave, which is nonphysical. This is commonly called a rarefaction shock and is due to using the Rankine-Hugoniot jump conditions across a continuous rarefaction wave. The positively conservative correction does a good job in reducing the discontinuity from the rarefaction shock due to the dissipation added by widening the rarefaction wave. However, in many cases the rarefaction wave can still have a small discontinuity around the sonic point. To correct this Harten's entropy fix is often added to Roe's scheme

$$|\lambda_{1,3}^{EF}| = \begin{bmatrix} |\lambda_{1,3}^{PC}| & \text{where} \quad |\lambda_{1,3}^{PC}| \geq \epsilon_{1,3} \\ \frac{|\lambda_{1,3}^{PC}|^2 + \epsilon_{1,3}^2}{2\epsilon_{1,3}} & \text{where} \quad |\lambda_{1,3}^{PC}| < \epsilon_{1,3} \end{bmatrix} \tag{1.42}$$

where

$$\epsilon_{1,3} = \max[0, (\lambda_{1,3}|_R - \lambda_{1,3}|_L)] \tag{1.43}$$

and $|_L$ and $|_R$ denoting to evaluate the given quantity at the left and right states.

Since Roe's scheme exactly captures the contact wave the scheme is suspectable to the carbuncle phenomenon. Similar to the entropy fix for the rarefaction waves of the Roe scheme there is a entropy fix that can be applied to the contact waves to eliminate the carbuncle phenomenon. With this entropy fix the exact representation of a stationary contact wave is lost. This could lead to some situations where the boundary layer is not accurately captured.

The entropy fix commonly applied to the contact wave is from Lin (1995):

$$|\lambda_2^{EF}| = \begin{bmatrix} |\hat{\lambda}_2| & \text{where} \quad |\hat{\lambda_2}| \geq \epsilon_2 \\ \frac{|\hat{\lambda}_2|^2+\epsilon_2^2}{2\epsilon_2} & \text{where} \quad |\hat{\lambda}_2| < \epsilon_2 \end{bmatrix} \tag{1.44}$$

where ϵ_2 is proportional to the Roe-averaged spectral radius:

$$\epsilon_2 = K * (\hat{q} + \hat{c}) \tag{1.45}$$

where K is a user defined constant.

It should be noted that none of the mentioned corrections to Roe's scheme fit into the formulation of Roe's scheme, but are corrections made after the fact.

1.2.5.3 van Leer Flux Splitting

FVS schemes have the interface fluxes constructed as a combination of forward and backward component flux vectors, that depend on the sign of the associated eigenvalues. This is accomplished by splitting the conservative flux $\mathbf{F}$ into two components F^+ and F^- such that

$$\mathbf{F}(U) = \mathbf{F}^+(U) + \mathbf{F}^-(U) \tag{1.46}$$

with the restrictions that the eigenvalues $\hat{\lambda}_i^+$ and $\hat{\lambda}_i^-$ of the Jacobian matrices

$$\hat{A}^+ = \frac{\partial F+}{\partial U} \quad \text{and} \quad \hat{A}^- = \frac{\partial F+}{\partial U} \tag{1.47}$$

satisfy the conditions

$$\hat{\lambda}_i^+ \geq 0 \quad \text{and} \quad \hat{\lambda}_i^- \leq 0. \tag{1.48}$$

The splitting is also required to reproduce regular upwinding when all the eigenvalues λ_i of the

Jacobian matrix $\mathbf{A}$ are one sided (all positive, all negative, or all zero). From the splitting of the fluxes we have the following properties:

$$\mathbf{A} = \mathbf{A}^+ + \mathbf{A}^- = \mathbf{K}\Lambda^+\mathbf{K}^{-1} + \mathbf{K}\Lambda^-\mathbf{K}^{-1} \tag{1.49}$$

with $\mathbf{K} = [\mathbf{K}^{(1)}, \mathbf{K}^{(1)}, \mathbf{K}^{(1)}]$ being the right eigenvectors of $\mathbf{A}$ and Λ is a diagonal matrix containing the eigenvalues of $\mathbf{A}$. The fluxes can also be split as:

$$\mathbf{F} = \mathbf{F}^+ + \mathbf{F}^- = \mathbf{A}^+\mathbf{U} + \mathbf{A}^-\mathbf{U} \tag{1.50}$$

The main difference with van Leer FVS scheme and other FVS schemes are that some extra desirable properties are enforced in the derivation:

- The split Jacobian matrices ($\hat{A}^+$ and $\hat{A}^-$) are required to be continuous.
- The split fluxes are degenerate for subsonic flows, that is $\hat{A}^+$ and $\hat{A}^-$ have a zero eigenvalue.

To accomplish this van Leer (1982) expresses $\mathbf{F}$ as a function of density, speed of sound, and Mach number $M = u/c$,

$$\mathbf{F} = \mathbf{F}(\rho, c, M) = \begin{bmatrix} \rho c M \\ \rho c^2(M^2 + \frac{1}{\gamma}) \\ \rho c^3 M(\frac{1}{2}M^2 + \frac{1}{\gamma - 1}) \end{bmatrix}. \tag{1.51}$$

The mass flux, $f_{mass} = \rho c M$, are split by requiring quadratics in M be split as

$$f^+_{mass} = \frac{1}{4}\rho c_L(1 + M_L)^2 \quad \text{and} \quad f^-_{mass} = -\frac{1}{4}\rho c_R(1 - M_R)^2. \tag{1.52}$$

The momentum fluxes are split as

$$f^+_{mom} = f^+_{mass}\frac{2c_L}{\gamma}[\frac{\gamma-1}{2}M_L + 1] \quad \text{and} \quad f^-_{mom} = f^-_{mass}\frac{2c_R}{\gamma}[\frac{\gamma-1}{2}M_R - 1], \tag{1.53}$$

and the energy fluxes are split as

$$f^+_{ene} = \frac{\gamma^2}{2(\gamma^2-1)}\frac{[f^+_{mom}]^2}{f^+_{mass}} \quad \text{and} \quad f^-_{ene} = \frac{\gamma^2}{2(\gamma^2-1)}\frac{[f^-_{mom}]^2}{f^-_{mass}}. \tag{1.54}$$

The above equations can be put into vector form and reformulated to include the cell faces having arbitrary orientations for the three-dimensional Euler equations. For the three-dimensional formulation the Mach number is now $M = q/c$ and n_x, n_y, and n_z are the x,y,z-components of the outward normal vector of the cell faces. There are three different results that the van Leer split fluxes can have depending on if the flow is supersonic to the left, supersonic to the right, or subsonic.

Case (a) -Left supersonic flow: all eigenvalues of $\mathbf{A}$ are negative and the split fluxes are

$$\mathbf{F}^+ = \mathbf{0} \quad \text{and} \quad \mathbf{F}^- = \mathbf{F}_L. \tag{1.55}$$

Case (b) -Right supersonic flow: all eigenvalues of $\mathbf{A}$ are positive and the split fluxes are

$$\mathbf{F}^+ = \mathbf{F}_R \quad \text{and} \quad \mathbf{F}^- = \mathbf{0}. \tag{1.56}$$

Case (c) -Subsonic flow: mixed eigenvalues of $\mathbf{A}$ (at least one positive and negative eigenvalue)

and the split fluxes are

$$\mathbf{F}^{+} = \frac{1}{4}\rho_L c_L (1+M_L)^2 \begin{bmatrix} 1 \\ u_L - \frac{\gamma}{\gamma-1}[q_L - 2c_L]n_x \\ v_L - \frac{\gamma}{\gamma-1}[q_L - 2c_L]n_y \\ w_L - \frac{\gamma}{\gamma-1}[q_L - 2c_L]n_z \\ \frac{1}{2}[\frac{1}{\gamma+1}q_L + \frac{1}{\gamma-1}2c_L] + \frac{1}{2}(u_L^2 + v_L^2 + w_L^2 - q_L^2) \end{bmatrix}. \tag{1.57}$$

and

$$\mathbf{F}^{-} = -\frac{1}{4}\rho_R c_R (1-M_R)^2 \begin{bmatrix} 1 \\ u_R - \frac{\gamma}{\gamma-1}[q_R + 2c_R]n_x \\ v_R - \frac{\gamma}{\gamma-1}[q_R + 2c_R]n_y \\ w_R - \frac{\gamma}{\gamma-1}[q_R + 2c_R]n_z \\ \frac{1}{2}[\frac{1}{\gamma+1}q_R - \frac{1}{\gamma-1}2c_R] + \frac{1}{2}(u_R^2 + v_R^2 + w_R^2 - q_R^2) \end{bmatrix}. \tag{1.58}$$

Since the van Leer scheme cannot accurately capture a contact wave the scheme is not susceptible to the carbuncle phenomenon. The van Leer scheme, however, has difficulty in accurately capturing the boundary layer due to the artificial dissipation added by not accurately capturing the contact wave.

1.2.5.4 HLL Scheme

The HLL scheme stands for **H**arten, **L**ax, and van **L**eer who proposed a novel idea of approximating the intercell numerical flux directly. The HLL and HLLC methods are both integral averaged state Riemann methods. For the HLL Riemann solver it is assumed that the solution consists of a single $\mathbf{U}^*$ state separated by two waves of speed S_L and S_R as shown in Figure 1.7. For the derivation of the HLL scheme it is assumed that the wave speeds S_L and S_R are known before the flux calculations. With the two wave speeds known, the Riemann problem can be integrated over the control volume

$[x_L, x_R] \times [0, T]$ to obtain the integral average solution of the Riemann problem between S_L and S_R:

$$\mathbf{U}^* = \frac{(\mathbf{F}_L - S_L\mathbf{U}_L) - (\mathbf{F}_R - S_R\mathbf{U}_R)}{S_R - S_L}. \tag{1.59}$$

To find the flux $\mathbf{F}^*$ we use the Rankine-Hugoniot jump conditions across the left and right waves,

$$\mathbf{F}^* = \mathbf{F}_L + S_L(\mathbf{U}^* - \mathbf{U}_L) \quad \text{and} \quad \mathbf{F}^* = \mathbf{F}_R + S_R(\mathbf{U}^* - \mathbf{U}_R), \tag{1.60}$$

from which the HLL flux between S_L and S_R can easily be obtained,

$$\mathbf{F}^* = \frac{S_R\mathbf{F}_L - S_L\mathbf{F}_R + S_LS_R(\mathbf{U}_R - \mathbf{U}_L)}{S_R - S_L}. \tag{1.61}$$

Putting it all together we have that the HLL approximate Riemann solver conserved variables and fluxes can be given as

$$\mathbf{U}^{HLL} = \begin{cases} \mathbf{U}_L & \text{if} \quad S_L > 0, \\ \mathbf{U}^* = \frac{(\mathbf{F}_L - S_L\mathbf{U}_L) - (\mathbf{F}_R - S_R\mathbf{U}_R)}{S_R - S_L} & \text{if} \quad S_L < 0 < S_R, \\ \mathbf{U}_R & \text{if} \quad S_R < 0, \end{cases} \tag{1.62}$$

and

$$\mathbf{F}^{HLL} = \begin{cases} \mathbf{U}_L & \text{if} \quad S_L > 0, \\ \mathbf{F}^* = \frac{S_R\mathbf{F}_L - S_L\mathbf{F}_R + S_LS_R(\mathbf{U}_R - \mathbf{U}_L)}{S_R - S_L} & S_L < 0 < S_R, \\ \mathbf{F}_R & \text{if} \quad S_R < 0. \end{cases} \tag{1.63}$$

The only thing missing from being able to calculate $\mathbf{F}^*$ is determining the the wave speeds S_L and S_R using information from the left and right states only. This is a very critical step in the HLL scheme, because if one or both of the wave speeds are small in magnitude, the algorithm can potentially miss information that exists in the true Riemann fan and the method can be unstable. If the wave speeds are calculated to be too large in magnitude, then information from outside the

Riemann fan will be included in the flux and the scheme will be overly dissipative.

The wave speed estimate of Einfeldt et al. (1991) is used due its desirable properties. The HLL scheme with the wave speeds of Einfeldt et al. (1991) is often referred to in the literature as the HLLE scheme. For this work the HLL scheme uses the wave speed estimate of Einfeldt et al. (1991) unless otherwise noted. The wave speed estimates of Einfeldt et al. (1991) use the Roe-averaged non-linear eigenvalues [Roe 1981]

$$S_L = \min(|\hat{\lambda}_1|, (q_L - c_L)) \quad \text{and} \quad S_R = \max(|\hat{\lambda}_3|, (q_R + c_R)) \tag{1.64}$$

where $\hat{\lambda}_{1,3}$ are the Roe-average non-linear eigenvalues. Batten et al. (1997) proves using the Roe-averaged nonlinear eigenvalues in conjunction with the HLL method ensures that the scheme will exactly capture stationary shocks and be free of rarefaction shocks without an entropy fix. The use of the above wave speed estimates also ensures that the method is positively conservative. A positively conservative scheme will always generate positive density, pressure, internal energy, and species mass fractions from initial conditions that are physically realizable. Physically realizable initial conditions are where the density, pressure, and speed of sound are finite and greater than zero, the velocity is finite, and the ratio of specific heats is greater than one. As a consequence of these properties it is impossible for the HLLE method to generate a vacuum state, even when such a state should exist theoretically. As an aside, the exact Riemann solver is also positively conservative, but only when the initial conditions do not cause a vacuum state.

1.2.5.5 HLLC Scheme

The HLLC scheme builds upon the HLL method by adding the contact wave to the Riemann fan (**C** stands for contact wave). To derive the HLLC scheme the wave problem is integrated over the control volume $[x_L, x_R] \times [0, T]$ to obtain an integral average solution of the Riemann problem between S_L and S_R.

The HLLC scheme includes the contact wave, with a wave speed of S_M, in the Riemann fan. With the middle contact wave included, the Star Region consists of two constant states separated from each other by the middle wave of speed S_M. With integration over the control volume this gives us two integral averages, $\mathbf{U}_L^*$ and $\mathbf{U}_R^*$, that can be related to the $\mathbf{U}^*$ found using the HLL scheme:

$$\left(\frac{S_M - S_L}{S_R - S_L}\right)\mathbf{U}_L^* + \left(\frac{S_R - S_M}{S_R - S_L}\right)\mathbf{U}_R^* = \mathbf{U}_{HLL}^*. \tag{1.65}$$

If we apply the Rankine-Hugoniot jump conditions across each of the waves of speeds S_L, S_M, and S_R we obtain

$$\begin{aligned} \mathbf{F}_L^* &= \mathbf{F}_L + S_L(\mathbf{U}_L^* - \mathbf{U}_L), \\ \mathbf{F}_R^* &= \mathbf{F}_L^* + S_M(\mathbf{U}_R^* - \mathbf{U}_L^*), \\ \mathbf{F}_R^* &= \mathbf{F}_R + S_R(\mathbf{U}_R^* - \mathbf{U}_R). \end{aligned} \tag{1.66}$$

Using the fact that the pressure and velocity-component normal to the contact wave are constant across contact waves we have

$$\begin{aligned} q_L^* = q_R^* = q^*, \\ P_L^* = P_R^* = P^*, \\ S_M = q^*. \end{aligned} \tag{1.67}$$

Using Equations 1.65 - 1.66 with the conditions of Equation 1.67 we can solve for the four unknown vectors of $\mathbf{U}_L^*$, $\mathbf{U}_R^*$, $\mathbf{F}_L^*$, and $\mathbf{F}_R^*$,

$$\mathbf{U}_{L,R}^* = \begin{bmatrix} \rho_L \frac{S_{L,R} - q_{L,R}}{S_{L,R} - S_M} \\ u_{L,R} + (S_M - q_{L,R})n_x \\ v_{L,R} + (S_M - q_{L,R})n_y \\ w_{L,R} + (S_M - q_{L,R})n_z \\ E_{L,R} + (S_M - q_{L,R})\left(S_M + \frac{P_{L,R}}{\rho_{L,R}(S_{L,R} - q_{L,R})}\right) \end{bmatrix}. \tag{1.68}$$

Putting it all together we have

$$\mathbf{U}^{hllc} = \begin{cases} \mathbf{U}_L & \text{if} \quad S_L > 0, \\ \mathbf{U}_L^* & \text{if} \quad S_L < 0 < S_M, \\ \mathbf{U}_R^* & \text{if} \quad S_M < 0 < S_R, \\ \mathbf{U}_R & \text{if} \quad S_R < 0. \end{cases} \tag{1.69}$$

The fluxes for the HLLC approximate Riemann solver are given as

$$\mathbf{F}^{hllc} = \begin{cases} \mathbf{F}_L & \text{if} \quad S_L > 0, \\ \mathbf{F}_L^* = \mathbf{F}_L + S_L(\mathbf{U}_L^* - \mathbf{U}_L) & \text{if} \quad S_L < 0 < S_M, \\ \mathbf{F}_R^* = \mathbf{F}_R + S_R(\mathbf{U}_R^* - \mathbf{U}_R) & \text{if} \quad S_M < 0 < S_R, \\ \mathbf{F}_R & \text{if} \quad S_R < 0. \end{cases} \tag{1.70}$$

For the HLLC technique the middle wave speed, S_M, (or equivalently the degenerate eigenvalues) must also be solved for in addition to solving for S_L and S_R using the wave speed estimates of Einfeldt et al. (1991). The wave speed estimate of Batten et al. (1997) is used to estimate S_M since Einfeldt's estimate allows the HLLC method to exactly capture stationary contact discontinuities. The wave speed estimate of Einfeldt et al. (1991) requires that S_M matches the average velocity in the HLL two-wave Riemann fan, this gives

$$S^* = \frac{P_R - P_L + \rho_L q_L(S_L - q_L) - \rho_R q_R(S_R - q_R)}{\rho_L(S_L - q_L) - \rho_R(S_R - q_R)}. \tag{1.71}$$

This relation for S_M guarantees that:

- the velocity is constant across the contact wave: $q_L^* = u_R^* = S_M$,
- constituency with the HLL scheme: $S_M = q_{HLL}^*$,
- the pressure is constant across the contact waves.

1.2.5.6 HLLEM scheme

The HLLEM scheme [Park and Kwon 2003] builds upon the above discussion by more accurately capturing the contact discontinuity by reusing information from the HLL flux. This is done by using the original HLL fluxes to figure out how much excessive dissipation to take out of the fluxes. The flux of the intermediate state of the HLL scheme is:

$$\mathbf{F}^{HLL} = \frac{S_R\mathbf{F}_L - S_L\mathbf{F}_R}{S_R - S_L} + \frac{S_L S_R}{S_R - S_L}(\mathbf{U}_R - \mathbf{U}_L) \tag{1.72}$$

where $\mathbf{U}$ is the conservative flow variable, $\mathbf{F}$ is the inviscid flux, S_L is the speed at which left nonlinear wave travels, and S_R is the speed at which the right nonlinear wave travels. S_R and S_L are the lower and upper bounds at which a physical signal can be transmitted by the initial discontinuity. To calculate S_L and S_R the wave speed estimate of Einfeldt (1988) (see Equation 1.64) is used. Using the wave speed estimates of Einfeldt (1988) with the HLL or HLLC scheme ensures that the schemes satisfy the entropy and positivity conditions and that the schemes can exactly capture stationary shocks.

Dissipation was first taken out of the HLL scheme by Einfeldt et al. (1991) using the numerical flux function HLLEM scheme which can be written as

$$\mathbf{F}^{HLLEM} = \mathbf{F}^{HLL} - \frac{S_L S_R}{S_R - S_L}\sum_{p=1}^{5}\bar{\delta}\alpha^p\mathbf{K}^p \tag{1.73}$$

where $\mathbf{K}^P$ are the right eigenvectors of the Roe scheme as shown in Equation 1.39 and α^p are the wave strengths of the Roe scheme as shown in Equation 1.38. The $\bar{\delta}$ term is the anti-diffusion coefficient that is used to take out extra dissipation that arises from neglecting the contact wave in

the analysis. The anti-diffusion coefficient $\bar{\delta}$ is defined as

$$\bar{\delta} = \begin{bmatrix} 0 \\ \frac{\hat{c}}{|S_M|+\hat{c}} \\ 0 \\ \frac{\hat{c}}{|S_M|+\hat{c}} \\ \frac{\hat{c}}{|S_M|+\hat{c}} \end{bmatrix} \tag{1.74}$$

where $\hat{c}$ is the Roe-averaged speed of sound and S_M is the approximate speed of the contact wave. The first and third terms are associated with the nonlinear waves (shock or rarefaction wave), so dissipation is not taken out of these terms.

The HLLEM scheme can capture boundary layers as effectively as the HLLC and Roe schemes due to the low dissipation of the scheme. The low dissipation of the HLLEM scheme makes the scheme prone to the carbuncle phenomenon like the HLLC and Roe schemes. Park and Kwon (2003) show that if the contact wave speed, S_M, is close to zero in the shock region, then the HLLEM scheme is prone to the carbuncle phenomenon and $\bar{\delta} \cong 1.0$. If S_M is not close to zero then the HLLEM scheme is not prone to the carbuncle phenomenon and $\bar{\delta} \neq 1.0$.

1.2.5.7 HLL+ scheme

To prevent the carbuncle phenomenon from occurring when using the HLLEM scheme Park and Kwon (2003) proposed the HLL+ scheme. The HLL+ scheme uses a switching mechanism to set the contact wave speed to be $S_M = \hat{c}$ near regions where it detected a shock instability could occur. Setting the contact wave speed to be the Roe-averaged speed of sound results in a non-zero contact wave speed, and thus prevents the carbuncle phenomenon. This approach is very close to Harten's entropy fix where the eigenvalues of the contact wave speed are prevented from having a zero value in regions near the shock.

2

Literature Survey of the Carbuncle Phenomenon

This chapter will give a brief background of the carbuncle phenomenon. The effect of the numerical shock structure and the numerical dissipation, added by the Riemann solver, on the carbuncle phenomenon will also be discussed. Several proposed cures to the carbuncle phenomenon will be discussed along with alternative numerical methods to solve the Navier-Stokes equations. This chapter will end with a literature survey of the effect of how the shock alignment with the mesh effects the accuracy of the surface heat fluxes of a blunt body.

2.1 Introduction

It is worth noting that not all upwind Riemann solvers suffer from the carbuncle phenomenon. Pandolfi and D'Ambrosio (2001) show that the carbuncle phenomenon only occurs with schemes that are able to capture the contact and shear discontinuities exactly. Schemes that are capable of doing this have low numerical dissipation. The HLLC [Batten et al. 1997; Toro 1999; Toro et al. 1994] scheme and Roe's [Roe 1981; Roe and Pike 1984] scheme can exactly capture the contact

and shear waves. Methods that do not exactly capture the contact and shear waves, such as the HLL [Batten et al. 1997; Toro 1999; Toro et al. 1994] method, are not susceptible to the carbuncle problem. This trend can be seen in Figure 2.1, which shows Roe's scheme having a bulge in the bow shock and the HLLC scheme producing incorrect density contours near the stagnation streamline. On the other hand the HLL scheme captures the density contours correctly. The methods that do not suffer from the carbuncle problem, such as HLL, are undesirable for use on flows with shear layers. The inability of these techniques to exactly capture the contact waves introduces excessive numerical dissipation into the solution and this can lead to incorrect predictions of the boundary layers [Lin 1995].

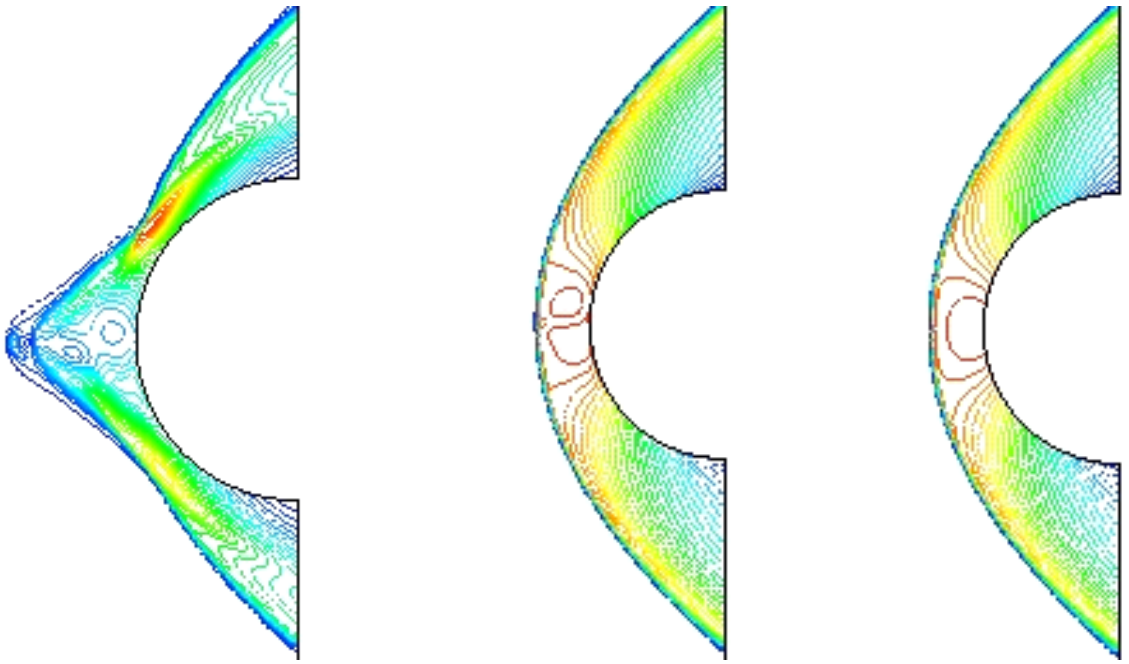

(a) Roe Scheme. (b) HLLC Scheme. (c) HLL Scheme.

Figure 2.1: Density contours for a Mach 20 blunt body.

Roe et al. (2005) breaks down the development of the carbuncle phenomenon into three stages:

Stage 1: "Pimples": The first stage has instabilities in the form of spots contained within the shock. These spots travel back and forth parallel to the shock perturbing the conservative and primitive variables. The exact structure of these spots depends on how the shock instability

is seeded from the initial data. These spots also produce blobs of spurious vorticity that are convected downstream of the shock.

Stage 2: "Bleeding": Depending on the upstream Mach number and the flux functions used, the first stage of pimples does not last very long. The pimples will bleed downstream of the shock forming a series of converging and diverging jets. The converging jets have the faster velocity which can be supersonic and the diverging jets possess a slower subsonic velocity. These velocity disturbances grow until the slow jets are virtually stagnant. This flow imbalance near the shock will cause a region of flow downstream of the shock to reverse its direction and penetrate the shock in the upstream direction.

Stage 3: "Carbuncles": Once the flow reversal begins, the normal shock breaks down into several self-similar regions featuring oblique shocks. These oblique shocks form a wedge shaped region downstream of the shock where the fluid flow is almost stagnant. In general, this wedge shaped region contains two rotating vortices that are roughly of the same magnitude and rotate in different directions. In general the two rotating vortices are not equivalent in magnitude and not symmetric. The angles of the oblique shocks are almost identical from run to run if the freestream conditions are kept the same. When the upstream Mach number is changed, the oblique angle shock changes slightly, but the overall pattern stays the same.

The first reporting of the carbuncle phenomenon was by Peery and Imlay (1988) for the computation of a supersonic flowfield around a blunt body. A simpler form of the carbuncle phenomenon has been demonstrated by Quirk (1994) for a one-dimensional shock propagating down a duct with the centerline grid perturbed by 10^{-6} of the channel width. These small perturbations in the grid result in the shock breaking up and taking on a shape similar to that of a carbuncle on a blunt body. This numerical simulation is often called Quirk's test. Other numerical instabilities that are similar to the carbuncle phenomenon include the double Mach reflection problem. The double Mach reflection problem has been reported for a moving shock on a 30° ramp by Quirk (1994), on

conical shock waves around slender bodies by Korte (1991), and for interstellar flow computations in astrophysics by Walder (1993). It is believed that if a numerical instability is seen in Quirk's test for a particular Riemann solver, then the carbuncle phenomenon also exists for blunt bodies.

The carbuncle phenomenon resembles experimentally measured two-dimensional flows [van Dyke 1982] and axisymmetric flows [Bogdonoff and Vas 1959] with some type of perturbation introduced upstream of the stagnation point. The perturbations are added to the flows with dust particles injected along the stagnation line [Holden 1983], or with energy deposited ahead of the shock [Riggins et al. 1999], or other methods. In numerical and physical experiments of mildly disturbed hypersonic blunt body flows Hornung and Lemieux (2001) have observed a shear layer instability that causes production of shock-perturbing and self-reinforcing vortices. Roe et al. (2005) state that these carbuncle-like phenomenon are not observed experimentally, unless provoked by some artificial perturbation ahead of the stagnation point, and this takes time to develop. From a computational perspective the carbuncle appears very quickly at a very small scale, one that would not be visible experimentally, and then gradually grows.

Even though the carbuncle phenomenon may lead to an incorrect steady state solution, Pandolfi and D'Ambrosio (2001) and other authors have noted that the carbuncle phenomenon passes all tests for the weak solution to the Euler equations. The shocks satisfy the Rankine-Hugoniot jump conditions and are compressive, entropy satisfying discontinuities. This means that carbuncles can physically occur and maybe we should not be so surprised when they show up computationally. The difference between the computational situations and the physical situation is that it takes much less of a perturbation computationally to cause the carbuncle phenomenon.

Roe (2005b) and Elling (2005; 2006) state that the carbuncle phenomenon is another entropy-satisfying solution that arises from the same initial data. The nonphysical entropy solution of the carbuncle phenomenon results from having insufficient dissipation interior to the shock and a perturbation being applied in the shock. In an experimental setting a hypersonic blunt body can produce a flowfield similar to the carbuncle phenomenon, except that the physical shock has more

dissipation and requires a larger perturbation to initiate the shock instability.

Pandolfi and D'Ambrosio (2001) also took a detailed look at the carbuncle phenomenon and gave numerous insights into its behavior. They state that the carbuncle phenomenon originates inside the narrow computational region where a normal shock is numerically captured. Round-off error in the computation can be the cause of the disturbance which can magnify to a noticeable disturbance in the flow solution.

2.1.1 Effect of Artificial Viscosity on the Carbuncle Phenomenon

LeVeque et al (1998) state that the numerical approximation of a shock wave is not a sharp discontinuity, but is smeared over one or more grid cells. Using a shock-capturing method to solve the Riemann problem for a single traveling shock for a nonlinear system such as the Euler equations can introduce nonphysical rarefaction and contact/shear waves in the smeared shock region. In most cases the shocks are captured rather well with very little noise from the nonphysical rarefaction and contact/shear waves. This is because most Riemann fluxes mimic the physical dissipation that is natural in viscous shocks (viscosity and heat conduction). As long as the numerical viscosity is of sufficient magnitude, the discrete shock will behave as a physical shock and not introduce nonphysical rarefaction and contact/shear waves.

Xu and Hu (1998) and Xu (1999) state that Riemann solvers implicitly assume that the gas at the faces of the cell is in an equilibrium state, whatever the actual flow situation. This can cause problems for the points that are interior to the numerical shock region, since this state is not in equilibrium. Also in a physical shock there is a large amount of dissipation present to convert kinetic energy to thermal energy and provide a smooth shock transition. However, when using Riemann solvers there is no implicit dissipation that exists inside the shock, and the only dissipation present is artificial dissipation. Xu and Hu (1998) and Xu (1999) state that no perfect Riemann solver will be obtained if the inviscid Euler equations are regarded as the governing equations. Artificial dissipation alone could hardly provide "appropriate and consistent" dissipation needed to prevent the carbuncle

instability. In order to have a more accurate and robust numerical scheme for compressible flow simulations, the viscous governing equations should be solved directly in the region of the shock [Xu 1999].

2.1.2 Effect of Shock Structure on the Carbuncle Phenomenon

Dumbser et al. (2004) state that the carbuncle phenomenon is not only governed by the upstream Mach number but also by the shock's internal structure. The stability of the shock is governed by where the state of the intermediate point in the shock is located. If the state of the intermediate point is sufficiently close to the downstream state, then any Riemann solver will be carbuncle free no matter how high the upstream Mach number [Chauvat et al. 2005]. The above finding may give some insight into when the carbuncle phenomena occurs, but a practical cure to the carbuncle phenomenon would involve modifying the flux functions to the Riemann solvers to force the intermediate point to be close to the downstream state.

It has also been shown by Dumbser et al. (2004) that the source of the carbuncle phenomenon is immediately upstream of the shock and the instability is convected downstream. This would explain why shock fitting schemes do not suffer from the carbuncle phenomenon, since they only capture the flow on the downstream side of the shock.

Kitamura et al. (2007) state that a shock wave is analytically regarded as a thin jump discontinuity, but the captured shock has internal structure. For example, the Godunov and Roe schemes both produce an intermediate state that lies on the Hugoniot curve joining $\mathbf{U}_R$ and $\mathbf{U}_L$, but the state does not preserve mass flux inside the shock. For all Riemann solvers at least one intermediate state is needed to represent a shock that is not located at a mesh interface.

The carbuncle phenomenon is often associated with multidimensional cases but Barth (1989) points out that one-dimensional steady shocks sometimes have a hard time being captured as a steady shock. Barth (1989) points out that the stability of the solution depends on the location of the shock with respect to the mesh. Several popular flux functions such as Godunov and Roe do not

produce steady one-dimensional shocks for all intermediate locations of the shock. Kitamura et al. (2007) point out this problem may be related to the failure of flux functions to satisfy the Second Law of Thermodynamics for intermediate states inside the captured shock.

To investigate hypersonic shock stability within a common framework for an upwind shock capturing scheme Kitamura et al. (2007) performed a broad range of numerical experiments where the relative position of the intermediate shock point was varied using a large range of popular upwind capturing schemes. From the numerical experiments it was found that only the Roe scheme with Harten's entropy fix [Harten 1983] and Roe's EC1-RV2 scheme [Ismail 2006] was found to be stable for all positions of the shock relative to the grid. The Roe EC1-RV2 scheme is a modified version of the standard Roe scheme were the Second Law of Thermodynamics is enforced locally. Contrary to claims of some upwind shock capturing schemes it was also found that no upwind shock capturing scheme was stable for all positions of the shock relative to the grid for multidimensional steady shocks. It was also found that if a one-dimensional steady shock was stable for a particular shock location and Mach number then this was a necessary condition for a flux function to be stable for the corresponding multidimensional case, but did not guarantee that the multidimensional shock would be stable.

Kitamura et al. (2007) also state that to eliminate the carbuncle phenomenon some form of multidimensional dissipation or a multidimensional upwind shock-capturing scheme is required. Kitamura et al. (2007) also state that the AUSMPW+ [Kim et al. 2001] and RoeM2 [Kim et al. 2003] schemes use multidimensional dissipation, but neither can be formulated for use on unstructured grids.

2.2 Proposed Cures for Carbuncle Phenomenon

Most cures for the carbuncle phenomena involve adding more dissipation to the scheme, but this leads to a loss of accuracy, since the scheme no longer captures the contact and shear wave exactly.

Most of the cures to the carbuncle phenomenon involve modifying the Riemann solver. Another approach to eliminating the carbuncle phenomenon is to use a numerical method other than a Riemann solver to solve the Navier-Stokes equations. For these alternative numerical methods to be practical they cannot have too great of a computational cost.

2.2.1 Proposed Cures using Riemann solvers

There are three main types of cures proposed to overcome the numerical instability caused by the carbuncle phenomenon. It has been suggested that the carbuncle phenomenon arises from an unfavorable coupling between the normal and perpendicular directions across the shock wave, which causes the numerical instability to occur on the perpendicular cell face. From this assumption it is not unreasonable to add artificial dissipation to these faces to prevent the carbuncle phenomenon. This class of cures is often referred to as an "entropy fix" which involves detecting the perpendicular cell faces that may have a numerical instability and adding sufficient numerical dissipation to prevent the numerical instability. The additional numerical dissipation is often added by limiting the minimum value of the wave speeds. The performance of the fix however depends on where the entropy fix is applied and the amount of numerical dissipation added [Kim et al. 2003]. An overly dissipative entropy fix may broaden the shock and deteriorate the boundary layer resolution [Kim et al. 2003]. Loh and Jorgenson (2007) recently proposed a model where artificial dissipation can be added to an existing Riemann solver. The artificial dissipation model is reported to be robust, time-accurate and works well with strong shocks, viscous flows, and acoustic waves.

A second proposed cure for the carbuncle problem comes from the hypothesis of Liou (2000). Liou states that the carbuncle phenomenon occurs for any flux function for which the mass flux across a cell interface depends on the pressure difference. Liou (2000) proposes that Riemann solvers can be designed that eliminate the pressure dependence of the mass flux; and that existing Riemann schemes can be modified to satisfy this hypothesis. Unfortunately, directly canceling the pressure terms from the mass flux degrades the stability of the Riemann solver and contradicts a fundamental physical

principle; a pressure difference produces a mass flux [Dumbser et al. 2004]. Liou's hypothesis has led to the development of the AUSM (Advected Upstream Splitting Method) scheme [Liou 2000] and other variants of the AUSM scheme that have this property.

If Liou's conjecture is true, it would imply that one could design a numerical flux function that does not show the carbuncle phenomenon and still maintains the exact resolution of the contact wave [Robinet et al. 2000]. This conclusion is in contradiction with Robinet et al.'s (2000) linear stability analysis which shows that strict stability for Quirk's test and exact resolution of the contact waves are incompatible. It should also be mentioned that both Ismail (2006) and Kitamura (2007) show that the AUSM schemes can suffer from the carbuncle phenomenon, but are less prone to the carbuncle phenomenon than other low dissipative upwind Riemann solvers.

Dumbser et al. (2004) state that Liou's conjecture (if the mass flux for a given numerical flux does not depend on pressure for any Mach number then the scheme is carbuncle free) should only apply to methods where the steady contact wave is exactly preserved. Using Quirk's case Liou (2000) and Moschetta (2001) have independently confirmed that introducing the mass flux of a carbuncle free scheme into a carbuncle prone scheme can eliminate the shock instability and vise versa. Dumbser et al. (2004) also state that Liou's observations indicate that the carbuncle phenomenon is a 2D shock instability whose origin lies in the formulation of the 1D numerical flux.

The third proposed class of cures for the carbuncle phenomenon involves the use of "blended" flux functions, which was first suggested by Quirk (1994). This method involves flagging cell faces that may have the carbuncle instability. To compute the flux across the flagged cells the Riemann solver is switched from the base Riemann solver, which captures the contact wave exactly, to the more dissipative partner which is a Riemann solver that does not capture the contact discontinuity exactly. This confines the use of the dissipative partner Riemann solver to areas of the flow where the strong shock is captured. Flux function blending is the method used by AVUS to stabilize strong shocks.

Most fixes to the carbuncle phenomenon degrade solution accuracy and often introduce tuning

parameters which must be adjusted for different flow problems [Quirk 1994; Donat and Marquina 1996]. Also, most fixes have little mathematical or physical basis [Liou 1994] and work by increasing dissipation levels.

2.2.2 Alternative Numerical Methods to Solve Navier-Stokes Equations

One suggestion for eliminating the carbuncle problem [Xu and Hu 1998; Xu 1999] is using the gas kinetic Bhatnagar-Gross-Krook (BGK) scheme [Bhatnagar et al. 1954] to solve the viscous governing equations where the dissipation is controlled by the collision time. The gas kinetic BGK scheme is used to solve multidimensional hypersonic viscous flows in Xu et al. (2005). The viscous results have good agreement with experimental results for a hypersonic blunt body and do not suffer from the carbuncle phenomenon. This is most likely since the gas kinetic BGK method solves the inviscid and viscous fluxes using a single distribution function. This causes the BGK method to better mimic the physical dissipation that is present in viscous shocks resulting in the viscous fluxes being more consistent with the Navier-Stokes equations.

The BGK scheme is a second-moment of the Boltzmann equation and accounts for the inviscid and viscous fluxes in a single distribution function. As mentioned before this causes the BGK method to better mimic the physical dissipation present in a viscous shock, thus providing enough dissipation to prevent the carbuncle phenomenon. Another work that has been proposed using the second-moment of the Boltzmann equation to solve for viscous flows is Suzuki and van Leer (2008). They propose replacing the Navier-Stokes equations with a set of first-order hyperbolic-relaxation PDEs, which contain the Navier-Stokes equations. The method they have proposed is cited as being more accurate and time efficient than using the Navier-Stokes equations.

The space-time Conservation Element Solution Element (CESE) method can be used to solve the Navier-Stokes equations for blunt bodies and does not seem to suffer from the carbuncle phenomenon. The formulation of the CESE method is different from typical upwind schemes where the inviscid fluxes are computed at the cell face, the viscous fluxes are calculated separately, and then the solution

is integrated forward in time.

The CESE method as proposed by Chang (1995) has been successfully used for a variety of multi-disciplinary computational physics problems including complex shock structures [Chang et al. 1999], aeroacoustic wave simulations [Loh et al. 2000], chemically reacting flows [Im et al. 2002], magneto-hydrodynamics [Zhang et al. 2006], and stress waves in solids [Cai et al. 2006]. The CESE method is second-order accurate in time and space for conservation laws and uses genuine multidimensional fluxes. The discretized equations conserve fluxes both locally and globally using a strong form of the conservation equations. The conserved variables are assumed to vary linearly with respect to time and all spatial directions. The numerical integration of the flux is carried out through a set of conservation elements that do not coincide with solution elements. This staggered arrangement of the conservation elements and solution element eliminates the need to solve a Riemann problem at the cell interfaces. The CESE method also differs from upwind schemes in that the fluxes are solved as a multidimensional space-time flux with the viscous fluxes calculated simultaneously with the inviscid fluxes.

The current largest problem with the CESE method is that the method becomes unstable when using high aspect ratio viscous meshes. The numerical problem becomes stiff when high aspect ratio cells are introduced. This causes difficulties in accurately capturing boundary layers that have steep gradients, as is often seen in hypersonic flows. This problem can be overcome by taking smaller time steps and/or using a method to calculate the fluxes that is more dissipative. This numerical instability is a separate phenomenon from the carbuncle phenomenon, since the carbuncle phenomenon occurs inside the shock and the numerical instability with the CESE method occurs in the boundary layer where the mesh has a very high aspect ratio.

Hypersonic blunt body results from Chang (2007) show excellent comparison between the CESE method and a shock fitting code for inviscid flow for both quadrilateral and tetrahedral unstructured grids. Chang (2007) also shows that the CESE method gives results for viscous blunt bodies in Mach 17 flow that do not suffer from the carbuncle phenomenon for both quadrilateral and tetrahedral

unstructured grids. Even though the CESE method gives heat transfer results that do not show signs of the carbuncle phenomenon, the CESE results have currently not been converged to steady state, due to the instability problem of having stiff equations with high aspect ratio grids.

2.3 Effect of Alignment of Shock with Grid on Carbuncle Phenomenon

If unstructured tetrahedral grids are used for hypersonic flows, it is very difficult to align the grids with the shock. This misalignment of the grid with the shock causes errors to be convected downstream into the boundary layer. Gnoffo and White (2004) state that the primary cause of poor heat transfer results is how the inviscid flow is calculated crossing the shock and not from the formulation of the viscous terms in the boundary layer. Furthermore, Gnoffo and White (2004) state that if the pressure and entropy at the boundary layer is not correct, there is no chance of getting good predictions of the heat transfer. Candler et al. (2007) show that if the grid is not aligned with the bow shock then some amount of momentum must be introduced into the flowfield in the direction parallel to the shock to balance the momentum in a computational cell. This spurious momentum is unphysical and increases as the grid is more misaligned with the bow shock.

Candler et al. (2007) and Gnoffo (2007) both state that grid design is extremely important in obtaining good heat flux results with a blunt body. The current state of the art in aerothermodynamic CFD solvers use quadrilateral or hexahedral grids that are aligned with the bow shock and have a cell Reynolds number less than one. This enhances chances of obtaining good results. The aligned bow shock is obtained using grid adaptation near the shock, with no grid adaption performed in the shock. Candler et al. (2007) also performed a grid study using unstructured tetrahedral, hexahedral, and quadrilateral cells and came to the conclusion that using unstructured tetrahedral grids produced too much error from grid misalignment with the bow shock to give accurate results. The hexahedral and quadrilateral grids give better results if they are aligned with the shock, since grid

alignment error is reduced.

Gnoffo (2007) shows that using a grid that gives good results for the two-dimensional blunt body case can give results that are not constant in the spanwise direction when a degree of freedom is added to the flow by extruding the cells in the spanwise direction. To correct this problem that occurs when using a three dimensional radially symmetric grid a grid patch is added to the stagnation region. The grid patch moves the grid singularity off of the axis of rotation.

Mazaheri and Kleb (2007) manipulate structured grids to mimic the grid skewness, asymmetries, and high and low frequency perturbations seen in unstructured grids. The purpose of this study was to find types of unstructured grids that produce accurate results for the heat transfer and skin friction on a hypersonic blunt body. The grids used were for flow over a cylindrical blunt body with a degree of freedom in the spanwise direction. The results of the study by Mazaheri and Kleb (2007) revealed the following trends:

1. In general, perturbed grids lead to an under-prediction of the surface quantities, but remain symmetric if the grid is symmetric.
2. Grid cells that are stretched in the spanwise direction under-predict the surface heat transfer rate, but do not lead to the axisymmetric results.
3. Asymmetric grid cells with low frequency perturbations result in asymmetric computational results.
4. Irregular symmetric grid cells with low frequency perturbations have a greater effect than those with higher frequency.
5. Grid perturbations in the boundary layer lead to large local errors in the 2^{nd} order quantities (e.g. heat transfer and skin friction), but do not affect the 1^{st} order quantities (e.g. pressure).

3

Thermodynamic Properties of High Temperature Air in Chemical Equilibrium

This dissertation is part of a project to increase the accuracy of the US Air Force CFD code named AVUS (Air Vehicles Unstructured Solver) which was formerly designated Cobalt_{60} [Strang et al. 1999]. Part of the work of increasing the accuracy of AVUS involves producing a computational routine that will predict accurate thermodynamic and transport properties for air as a function of temperature that includes the effects of composition change.

There are two major parts of the chemical composition portion of this project: the first is the determination of the equilibrium chemical composition and the second is the determination of the nonequilibrium composition. Both the equilibrium and nonequilibrium calculations will be coupled with AVUS. This chapter only deals with calculating the chemical equilibrium composition.

The original intent of this project was to calculate the composition and thermodynamic and transport properties of chemical equilibrium air using the CANTERA program. These results would

then be coupled with the AVUS code to include the effects chemical reactions in hypersonic flows. It was later decided that the "Tannehill curve fits" of Srinivasan et al. (1987a and 1987b) would be used to calculate the thermodynamic and transport properties of equilibrium air. A high priority of upgrading AVUS in this project was keeping the computational time of the equilibrium version of AVUS as close as possible to the already existing perfect gas version of AVUS. For this reason the decision was made to use the already determined Tannehill curve fits of the thermodynamic and transport properties. This is due to the fact that using curve fits of thermodynamic and transport properties of equilibrium air use less computational time than calculating the equilibrium composition of air using the CANTERA program.

It should be noted that the Tannehill curve fits only allow for flows with an initial composition of 79% N_2 and 21% O_2. Using the CANTERA program to calculate the chemical equilibrium composition of the gas would allow the flexibility of using other initial gas compositions. For instance H_2 or various hydrocarbons could be included in the analysis to account for combustion in a gas turbine.

The results of this chapter show that the Tannehill curve fits have very good agreement with the thermodynamic results obtained from CANTERA, except for very high temperatures and low pressures where doubly and triply ionized species start to become dominant. In most cases where doubly and triply ionized species are present, the air flow is fast enough that chemical reactions do not have time to occur instantaneously at a given location and the flow is in chemical nonequilibrium.

The details of using the Tannehill curve fits to add chemical equilibrium to AVUS is covered in Chapter 4. The task of modifying the AVUS code to add chemical nonequilibrium was not part of the work of this dissertation. The chemical nonequilibrium version of AVUS is used in Chapter 5 to computationally determine the regions of applicability of the different continuum gas models.

The objective of this chapter is to determine the thermodynamic properties of air up to 30,000 K for a pressure range covering $1x10^{-4}$ atm to 100 atm. The emphasis will be on the lower pressure range. In order to determine these properties it is important to determine the equilibrium compo-

sition of air first. This is performed by using the element potential method which was discussed in Section 1.2.2. Once the equilibrium composition has been determined the thermodynamic properties of the mixture can be obtained from the thermodynamic properties of the individual components. The thermodynamic properties determined will be the constant pressure specific heat, specific internal energy, specific enthalpy, specific entropy, molecular weight ratio, equilibrium speed of sound, and the isentropic index.

3.1 CANTERA Program

The particular program used to perform these calculations is called CANTERA[1]. CANTERA is an open-source, object-oriented software package for problems involving chemically-reacting flows developed and maintained by the Division of Engineering and Applied Science at the California Institute of Technology. The version of CANTERA being used is 1.5. In order to utilize the CANTERA suite of software a user interface must be written. This user interface can be written in a number of languages that include: FORTRAN, PYTHON, MATLAB and C^{++}. Since FORTRAN is a CPU time efficient computer language, the user interface required for this project will be written in FORTRAN. All user interfaces to CANTERA utilize a common C^{++} kernel. All, but the C^{++} interface, utilizes a C interface library.

Results from CANTERA have been compared to those from the popular commercial software CHEMKIN-II[2]. The results obtained from the two sets of software were identical out to several significant figures, but CANTERA took less than one-third the computational time. Computational speed was an important consideration in the writing of CANTERA. Property caching is utilized so that expensive reaction rates are only computed when the temperature changes. Virtual methods are used sparingly, inlining is allowed, and since the source code is available other optimization techniques can be implemented.

[1]The CANTERA documentation and code can be found on: URL http://cantera.org [Cited June 2007].
[2]URL http://www.ca.sandia.gov/chemkin/index.html [Cited June 2007].

CANTERA has the capabilities to perform both the chemical composition tasks of interest for this project: the chemical equilibrium calculations and the chemical reaction rate calculations required for the chemical non-equilibrium composition determination. In addition to these capabilities, there are modules for determining the thermodynamic properties and transport properties.

3.2 Individual Species Property Determination

The second major task that needs to be performed by the user of CANTERA is the gathering of fundamental data for each species included in the product mixture. The fundamental data that is needed to determine the equilibrium composition and thermodynamic properties of the gas are the molar specific heat at constant pressure, C_p°, molar enthalpy, h°, and molar entropy, s°, of each chemical species that is included in the products. This data has to be entered as a function of temperature.

For the 22 species of interest in this work, N_2, O_2, Ar, O, N, NO, N_2^+, O_2^+, NO^+, N^+, N^{+2}, N^{+3}, O^+, O^{+2}, O^{+3}, Ar^+, Ar^{+2}, Ar^{+3}, N^-, O^-, O_2^- and e^-, this has been done for the temperature range from 300 to 30,000 K. The thermodynamic properties of the individual species were obtained from publications by the NASA Glenn Research Center [McBride et al. 2002; Gordon and McBride 1999] for the temperature range from 300 to 20,000 K. These publications provide the thermodynamic data for over 2000 chemical species. The thermodynamic properties provided are h°, s°, and C_P° as a function of temperature using polynomials with nine coefficients. These nine coefficient polynomials need to be altered because CANTERA utilizes seven coefficient polynomials [Goodwin 2003]. The thermodynamic properties of the individual species can also be obtained from the NASA Glenn website[3]. It should be noted that the enthalpy of formation is given in terms of the reference

[3]URL: http://cea.grc.nasa.gov [Cited June 2007].

temperature of 298.15 K. The seven coefficient polynomials required by CANTERA are of the form

$$\frac{C_P^\circ(T)}{\Re} = a_0 + a_1T + a_2T^2 + a_3T^3 + a_4T^4, \tag{3.1}$$

$$\frac{h^\circ(T) - h^\circ(298.15)}{\Re\, T} = a_0 + \frac{a_1T}{2} + \frac{a_2T^2}{3} + \frac{a_3T^3}{4} + \frac{a_4T^4}{5} + \frac{a_5}{T}, \tag{3.2}$$

$$\frac{s^\circ(T)}{\Re} = a_0\, \ln T + a_1T + \frac{a_2T^2}{2} + \frac{a_3T^3}{3} + \frac{a_4T^4}{4} + a_6. \tag{3.3}$$

The nine coefficient polynomials provided by the NASA Glenn website are of the form

$$\frac{C_P^\circ(T)}{\Re} = \frac{a_1}{T^2} + \frac{a_1}{T} + a_3 + a_4T + a_5T^2 + a_6T^3 + a_7T^4, \tag{3.4}$$

$$\frac{h^\circ(T) - h^\circ(298.15)}{\Re\, T} = -\frac{a_1}{T^2} + \frac{a_2\, \ln(T)}{T} + a_3 + \frac{a_4T}{2} + \frac{a_5T^2}{3} + \frac{a_6T^3}{4} + \frac{a_7T^4}{5} + \frac{b_1}{T}, \tag{3.5}$$

$$\frac{s^\circ(T)}{\Re} = -\frac{a_1}{2T^2} - \frac{a_2}{T} + a_3\, \ln(T) + a_4T + \frac{a_5T^2}{2} + \frac{a_6T^3}{3} + \frac{a_7T^4}{4} + b_2. \tag{3.6}$$

In these six equations the a's are the desired coefficients, T is temperature, and $\Re$ is the universal gas constant. The nine coefficient data provided by NASA Glenn was transformed to the 7 coefficient form required by CANTERA by using a least squares fit. This has been done for the given temperature range with a maximum difference in the two types of correlations of less than 3%. A majority of the conversion was done with a difference of less than 1%.

The thermodynamic properties for all the monatomic atoms and ions were calculated using partition functions for the temperature range of 6000 to 30,000 K. The reason for this is that the NASA Glenn Research Center [McBride et al. 2002; Gordon and McBride 1999] only provides thermodynamic properties up to 20,000 K. Diatomic species were not included past 20,000 K because it can be shown from the equilibrium composition results that they are almost completely disassociated at these high temperatures. The reason for calculating the partition functions from 6,000 to 30,000 K for monatomic species was that the thermodynamic properties obtained from the literature were compared to the thermodynamic data of the NASA Glenn Research Center [Gordon and McBride 1999] at 20,000 K and a slight difference could be seen in the values of h°, s°, and C_P°. However,

when the data obtained from this work using partition functions was compared to the data of the NASA Glenn Research Center at 6000 K, there was excellent agreement. With this approach a jump in the mole fractions and thermodynamic properties of the air is not seen at 20,000 K.

The code used to obtain the partition functions for the monatomic species and their thermodynamic properties was the NASA code PAC99, which was also developed by the NASA Glenn Research Center. A brief description of the capabilities of the code is given in McBride and Gordon (1992) and Gordon and McBride (1999). PAC99 calculates the internal partition functions for monatomic gases from the following equation:

$$Q = \sum_{m=1}^{\infty} Q^m = \sum_{m=1}^{\infty} g_m e^{-\epsilon_m / k_b T} \tag{3.7}$$

where Q^m, g_m, and ϵ_m are the molecular partition function, degeneracy, and electronic excitation energy respectively for the m^{th} energy level. This equation also involves two constants, the Boltzmann constant, k_b, and the Avagradro's number, N_a. In order to obtain the molecular partition function, all of the electronic energy levels of the monatomic species are required, along with the associated degeneracies. All of this information can easily be obtained from the NIST Atomic Spectra Data Base website[4].

Once the internal partition functions are calculated the thermodynamic functions C_p°, h°, and s° can be calculated as functions of the internal partition function, Q:

$$\frac{C_p^\circ(T)}{\Re} = T^2 \frac{d^2(\ln Q)}{dT^2} + \frac{5}{2} \tag{3.8}$$

$$\frac{h^\circ(T) - h^\circ(0)}{\Re T} = T \frac{d(\ln Q)}{dT} + \frac{5}{2} \tag{3.9}$$

$$\frac{s^\circ(T)}{\Re} = T \frac{d(\ln Q)}{dT} + \ln Q + \frac{3}{2} \ln \mathcal{M} + \frac{5}{2} \ln T + S_c \tag{3.10}$$

where $\mathcal{M}$ is the molecular weight and S_c is the Sackur-Tetrode constant which has a value of 1.164856 when using 1 atm as the standard pressure.

[4]URL: http://physics.nist.gov/PhysRefData/ASD/index.html [Cited June 2007].

Once the thermodynamic functions are calculated using Equations (3.9)-(3.10) for the temperature range of interest a least squares fit of the data is performed to fit the data to the 9 coefficient polynomials shown in Equations (3.4)-(3.6). The only additional piece of information that is needed to calculate the thermodynamic properties are the enthalpies of formation at 298.15 K. The arbitrary base of having the enthalpy of formation, $\triangle h_f^\circ(298.15)$, and molar enthalpy, $h^\circ(298.15)$, equal each other at a temperature of 298.15 K is used to account for the chemical energy present in the ions and molecules. This information can be found either in the NASA Glenn Research Center data [McBride et al. 2002; Gordon and McBride 1999; McBride and Gordon 1992] or by using the following equation for the case of ions,

$$\triangle H_{f,\mathcal{Z}^{n+1}}^\circ(298.15) = \triangle H_{f,\mathcal{Z}^n}^\circ(298.15) + I_{\mathcal{Z}^n} - \triangle H_{f,e^-}^\circ(298.15) \tag{3.11}$$

where $\triangle H_{f,\mathcal{Z}^n}^\circ$ is the enthalpy of formation of the species being ionized and $\triangle H_{f,\mathcal{Z}^{n+1}}^\circ$ is the enthalpy of formation of the ionized species. The neutral species being ionized is $\mathcal{Z}$, the degree of ionization of the species being ionized is n, the ionization energy required to ionize the species is $I_{\mathcal{Z}^n}$, and the enthalpy of formation of an electron is $\triangle H_{f,e^-}^\circ$.

3.3 Results

In this work air is assumed to be composed of 21% diatomic oxygen, 78% diatomic nitrogen, and 1% argon at room temperature. At elevated temperatures these three fundamental species are allowed to react into the following 22 species: N_2, O_2, Ar, O, N, NO, N_2^+, O_2^+, NO^+, N^+, N^{+2}, N^{+3}, O^+, O^{+2}, O^{+3}, Ar^+, Ar^{+2}, Ar^{+3}, N^-, O^-, O_2^- and e^-. Included in this list of 22 species are diatomic molecules, monotonic molecules, positive ions, negative ions, and free electrons. This is a fairly inclusive list for temperatures below 30,000 K.

The composition and thermodynamic results of equilibrium air are presented in the literature by a large number of authors using different models. Some of the differences in the various models are

Table 3.1: Models used for comparison of results

Researcher(s)	Included Species	Corrections*	Curve Fit
Present Work	O_2, O, O^+, O^{+2}, O^{+3}, O_2^+, O^-, O_2^-, N_2, N, N^+, N^{+2}, N^{+3}, N_2^+, N^-,NO, NO^+, Ar, Ar^+, Ar^{+2}, Ar^{+3}, e^-	no	no
Gupta:91	O_2, O, O^+, O^{+2}, N_2, N, N^+, N^{+2}, NO, NO^+, e^-	no	yes
Boulos:94	O_2, O, O^+, O^{+2}, O_2^+, N_2, N, N^+, N^{+2}, N_2^+, NO, NO_2, N_2O, NO^+, Ar, Ar^+, Ar^{+2}, e^-	yes	no
Hansen:59	O_2, O, O^+, N_2, N, N^+, e^-	no	no
Srinivasan:87a	O_2, O, O^+, N_2, N, N^+, NO, NO^+, e^-	no	yes
Hillensrath & Klein:65	O_2, O, O^+, O^{+2}, O_2^+, O^-, O_2^-, N_2, N, N^+, N^{+2}, N_2^+, N^-, NO, NO^+, NO_2, N_2O, Ar, Ar^+, Ar^{+2}, C, C^+, C^{+2}, CO, CO_2, CO^+, Ne, Ne^+, e^-	yes	no

* Debye and Virial Corrections.

the number of species included, the thermodynamic data used for the individual species, and whether or not the Debye and second virial corrections are used. The virial correction takes into account the interaction potential of the particles as they approach each other. The Debye correction takes into account the long range interactions between charged particles. The form in which the thermodynamic results are presented as also vary from researcher to researcher, with the most common forms being tabulated data, graphical, and curve fits. To verify the computational results being produced as part of this work, a number of comparisons are made to the works of the researchers shown in Table 3.1.

3.3.1 Equilibrium Composition Results

To verify the results of the equilibrium composition the mole fractions of this work are compared to mole fractions from Hillsenrath & Klein (1965) at pressures of 1x10^{-6} and 1 atm for a temperature range of 1000 to 15,000 K as shown in Figure 3.1. Figure 3.1(a) presents the mole fractions of the neutral species at 1x10^{-6} atm and Figure 3.1(b) presents the mole fractions of the ionized species at 1x10^{-6} atm. The neutral and ionized species mole fractions were split into two figures for easier viewing. Hillsenrath & Klein (1965) have the most detailed model of all of the results that are compared to in this work, with Hillensrath & Klein's equilibrium air model having 29 species and

including the Debye correction and the second virial corrections. Hillensrath & Klein also include the species NO_2, N_2O, C, C^+, C^{+2}, CO, CO_2, CO^+, Ne, and Ne^+ which are not included in this work. Figure 3.1 shows that species included in Hillensrath & Klein, but neglected in this work, are all present in trace amounts (mole fractions $< 5x10^{-4}$) for the range of temperatures and pressures of interest. This work includes the species O^{+3}, N^{+3}, and Ar^{+3} which are not included in Hillensrath & Klein. These species being absent in Hillensrath & Klein's model, however, do not affect the comparisons since Hillensrath & Klein only present results with temperatures up to 15,000 K. At these temperatures the triply ionized species are not present in significant amounts. For the range of pressures of interest, the triply ionized species are not important until temperatures greater than 20,000 K.

Figure 3.1(a) shows excellent agreement between the mole fraction results of the present work and that of Hillensrath & Klein for all of the neutral species. Hillensrath & Klein show slightly lower mole fractions for argon at lower temperatures, but this is due to C and Ne species being included in the model and specifying the initial mole fraction of Ar to be lower than specified in the model used in this work. Figure 3.1(b) shows excellent agreement between the mole fraction results for all of the ionized species.

Figure 3.2(a) presents the mole fractions of the neutral species at 1 atm and Figure 3.2(b) presents the mole fractions of the ionized species at 1 atm. The neutral and ionized species mole fractions are again split into two figures for viewing purposes. The mole fractions of the neutral species at 1 atm presented in Figure 3.2(a) show that there is excellent agreement between all of the species. The slight discrepancy between the mole fractions of Ar at lower temperatures is again probably due to the different initial mole fractions specified in the two models.

For the mole fractions of the ionized species at 1 atm shown in Figure 3.2(b), it can be seen that there is excellent agreement between the mole fractions for the species of N^+ and Ar^+, however, the agreement between the mole fractions of the species of O^+, N_2^+, NO^+, O^-, and N^- are not as good. This is probably due to discrepancies between the partition functions of the diatomic and

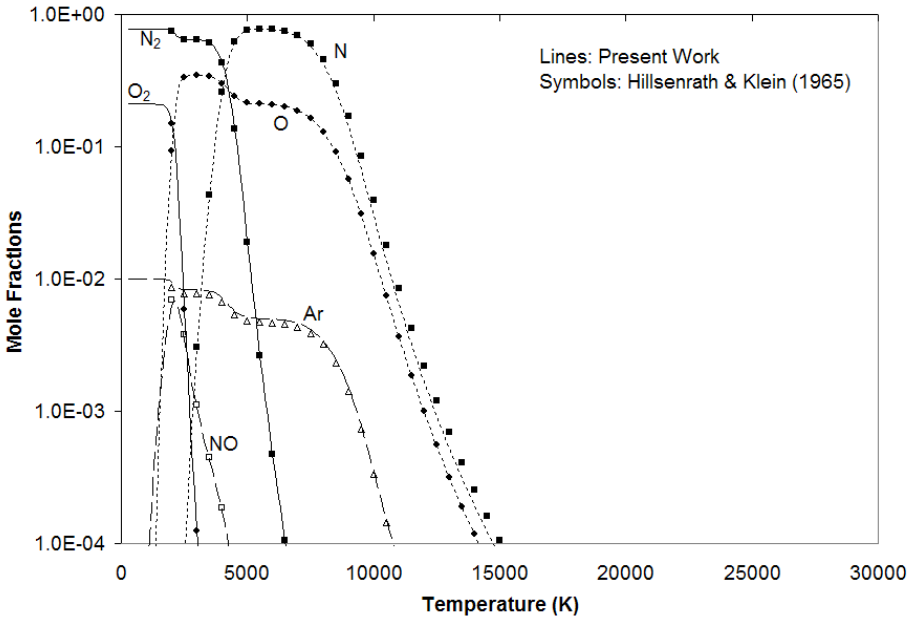

(a) Neutral species.

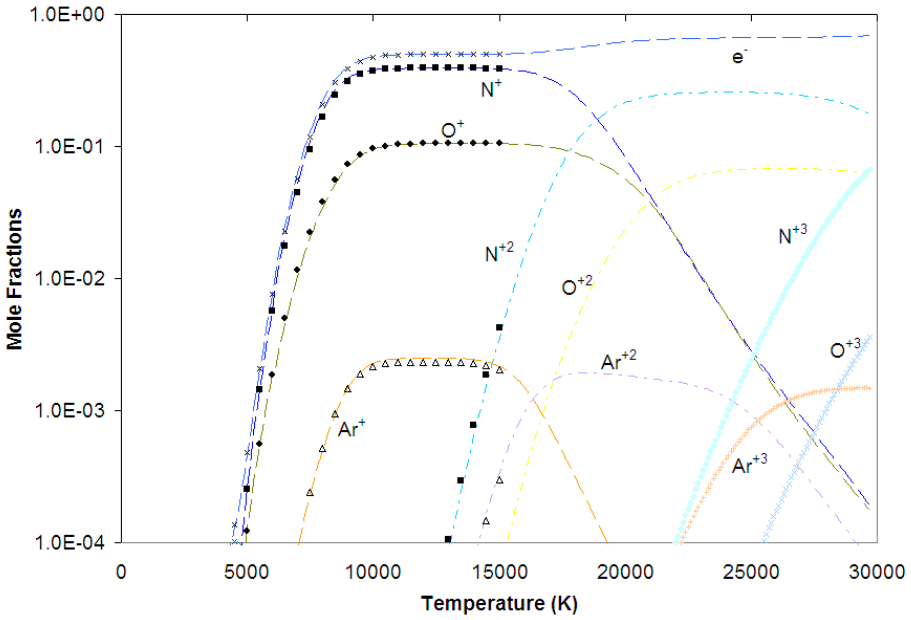

(b) Ionized species.

Figure 3.1: Mole fractions at 1x10^{-6} atm.

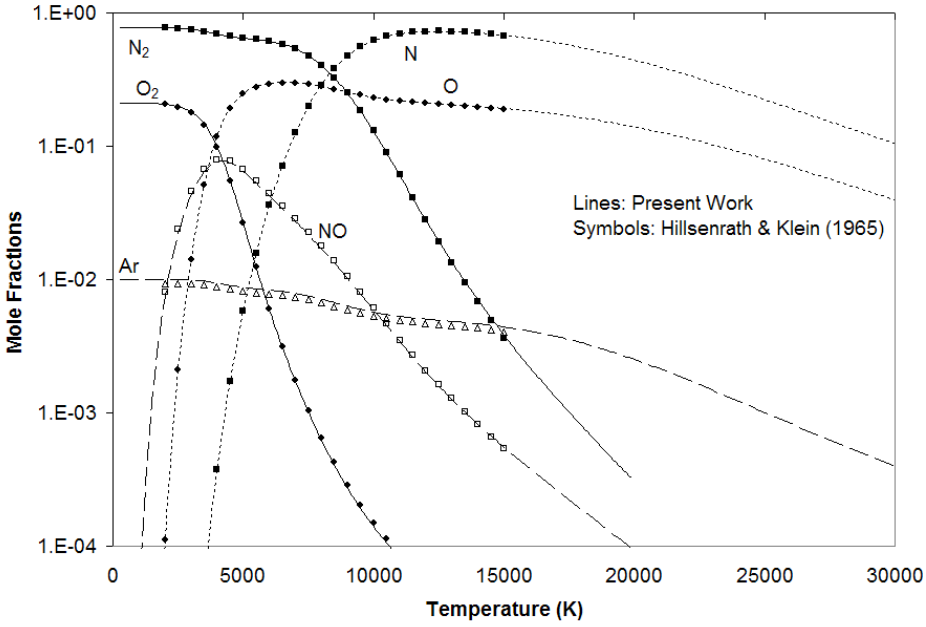

(a) Neutral species.

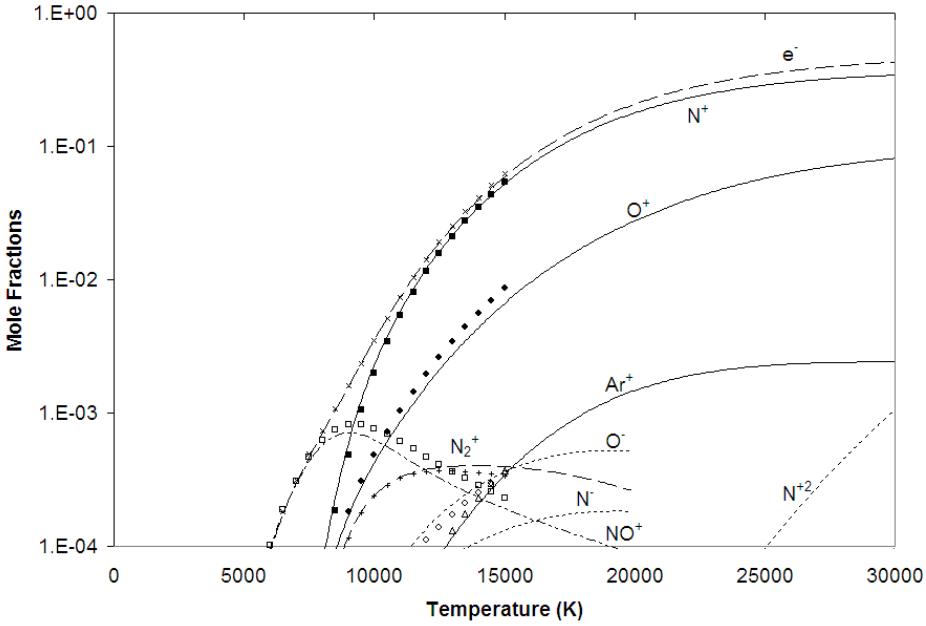

(b) Ionized species.

Figure 3.2: Mole fractions at 1 atm.

negative ions at higher temperatures ($\sim$ T > 10,000 K). The partition functions used in calculating the thermodynamic properties in Hillensrath & Klein were obtained during the 1960's, while the partition functions obtained from this work were obtained from the NASA Glenn website[5] and from the NIST website[6]. The data on these websites is frequently updated for what is viewed as the most accurate values of the partition functions. The reason these differences do not show up at lower pressures in Figure 3.1(b) is that diatomic species dissociate at higher temperatures for higher pressures, thus the diatomic species do not have a chance to ionize in significant amounts since they disassociate before a high enough temperature is reached for ionization. This same trend can be seen for ionization, where species ionize at higher temperatures as the pressure is increased.

For all the pressures surveyed the dominant species at the lower temperatures are N_2 and O_2. For the middle range of temperatures the dominant species are N, O and NO. For the higher temperatures N^+ and O^+ are the dominant species. At still higher temperatures N^{+2} and O^{+2} become the dominant species with N^{+3} and O^{+3} starting to become important above 25,000 K for lower pressures. The double and triply ionized species become more important at lower temperatures as the pressure decreases. In fact, N^{+2} and O^{+2} are more dominant than N^+ and O^+ at temperatures higher than 15,000 K for lower pressures. The species NO is rather important in the range of temperatures from about 1000 to 8000 K depending on the pressure. Argon is only 1% of the mixture at 300 K and it drops from there as other particles are formed and neutral argon becomes ionized. The negative ion species and the positive ion diatomic molecules are never a significant percentage of the total number of particles. These species can be important if looking at the electrical properties of the gas at low temperatures.

3.3.2 Thermodynamic Property Results

The thermodynamic property results of this work are compared to the thermodynamic results of Gupta et al. (1991) , Boulos et al. (1994) , Hansen (1959) , and Srinivasan (1987a) to verify

[5]URL: http://cea.grc.nasa.gov [Cited June 2007].
[6]URL: http://physics.nist.gov/PhysRefData/ASD/index.html [Cited June 2007].

results of this work. Boulos et al.'s (1994) work is the most detailed model used in comparing the thermodynamic property results, with the model containing 18 air species and using Debye and second virial corrections. The Boulos et al. (1994) model, however, does not include triply ionized species and only presents results at 1 atm for temperatures up to 24,000 K. The second most detailed model is that of Gupta et al. (1991), which uses 11 air species and spliced polynomial curve fits to present the thermodynamic results. The Gupta et al. (1991) model does not include triply ionized species and presents results up to 30,000 K. The third most detailed model is Srinivasan et al. (1987a) which uses a 9 species air model and produces spliced polynomial curve fits. The Srinivasan et al. (1987a) model does not include double or triply ionized species and presents results to ∼20,000 K. The least detailed model compared to is Hansen (1959) which uses a 7 species air model that does not include double or triply ionized species, NO, and NO^+.

The mixture enthalpy of equilibrium air is presented in nondimensional form for three different pressures in Figure 3.3(a). The enthalpy is nondimensionalized by dividing the enthalpy by the specific gas constant of the undissociated air, $R_o = 286.99$ J/kg-K, and the temperature. For all three of the presented pressures the enthalpies of the various models show excellent agreement with the results of this work. The results of Gupta et al. (1991) and Srinivasan et al. (1987a) have enthalpies that tend to oscillate above and below the enthalpies of the present work. This is due to the fact that both of these models use spliced polynomial curve fits to present their results.

The mixture entropy of equilibrium air is presented in nondimensional form for three different pressures as shown in Figure 3.3(b). The entropy is nondimensionlized by dividing the entropy by R_o. The entropy results of Hansen (1959) and Srinivasan et al. (1987a) show excellent agreement to the entropy results of this work. The results of Srinivasan et al. (1987a) again show oscillations about the entropy results of the present work, because of the spliced polynomial curve fits. The molecular weight ratio of Figure 3.4(a) shows excellent agreement between all of the various models and the results of this work for all pressures. The minor differences between the various models and the results of this work are due to the same causes discussed with the enthalpy comparisons.

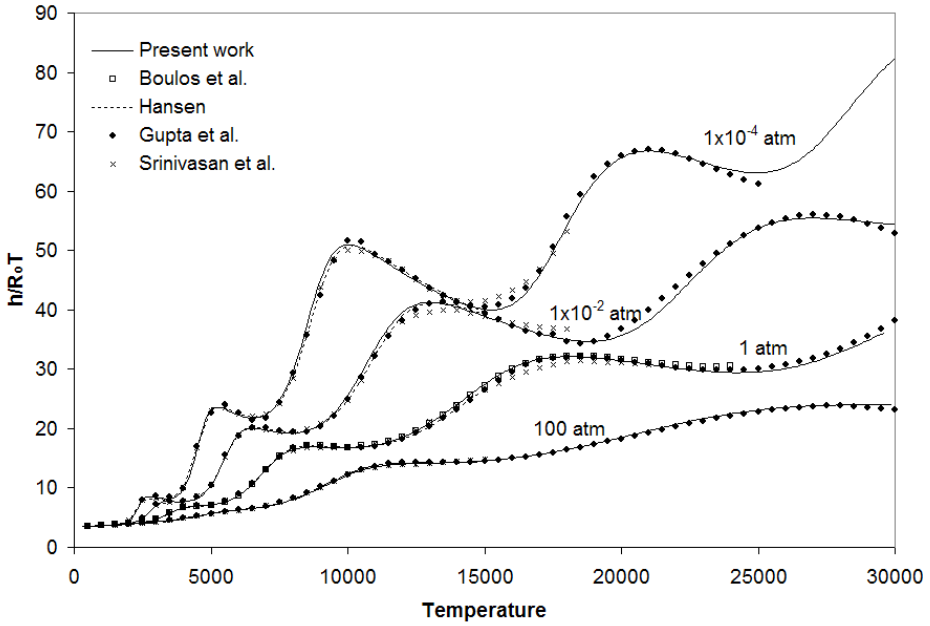

(a) Nondimesional enthalpy.

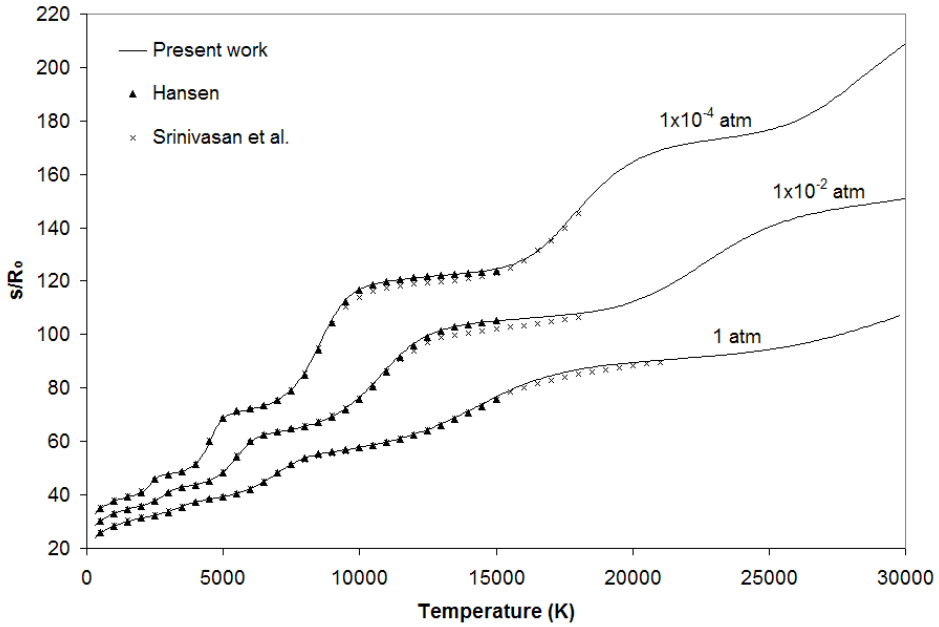

(b) Nondimensional entropy.

Figure 3.3: Comparison of enthalpy and entropy at various pressures.

For comparisons of the mixture specific heats at constant pressure the results are also presented as nondimensional specific heats at constant pressure for three different pressures as shown in Figure 3.4(b). The specific heat at constant pressure is nondimensionlized by dividing $C_{P,m}$ by R_o. The results of Hansen (1959) and Gupta et al. (1991) show excellent agreement with the results of this work, except for the upper temperature range of these models. Looking at the $C_{P,m}$ results of Hansen (1959) we can see that $C_{P,m}$ levels off at about 13,000 K at a pressure of 1x10^{-4} atm, while the results of this work show $C_{P,m}$ starting to increase in this region. The reason for this difference is due to Hansen (1959) not including doubly ionized species and double ionized species starting to become important at about 13,000 K for a pressure of 1x10^{-4} atm. This same leveling off behavior can be seen when comparing the results of Gupta et al. (1991) to the results of this work at 24,000 K at 1x10^{-2} atm and 27,000 K at 1x10^{-4} atm. These differences are due to Gupta et al. (1991) neglecting triply ionized species in the model and the triply ionized species starting to significantly ionize at these temperatures and pressures.

In looking at Figures 3.3(a) - 3.4(a) for the specific enthalpy, specific entropy, and the ratio of molecular weights it can be seen that there are certain temperature regions where these properties are changing rapidly and other regions where these properties level off. The rapid changes are due to the disassociation of the molecules and ionization of the species. The effects of disassociation and ionization can be seen even more drastically in the specific heat (see Figure 3.4(b)). The large humps in these results correspond to rapid changes in the enthalpy. These are the regions where disassociation and ionization are occurring in a strong way. The first hump corresponds to the disassociation of O_2, the second hump corresponds to the disassociation of N_2, the third hump corresponds to the ionization of O and N, the fourth hump corresponds to the ionization of N^+ and O^+, and the fifth hump corresponds to the ionization of N^{+2} and O^{+2}. It should be noted that the enthalpy also has regions where it levels off. Figure 3.3(a) shows the nondimensional enthalpy decreasing in certain regions, but the enthalpy is actually constant in these regions since the nondimensional enthalpy is divided by the temperature.

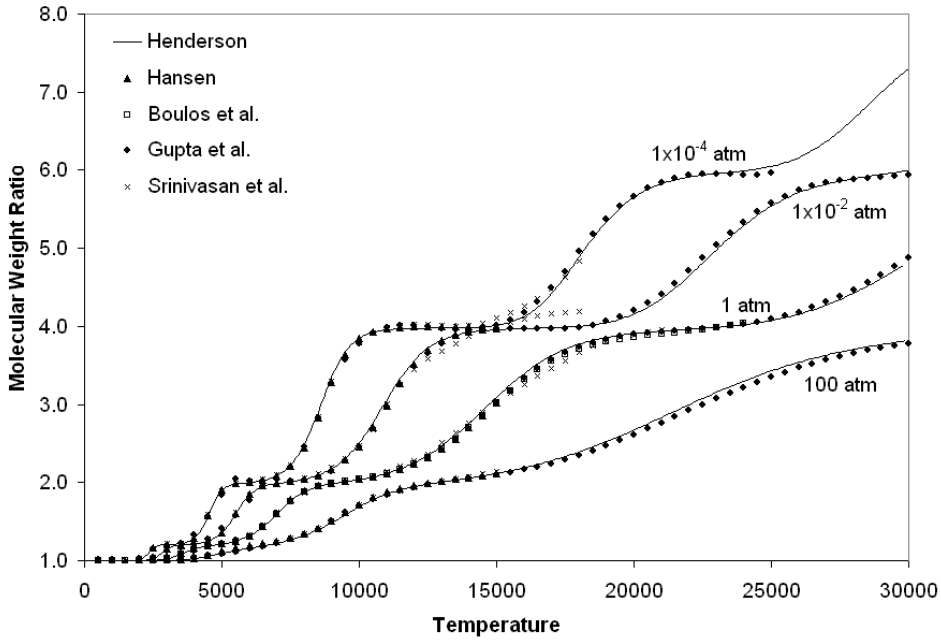

(a) Molecular weight ratio.

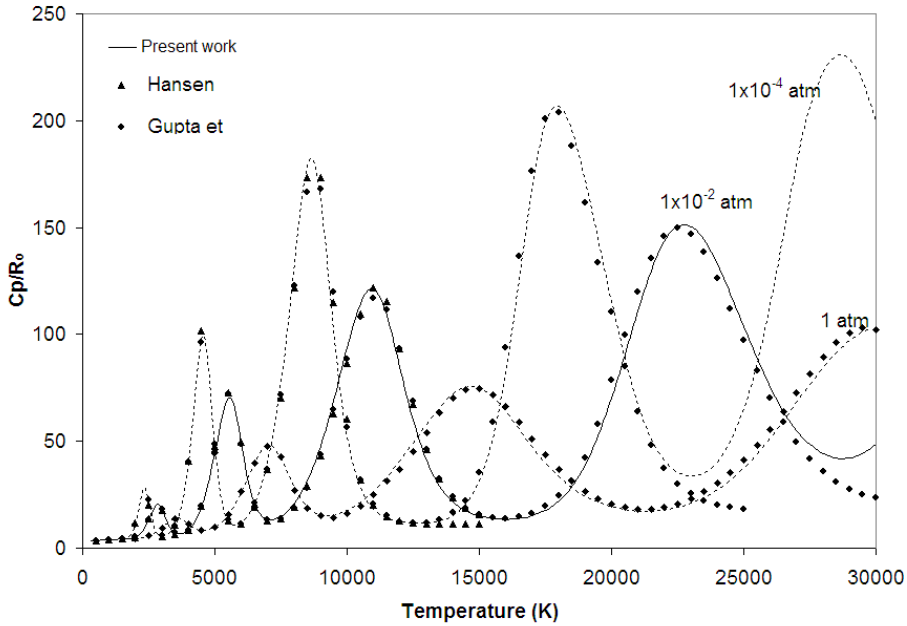

(b) Nondimesional specific heat at constant pressure.

Figure 3.4: Comparison of molecular weight ratio and specific heat at various pressures.

Figure 3.5 shows the comparisons of all the gamma parameters to the results of Hansen (1959) and Srinivasan et al. (1987a) for the pressures of 1x10^{-4} and 1 atm respectively. Looking at Figure 3.5 we can see that γ_{fr}, γ_{eq}, and γ_s all converge to the same value for temperatures less than 3000 K. This shows that the frozen specific heat assumption is good for low temperatures and only a single gamma parameter is needed. The $\overline{\gamma}$ parameter converges to γ_{fr} at around room temperature. Comparing γ_{fr} and γ_{eq}, it can be seen that γ_{fr} overpredicts γ_{eq}. This occurs because the γ_{eq} parameter takes into account the chemical reactions occurring in the equilibrium air. It can be seen that γ_{eq} and γ_s follow the same pattern of having large humps. These large humps correspond to regions where dissociation and ionization are occurring in a strong way and the different peaks are the same as those discussed with the enthalpy.

From the comparison of the γ_{eq} results of Hansen (1959) to this work it can be seen that the results show excellent agreement for 1 atm and show excellent agreement for 1x10^{-4} atm for temperatures up to 13,000 K. The reason for the disagreement at higher temperatures is that Hansen (1959) does not include doubly ionized species in his model and these species are starting to ionize significantly in this region. The agreement of the isentropic exponent, γ_s, between the results of Hansen (1959), Srinivasan et al. (1987a), and this work is good for lower temperatures, but only fair for higher temperatures. This is probably due to the calculation of the isentropic index which involves the calculation of the derivative $\left.\frac{\partial P}{\partial \rho}\right|_T$. Since the density can vary rather wildly with changes in pressure, this effect can become magnified in the isentropic exponent. The agreement of $\overline{\gamma}$ between the results of Srinivasan et al. (1987a) and the present work is excellent for both pressures. This is due to the fact that the curve fits of Srinivasan et al. (1987a) were formulated using Equation (1.12) with the curve fit values of P, ρ, and e. Finally, looking at Figures 3.5, we can see that the gamma parameters are functions of both temperature and pressure, and these values can differ significantly.

Figure 3.6 - 3.7 shows comparisons of the enthalpy, entropy, and molecular weight ratio results of Hillensrath and Klein (1965) to this work for the densities of 1x10^{-6}, 1x10^{-4}, 1x10^{-2}, and 1 amagats, where an amagat is the density divided by the density at sea level. Excellent agreement between

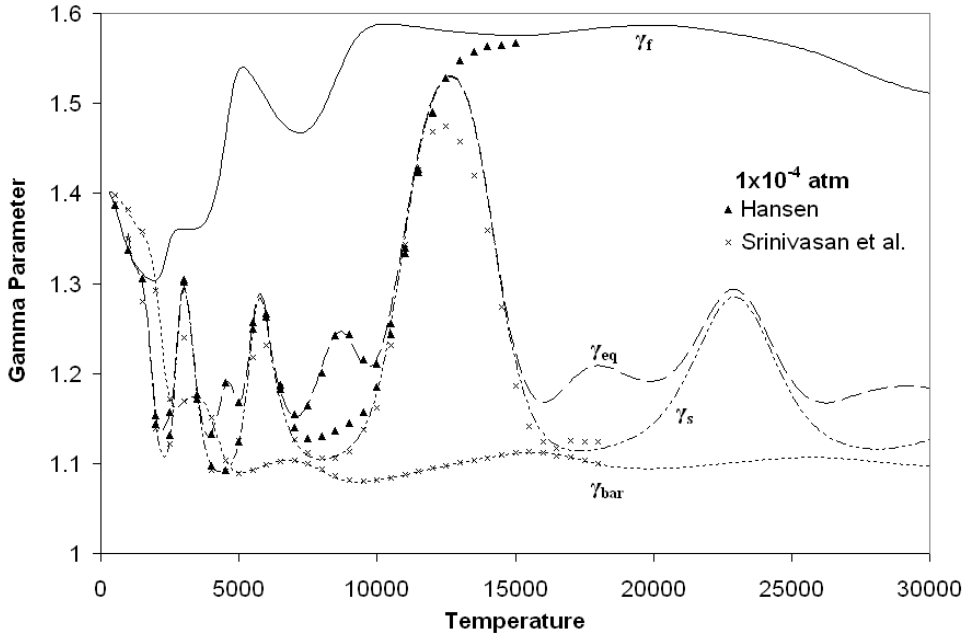

(a) 1x10^{-4} atm.

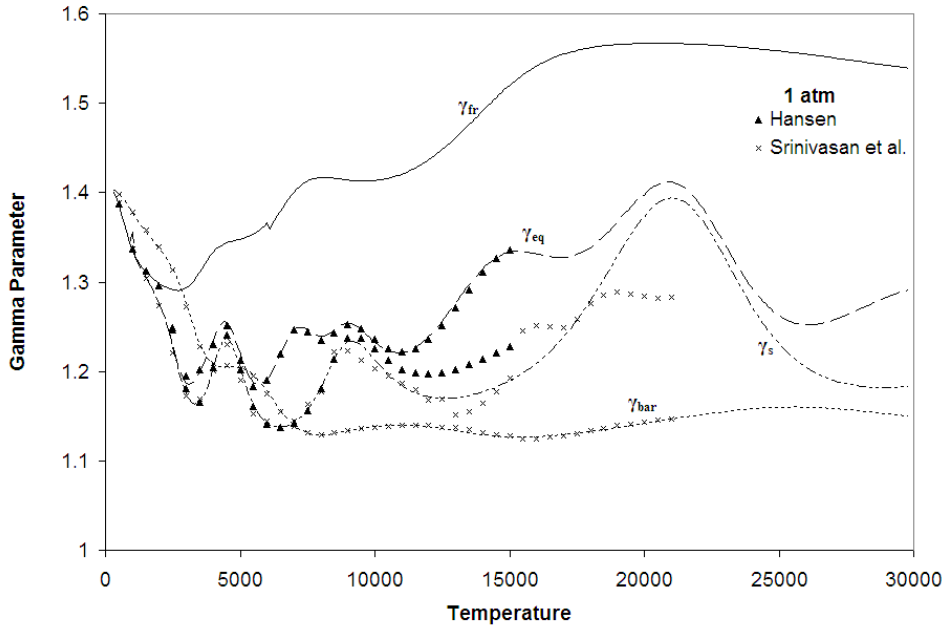

(b) 1 atm.

Figure 3.5: Gamma parameters. Lines are for results from this work

the thermodynamic results of Hillensrath and Klein (1965) and this work are obtained for all the densities of interest.

3.4 Conclusions

It was found that the thermodynamic properties of this work compare well to the thermodynamic properties determined by other investigators [Boulos et al. 1994; Hillensrath and Klein 1965; Hansen 1959; Srinivasan et al. 1987a; Gupta et al. 1991]. In certain regions the effects of not including the higher ionized species can be seen. This is more pronounced at lower pressures. This work is included up to the third ionization stage. From these findings it can be deduced that the Debye correction and second virial correction are not critical for the range of pressures studied in this work. It is shown in the comparisons of the thermodynamic results that neglecting the trace species of Ar, Ar^{+}, Ar^{+2}, Ar^{+3}, O_2^{+}, N_2^{+}, O^{-}, and N^{-} does not significantly affect the results. If the desired temperature range is not too high, neglecting the triply and/or doubly ionized species gives good results. With good accuracy over a range of pressures and temperatures this data can be coupled with AVUS to perform accurate CFD calculations for high-speed flight simulations.

It was found that there was excellent agreement between the thermodynamic results of this work using CANTERA and the results of Srinivasan et al. (1987a) for temperatures up to 20,000 K. This supports the decision of using the "Tannehill" curve fits instead of the CANTERA program to add chemical equilibrium capability to AVUS. The Tannehill curve fits are based on the work of Srinivasan et al. (1987a).

It is known that there are a number of software programs that exist for determining the equilibrium composition of air. To name a few of the more popular equilibrium composition programs there is the popular CHEMKIN-II program, the NASA CEA [McBride and Gordon 1992; Gordon and McBride 1994; Gordon 1970] code for the calculation of complex chemical equilibrium compositions, the popular STANJAN [Reynolds 1986] program of Stanford University that uses the element

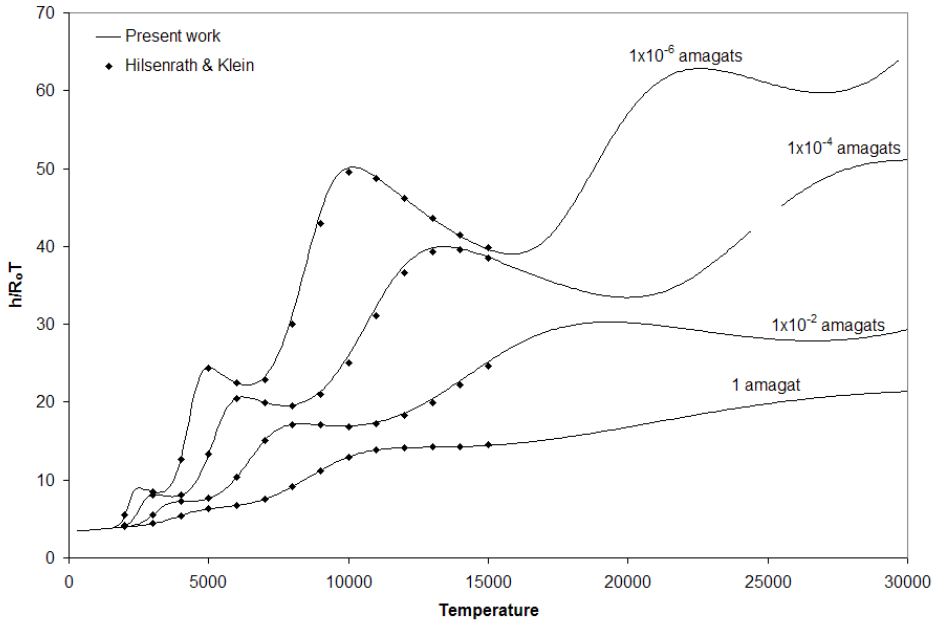

(a) Nondimesional Enthalpy.

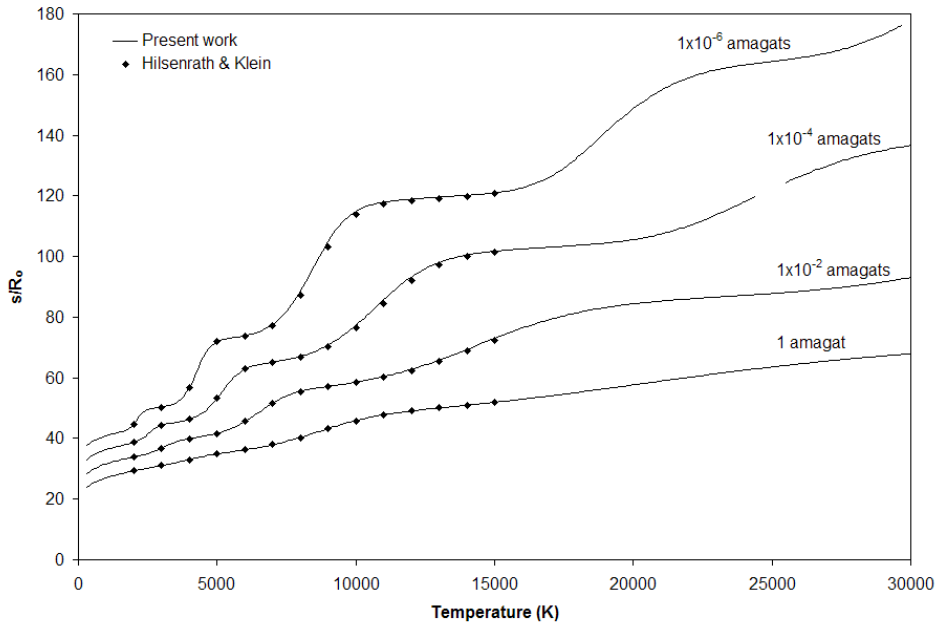

(b) Nondimesional Entropy.

Figure 3.6: Comparison of thermodynamic results to Hillensrath and Klein (1965) results.

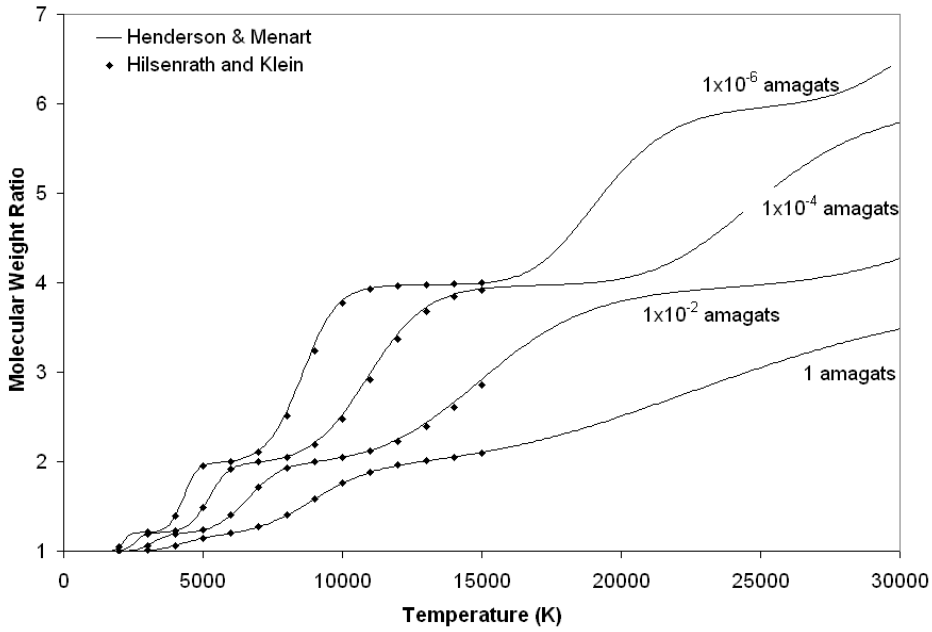

Figure 3.7: Comparison of ratio of molecular weight results to Hillensrath and Klein (1965) results.

potential method and the PEGASE [Bottin 1997] code of the Von Karman Institute. There are also a large number of published results for the thermodynamic properties of equilibrium air that were not included due to space constraints. Even though this is the case there is still room for more published data on high temperature properties of air, especially at the lower pressures. This is needed in this day and age where hypersonic aircraft are seriously being researched.

4

Adding Chemical Equilibrium to AVUS

In this chapter the procedure used to add equilibrium chemistry air to AVUS is discussed. To perform this task the Tannehill curve fits of Srinivasan et al. (1987a and 1987b) are used to determine the thermodynamic and transport properties of the air at various stages of disassociation and ionization. This chapter will give a brief description of the AVUS program and will discuss the changes that were made to the AVUS code to add equilibrium air chemistry.

The results section of this chapter compare the results of the AVUS code to the results published by other authors using the perfect gas and equilibrium air model. To verify the inviscid part of the AVUS code the results are compared to the results of Prabhu et al. (1989) for a two-dimensional blunt body. To verify the viscous part of the code, results are compared to those of Rosen (1991) for supersonic and hypersonic laminar flow over a flat plate, and to those of Tannehill et al. (1990) for hypersonic, laminar flow over a two-dimensional wedge and axisymmetric cone. AVUS is also run in the three-dimensional mode and compared to the axisymmetric cone results of Tannehill et al. (1990). Comparisons are presented for flows based on perfect gas properties and flows based on equilibrium air properties.

4.1 Adding Equilibrium Air to AVUS

In order to solve the Euler/Navier-Stokes equations the thermodynamic and transport properties are required. For a calorically perfect gas there are simple analytical relationships available to determine the required thermodynamic and transport properties. The relationship between pressure, temperature, and density can be obtained from the ideal gas equation. The relationship for enthalpy and internal energy can be obtained from simple equations relating them to the specific heats and temperatures, and the transport properties of viscosity and thermal conductivity can be obtained from Sutherland's formulas [White 1974]. These formulas are used in AVUS to implement the perfect gas model. To account for chemical reactions occurring in a high speed flow, a model other than the perfect gas model has to be implemented. If the chemical reactions are assumed to happen instantaneously, the gas can be considered to be in chemical equilibrium. A gaseous mixture in chemical equilibrium is a unique function of two intensive thermodynamic properties with a set chemical composition for that thermodynamic state.

4.1.1 Tannehill Curve Fits

For the present work the approximate curve fits of Srinivasan et al. (1987a and 1987b) are used to determine the thermodynamic and transport properties. The species considered by Srinivasan et al. (1987a and 1987b) are O_2, O, O^+, N_2, N, N^+, NO, NO^+, and negatively charged free electrons. The thermodynamic property curve fits of Srinivasan et al. (1987a) are based on the calculated thermodynamic properties from the NASA RGAS program [Bailey 1967]. The transport property curve fits of Srinivasan et al. (1987b) are based on the transport properties of Peng and Pindroh (1962). The published range of validity for the thermodynamic property curve fits is for temperatures up to 25,000 K and densities from 10^{-7} to 10^3 amagats (ρ/ρ_o). The published range of applicability of the transport property curve fits is for temperatures up to 15,000 K and for densities from 10^{-5} to 10^3 amagats. Thus, the upper temperature limit for the equilibrium air version of

AVUS being developed here is 15000 K. The curve fits for thermodynamic and transport properties from Srinivasan et al. (1987a and 1987b) are often referred to as the "Tannehill curve fits" in the literature and this name will be used throughout this dissertation.

The Tannehill curve fits used in this work are the following:

$$\begin{array}{llll} T = T(e,\rho) & T = T(P,\rho) & P = P(e,\rho) & \rho = \rho(P,s) \\ c = c(e,\rho) & c = c(P,s) & e = e(P,s) & h = h(P,\rho) \\ s = s(e,\rho) & \mu = \mu(e,\rho) & k = k(e,\rho). & \end{array} \tag{4.1}$$

In this set of equations the property being considered is on the left-hand side of the equation and the two properties of which it is a function are given on the right-hand side. The duplication of the property variable on the right-hand side of these equations indicates a functional dependence on the two properties in parenthesis. In addition to the Tannehill curve fits, the following equation is used to relate equilibrium air properties,

$$P = (\overline{\gamma} - 1)\rho e \tag{4.2}$$

where

$$\overline{\gamma} = h/e. \tag{4.3}$$

The first step in converting AVUS from perfect gas properties to equilibrium air properties was to write subroutines that solve the Tannehill curve fit equations as shown in Equation 4.1. Some of these subroutines directly solve Tannehill's curve fit equations, while others use iterative techniques to solve one or two of Tannehill's curve fit equations. This is needed because curve fits for every property required in terms of two known properties are not provided as part of the Tannehill curve fits. All the equilibrium air property information required by AVUS is provided by the Tannehill curve fits; however, it is not provided explicitly. Some of the boundary conditions and post processing routines used in AVUS require inverse forms of the Tannehill curve fits which require an iterative solution.

Once subroutines for the Tannehill curve fit equations are inserted in the AVUS computer code, changes had to be made to the AVUS code itself. Every location in the AVUS computer code that used perfect gas properties had to be switched to use equilibrium air properties. In most situations this meant adding the appropriate subroutine call or using Equations 4.2 or 4.3. In other situations more had to be done. For some portions of the code the perfect gas equations had to be rewritten. The only change that had to be made to the Riemann solver used in AVUS was to send it the appropriate equilibrium air properties.

Because of the manner in which AVUS is written the ratio of specific heats, γ, is used many times. For equilibrium air γ is meaningless because the definition of γ assumes that the chemical composition of the gas is frozen. In a perfect gas compressible flow problem the ratio of specific heats is used to determine the speed of sound, to determine the pressure in terms of the internal energy and density, to calculate the Rankine-Hugoniot jump conditions, and to calculate the stagnation properties. For some of the equations in AVUS γ could simply be replaced by its equilibrium air counterpart, $\overline{\gamma}$. This is the case for the determination of the pressure as shown in Equation 4.2 above. Using the definition of enthalpy,

$$h = e + \frac{P}{\rho}, \tag{4.4}$$

and the definition of $\overline{\gamma}$ it can be shown that Equation 4.2 is the chemical equilibrium equivalent of the perfect gas equation

$$P = (\gamma - 1)\rho e. \tag{4.5}$$

There is one place in the equilibrium air version of AVUS where a different property is used than was used in the perfect gas version. In the perfect gas version of AVUS some limiting must be performed in applying the left and right cell face values used by the Riemann solver to obtain second order accuracy in space using the MUSCL scheme. This must be done to ensure a physical solution. The limiter used in the perfect gas version of AVUS is entropy. For the equilibrium air

version of AVUS density is used. Entropy was not used in the equilibrium air version because the solution becomes unstable under certain conditions. Using the density limiter instead of the entropy limiter can sometimes slow the convergence of the residuals. This slight reduction in convergence of the residuals is accepted in exchange for increased stability of the Riemann solver.

A switch was added to the AVUS code that allows the user to choose between the perfect gas model or the equilibrium air model. With the perfect gas version of AVUS the gas property equations were scattered throughout the code. When using equilibrium air properties, the thermodynamic and transport properties are all contained in subroutines with iterative searches necessary in some cases to find the equilibrium air properties. To streamline the code, the perfect gas properties were added to the subroutines that contained the equilibrium air properties. In certain cases an iterative search was also needed to find the equilibrium air properties using an initial guess from the analytical perfect gas equations. When using perfect gas properties, an iterative search is also used, where it would be required when using equilibrium air; however, when using a perfect gas the iterative procedure converges in one iteration, since the initial guess is the actual solution.

The programming logic of adding the equilibrium air model can be checked by running the two versions of AVUS that use the perfect gas model. This is due to the fact that the new version of AVUS calls the same subroutines to get the thermodynamic and transport properties for the perfect gas and equilibrium air models. The original perfect gas version of AVUS used analytical equations to find the thermodynamic and transport properties, and did not require calling subroutines to find the properties. When the perfect gas results of the new version of AVUS were compared to those of the original AVUS code, they compared to 10 significant figures. This is evidence that the programming logic of using subroutines to call the gas properties and perform the iterative searches is working properly. This does not verify that the equilibrium air model is working properly in the AVUS code. This requires running the AVUS code with the equilibrium air model and comparing the results to the experimental or computational results of other researchers.

4.1.2 Iterative Searches using Tannehill Curve Fits

One of the instances where the perfect gas equations had to be rewritten is for the no slip thermal boundary conditions applied to the walls. This boundary condition is obtained from an energy balance at the wall noting that the pressure gradient normal to the wall is zero. The energy balance used at the wall is derived on a per unit area basis and is

$$(k\overrightarrow{\nabla}T \cdot \overrightarrow{n})_w = q_w^{'} + h_c(T_w - T_{res}) \tag{4.6}$$

with $q_w^{'}$ being the heat flux per unit area from effects other than conduction or convection, h_c the convective heat transfer coefficient, T_{res} the thermal reservoir temperature, and $\overrightarrow{\nabla}$ the gradient operator. There are two unknowns in Equation 4.6 since $q_w^{'}$, h_c, and T_{res} are specified as inputs and we know that there is a zero pressure gradient at the wall, so the pressure at the wall is the same as the grid point adjacent to the wall. These two unknowns are the thermal conductivity at the wall, k_w, and the temperature at the wall, T_w. The cases of an adiabatic wall and an isothermal wall are easy to solve using a wall energy balance. For an adiabatic wall $h_c = 0$ and $q_w^{'} = 0$, thus Equation 4.6 says $T_w = T_c$. For an isothermal wall h_c is taken as infinite and $q_w^{'}$ is taken as zero; thus Equation 4.6 says $T_w = T_{res}$. For the general case of some arbitrary specification of $q_w^{'}$, h_c, and T_{res}, Equation 4.6 must be solved for T_w. The problem with doing this is that k_w is a function of T_w. Thus for a general no-slip, thermal wall boundary condition an iterative procedure is used to solve for the wall temperature. This iterative procedure uses the following logic:

1. An initial guess for k_w is made based on the current pressure and density at the wall.
2. A numerical form of Equation 4.6 is used to update the value of T_w.
3. The value of k_w is updated using the current P_w and T_w. This process involves a Newton-Raphson iterative scheme utilizing the Tannehill curve fits.
4. Steps 2 and 3 are repeated until convergence of T_w is obtained.

The farfield Riemann invariant boundary condition also requires an iterative search. This occurs because the pressure and speed of sound are held constant while the other properties are allowed to float when using the Riemann invariant boundary condition. The only properties that can be used as inputs for the Tannehill curve fits are the pressure and speed of sound. However, none of the Tannehill curve fits in Equation 4.1 contain both pressure and speed of sound on the right hand side. The initial condition also requires an iterative, search since the pressure and temperature are provided as inputs and none of the Tannehill curve fits contain both of these properties as inputs.

In the post processing portion of AVUS an iterative solution is required to find the pitot tube pressure at a specified point in the flow field. To find pitot pressure from a known pressure upstream of the entrance to the pitot tube, an iterative solution of the Rankine-Hugonoit equations is performed. Using conservation of mass an equation can be written to obtain the ratio of density upstream and downstream of a normal shock at the pitot tube entrance,

$$\frac{\rho_2}{\rho_1} = \frac{V_1}{V_2} = \eta \tag{4.7}$$

where subscript 1 specifies the property immediately upstream of the shock and subscript 2 specifies the property immediately downstream of the shock and $V = \sqrt{u^2 + v^2 + w^2}$ is the velocity magnitude. Using conservation of momentum and conservation of energy the pressure and enthalpy downstream of the normal shock can be found from the known upstream conditions and the density ratio across the shock,

$$\frac{P_2}{P_1} = 1 + \left(\frac{V_1^2}{P_1/\rho_1}\right)\left(1 - \frac{1}{\eta}\right) \tag{4.8}$$

and

$$\frac{h_2}{h_1} = 1 + \left(\frac{V_1^2}{2h_1}\right)\left(1 - \frac{1}{\eta^2}\right). \tag{4.9}$$

These three equations can be solved using a Newton-Raphson technique. Iteratively repeating this procedure eight times gives good convergence of the Rankine-Hugonoit jump conditions.

The other post processing task in AVUS that had to be changed was determining stagnation properties. With equilibrium air properties the standard stagnation property equations used for a perfect gas can no longer be used. A stagnation property is determined from theoretically bringing a flow to rest in an isentropic process. This means that the entropy of the flow, s, in the moving condition is the same as the entropy of the flow in the stagnation condition, s_o. This provides one independent property for determining the stagnation properties. A second independent property can be obtained at the stagnation state by realizing the stagnation enthalpy, h_o, is equal to the static enthalpy, h, plus the kinetic energy at the point of interest,

$$h_o = h + \frac{V^2}{2}. \tag{4.10}$$

With these two properties, s_o and h_o, any other stagnation property can be determined with the Tannehill curve fits.

4.2 Results

4.2.1 Inviscid Blunt Body

To verify the inviscid part of AVUS equilibrium air our results are compared to the results of Prabhu et al. (1989) for a two-dimensional blunt body. The blunt body has a 5° wedge with a half cylinder leading edge. The freestream conditions for the blunt body are a Mach number of 15, a freestream pressure of 169.33 Pa, a freestream density of 0.002 kg/m^3, and a freestream temperature of 295 K. The inflow and outflow boundary conditions used are the farfield type using modified Riemann invariants and a slip wall boundary condition. The mesh used is a 41x81 structured mesh with uniform spacing.

Figure 4.1 shows three contour plots of comparisons between the perfect gas and equilibrium air model of AVUS. In the legend of this figure and figures to follow the perfect gas results are labeled

"PF" and the equilibrium air results are labeled "EQ". Comparing the perfect gas and equilibrium air results it can be seen that equilibrium gas properties produce a smaller shock standoff distance. The density of the gas using equilibrium air properties is lower than when perfect gas properties are used. This is the physical behavior you would expect for a blunt body bow shock when comparing results using perfect gas properties to equilibrium air properties [Anderson 1989].

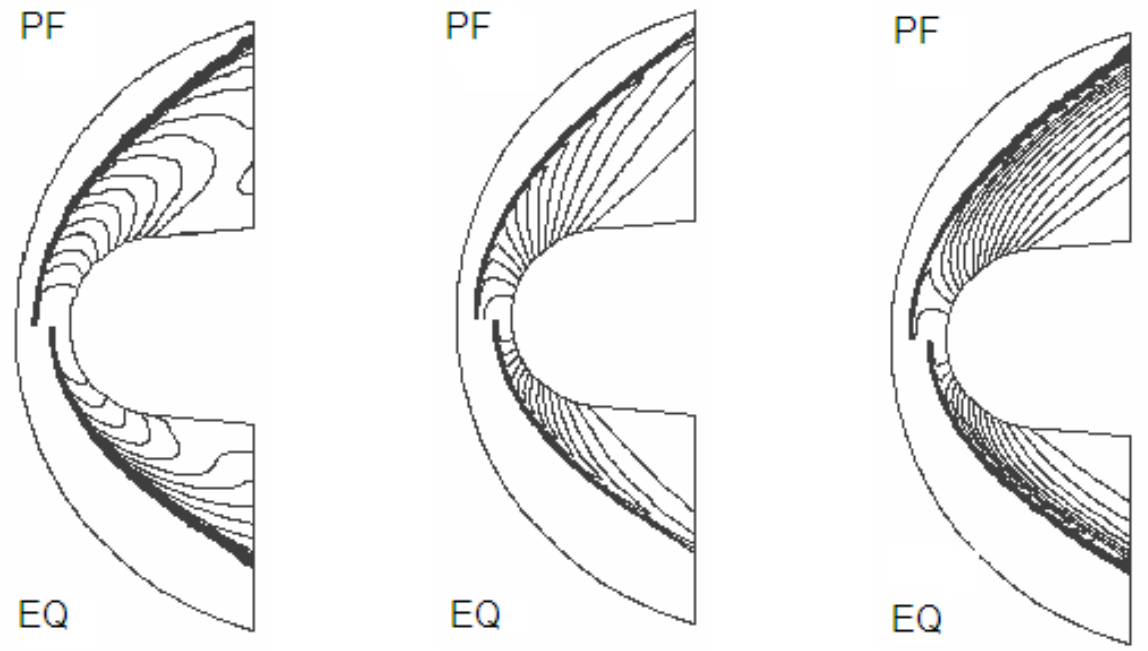

(a) Temperature. (b) Pressure. (c) Density.

Figure 4.1: Comparison between perfect gas (PF) and equilibrium air (EQ) results for inviscid flow past a blunt body.

A comparison of the temperature and pressure along the stagnation streamline with the corresponding results of Prabhu et al. (1989) is made in Figure 4.2. In these two figures the temperature and pressure are plotted in nondimensional form where the dimensional value has been divided by the freestream value. The flow direction coordinate has also been nondimensionalized relative to the nose radius of the blunt body, where the zero position has been taken as the center of the nose radius. The flow in all these figures is from left to right. The results from AVUS compare very well to the results of Prabhu et al. for both the perfect gas and equilibrium air cases. Prabhu et al. (1989) shows the same shock positions as obtained from AVUS. Essentially the results compare

within the numerical convergence criteria used in the two simulations and the ability of the author to read the plots provided by Prabhu (1989)

From Figure 4.2 it can be seen that using perfect gas properties causes the temperature in the stagnation region to be more than twice that using equilibrium air properties. This occurs since the perfect gas model does not account for all the modes of energy storage of the molecules. Figure 4.2 also shows that the pressure does not change as much as the temperature. Both graphs in Figure 4.2 show the shock standoff distance for the perfect gas being twice the equilibrium air standoff distance.

4.2.2 Supersonic Laminar Flat Plate

This test case consists of supersonic laminar flow over a flat plate with results being compared to the work of Rosen (1991). The flow conditions are a Mach number of 2.0, a freestream pressure of 2550 Pa, a freestream density of $4.001\text{x}10^{-2}$ kg/m^3, and a freestream temperature of 221.6 K. This corresponds to a unit Reynolds number of $1.65\text{x}10^{6}$ m^{-1}. The inflow and outflow boundary conditions are far-field conditions with modified Riemann invariants. The wall boundary condition is isothermal with no-slip and a wall temperature of 211.6 K. The mesh used consists of 51 grid points in the streamwise direction and 100 grid points normal to the surface. A grid spacing of $4.3\text{x}10^{-3}$ m normal to the surface is used.

The computed supersonic boundary layer results of AVUS are compared to the results of Rosen (1991) who used the CFL3D code that uses an upwind Riemann solver. The results of Rosen show good comparison to conventional boundary layer results. The temperature and tangential velocity profiles are presented in Figure 4.3 for a supersonic laminar flat plate at an axial location 1 m downstream of the leading edge. The temperature and tangential velocity are both nondimensionlized by dividing these values by their freestream values. The skin friction coefficient, C_f, and coefficient of heat transfer, C_h, are presented in Figure 4.4.

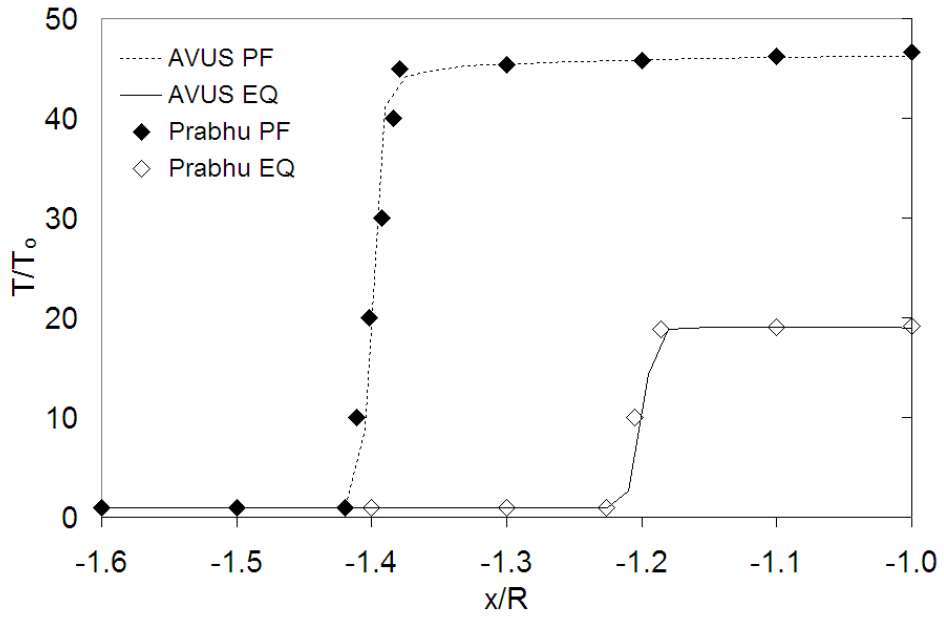

(a) Nondimensional temperature.

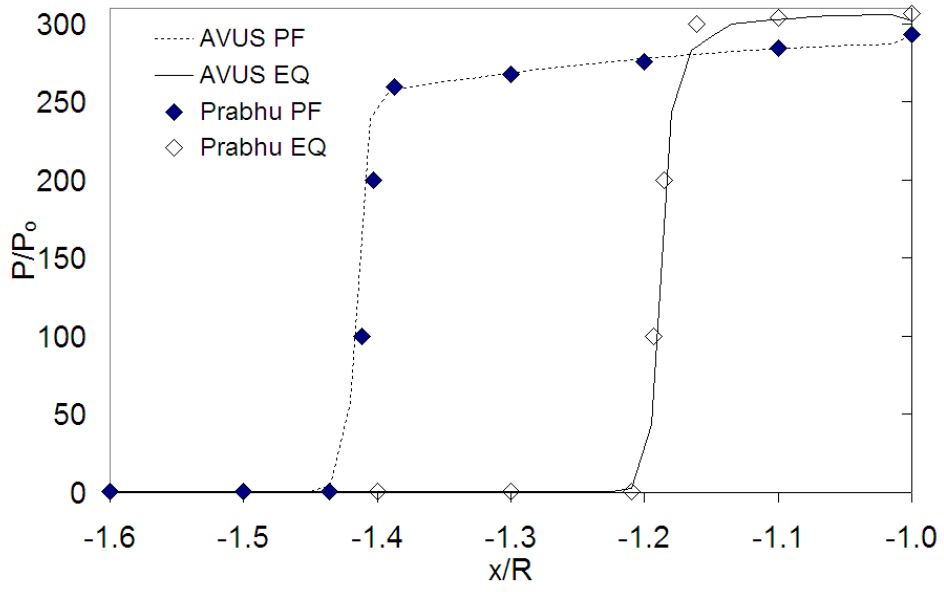

(b) Nondimensional pressure.

Figure 4.2: Comparison to the results of Prabhu et al. (1989) for properties along the stagnation streamline for inviscid Mach 15 flow past a blunt body.

The skin friction coefficient, C_f, is defined as

$$C_f = \frac{\tau_w}{\frac{1}{2}\rho_\infty V_\infty^2} \tag{4.11}$$

with the shear stress at the wall, τ_w, defined by Newton's law of friction,

$$\tau_w = \mu_w \frac{\partial V_t}{\partial n}. \tag{4.12}$$

In this equation ρ_∞ is the freestream density, V_∞ is the freestream velocity, μ_w is the dynamic viscosity at the wall, V_t is the velocity tangential to the wall, and n is the distance normal to the wall.

The coefficient of heat transfer, C_h, is defined as

$$C_h = \frac{Nu_L}{Re_\infty Pr} = \frac{q_w}{\rho_w C_p (T_w - T_\infty) V_\infty} \tag{4.13}$$

with

$$q_w = k_w \frac{\partial T}{\partial n} \tag{4.14}$$

$$Nu_L = \frac{q_w L}{k_w (T_w - T_\infty)} \tag{4.15}$$

$$Re_\infty = \frac{\rho_\infty V_\infty L}{\mu_\infty} \tag{4.16}$$

$$Pr = \frac{\mu_w C_p}{k_w} \tag{4.17}$$

where q_w is the heat transfer at the wall, C_p is the specific heat at constant pressure at the wall, k_w is the thermal conductivity at the wall, and L is the characteristic length. The Nusselt number, Nu_L, is a dimensionless heat transfer parameter. The Reynolds number, Re, is a dimensionless ratio relating inertia to viscous forces. The Prandtl number, Pr, is the dimensionless ratio relating viscous to thermal diffusion rates.

For hypersonic flows C_f and C_h can be reformulated to a more convenient form for hypersonic flows [Tannehill et al. 1990]:

$$C_f = \frac{\tau_w}{\frac{1}{2}\gamma P_\infty M_\infty^2} \tag{4.18}$$

$$C_h = \frac{1}{\left[\frac{(\gamma-1)M_\infty^2}{2}+1\right]T_w - T_o}\frac{\mu_w}{\mu_\infty}\frac{L}{PrRe_\infty}\frac{\partial T}{\partial n} \tag{4.19}$$

where T_o is the stagnation temperature and M_∞ is the freestream Mach number. It should be noted that for this new form of C_h, the reference temperature is changed from T_∞ to T_o for the Nusselt number. The Prandtl number and ratio of specific heats used for the results in this chapter are $Pr = 0.72$ and $\gamma = 1.4$.

The results from Rosen (1991) are calculated using a perfect gas; the AVUS code results are for both a perfect gas and equilibrium air and are so denoted on the graphs. All of the computed results show excellent comparisons with the results of Rosen. It can be seen that equilibrium gas effects are not significant for the supersonic case, due to the relatively low Mach number and low wall temperature. The only quantity which shows some slight deviation between the perfect gas and equilibrium air results is the heat transfer coefficient.

4.2.3 Hypersonic Laminar Flat Plate

This test case consists of hypersonic laminar flow over a flat plate with results being compared to the work of Rosen (1991). The flow conditions are a Mach number of 20.0, a freestream pressure of 9.922 Pa, a freestream density of 3.457x10^{-4} kg/m^3, and a freestream temperature of 100.0 K. This corresponds to a unit Reynolds number of 2.0x10^5 m^{-1}. The inflow and outflow boundary conditions are of the far-field type using modified Riemann invariants. The wall boundary condition is an isothermal, no-slip boundary condition with a wall temperature of 1000 K. The mesh used consists of 64 grid points in the streamwise direction and 64 grid points normal to the surface. The grid spacing is 1.0x10^{-2} m normal to the surface.

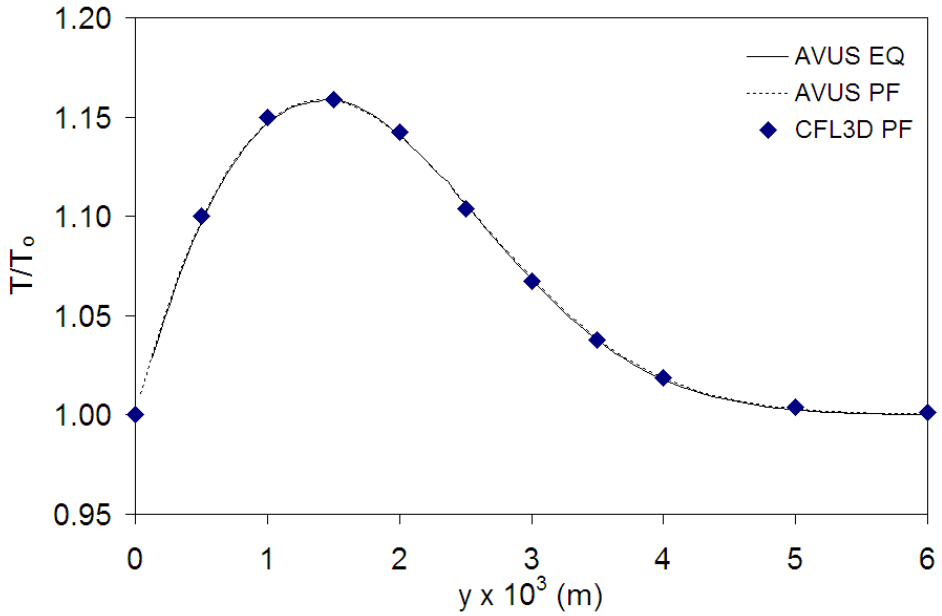

(a) Nondimensional temperature.

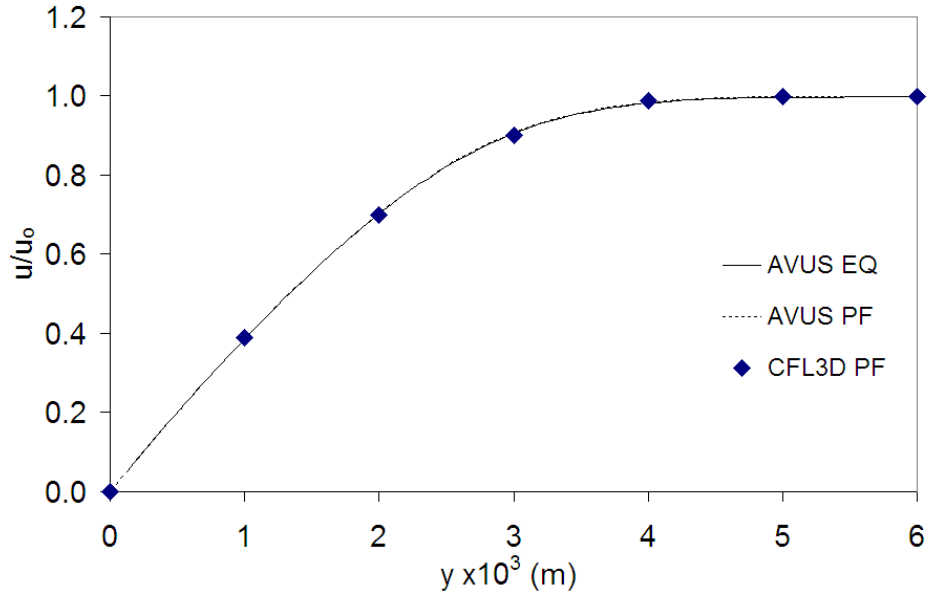

(b) Nondimensional tangential velocity.

Figure 4.3: Comparison to the results of Rosen (1991) of properties at $x = 1$ m for a supersonic flat plate boundary layer at Mach 2.0.

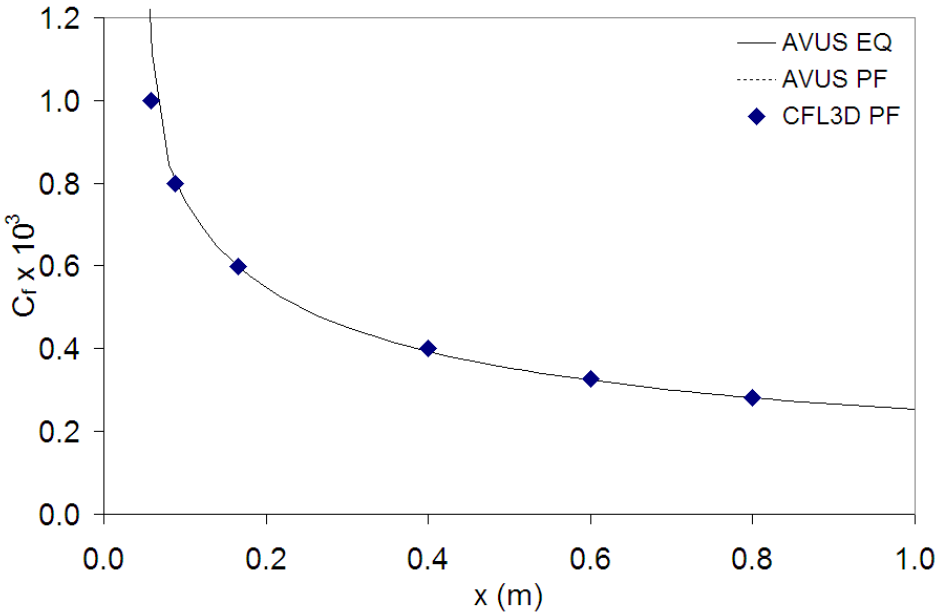

(a) Skin friction coefficient.

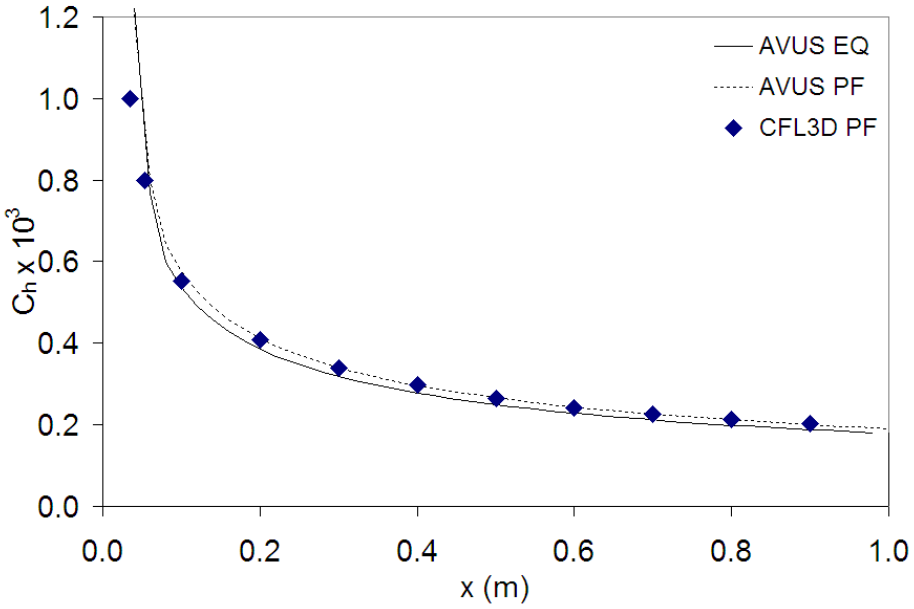

(b) Heat transfer coefficient.

Figure 4.4: Comparison to the results of Rosen (1991) of surface distributions of properties for a supersonic flat plate boundary layer at Mach 2.0.

The computed hypersonic boundary layer results of AVUS are compared to the results of Rosen (1991) who used the CFL3D code. The temperature and tangential velocity profiles at an axial location of $x = 1$ m are presented in Figure 4.5. The skin friction, C_f, and the coefficient of heat transfer, C_h, are presented in Figure 4.6. The results of Rosen are calculated using equilibrium air and the AVUS code results are for both perfect gas and equilibrium air. The tangential velocity and skin friction results show excellent comparison with the results of Rosen. The AVUS temperature results show a slightly lower peak temperatures in the boundary layer than Rosen using equilibrium air, but the results are still very close overall. It is not known why these two results vary at this particular location. Using the AVUS code with a perfect gas shows that equilibrium gas effects are significant for this case. The heat transfer results of Figure 4.6(b) show excellent comparisons to the results of Rosen.

4.2.4 Hypersonic Laminar Wedge and Cone

Another verification that the perfect gas and equilibrium portions of the computer code AVUS are working properly is the comparison of our results to the high Mach number results of Tannehill et al. (1990). This case consist of a two-dimensional wedge and an axisymmetric cone geometry with a 10° half-angle. The flow is viscous, laminar flow at a Mach number of 25. The inflow and outflow boundary conditions are of the far-field type using modified Riemann invariants. The wall boundary condition is an isothermal, no-slip type with a wall temperature of 1200 K. The freestream conditions of the flow are a Mach number of 25, a static pressure of 20.35 Pa, a density of 2.807x10^{-4} kg/m^3, and a temperature of 252.6 K. This corresponds to atmospheric conditions at an altitude of 60.96 km. The unit Reynolds number for this flow is 1.403x10^5/m. The grid used consists of 200 points in the streamwise direction and 60 grid points normal to the surface. The grid spacing is 1.0x10^{-4} m normal to the surface. The height of the top boundary was kept fixed at 0.15 m from the body surface. The two-dimensional axisymmetric cone uses the same grid as the wedge. A three-dimensional cone was also used which had the same grid spacing in the x and

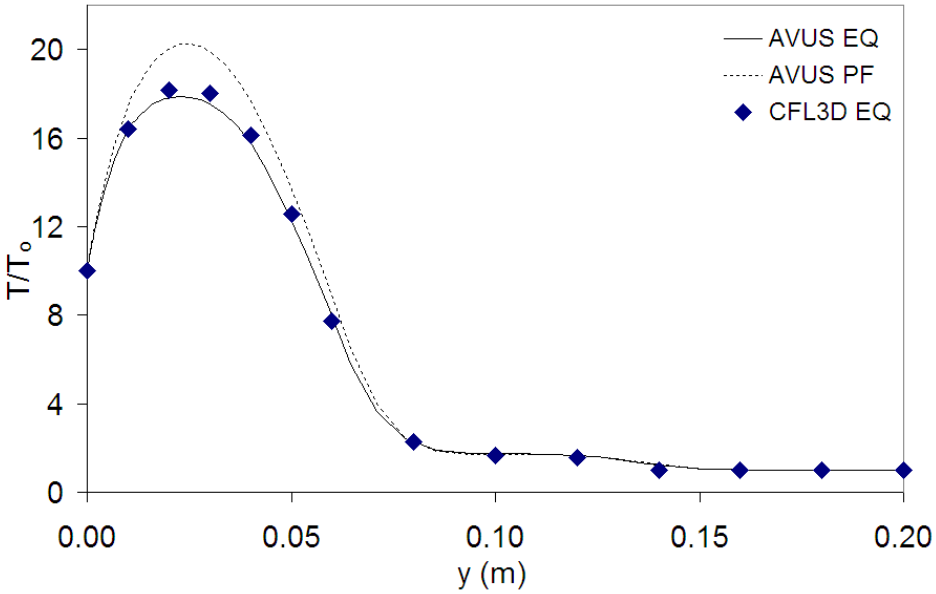

(a) Nondimensional temperature.

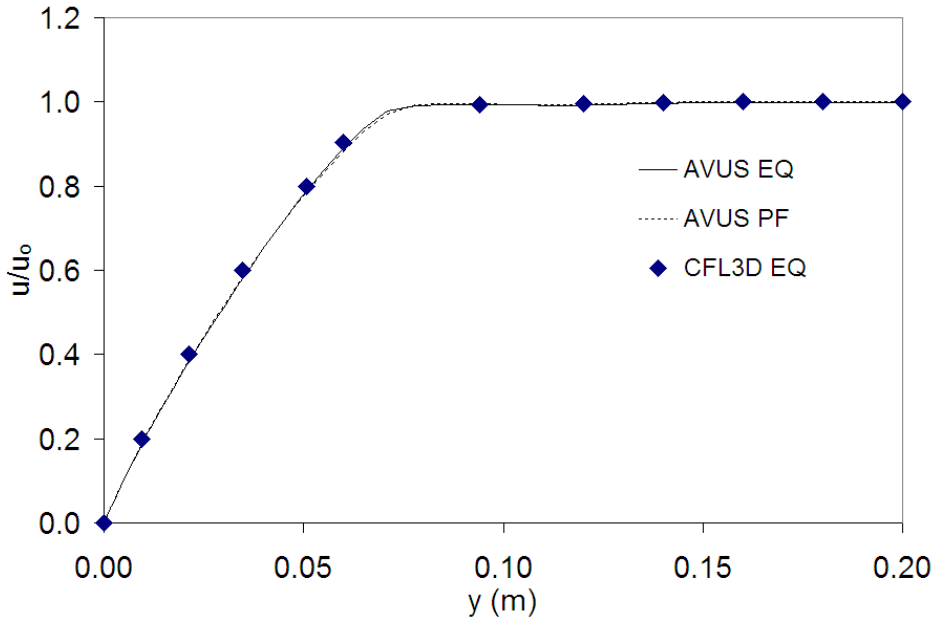

(b) Nondimensional tangential velocity.

Figure 4.5: Comparison to the results of Rosen (1991) of properties at $x = 1$ m for a hypersonic flat plate boundary layer at Mach 20.0.

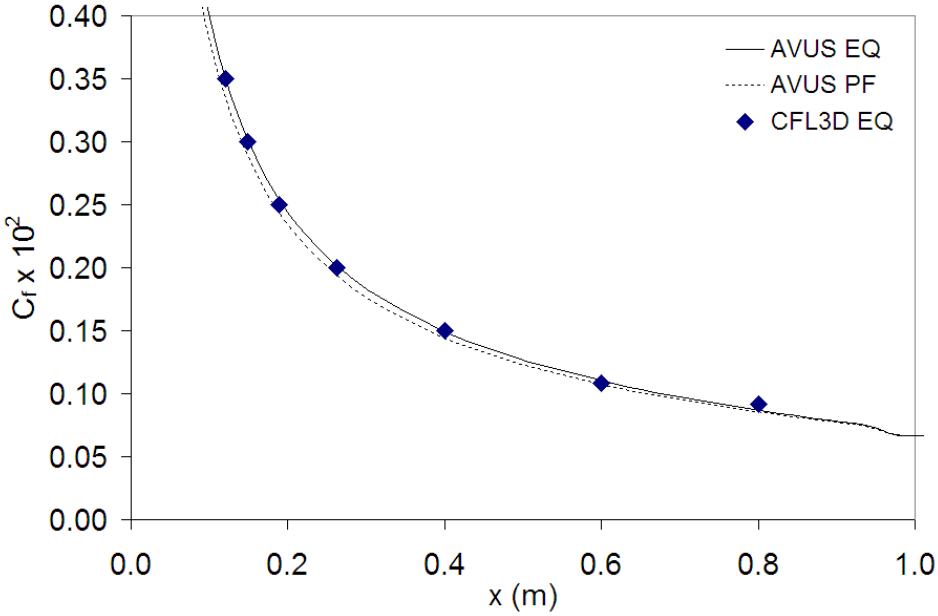

(a) Skin friction coefficient.

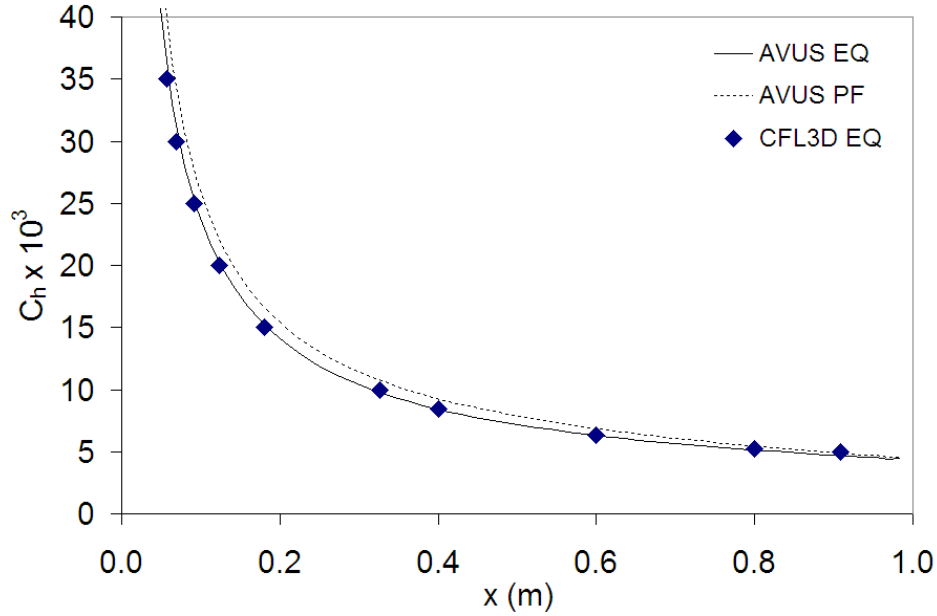

(b) Heat transfer coefficient.

Figure 4.6: Comparison to the results of Rosen (1991) of surface distributions of properties for a hypersonic flat plate boundary layer at Mach 20.0.

y-directions as the two-dimensional wedge and had 10 grid points in the azimuthal direction.

The Tannehill et al. (1990) code was only capable of solving two-dimensional geometries so it only has results for the two-dimensional, axisymmetric cone and two-dimensional planar wedge. The reason for including three-dimensional AVUS results for the axisymmetric cone is to prove that the equilibrium version of AVUS is working properly for three-dimensional geometries. The results presented by Tannehill et al. (1990) were a nondimensionlized temperature profile in the y-direction taken 1.0 m downstream of the leading edge of the wedge or cone. This profile went from the body surface ($y = 0$) to the freestream above the shock.

Tannehill et al. (1990) obtained their results by solving the parabolized Navier-Stokes equations. An upwind, finite volume algorithm developed by Lawrence et al. (1986) was used to solve the parabolized Navier-Stokes equations. The upwind algorithm used was an adapted version of Roe's scheme [Roe 1981] for real gases based on the work of Grossman and Walters (1987) and Colella and Glaz (1985) . A detailed description of this procedure is given in Tannehill et al. (1990). The equilibrium air properties used by Tannehill et al. are essentially the same ones used in AVUS for this work and come from the curve fits of Srinivasan et al. (1987a and 1987b).

Figure 4.7(a) shows the comparison of AVUS and Tannehill et al. results for the 10° half-angle, planar wedge for the perfect gas case. It should be noted that all of the Tannehill et al. results were taken off a graphical plot, so some error is incurred in this procedure. Figure 4.7(a) shows comparisons between the results of Tannehill et al. and the results of AVUS using equilibrium air properties for a perfect gas. Overall the comparisons between the results are in good agreement, except for a slight difference in the location where the shock occurs and a difference in the downward side of the boundary layer temperature profile. Figure 4.7(b) shows the comparison of AVUS and Tannehill et al. results for the 10° half-angle wedge for the equilibrium air case. Figure 4.7(b) shows reasonable comparisons between the results, except in regions of high-curvature.

Figure 4.7(b) shows the comparisons between the published results of Tannehill et al. (1990) and the current results of AVUS using equilibrium air properties and perfect gas properties for an

axisymmetric cone. On this plot there are two results from AVUS; one using the two-dimensional axisymmetric option of AVUS and the other using a full three-dimensional grid. The two and three-dimensional AVUS results are almost on top of one another, except for some small differences at the shock. Since the two-dimensional axisymmetric results and full three-dimensional results from AVUS use the same code, the deviations are probably due to discretization in the azimuthal direction. Looking at the two-dimensional axisymmetric AVUS results and those of Tannehill et al. it can be seen that these cases compare well in all regions with only small deviations. These deviations could be caused by the accuracy with which Tannehill et al. results could be read from the published graphs.

Both Figures 4.7(a) and 4.7(b) show large differences in the perfect gas and equilibrium air results. This is due to the high temperatures caused by the Mach 25 flow. These differences are large because of the change in the air composition from that of a perfect gas at room temperature. The equilibrium air shows smaller temperature changes because it can store energy in the chemical changes occurring as well as the other degrees of freedom. The perfect gas can only store energy in the translational motion of the molecules which is proportional to the temperature of the gas.

4.3 Conclusions

Chemical equilibrium air properties have been added to AVUS so that it is now capable of performing calculations that capture the effects of property changes in high temperature air flows. AVUS is now able to calculate two-dimensional, axisymmetric, and three-dimensional hypersonic flow fields and account for property changes as the temperature and pressure of the gas change. The procedure for adding equilibrium air properties to AVUS utilizing the curve fits of Srinivasan et al. (1987a and 1987b) has been discussed in this chapter. A large number of comparisons to other investigator's published results have been provided to show that correct results are being obtained from the new equilibrium air version of AVUS.

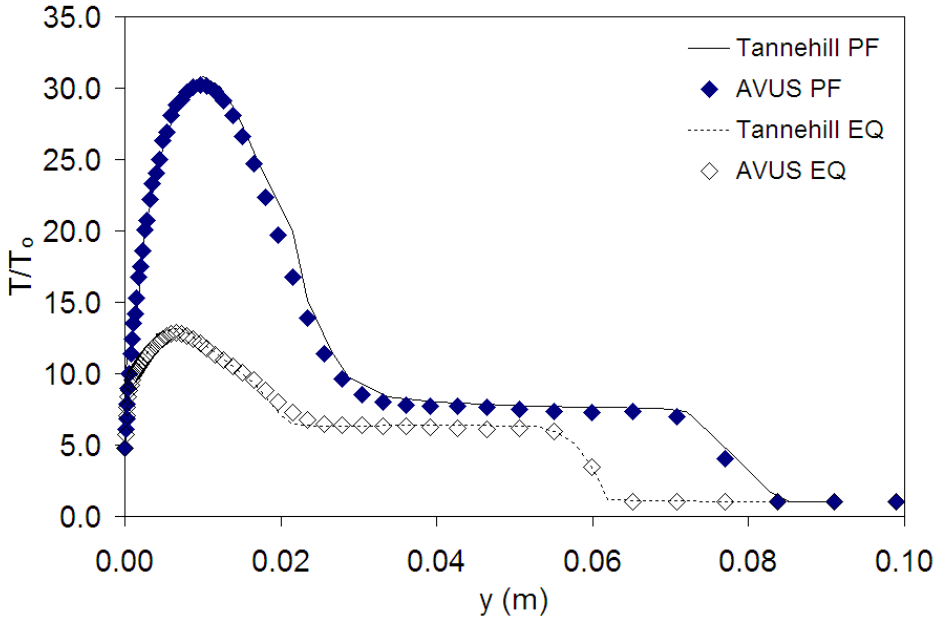

(a) 10° planar wedge.

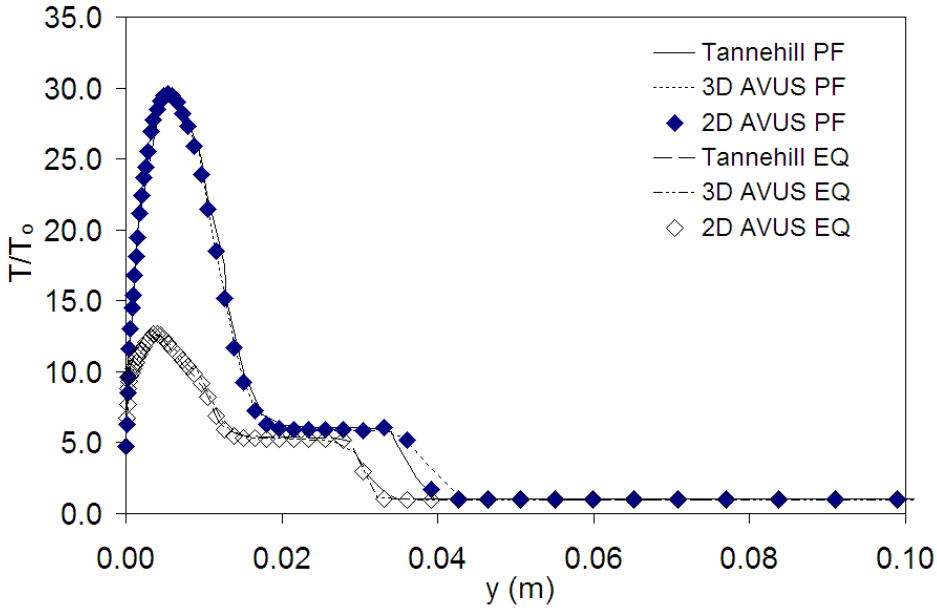

(b) 10° cone.

Figure 4.7: Comparison of end temperature profile utilizing a perfect gas and equilibrium air.

To verify the inviscid part of the new AVUS code, results have been compared to the work of Prabhu et al. (1989) for a blunt body. This comparison shows excellent agreement. To verify the viscous part of the code the results have been compared to the work of Rosen (1991) using the CFL3D code for supersonic and hypersonic flat plate cases. Both of these flat plate cases show excellent agreement with the CFL3D code results. To see the effects of a strong shock for a high Mach number case the results were compared to the work of Tannehill (1990) for a Mach 25 hypersonic flow over a wedge and an axisymmetric cone. The AVUS results show good agreement to the work of Tannehill et al. To check the three-dimensional version of the equilibrium air AVUS code it was run using a full three-dimensional grid for the axisymmetric cone case. These results were compared to Tannehill et al.'s axisymmetric cone case. The comparisons were good indicating that the three-dimensional portion of the equilibrium air AVUS code is working properly.

5

Computationally Determining the Flight Regimes for Blunt Bodies

Given the complexity and increased CPU time of the equilibrium air version of AVUS compared to the perfect gas version of AVUS; and the increased complexity and run time of the nonequilibrium air version of AVUS compared to the equilibrium air version, it would be beneficial to have an idea of the range of applicability of each of these techniques. To a small extent this work has been done by other authors [Hansen 1959; Gupta et al. 1991]. These authors have presented a graph of regions of the applicability of the different air models. These curves appear to be credible, but it is not known what criteria was used for determining the cutoff between the three models. It is believed that the residence time is the determining factor in making these divisions. One of these graphs that show the region of applicability of the various chemical models is shown in Figure 5.1. A more precise plot of the dividing line between these four continuum air models should be produced. This is done in this work by comparing key quantities determined by a CFD code for the different air models.

This chapter computationally determines the regions of applicability of the perfect gas model and the chemical equilibrium air model over a range of pressures and altitudes. The CFD code

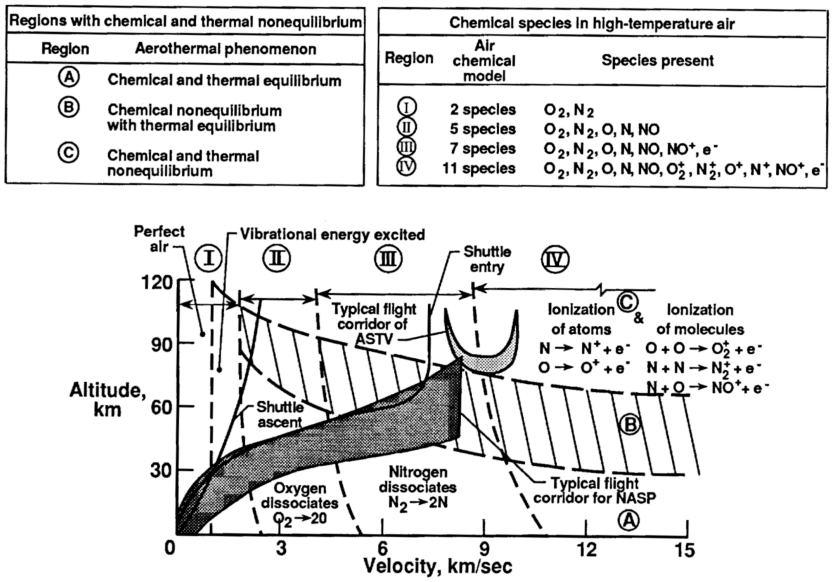

Figure 5.1: Flight stagnation region air chemistry of a 0.305 m radius sphere as published by Gupta et al. (1990).

used to carry out this study is AVUS. With this version of AVUS the regions of applicability of the calorically perfect gas and chemical equilibrium air models will be found by comparing output parameters from the CFD analysis. The dividing line between the chemical equilibrium air model and the chemical nonequilibrium air model with thermal equilibrium will also be found based on output parameters from the CFD analysis. The dividing line between the regions of applicability of the thermal equilibrium and thermal nonequilibrium models is not found in this study. The reason for this is that thermal nonequilibrium region does not become significant for most blunt bodies at altitudes below 80 km. For altitudes above 80 km the continuum assumption of CFD begins to fall apart and the results become unreliable.

To accomplish finding the dividing line between chemical equilibrium air and chemical nonequilibrium air another version of AVUS capable of doing calculations for chemical nonequilibrium air in both thermal equilibrium and thermal nonequilibrium is used [Hudson et al. 2005]. The nonequilibrium version of AVUS has a generalized model for finite-rate chemistry. It is able to model the

thermal nonequilibrium effects of the chemical reactions through Park's T-T_v model [Park 1990]. As mentioned above thermal nonequilibrium is not important for altitudes below 80 km. This code was used to verify this conclusion.

5.1 Separation of Perfect Gas and Equilibrium Air Regions

A number of quantities can be used to determine where perfect gas results start to deviate from equilibrium air results. In this work it was found that the temperatures downstream of the shock have the most sensitivity to the chemistry model chosen. This is a reasonable finding because the equilibrium air model allows more internal modes of energy storage than the perfect gas model. While values of pressure, x-velocity, and other flow properties where analyzed, they did not show as much difference between the results obtained using the the perfect gas and equilibrium air models as was obtained using temperature.

There are several reason why the inviscid blunt body was used for this study instead of a viscous blunt body. First of all, when using a viscous blunt body a complication of what is the appropriate boundary condition to apply at the blunt body wall arises. With inviscid flow the only choice is to to apply a slip wall boundary condition. For a viscous blunt body there are several types of wall boundary conditions that can be applied: adiabatic, isothermal, fixed convective coefficient, or fixed heat flux. For the chemical nonequilibrium air model the additional wall boundary conditions of fully catalytic and partially catalytic walls can be applied. A wall boundary condition that is appropriate to apply at a certain velocity and altitude may not be appropriate to apply at another velocity and altitude. Another difficulty is creating grids for a viscous blunt body that correctly capture the boundary layer. The boundary layer thickness can vary considerably depending on the velocity and altitude of the blunt body. accurately capture the boundary layer, it is necessary to perform a grid refinement study. Yet another additional complication of having a viscous blunt body is at higher altitudes the boundary layer can almost merge with the shock creating additional

computational difficulties.

A difficulty in using the heat transfer profile as a metric for finding the dividing line between the various chemical models, is that the heat transfer profiles can be distorted by a grid- shock misalignment. To correct this problem an adaptive grid solver must be used or a new grid be created that is better aligned to the shock. In addition, heat transfer profiles can vary considerably under certain conditions, depending on what type of boundary condition is applied at the wall. In certain instances the heat transfer profiles obtained from using the chemical equilibrium and chemical nonequilibrium models may be very similar; however, the temperature that is obtained along the stagnation streamline using the two models may be significantly different.

From this discussion it can be seen that the computational time required for a simulation is greatly increased by using the heat transfer profile, instead of the temperature along the stagnation streamline, for a metric. Using the temperature along the stagnation streamline for an inviscid blunt body is a more consistent metric, more computationally efficient metric, and provides a more sensitive indicator of the differences produced by the different air models.

The results in the rest of this section are obtained using the Euler equations with a slip wall boundary condition. The perfect gas model results are identified as "PF" in the figures and are presented as solid lines. The equilibrium air model results are identified as "EQ" in the figures and are presented as dashed lines.

The pressure profiles along the x-axis using the perfect gas and chemical equilibrium air models at an altitude of 40 km are presented at various Mach numbers in Figure 5.2(a). It can be seen from these results that the perfect gas and chemical equilibrium air results are almost identical, with the only significant difference being the shock stand-off distance. This is expected for external flow since it has been stated by Anderson (1989) and Bertin (1994) that pressure is a "mechanically" oriented variable that is governed mainly by the fluid mechanics of the flow. The differences in shock stand-off distances are strongly affected by the temperature of the gas between the shock and the body. The x-velocity along the x-axis at an altitude of 40 km is presented in Figure 5.2(b). The

x-velocity results are also similar for both the perfect gas and equilibrium air results. Again this is because the velocities are mechanically oriented variables.

It should be noted that changes in the pressures and velocities can may be more significant if viscous effects are included in the flow or the geometry is different; however, this does not have to occur. The pressure along the x-axis for the laminar blunt body of radius 0.305 m at an altitude of 40 km is shown in Figure 5.3. From these results it can be seen that even for a flow including viscous effects and higher Mach numbers, the difference between pressures using the perfect gas and the chemical equilibrium air models is rather small. As a final note it should be mentioned that even though the chemistry only slightly affects the pressure, these slight changes can significantly alter the pitching moments and lift of the blunt body, especially if the blunt body is at an angle of attack.

The temperature profiles along the x-axis using the perfect gas and chemical equilibrium air models at an altitude of 40 km are presented for various Mach numbers in Figure 5.4(a). The temperatures for the equilibrium air model are smaller than the perfect gas results, with the temperature difference increasing with higher Mach numbers. The other thing to notice is that the temperature profiles are relatively flat downstream of the shock. It should also be noted that the shock location depends on the chemical model used, with the shock standoff distance being smaller for the chemical equilibrium air results.

Another possible temperature profile for determining the dividing lines in Figure 5.5 would be to use the temperature at the surface of the blunt body. The temperature profiles at the body surface at an altitude of 40 km are shown in Figure 5.4(b). Once again, as the Mach number increases the difference between the perfect gas and equilibrium air results increase. The $T_{\%diff}$ calculated using temperatures at the body surface is not as great as that calculated using the temperatures on the x-axis.

In addition to choosing the temperature to determine the region of applicability of the perfect gas model, it is also necessary to choose the location of the temperature to make this choice. In this

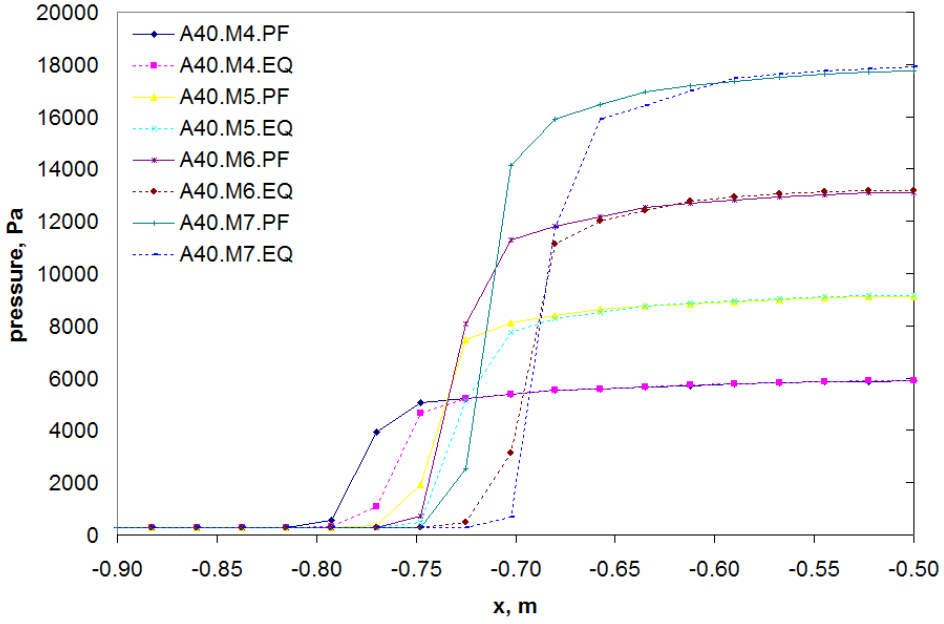

(a) Pressure.

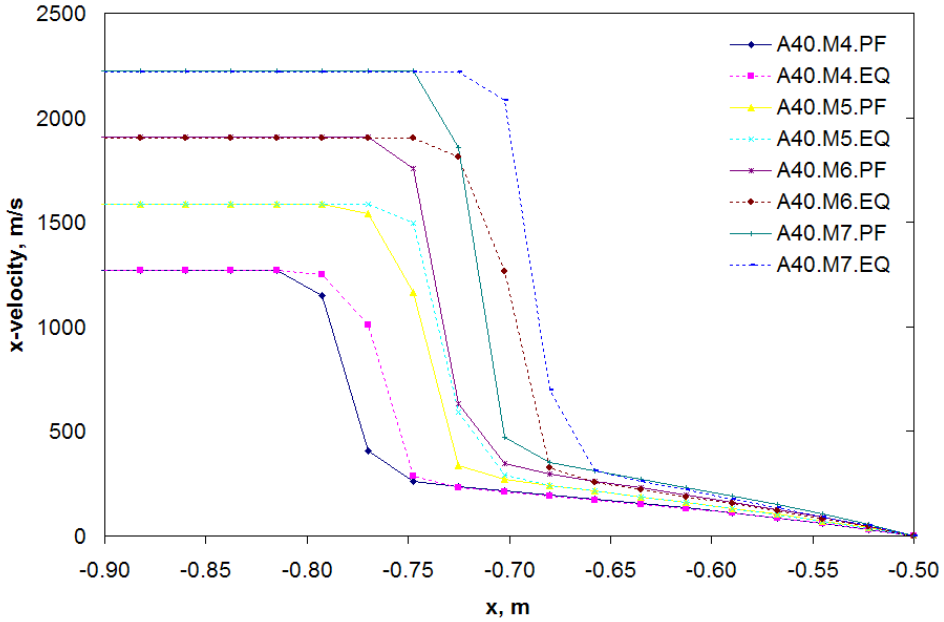

(b) X-velocity.

Figure 5.2: Properties along x-axis at an altitude of 40 km.

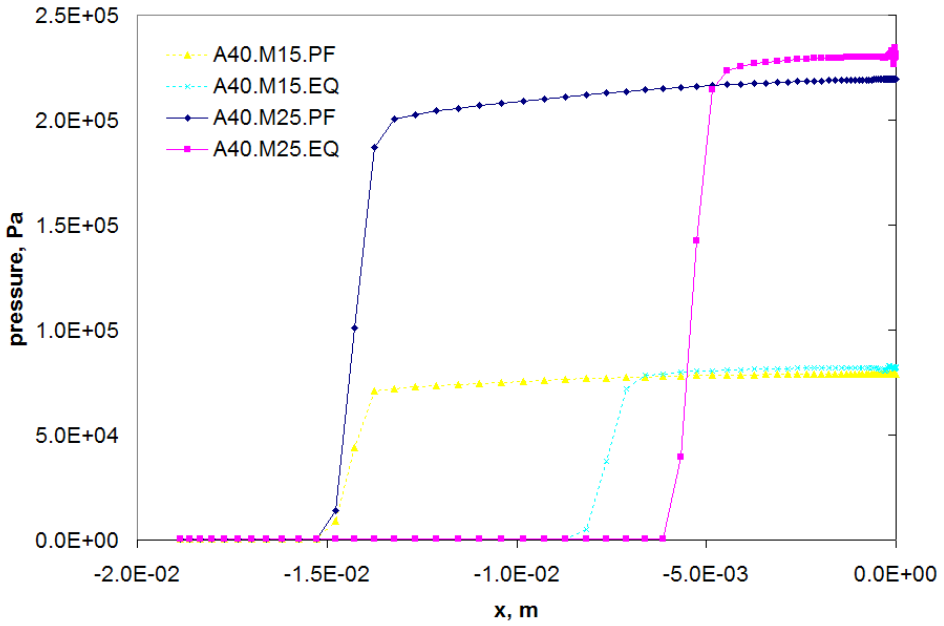

Figure 5.3: Pressure for viscous blunt body along x-axis at an altitude of 40 km.

work it was decided to take the percent difference of the volume average temperature downstream of the shock on the x-axis. The formula for the percent deviation of the perfect gas model from the equilibrium air model is

$$T_{\%diff} = \frac{T_{PF} - T_{EQ}}{T_{EQ}} * 100.0 \tag{5.1}$$

where T_{PF} is the volume-averaged temperature downstream of the shock on the stagnation streamline that is predicted by the perfect gas model and T_{EQ} is the volume-averaged temperature downstream of the shock on the stagnation streamline predicted by the equilibrium air model. Essentially this equation gives the percent difference between the temperatures predicted by the two models downstream of the shock.

To obtain the dividing lines between the perfect gas and chemical equilibrium models the following procedure is employed.

1. The inviscid blunt body model is run using AVUS for both the perfect gas and equilibrium air models. Data is collected from both of the chemical models for Mach numbers ranging from 0

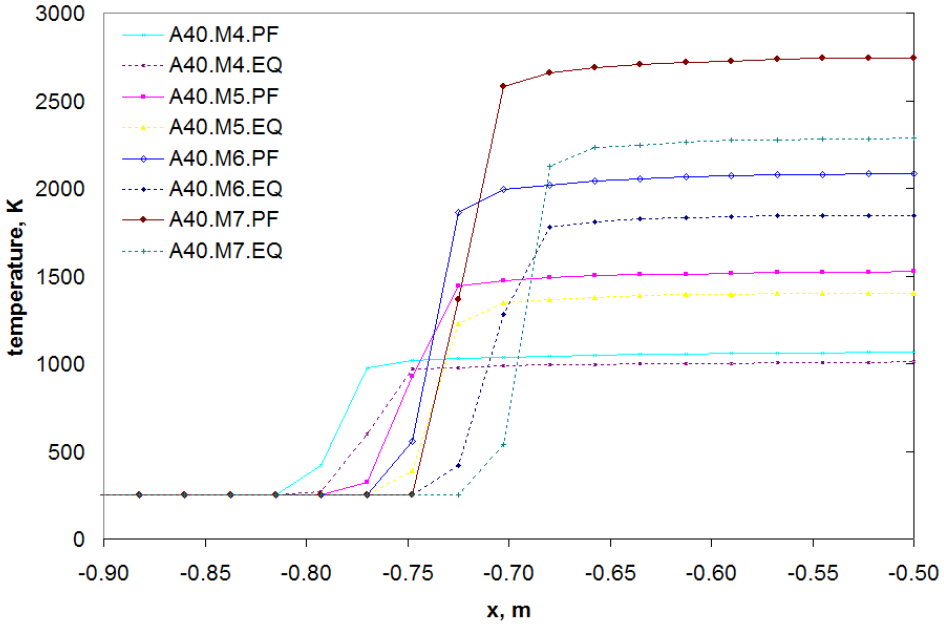

(a) Along x-axis.

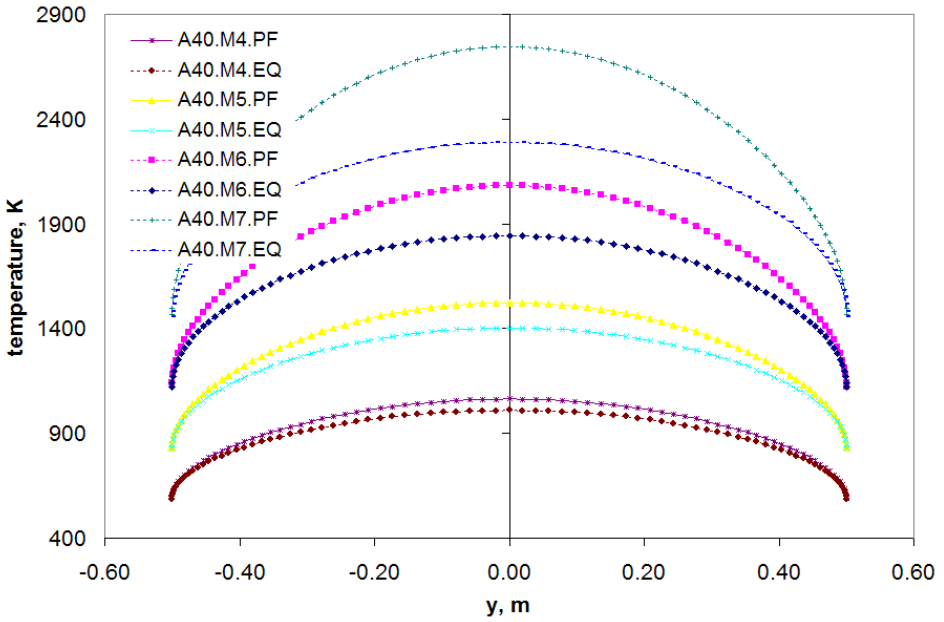

(b) Body surface.

Figure 5.4: Temperature profiles along x-axis and at body surface at an altitude of 40 km.

to 10 at intervals of 1 with freestream conditions corresponding to altitudes ranging from 0 km to 80 km at 10 km intervals.

2. At each of the data points Equation 5.1 is used to find $T_{\%diff}$.

3. To obtain the 5%, 10%, and 20% dividing lines interpolation between the existing $T_{\%diff}$ data points at a fixed altitude is performed.

The results for the 5%, 10%, and 20% temperature deviations, as calculated by Equation 5.1, are shown in Figure 5.5. For the most part the 5% temperature deviations occur at a velocity of 1.2 km/s, the 10% temperature deviations occur at 1.7 km/s, and the 20% temperature deviations occur at a velocity of 2.2 km/s. There are some small changes with elevation, but they are rather unimportant. These velocities are in the neighborhood of the Mach 5 line. The region to the left of the 5%, 10%, or 20% line is the area where the perfect gas model can be used with confidence, and the region to the right of these lines is where the equilibrium air model should be used.

5.2 Separation of Chemical Equilibrium and Nonequilibrium Regions

The temperature downstream of the shock on the x-axis for an inviscid blunt body was also used to determine the dividing line between the chemical equilibrium and chemical nonequilibrium models. The formula for the deviation of the equilibrium air model from the nonequilibrium air model is

$$T_{\%diff} = \frac{T_{NEQ} - T_{EQ}}{T_{NEQ}} * 100.0 \tag{5.2}$$

where T_{EQ} is the volume-averaged temperature downstream of the shock on the stagnation streamline that is predicted by the equilibrium air model and T_{NEQ} is the volume-averaged temperature downstream of the shock on the stagnation streamline predicted by the noequilibrium air model.

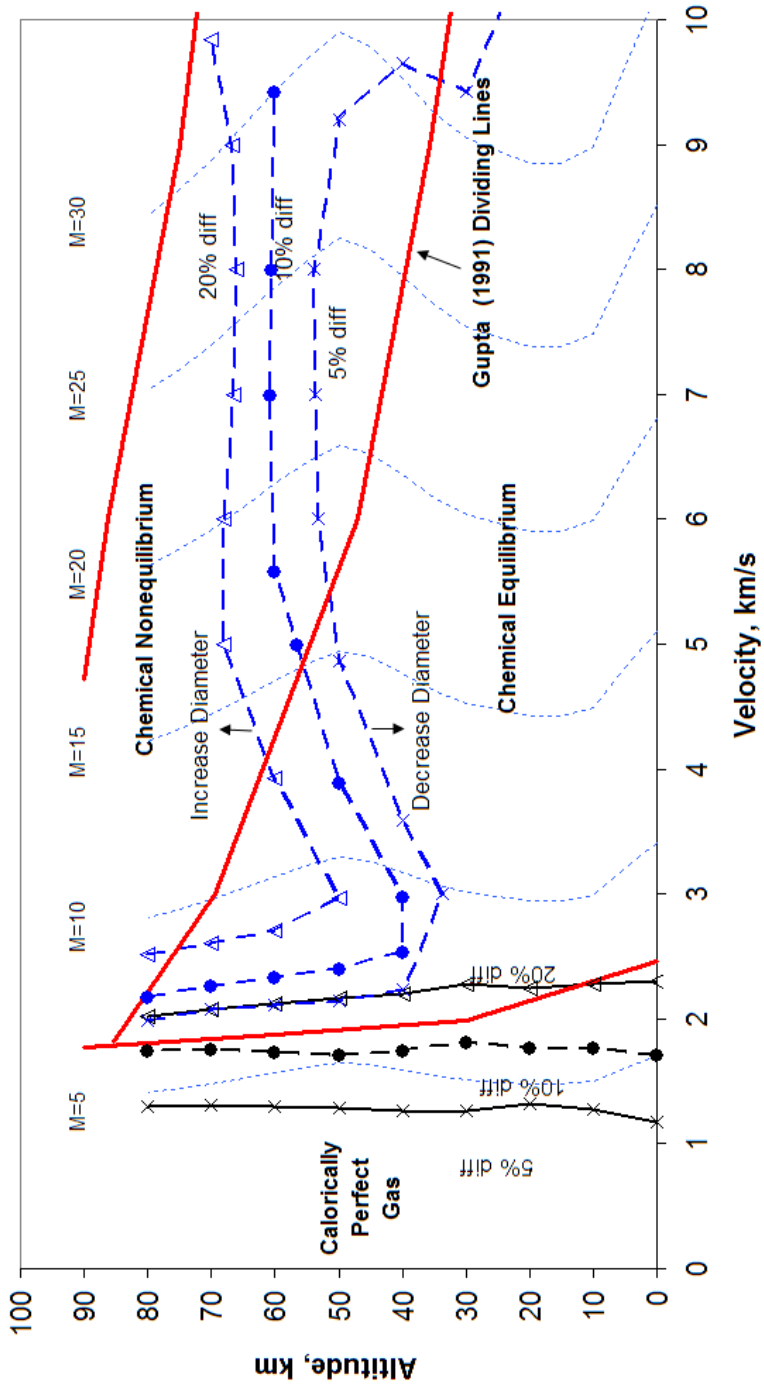

Figure 5.5: Region of applicability of perfect gas, equilibrium air, and nonequilibrium air models for a 0.5 m diameter blunt body in air.

Essentially this equation gives the percent difference between the temperatures predicted by the two models downstream of the shock. As with the perfect gas and chemical equilibrium results, the freestream conditions are changed from sea level to 80,000 km. The free stream Mach number is altered enough to obtain the 5%, 10% and 20% deviation lines for all elevations.

The dividing lines between chemical equilibrium and chemical nonequilibrium regions were obtained for a blunt body of radius of 0.5 m. Figure 5.6 shows that the chemical equilibrium results do not depend on the radius of the blunt body used, but the chemical nonequilibrium results do depend on the radius of the blunt body used. In this figure the 0.5 m and 50 m chemical equilibrium results fall right on top of one another and the 50 m results are not visible. With a larger radius blunt body the flow has more time to reach an equilibrium distribution before it comes in contact with the blunt body causing the chemical nonequilibrium results to be a function of the body radius. From these findings it can be seen that if a larger radius blunt body is used, the dividing line between chemical equilibrium and chemical nonequilibrium will move to higher altitudes, and if a smaller radius blunt body is used the dividing line will move toward lower altitudes.

The dividing lines between the chemical equilibrium and chemical non-equilibrium models obtained from this work show dips around 3 km/s and around 10 km/s (see Figure 5.5). The dividing lines found by other researchers using the residence time do not show these dips. To aid in the discussion of this phenomenon the temperature profiles and mole fractions of O_2 along the stagnation streamline are provided at an altitude of 40 km. The first dip in Figure 5.5 corresponds to the region where O_2 starts to dissociate strongly. As O_2 starts to dissociate, the energy jump across the shock is not strong enough to cause the O_2 to reach a fully dissociated state as the fluid passes through the shock. Due to the increased temperature on the downstream side of the shock, the O_2 dissociates more as it flows downstream of the shock, until it reaches an equilibrium distribution. As Mach number increases the velocity increases linearly, but the gas temperature and density increases in a quadratic fashion. Therefore, further increases in Mach number may lead to a large enough thermal energy and density jump across the shock for all of the O_2 to fully dissociate as it passes through the

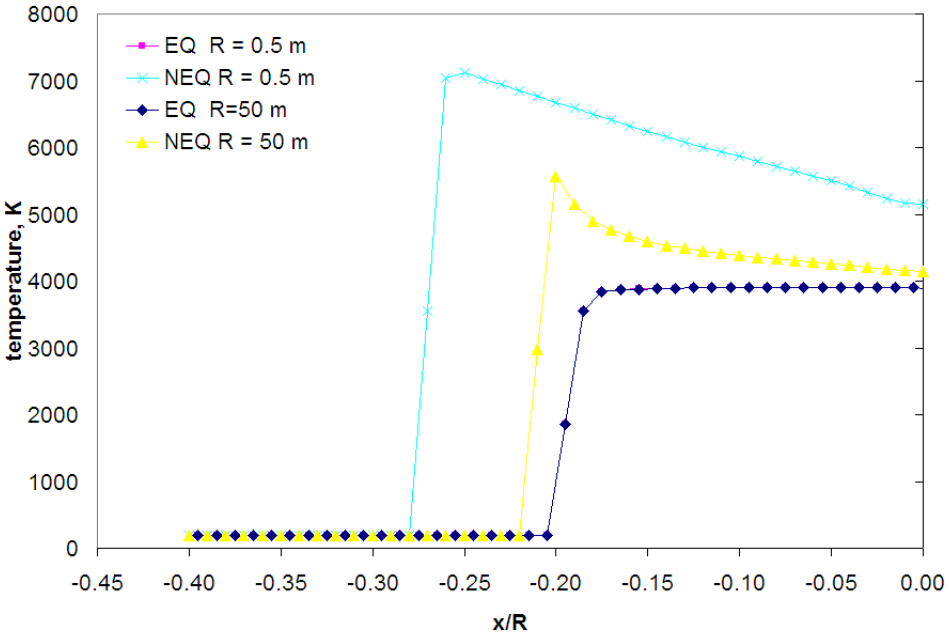

Figure 5.6: Effect of radius on an inviscid blunt body. The blunt body is at altitude of 80 km and a Mach number of 15.0

shock. This leads to the air being close to an equilibrium distribution downstream of the shock. The second dip in the dividing lines between chemical equilibrium and chemical nonequilibrium shown in Figure 5.5 occur in the region where the dissociation of N_2 is occurring. At higher altitudes the gas density decreases so it takes longer for particle collisions to occur, this causes it to take longer for the air to reach an equilibrium distribution. This means that as the blunt body increases in altitude, the air will deviate more from a chemical equilibrium distribution.

To verify that the two dips seen in the dividing lines are due to O_2 and N_2 disassociating a comparison of the results from AVUS and CANTERA is made. The first dip occurs around Mach 10 at altitudes of 40-70 km. The AVUS results using the chemical equilibrium air model under these conditions give the temperature downstream of the shock to be 2,900 K - 3200 K. From the results of Figures 3.1(a) and 3.2(a) using CANTERA it can be seen that O_2 starts to dissociate around 3000 K - 6000 K. The second dip occurs around Mach 30 at altitudes of 40-70 km. The AVUS results using the chemical equilibrium air model under these conditions give the temperature downstream of the

shock to be 8,900 K - 10,000 K. From the results of Figures 3.1(a) and 3.2(a) using CANTERA it can be seen that N_2 starts to dissociate around 6000 K - 12,000 K.

5.3 Conclusion

This work has produced quantitative dividing lines between a regime where the perfect gas model can be used, a regime where the chemical equilibrium model can be used, and a regime where the chemical nonequilibrium model can be used with accuracy. The 5% deviation, 10% deviation, and 20% deviation lines between each of these three regimes is given. The parameter used to determined these percent differences in the model predictions is the volume averaged temperatures along the stagnation streamlines between the shock and the surface of the blunt body. Volume weighted average temperatures were chosen to determine the differences in the model results because the perfect gas model and the chemical equilibrium model showed the most deviation in this parameter for blunt body flow. This is also the best parameter to chose for the deviations between the chemical equilibrium air model and the chemical nonequilibrium air model, but it is not as sensitive as the deviations between the perfect gas and chemical equilibrium models. This is the first time that such a detailed survey of the differences in results produced by these three models for different altitudes and air flow speeds has been produced. The only other work that has laid out the regimes of applicability of the perfect gas model, the chemical equilibrium model, and the chemical nonequilibrium model utilizes residence times. This is a good first attempt at outlining these regimes, but not as detailed or precise as using full CFD calculations for high-speed air flow over a blunt body as done in this work. There are differences in the regime dividing lines from this work and those based simply on residence time calculations. The extreme detail of the work done here shows these differences when looking at the dividing lines between the regimes where the equilibrium air model can be used and the regime where the nonequilibrium air model must be used to obtain good accuracy.

This study has revealed that the dividing line where the perfect gas model gives way to an

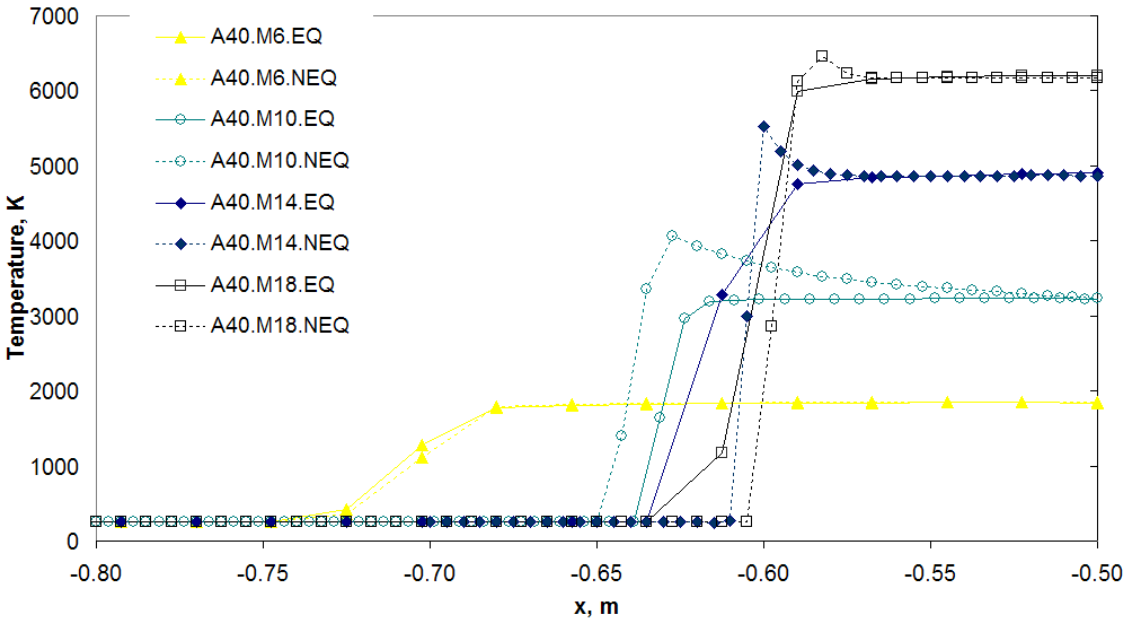

(a) Temperature profile along stagnation streamline.

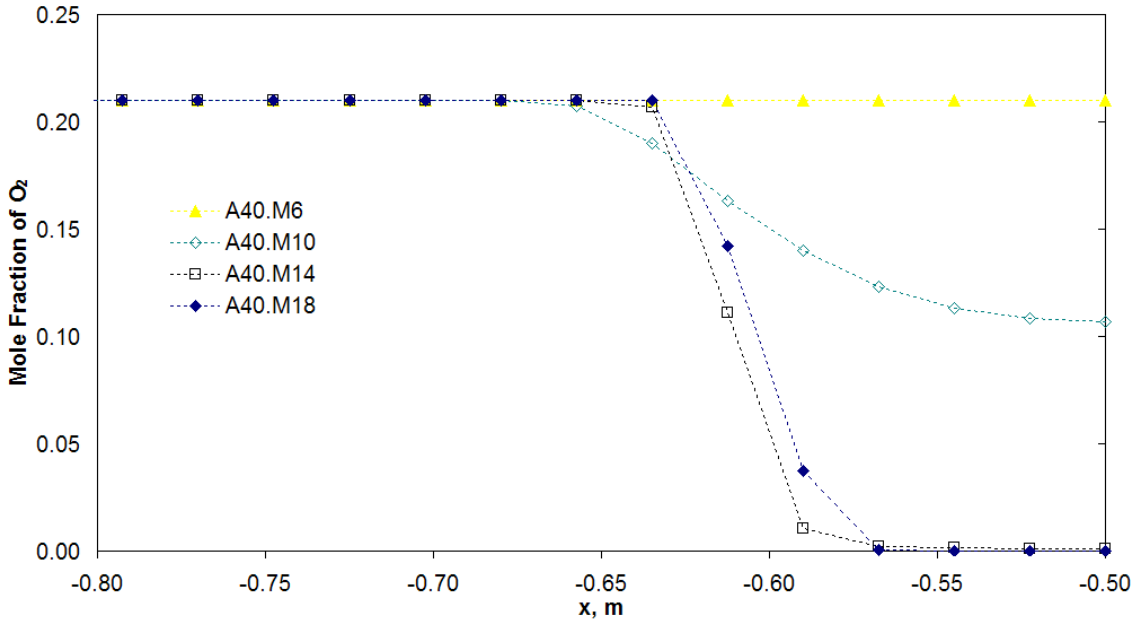

(b) Mole fractions of O_2 along stagnation streamline.

Figure 5.7: Effect of chemical model used on properties of inviscid blunt body at an altitude of 40 km.

equilibrium air model is in the neighborhood of Mach 5. Depending on what type of accuracy is desired this dividing line can be lowered or increased. For the most part the deviation between the two models is a weak function of elevation up to 80 km. The dividing lines between chemical equilibrium and chemical nonequilibrium for a 0.5 m radius blunt body was found to lie at an elevation of about 55 km for Mach numbers greater than 10. For Mach numbers less than 5 the perfect gas model can be used. Between Mach 5 and Mach 10 for altitudes greater than 55 km a transition is quickly taking place from the perfect gas model, to the equilibrium air model, to the the nonequilibrium air model. A detailed plot of the regimes of applicability is given in Figure 5.5. This figure provides a great deal of quantitative information and should be very useful to the high-speed flow CFD community.

This work has also shown that the equilibrium air results are not a function of the radius of the blunt body. However, the nonequilibrium air results are a function of the radius of the blunt body. As the radius of the blunt body increases the nonequilibrium air results approach those of the equilibrium air model. Thus for radii greater than the 0.5 m radius used in this work the dividing line between the equilibrium air results and the nonequilibrium air results moves to higher elevations. For smaller radii blunt bodies the dividing line moves to lower elevations.

6

Grid Study of the Carbuncle Phenomena for Blunt Bodies

6.1 Research Objectives

Upwind Riemann solvers are often the numerical method of choice for capturing strong shock waves that characterize high-speed flows. This is due to their low numerical dissipation, their high level of robustness, and their ability to exactly capture discontinuities. Even with these desirable properties, upwind Riemann solvers have their own peculiar flaws. One of these flaws, which routinely affects blunt bodies, is the carbuncle phenomenon. The carbuncle phenomenon is a numerical instability that affects the numerical capturing of shock waves. The carbuncle phenomenon can be described as a pair of oblique shocks in the stagnation region instead of a smooth bow shock. This can be seen in Figure 2.1(a) for the numerical simulation of a Mach 20 inviscid flow around a circular cylinder using Roe's scheme [Roe 1981; Roe and Pike 1984]. The oblique shocks are also weaker than the bow shock so the jump conditions are in error. As a result of incorrect shock jump conditions and spurious vorticity the heat transfer results can be highly inaccurate.

Various cures have been proposed for the carbuncle problem. These cures generally involve

adding dissipation to the numerical routine in order to eliminate the carbuncle. This work will show results of a detailed study of how a structured grid affects the carbuncle phenomenon and how well it captures a strong shock. Recommendations on what is a "good" grid for capturing strong shocks on blunt bodies, and still avoid the carbuncle phenomenon will be made. The CFD code used to perform this study is AVUS, formally known as Cobalt_{60} [Strang et al. 1999]. The usage of blended flux function has been implemented in AVUS to provide large reductions in the carbuncle phenomenon.

As discussed in Chapter 1 a blended flux function involves flagging the cell faces that may suffer from the carbuncle phenomenon. If a cell face is not flagged then a low dissipative flux function is used; however if a cell face is flagged then a more dissipative flux function is used. This confines the use of the more dissipative flux function to regions near the strong shock.

This work will show that the heat transfer profiles in the stagnation region of a hypersonic blunt body are very sensitive to the upstream flow field perturbations. This even occurs when blended flux functions are used. Numerical experiments support the theory that upstream flowfield perturbations are magnified in the internal shock structure and convected downstream to degrade the wall heat transfer predictions. These errors may arise from either the flux functions or from the grid quality in the region of the shock. The performed grid study shows that the grid quality in the region of the strong shock is one of the major factors contributing to these errors.

One of the problems encountered at the beginning of this study was causing the carbuncle phenomenon to occur. This is because the prior work done by Strang (2005) in adding blended flux functions to AVUS has greatly reduced the carbuncle phenomenon. The use of the blended flux functions has produced a large reduction in the carbuncle phenomenon for strong shocks. For this reason results with the blended flux functions are used as a check to see when the carbuncle phenomenon is occurring. Low dissipation flux functions are used to test which variables affect the carbuncle phenomenon. It is with the low dissipation flux functions that the carbuncle phenomenon can be seen.

The first results presented are for Quirk's case for a normal shock traveling down a straight duct assuming inviscid flow. Quirk's case provides insight into the carbuncle phenomenon, while having a simpler geometry than the blunt body problem. The second results presented are the grid study of the blunt body using the Euler flow solver. These results show that the carbuncle phenomenon is heavily influenced by the type of grid used near the shock. In particular, the aspect ratio near the shock and how the cell faces are aligned with the shock influence the effect of the carbuncle phenomenon.

The viscous grid study presents results using a laminar blunt body with an isothermal wall. The viscous grid study shows that the heat transfer profile cannot be accurately captured solely using a low dissipative flux function, even with a "good" quality grid. Even with the use of the blended flux function the heat transfer profiles are still distorted to some degree depending on the grid used. The grid study also shows that more accurate heat transfer profiles are obtained when the HLL flux function is used on the cell faces parallel to the shock, instead of the van Leer flux function.

The remaining portion of the grid study in this chapter supports the hypothesis that the non-alignment of the grid with the shock is another source of error preventing the wall heat transfer profiles from being properly captured. This research also supports the hypothesis that the carbuncle phenomenon and the misalignment of the shock with the grid are two independent causes of the distorted heat transfer profile.

6.2 Grid Study Using Quirk's Case

The results presented in this section are for Quirk's case [Quirk 1994]. Quirk's case consists of a normal shock traveling down a straight duct. The shock will sometimes break apart and takes on a shape similar to the carbuncle phenomenon seen with blunt bodies. The shock breaks up due to odd-even perturbations being applied along the centerline of the channel or simply from the round-off error due to machine accuracy of the computer. In this work the carbuncle phenomenon occurs

in all the cases due to machine accuracy, unless noted in the particular case. All of the cases consist of a straight duct that is 1.0 m wide with slip walls. All the cells are rectangular and the aspect ratio (length of cell face parallel to shock/length of cell face perpendicular to shock = $\triangle y/\triangle x$) is controlled by either keeping $\triangle x$ or $\triangle y$ constant and varying the length of the cell in the other direction.

The Riemann problem is initiated for all of the cases studied by a discontinuity at 0.5 m from the entrance of the straight duct. All of the cases produce a single shock wave that travels to the right at Mach 6.0, except for the study on the threshold Mach number. To create the Mach 6.0 shock the high pressure driver gas has the properties of $\rho_L^* = 5.2683$, $u_L^* = 5.75172$, $v_L^* = 0.0$ and $P_L^* = 41.833$, and the low pressure driven gas has the properties of $\rho_R^* = 1.0$, $u_R^* = 0.0$, $v_R^* = 0.0$ and $P_R^* = 1.0$. All Quirk's cases are run with double precision numerical accuracy, a CFL number of 0.8, and the air is taken to be a perfect gas unless otherwise noted. The left and right states are nondimensionalized by

$$\rho^* = \frac{\rho}{\rho_\infty}, \quad u^* = \frac{u}{u_\infty}, \quad v^* = \frac{v}{v_\infty}, \quad P^* = \frac{P}{\rho_\infty c_\infty^2}. \tag{6.1}$$

It should also be noted that the results of Quirk's case are from running a 2D prototype version of the AVUS code that reads in the left and right states as nondimensionlized values. This 2D code uses explicit time integration instead of the more sophisticated implicit time integration methods of AVUS. The 2D code also does not include the use of the van Leer flux scheme [van Leer 1982] for the cell faces parallel to the shock and is 1^{st} order accuracy in space.

Through running a number of different cases it was found that the maximum magnitude of the v-velocity in the entire computational domain was the best parameter to use to show the magnitude of the carbuncle phenomenon. Physically, for a normal shock traveling down a straight duct with no viscous forces the v-velocities should be zero. Any v-velocities that show up are due to shock instabilities resulting from the carbuncle phenomenon. It was found that the carbuncle phenomenon

develops with the number of time steps the flow solver has taken and not the distance the shock has traveled down the duct.

All of the results for Quirk's case are presented using the low dissipative flux function instead of the blended flux function. The blended flux function does not show the carbuncle problem for Quirk's case, but captured the normal shock with no distortions and kept the v-velocities on the order of machine precision for all cases.

The purpose of Figure 6.1 is to show how strongly the aspect ratio of the cells is related to the carbuncle phenomenon. This is a rather severe case of the carbuncle phenomenon with the centerline of the channel being perturbed by an odd-even grid line perturbation of $1x10^{-3}$ m. Figure 6.1 shows contour plots of density in the region of the normal shock for various aspect ratios. Figure 6.1(a) with an aspect ratio of 1 shows that the carbuncle phenomenon has caused the normal shock to form a bulge near the centerline which is nonphysical. For higher aspect ratios the shock looks more like a normal shock, but properties are not completely uniform downstream of the shock, as they should be. The higher aspect ratio cases, however, show more uniform properties downstream of the shock than the lower aspect ratio cases.

All of the plots in Figures 6.2 -6.4 show that the magnitude of the errors caused by the carbuncle phenomenon grow with each iteration. This occurs to a point where the growth in the error levels off. The leveling off position, asymptotic value, and number of iterations to achieve this asymptotic values varies depending on a number of factors as shown in these figures. These findings reinforce the assumption that the carbuncle phenomenon is caused by a numerical instability. The quantity plotted on the y-axis is the absolute value of the maximum v-velocity in the computational domain and the quantity plotted on the x-axis is the number of time steps the solver has taken.

A number of aspect ratios and cell sizes were run to obtain the results in Figure 6.2(a). For an aspect ratio of 1.0 a number of result sets were calculated. The only difference for these result sets is different cell sizes were used with the aspect ratio being held at 1.0. These results show that the carbuncle phenomenon is independent of cell size. In a dramatic way Figure 6.2(a) shows that the

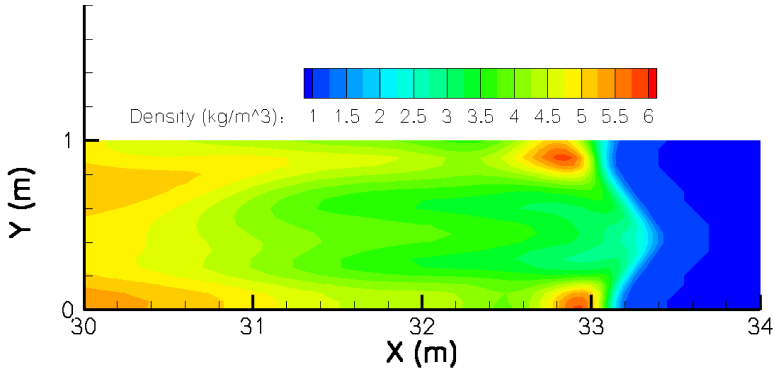

(a) Aspect ratio = 1.0.

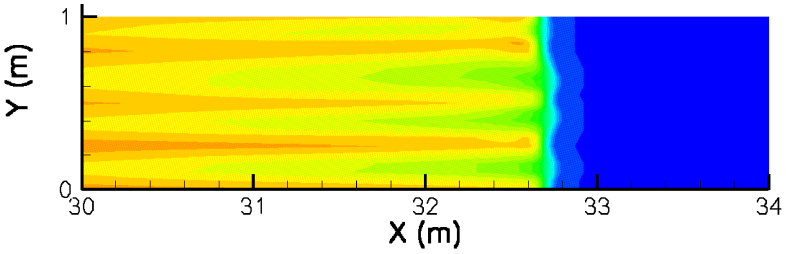

(b) Aspect ratio = 2.0.

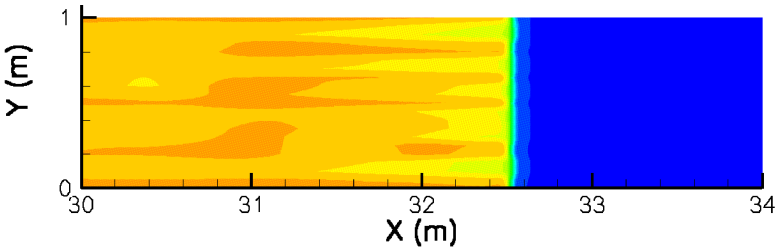

(c) Aspect ratio = 4.0.

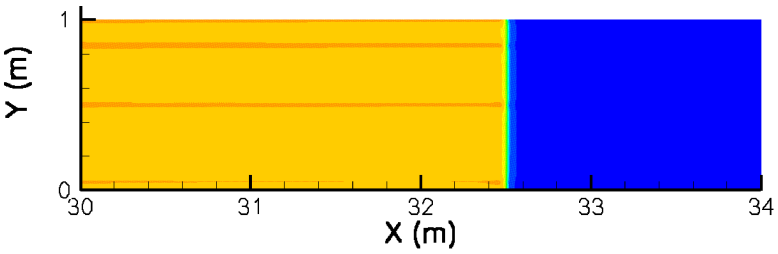

(d) Aspect ratio = 8.0.

Figure 6.1: Contour plots of density for Quirk's case with a centerline perturbation of $1x10^{-3}$ m.

rate that the carbuncle phenomenon grows can be greatly reduced by increasing the aspect ratio of the cells. In addition it can be seen that the asymptotic value of the carbuncle phenomenon decreases as the aspect ratio increases.

Figure 6.2(b) shows how machine precision affects the growth and asymptotic behavior of the carbuncle phenomenon. The results show that the carbuncle phenomenon starts at machine precision and grows from there. The rates for double and single precision are similar, but single precision reaches an asymptotic value more quickly since it starts at a larger value. The machine roundoff error for single precision is $1\text{x}10^{-6}$, while the machine roundoff error for double precision is $1\text{x}10^{-15}$. The machine precision used in the simulation does not significantly affect the asymptotic value of the carbuncle phenomenon, but a slightly smaller value is obtained with double precision.

Figure 6.3(a) shows the effect of changing the magnitude of the time steps without changing the grid used. This is accomplished by changing the CFL number. From these results it can be seen that using a smaller CFL number does not change the asymptotic behavior of the carbuncle phenomenon, but it does greatly increase the required computational time. This is understandable since much smaller time steps are taken.

Figure 6.3(b) shows how the threshold Mach number and the severity of the carbuncle phenomenon are affected by the aspect ratio of the cells. The results plotted in this figure are the asymptotic values for each data point. The results show that the threshold Mach number is around 2, no matter what the aspect ratio. Figure 6.3(b) also shows that increasing the aspect ratio causes the carbuncle phenomenon to be less severe for any Mach number greater than the threshold of 2.

The blended flux functions are a linear weighted average of the low dissipation flux function and the more dissipative flux partner. For shorthand the blending parameter α is used, which is the percent of the more dissipative flux partner in the blended flux function. Therefore $\alpha = 0.6$ is a blend of 40% of the low dissipative flux function and 60% of the more dissipative flux partner. All of the previous results for Quirk's case used $\alpha = 0.5$. Figure 6.4 shows the effect of using various levels of the blending parameter α to find the amount of dissipation needed to eliminate the carbuncle

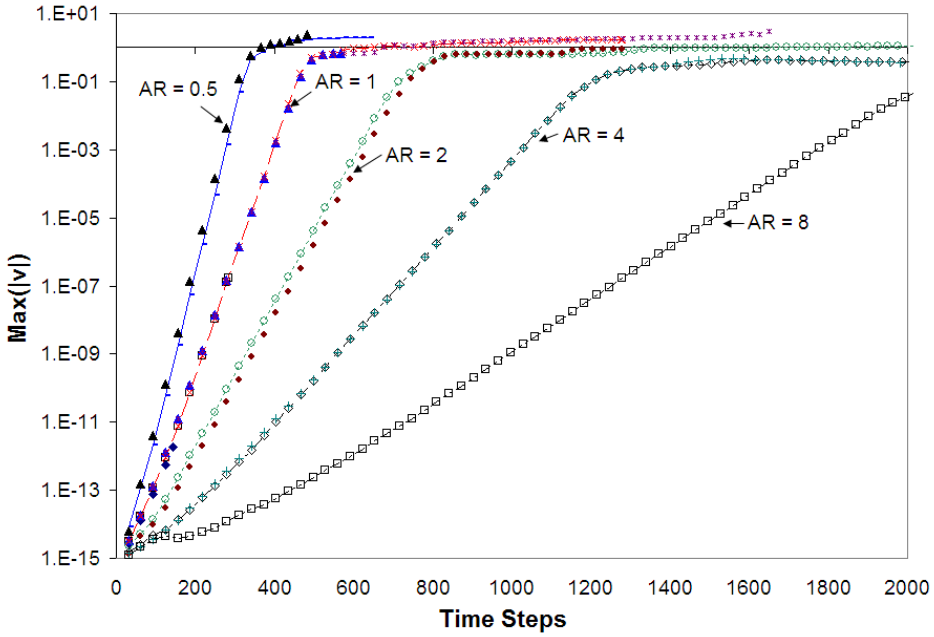

(a) Aspect ratio.

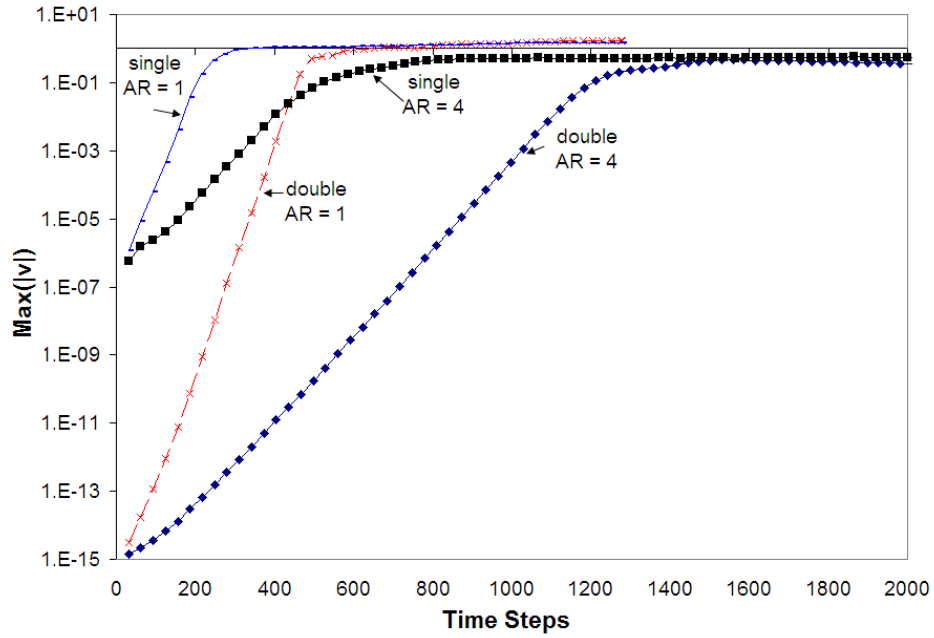

(b) Machine precision.

Figure 6.2: Grid study of Quirk's case looking at grid aspect ratio and machine precision..

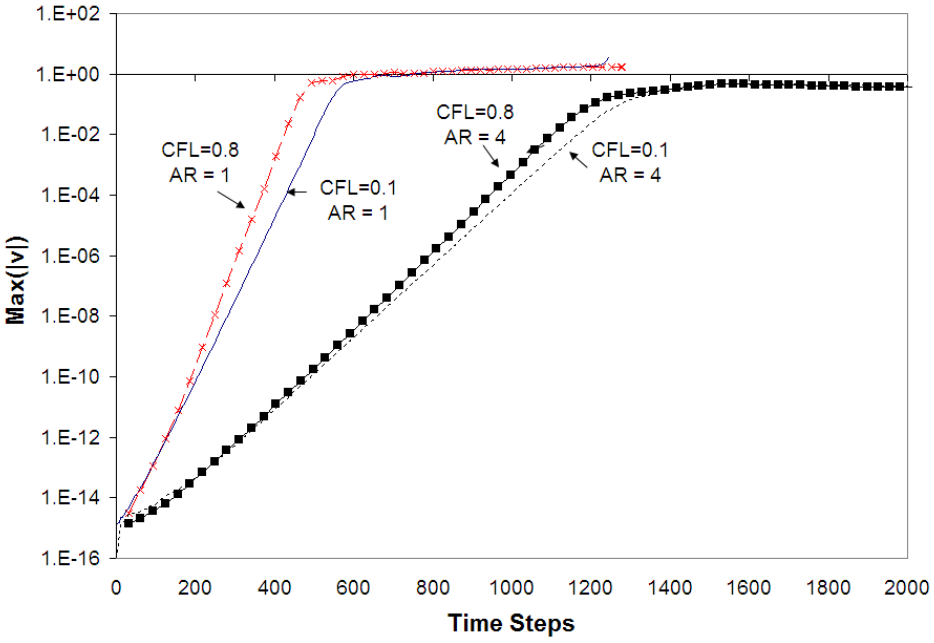

(a) CFL number.

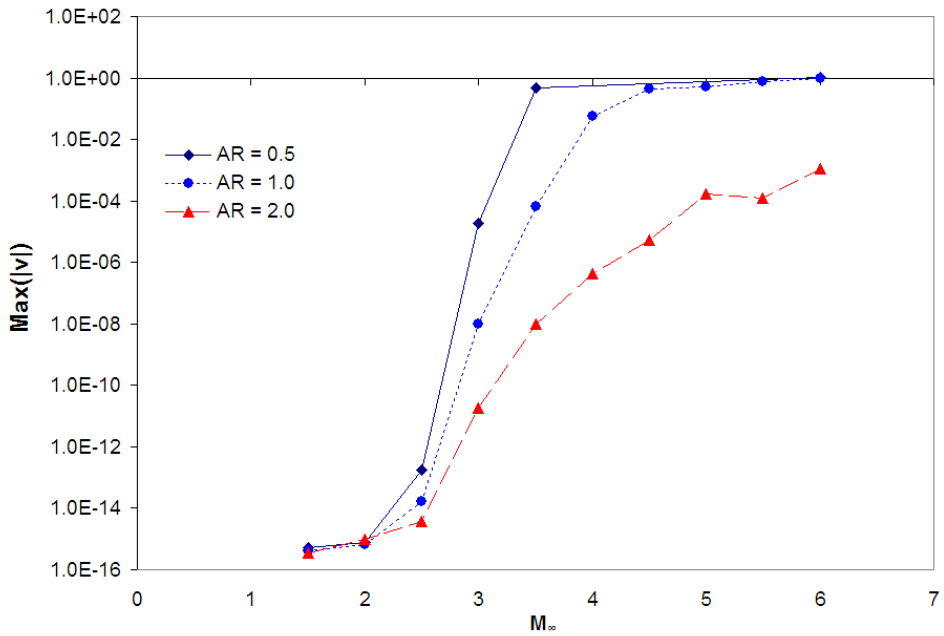

(b) Study of threshold Mach number.

Figure 6.3: Grid study of Quirk's case.

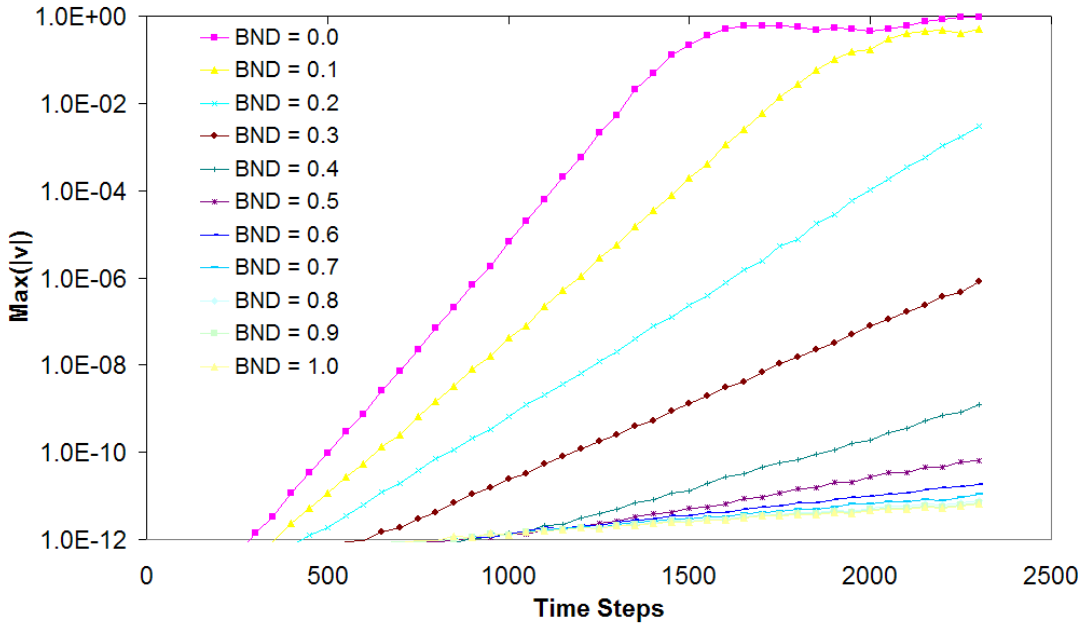

Figure 6.4: Effect of blending parameter α.

phenomenon. The grid used for Figure 6.4 has an aspect ratio of 1.0. From these results it can be seen that as α increases the growth rate of the carbuncle phenomenon decreases. For $\alpha > 0.5$ there is sufficient dissipation from the more dissipative flux partner to suppress the carbuncle phenomenon. It should be mentioned that for this study of the effect of α, Quirk's case was run using the full blown version of AVUS. The full blown version of AVUS uses implicit time integration instead of the explicit time integration used by the prototype version of AVUS. This is the reason why the growth rate of the v-velocity is slower for the $\alpha = 0.0$ result set in Figure 6.4 than the AR = 1.0 result set of Figure 6.2(a).

6.3 Grid Study for Inviscid Flow over a Blunt Body

All of the results presented in this section are for a two-dimensional cylindrical blunt body with a radius of 0.5 m. The same computational domain is used for all the grids in this study of the inviscid blunt body. The difference between the various grids used is how many grid points are placed in the

radial and circumferential directions, and how the grid points are distributed in the computational domain. The shape of the computational domain was chosen so the bow shock can be captured with very little distortion. All of the grids presented using blunt bodies state the number of grid points in the radial direction first and the number of grid points in the circumferential direction second. For example, a 21x321 grid has 21 grid points in the radial direction and 321 grid points in the circumferential direction.

From the results of Quirk's case it was found that increasing the freestream Mach number increases the chances of the carbuncle phenomena occurring and the resulting magnitude of the carbuncle phenomena. For all of the cases studied using the inviscid blunt body, a strong shock with a freestream Mach number of 20 was used to ensure that the carbuncle phenomena would occur. The freestream conditions were arbitrarily chosen to be the properties of air at sea level, (T_∞ = 288.15 K, P_∞ = 101325 Pa, and ρ_∞ = 1.225 kg/m^3). In all cases the air is taken to be a perfect gas, a first-order accurate in space numerical scheme is used, and the machine accuracy is double precision. First-order accurate in space is used since a second-order accurate in space technique can cause the carbuncle phenomenon to be worse by decreasing the amount of numerical dissipation that is present near the shock.

A number of different properties of the flow are investigated to see their effect on the carbuncle phenomenon. For the rest of this report the blended flux function uses an α of 0.5, which was the value suggested by Strang (2005). The van Leer flux function[van Leer 1982] is used on the cell faces parallel to the shock if a strong shock is present, as was used in the Strang (2005) upgrades to AVUS.

It was found that the u-velocity along the stagnation streamline is sensitive to the carbuncle phenomenon. The density at the surface of the blunt body is also a good metric to identify when the carbuncle phenomenon is occurring.

The density at the wall and the u-velocity along the stagnation streamline show a difference between the $\alpha = 0.5$ and $\alpha = 0.0$ results when the carbuncle phenomenon is occurring. The results

of the density at the wall for various cases show that the maximum difference between the $\alpha = 0.5$ and $\alpha = 0.0$ results does not always occur at the stagnation point. Since the properties at the wall always detect the maximum difference between the $\alpha = 0.5$ and $\alpha = 0.0$ results, the density at the wall is used to determine when the carbuncle phenomenon is occurring for inviscid blunt bodies. The maximum difference between the $\alpha = 0.0$ and $\alpha = 0.5$ results is referred to as $\Delta\rho_{blended}$.

6.3.1 Effect of Grid Aspect Ratio

To study the effect of the aspect ratio of the cells near the shock on the carbuncle phenomenon several case studies were performed. For quadrilateral cells the aspect ratio can be controlled by changing the number of grid points in the radial direction, changing the number of grid points in the circumferential direction, or clustering grid points near the shock. The results from these three case studies are shown in Figure 6.5. The results show that increasing the aspect ratio significantly decreases $\Delta\rho_{blended}$.

All three of the methods of controlling the aspect ratio near the shock give similar results. The method of clustering grid points near the shock has the advantage that fewer grid points are required to obtain the desired aspect ratio near the shock. Using a grid with fewer grid points near the shock can greatly reduce the computational cost of the simulation. The main disadvantage of clustering grids points near the shock is that the steady-state location of the shock needs to be known in order to create the grid, or grid adaption must be applied.

6.3.2 Effect of Angle of Transverse Face

To study how the angle of the cell face perpendicular to the shock effects the magnitude of the carbuncle phenomenon several grids were created where the aspect ratio at the shock was kept constant for each case; but the angle of the cell face perpendicular to the shock was varied. This is referred to as the transverse face of the control volume. The deviation of the cell face from being perpendicular to the shock is denoted as θ degrees. From Figure 6.6 it can be seen that increasing θ

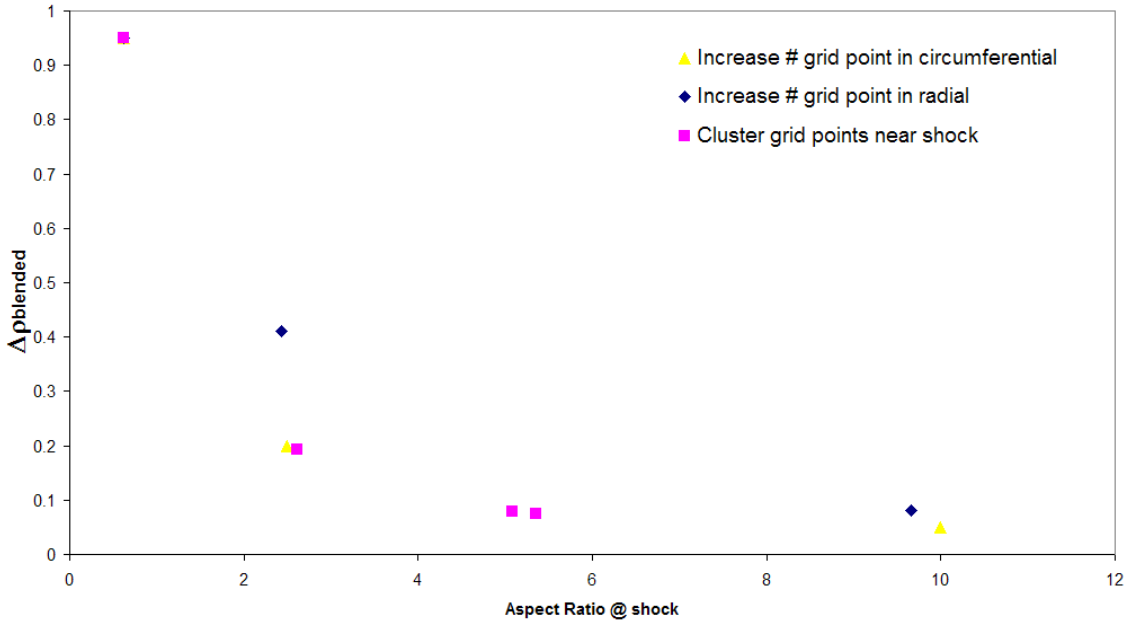

Figure 6.5: Effect of aspect ratio near the shock on the carbuncle phenomenon.

significantly decreases $\Delta\rho_{blended}$. This trend can be seen for two different cases with different aspect ratio cells.

The results from Quirks case show that the carbuncle phenomenon is invariant to the cell size. It would be reasonable to assume that the carbuncle phenomenon is invariant to the cell size for blunt bodies also. Several meshes were created for inviscid blunt bodies with varying cell sizes and constant aspect ratios. Due to the curvature of the blunt bodies θ decreases as the cell size decreases. The results of Figure 6.6 show that the magnitude of the carbuncle phenomenon does change as the cell size changes. This trend is due to θ changing, and not the change of the cell size. The cell sizes used in this plot are varied in size up to a factor of size change of 8.

6.3.3 Effect of Blending Parameter α

The results of Quirk's case show that increasing the numerical dissipation of the blended fluxes, by increasing the magnitude of the blending parameter α, decreases the magnitude of the carbuncle phenomenon. The same results are shown in Figure 6.7 for the blunt body. It can be seen that even

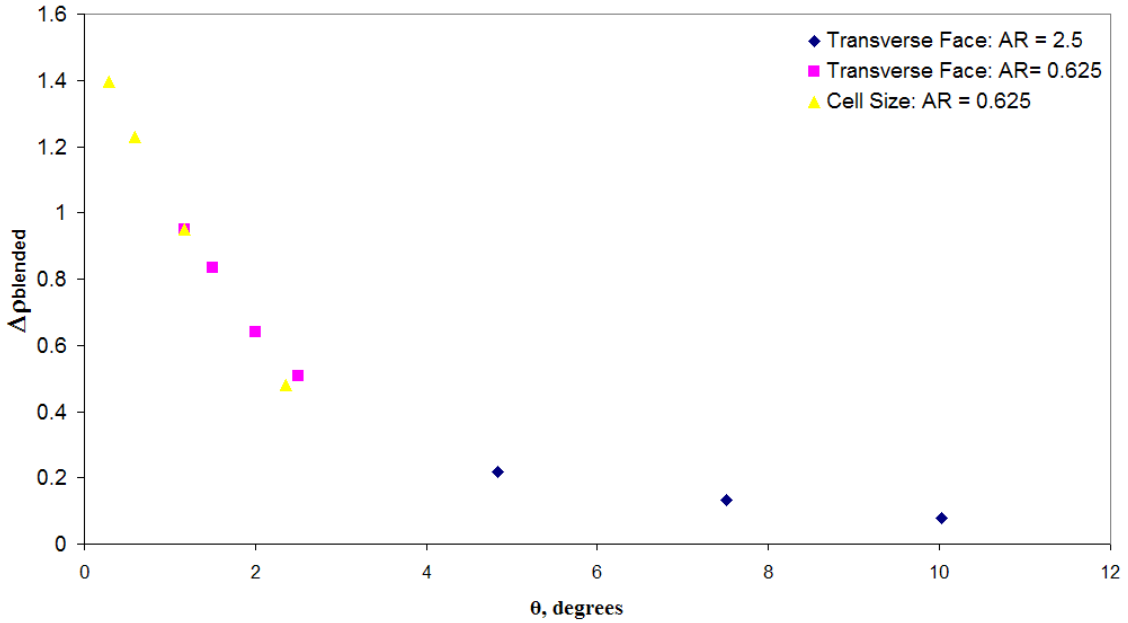

Figure 6.6: Effect of angle of cell face perpendicular to shock and cell size on the carbuncle phenomenon.

the low-dissipative blended flux of $\alpha = 0.2$ almost fully suppresses the carbuncle phenomenon for the 21x321 grid with an aspect ratio 0.6247 near the shock.

6.4 Effect of Dissipation on the Carbuncle Phenomenon

The stagnation region of blunt bodies and other configurations can have very high heat fluxes. The carbuncle phenomenon primarily disrupts the stagnation region causing the high heat fluxes to be noticeably distorted. For this reason it is important to eliminate the carbuncle phenomenon. The inviscid grid study was performed so the complications of a boundary layer did not have to be considered. From the grid study for inviscid blunt bodies it was found that the grid aspect ratio has the largest influence on suppressing the carbuncle phenomenon. This also holds true for the viscous case. In this section the effects of viscous dissipation, both numerical and physical, are studied along with the alignment of the grids with the shock.

The wall heat transfer is the primary parameter that is used to determine the magnitude of

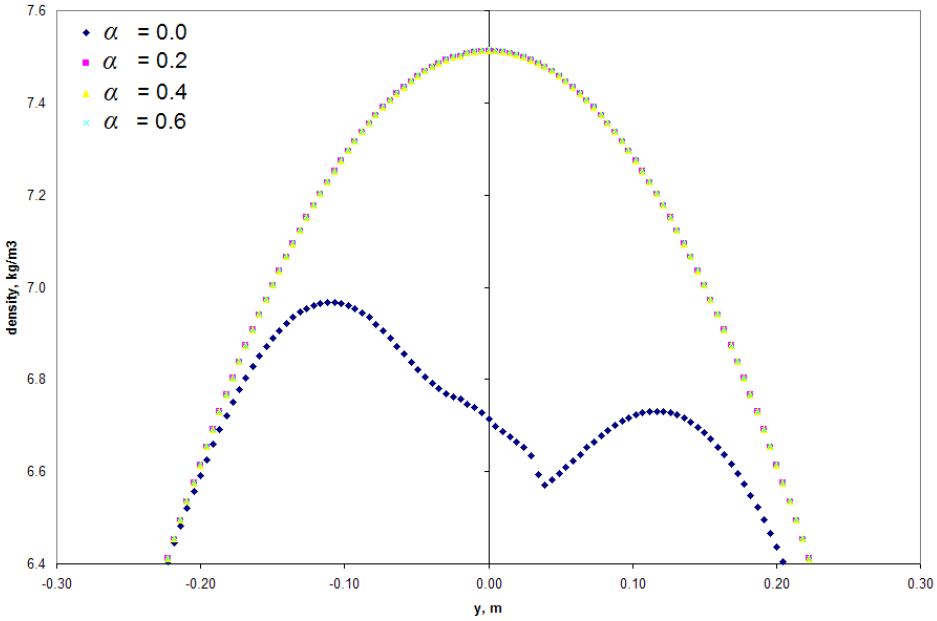

Figure 6.7: Effect of blending parameter α on blunt body results.

the carbuncle phenomenon. Because the heat transfer depends on the temperature gradients in the boundary layer, which can be very steep, the heat transfer is more sensitive to slight perturbations in the flow than properties that do not depend on spatial gradients.

All the results in this section are for a two dimensional blunt body with a radius of 0.0381 m. The freestream flow conditions are a Mach number of 16.34, freestream pressure of 82.95 Pa, freestream temperature of 52.0 K, and a Prandtl number of 0.73. These properties correspond to a unit Reynolds number of 3.9x10^6 m^{-1}. The wall boundary condition is an isothermal wall with a wall temperature of 294.4 K. These conditions are used in this study since Holden et al. (1998) has experimental heat transfer results for this flow configuration and Fay and Riddell (1958) have a theoretical value for the wall heat transfer at the stagnation point.

In this subsection two causes of the carbuncle phenomenon are studied. The first is the lack of numerical dissipation in the numerical routines used to model hypersonic flow through a shock. The second is the effect of the alignment of the grid with the shock. The first of these possible causes of the carbuncle phenomenon is the improper amount of dissipation being added to the shock, which

effects flow quantities downstream of the shock. The second is grid alignment, which only effects second-order quantities, like the heat transfer profile at the blunt body wall. Up until this point it can be seen that adding numerical dissipation lessens the effect of the carbuncle phenomenon. This numerical dissipation can be obtained by changing the aspect ratio of the grids, the alignment of the grids, or increasing the blending parameter.

In this section results will be given where the physical viscosity is changed to study the effect of physical dissipation. In the previous sections of this chapter the only dissipation used was numerical dissipation, as all cases utilized inviscid flow. The alignment of the grid with the shock does not affect first-order quantities like density, temperature, and pressure, but affects second-order quantities like heat transfer. It is believed that misalignment of the mesh with the shock is still causing numerical errors for the inviscid cases, but the numerical errors are too small to be seen by first-order quantities.

The author views the lack of dissipation cause of the carbuncle phenomenon and the nonalignment of the grids with the shock as being independent numerical problems. It is believed that one can be eliminated and the other will still exist. Another reason for looking at these causes as being independent is the cure for each is different. It would seem the cure for the lack of dissipation would be to apply the correct amount of dissipation. At present it is not known what is the correct amount. It would also seem that the cure for grid misalignment with the shock is to align the grid with the shock. However, since one does not know the exact location or shape of the shock before the simulation is run, this is not an easy task. On top of this, it appears that the carbuncle phenomenon is quite sensitive to small misalignments between the grid and the shock. In the following sections results will be presented that support these hypotheses.

6.4.1 Effect of Physical Viscosity on the Carbuncle Phenomenon

Since most methods use numerical viscosity to stabilize the carbuncle phenomenon it is not unreasonable to suspect that physical viscosity may have enough dissipation to stabilize the carbuncle phenomenon. To test this hypothesis natural viscosity was added throughout the flow field to a grid

which has uniform grid spacing and an aspect ratio of 0.6247 near the shock. Since the purpose of this study is to see how dissipation effects the shock instability, it does not matter that the mesh is not refined near the blunt body wall to properly capture the boundary layer. It was found that the dynamic viscosity calculated using the Sutherland correlation did not provide enough dissipation to stabilize the carbuncle phenomenon. To add further dissipation, the dynamic viscosity calculated by the Sutherland correlation was multiplied by a factor. From the results of Figure 6.8 it can be seen that adding more physical viscosity does stabilize the shock. It can also be seen that around 6,000 times the dynamic viscosity calculated using the Sutherland correlation is required to start suppressing the carbuncle phenomenon. The results also show that adding too much physical viscosity near the shock can give the wrong solution.

The reason that such a large amount of physical viscosity is required to stabilize the shock is how the dissipation is distributed on the cell faces. For a mesh that is aligned with the shock a majority of the dissipation is applied to the cell faces that are parallel to the shock. It is the faces that are perpendicular to the shock that require additional dissipation to prevent the carbuncle phenomenon.

6.4.2 Effect of Blending Parameter on Heat Transfer Profiles

The effect of the blending parameter, α, on viscous blunt bodies is performed uses a grid which has an aspect ratio of 0.5298 near the shock. This case was first run using various levels of the blending parameter, α, with van Leer fluxes used on the cell faces parallel to the shock, as recommended by Strang (2005). The results of Figure 6.9(a) show that using $\alpha < 0.2$ causes the heat transfer profile to be distorted along the entire wall of the blunt body. As α is increased the magnitude of the carbuncle phenomenon decreases. It can also be seen that using $\alpha = 0.5$ does not fully eliminate the carbuncle phenomenon, as it does for the inviscid blunt body cases. As seen from Figure 6.9(a), $\alpha = 1.0$ is required to fully eliminate the carbuncle phenomenon when van Leer fluxes are used for the cell faces parallel to the shock. The results do not show the trend of the magnitude of

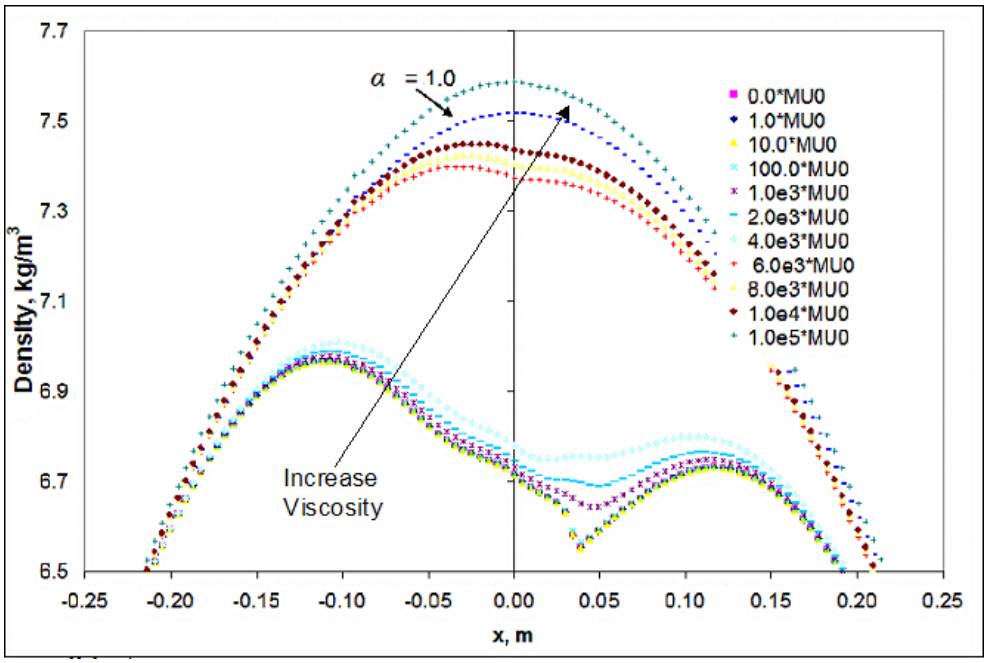

Figure 6.8: Effect of using physical viscosity to stabilize the carbuncle phenomenon.

the carbuncle phenomenon decreasing as α increases . Instead as α increases from 0.0 to 0.5 the results improve; however as α increases from 0.5 to 0.8 a dip forms in the heat transfer profile in the stagnation region. At $\alpha = 1.0$ the dip is gone.

The van Leer flux is used on the cell faces parallel to the shock since van Leer fluxes capture slowly moving shocks accurately. Since the blunt body case does not involve slowly moving shocks, it was decided to rerun the study using HLL instead of van Leer for the cell faces parallel to the shock. From the results in Figure 6.9(b) it can be seen that the heat transfer profiles compare much better to the results of Fay and Riddell (1958) for all levels of α. The results also show that using the HLL scheme for the parallel cell faces results in the comparison between the numerical results and the theoretical results of Fay and Riddell (1958) steadily becoming better as α is increased. From these results it is suggested that HLL should be used for the cell faces parallel to the shock instead of van Leer if slowly moving shocks are not expected to be present.

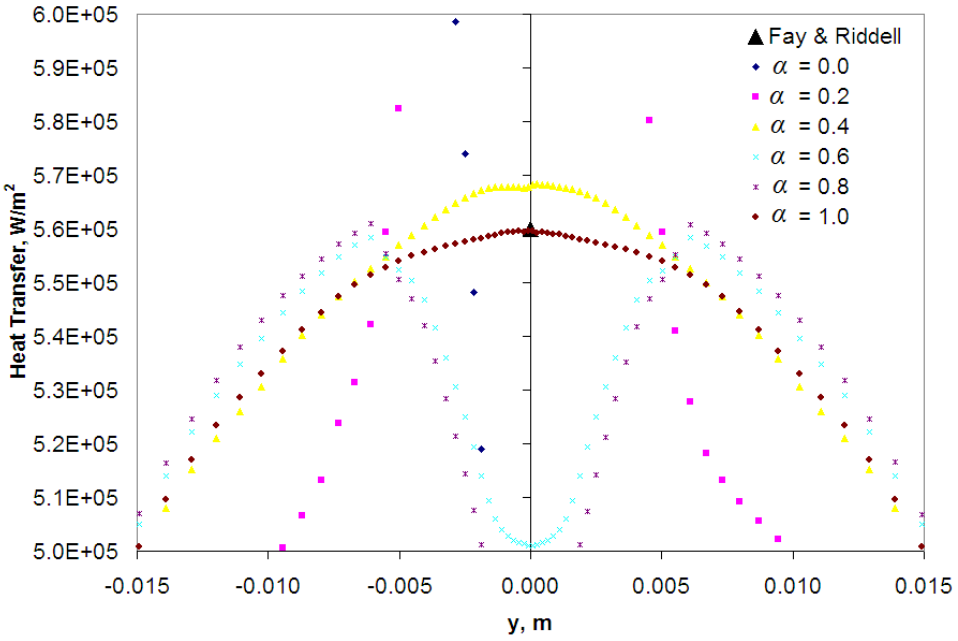

(a) With van Leer fluxes and zoomed in around stagnation point.

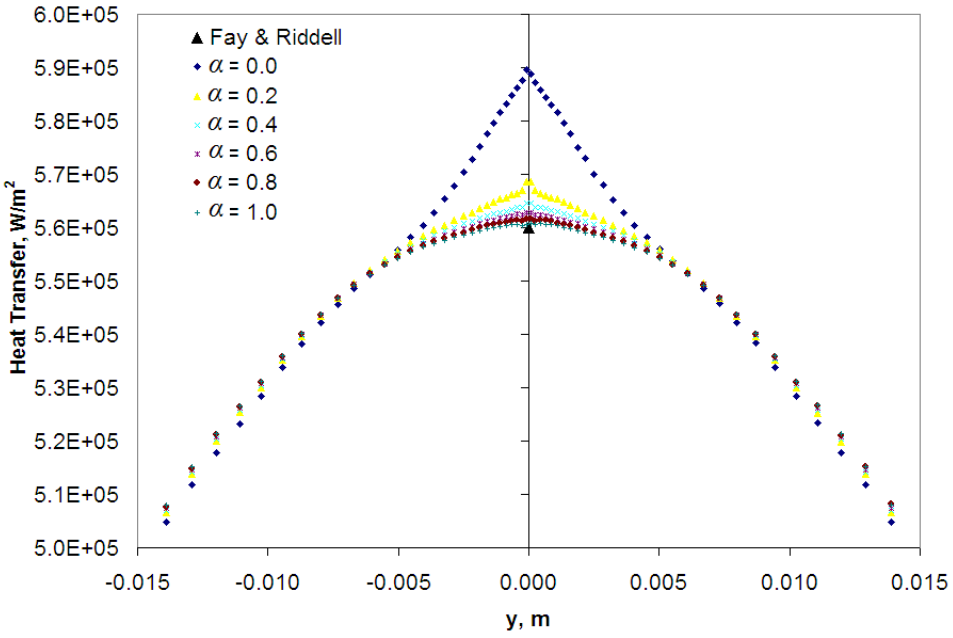

(b) No van Leer fluxes and zoomed in around stagnation point.

Figure 6.9: Heat transfer results for Mach 16.34 flow using various levels of α.

6.4.3 A Proposed Cure For the Carbuncle Phenomenon

The HLL+ scheme takes excessive numerical dissipation out of the HLL scheme [Batten et al. 1997; Toro 1999; Toro et al. 1994] so that the scheme can accurately capture boundary layers. With the removal of excess numerical dissipation from the HLL+ scheme [Park and Kwon 2003], the scheme is carbuncle prone. To prevent the carbuncle phenomenon from occurring the HLL+ scheme limits the contact wave speed from having values close to zero. The HLLC scheme [Batten et al. 1997; Toro 1999; Toro et al. 1994], however, is a low numerical diffusion scheme so it can accurately capture boundary layers, but suffers from the carbuncle phenomenon. The HLL+ fluxes that are not in the shock region mimic the fluxes of the HLLC flux due to the correct amount of numerical dissipation being taken out of the HLL scheme. To prevent the carbuncle phenomenon with the HLLC scheme the appropriate amount of numerical dissipation must be added, but not too much so the scheme is overly dissipative.

The HLL scheme captures shocks very accurately and does not suffer from the carbuncle phenomenon. From this it can be concluded that the excessive numerical dissipation of the HLL scheme is an appropriate amount of numerical dissipation to add to damp out the carbuncle phenomenon. A new numerical flux function is developed from the conclusions drawn from the HLL+ scheme. The new flux function is named the HLLC+ scheme. Since the HLLC scheme accurately captures boundary layers the HLLC scheme is used throughout the fluid domain, except in the shock region where the excessive numerical dissipation of the HLL scheme is added to damp out the carbuncle phenomenon. The HLLC+ scheme can be summarized as:

$$\mathbf{F}^{HLLC+} = \begin{bmatrix} \mathbf{F}^{HLLC} + \frac{S_L S_R}{S_R - S_L} \sum_{p=1}^{5} \bar{\delta}\alpha^p \mathbf{K}^p & \text{if at shock} \\ \mathbf{F}^{HLLC} & \text{otherwise} \end{bmatrix} \tag{6.2}$$

The HLL+ and HLLC+ schemes produce results that are almost identical to the blended flux functions, as seen in Figure 6.10(a). This can be explained by the fact that the blended flux functions

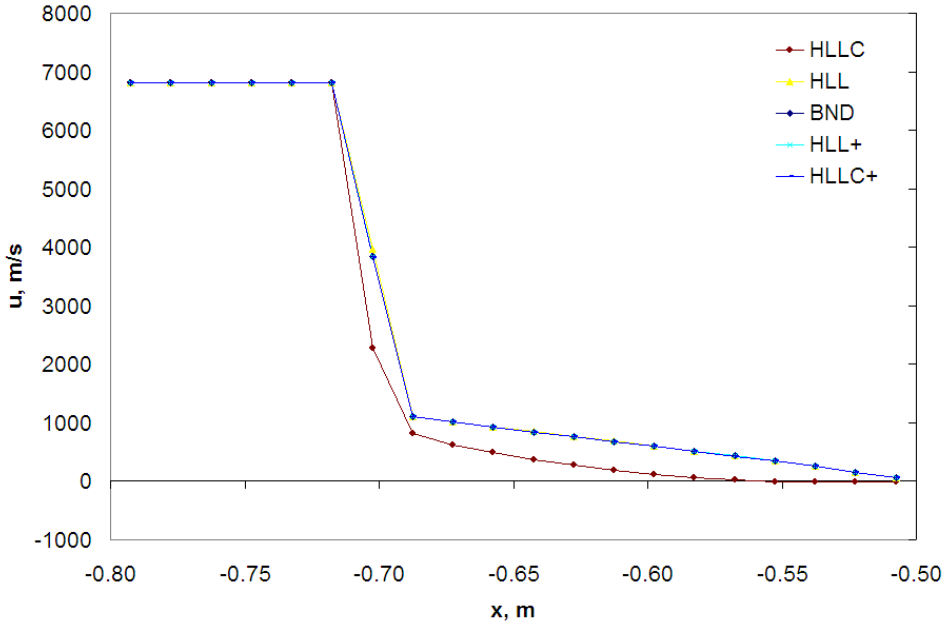

(a) u-velocity.

Figure 6.10: U-velocity results for 21x321 grid using HLL, HLLC, BND, HLL+, and HLLC+ schemes.

use the HLLC flux function throughout the flow field, except in regions near the shock where a more dissipative flux function is needed. In these regions the more dissipative HLL scheme is used. The HLL+ scheme mimics the blended flux functions by starting out with the HLL scheme applied to the entire flow field, then takes the excessive dissipation out of the HLL flux except in regions near the shock. This produces a flux function that is essentially the HLL scheme near the shock and HLLC throughout the rest of the flowfield. The HLLC+ scheme mimics the blended flux functions by starting out with the HLLC scheme applied to the entire flowfield and adding enough dissipation near the shock to the mimic the HLL scheme in this region. Since the HLL+ and HLLC+ schemes essentially mimic the blended flux functions, it was decided to use the simpler formulation of the blended flux functions. The discussion of the HLL and HLLC fluxes aids in the understanding of the importance of adding the correct amount of dissipation to eliminate the carbuncle phenomenon.

6.5 Shock Alignment and the Carbuncle Phenomenon

For a measure of the degree the shock is misaligned from the mesh the maximum L2 momentum residuals near the shock were used. The maximum L2 residual is defined as,

$$L2_{max} = max\left(\frac{abs(Q_i - QO_i)}{\triangle t}\right) \tag{6.3}$$

where $\triangle t$ is the time step of cell i, Q_i is either the u-momentum or v-momentum of cell i at the current time step, and QO_i is either the u-momentum or v-momentum of cell i at the previous time step.

For cases where the shock is not well aligned with the mesh the shock may have difficulty in finding a grid point to "settle" on. In certain cases the shock may stay at a certain grid point, but the shocks internal state will not reach a steady state. This behavior can be observed by looking at time history contour plots of the Mach number. The shock moving back and forth between grid points can cause the momentum residuals to converge poorly for cells near the shock.

For a metric indicating the effect of the shock being misaligned with the mesh, the wall heat transfer profile and the percent difference of the stagnation heat transfer profile from the theoretical value of $5.6x10^5$ W/m^2 from Fay and Riddell (1958) are used. For a blunt body in hypersonic flow the heat transfer profile should be parabolic. However, many heat transfer profiles obtained using Riemann solvers there may have a dip or peak in the heat transfer profile near the stagnation region.

The results of Figure 6.11 have a grid with points that are clustered around the stagnation streamline in the circumferential direction. All three of the grids have the same aspect ratio of 1.0738 and the same distribution of grid points. The two grids with smaller cell sizes result from refining the grid in the circumferential and radial directions. Figures 6.11 - 6.12 shows a strong correlation between the maximum L2 momentum residuals and the percent difference of the stagnation point heat transfer. It is also observed that two of the cell sizes show dips in the heat transfer profile near the stagnation point. This is a good indication that the alignment between the shock and the mesh

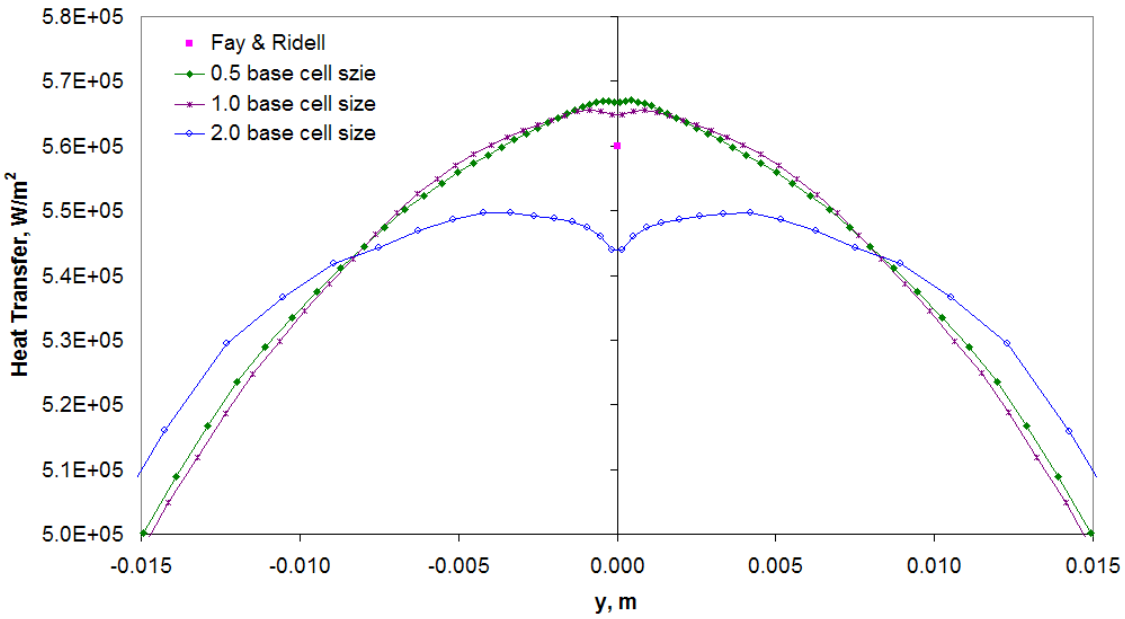

Figure 6.11: Mach 16.34 flow for grids with points clustered near the stagnation line with an aspect ratio of 1.0738 for all cases.

is influencing the magnitude of the stagnation point heat transfer. It is also observed dips become smaller as the cell size is reduced. This is most likely due to the grid points being closer together so that the shock is more likely to find a grid point to settle down at.

The case presented in Figures 6.13 - 6.14 shows how the shock-mesh alignment affects the stagnation heat transfer profile. This case has a baseline grid with an aspect ratio of 0.5298, while the other grids use the same mesh, except that it is stretched along the stagnation streamline. This stretching of the mesh varies the degree that the bow shock is aligned with the mesh. The percent difference of the stagnation point heat transfer is much smaller for the case with the smaller maximum L2 momentum residuals. The correlation between the maximum L2 x-momentum residual and the percent difference in the stagnation point heat transfer is not strong. The correlation between the maximum L2 y-momentum residuals and percent difference in the stagnation heat transfer profile is fair, showing that as the maximum L2 y-momentum residual either increases or decreases the stagnation heat transfer profile follows the same trend. The most likely reason the correlation

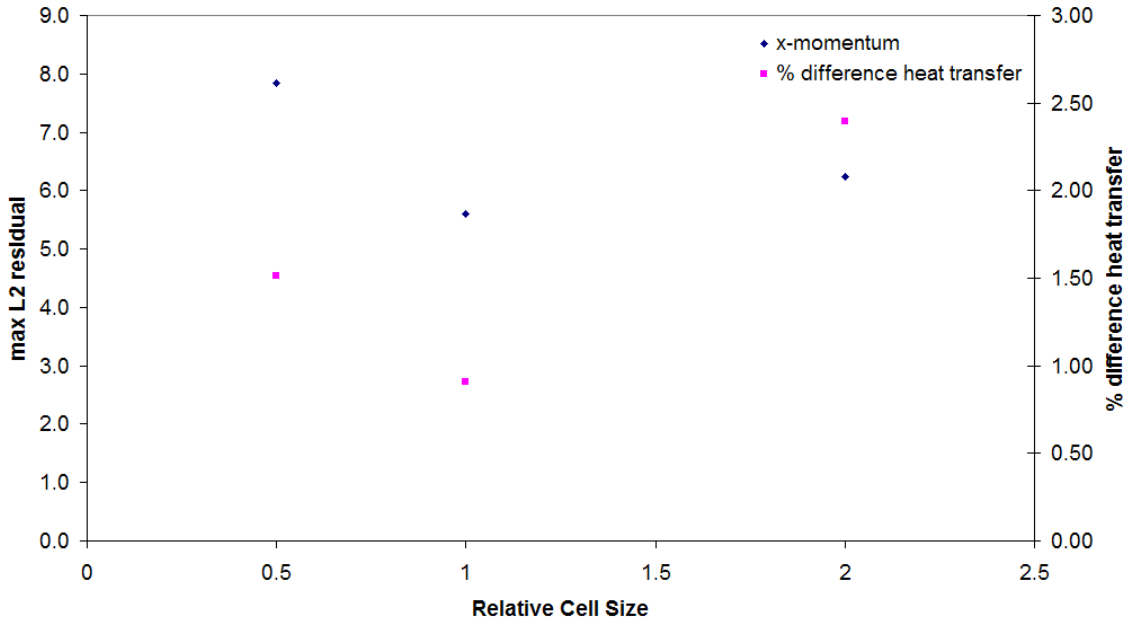

(a) Maximum L2 residuals of x-momentum.

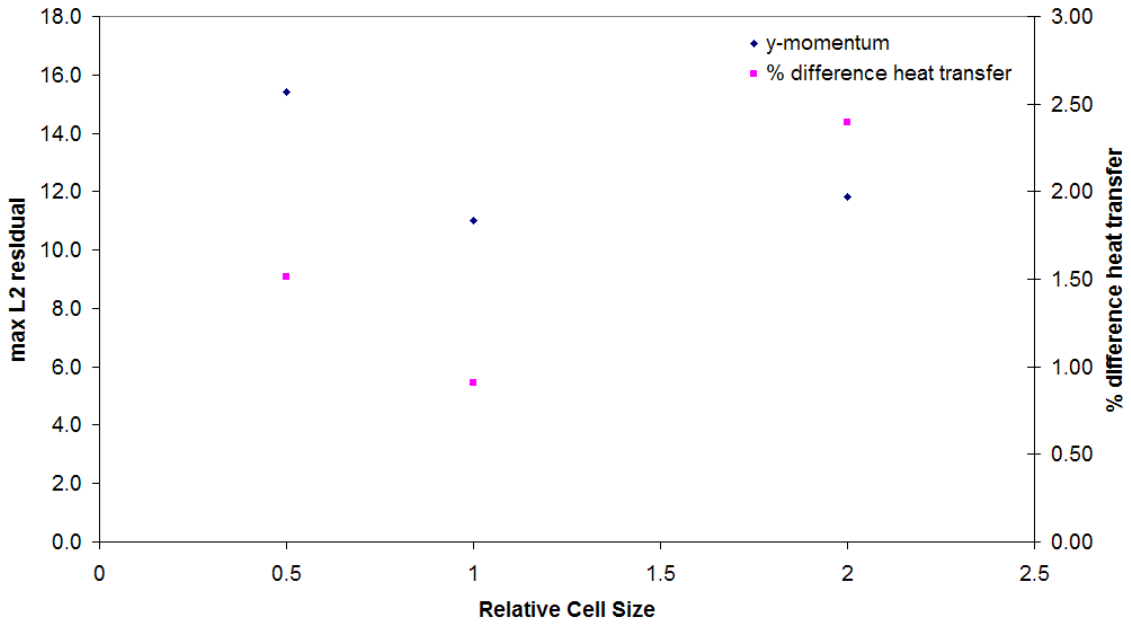

(b) Maximum L2 residuals of y-momentum.

Figure 6.12: Mach 16.34 flow for grids with points clustered near the stagnation line with an aspect ratio of 1.0738 for all cases.

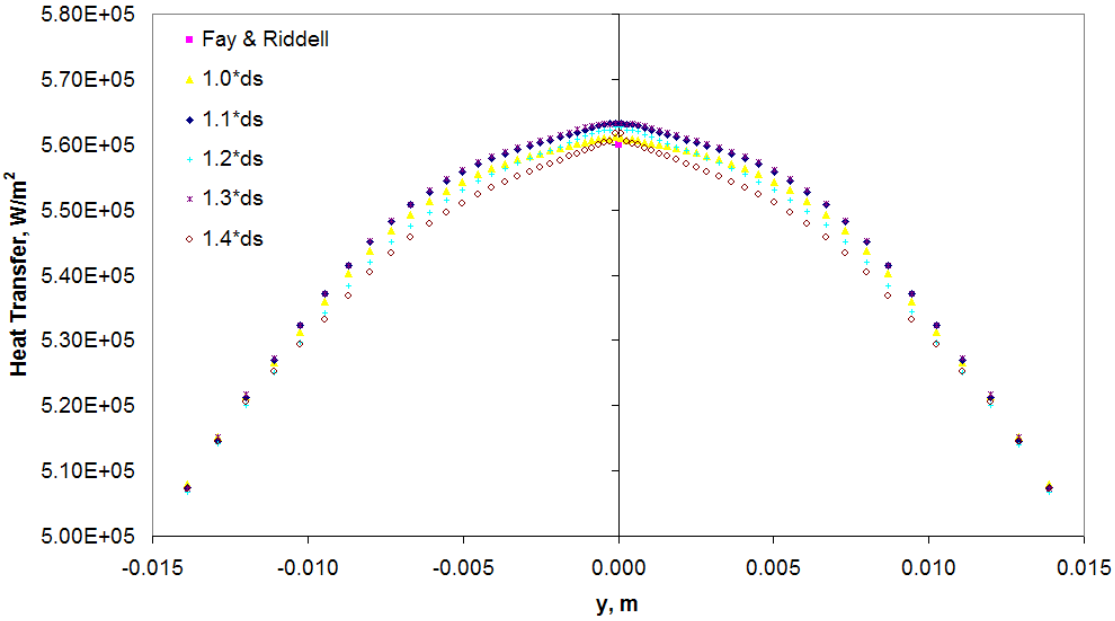

Figure 6.13: Mach 16.34 flow for similar grids with different degrees of shock misalignment.

between heat transfer and momentum residuals is not as strong for this case is that the mesh is already aligned with the shock fairly well.

The case presented in Figures 6.15 - 6.16 studies how the shock-mesh alignment affects the stagnation heat transfer profile. For this case the effect of increasing the aspect ratio by decreasing the number of grid points in the circumferential direction for grids with no cell centers on the stagnation streamline is studied. These grids have constant grid spacing in the circumferential direction. The results show that as aspect ratio increases the L2 momentum residuals and the percent difference of the stagnation point heat transfer profile increase. This is strong evidence that the poor approximation of the stagnation heat transfer is partly due to the misalignment of the shock with the mesh and not the carbuncle phenomenon. This occur because an increase in the aspect ratio of the cells near the shock should lead to a reduction in the effect of the carbuncle phenomenon.

The case presented in Figures 6.17 - 6.18 studies how the shock-mesh alignment affects the stagnation heat transfer profile. This case shows the effect of increasing the aspect ratio by decreasing

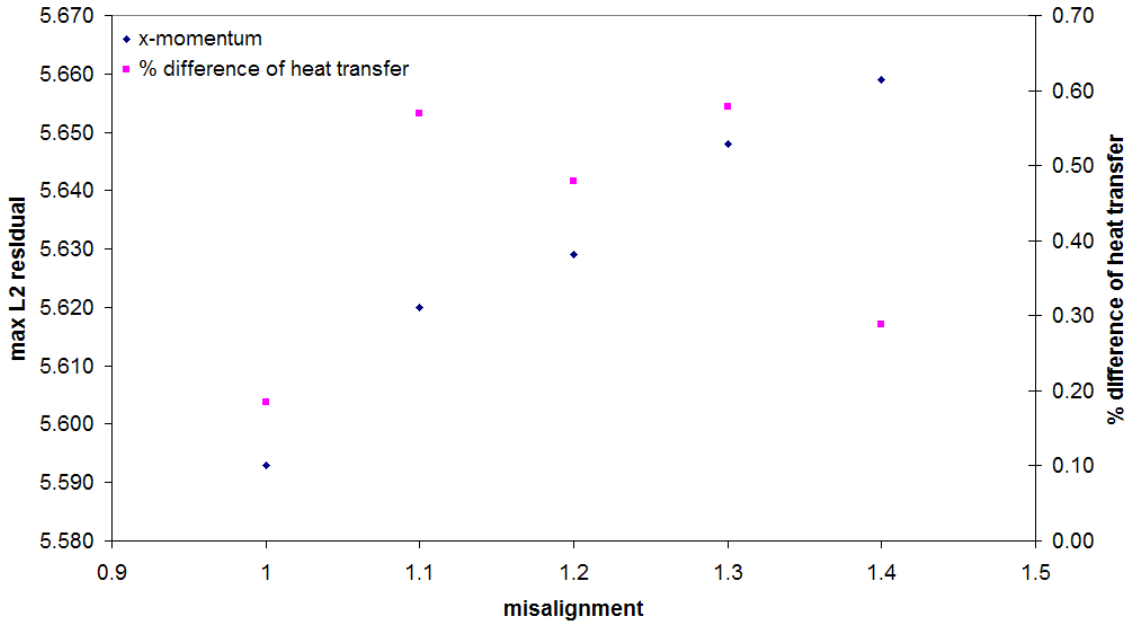

(a) Maximum L2 residuals of x-momentum.

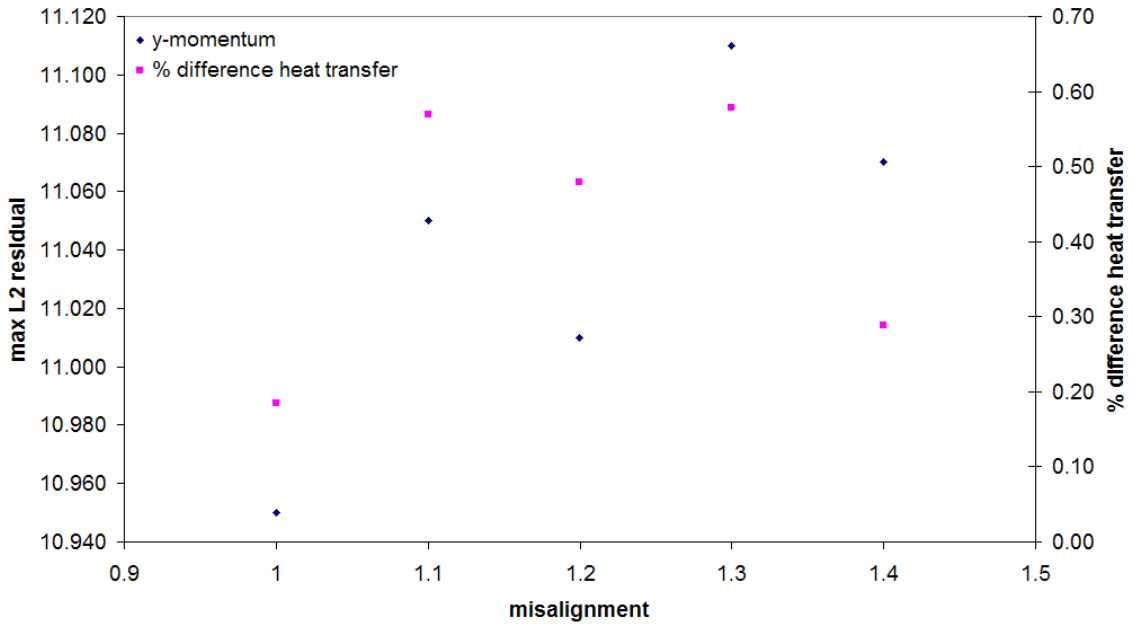

(b) Maximum L2 residuals of y-momentum.

Figure 6.14: Mach 16.34 flow for similar grids with different degrees of shock misalignment.

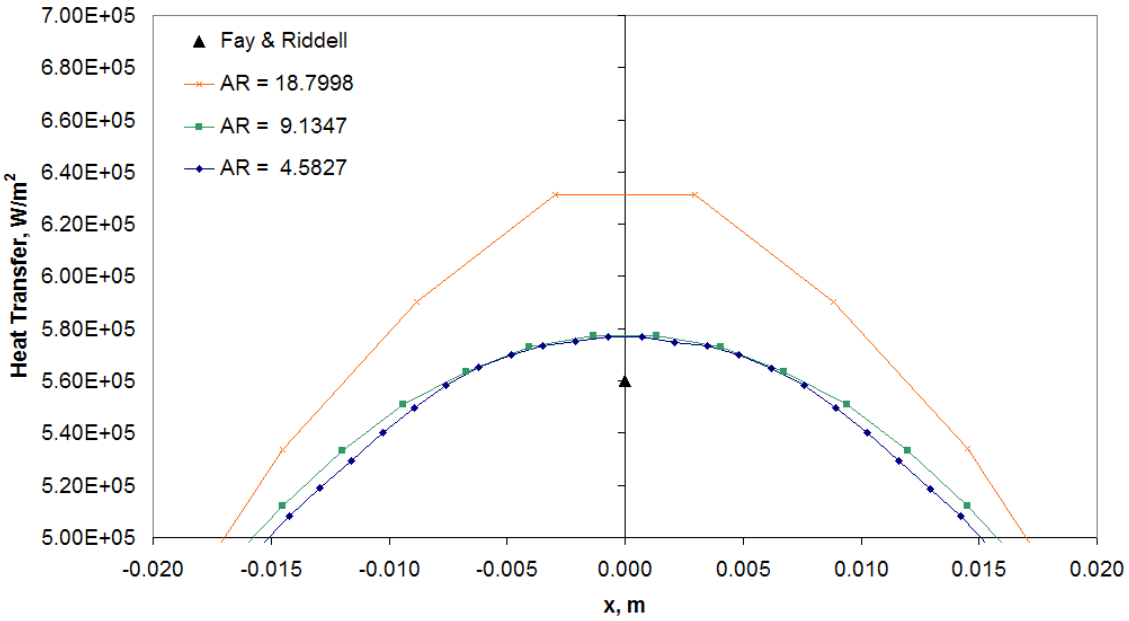

Figure 6.15: Mach 16.34 flow for constant grid spacing in circumferential direction. Cell center not on stagnation streamline

the number of grid points in the circumferential direction for grids with cell centers on the stagnation streamline. The results of this case show the same trends as the previous case shown in Figures 6.15 - 6.16. The results from Figure 6.17 also show that the approximation of the stagnation point heat transfer is poorer than the results of Figure 6.15, even though the same aspect ratios are used in both cases. This is due to how the grid is aligned with the shock.

The final case has 141 grid points in the circumferential direction that are clustered around the stagnation streamline to produce different aspect ratios at the shock. Only an odd number of grid points are used in the circumferential direction in this case, since it was found that having cell centers on the stagnation streamline caused the approximation to the stagnation point heat transfer to be worse than having no cell centers on the stagnation streamline. The results of Figures 6.19 - 6.20 show that the poor approximation of the stagnation point heat transfer is due to the shock misalignment and not from the carbuncle phenomenon. This occurs because the stagnation point heat transfer gets worse as the aspect ratio of the cells is increased.

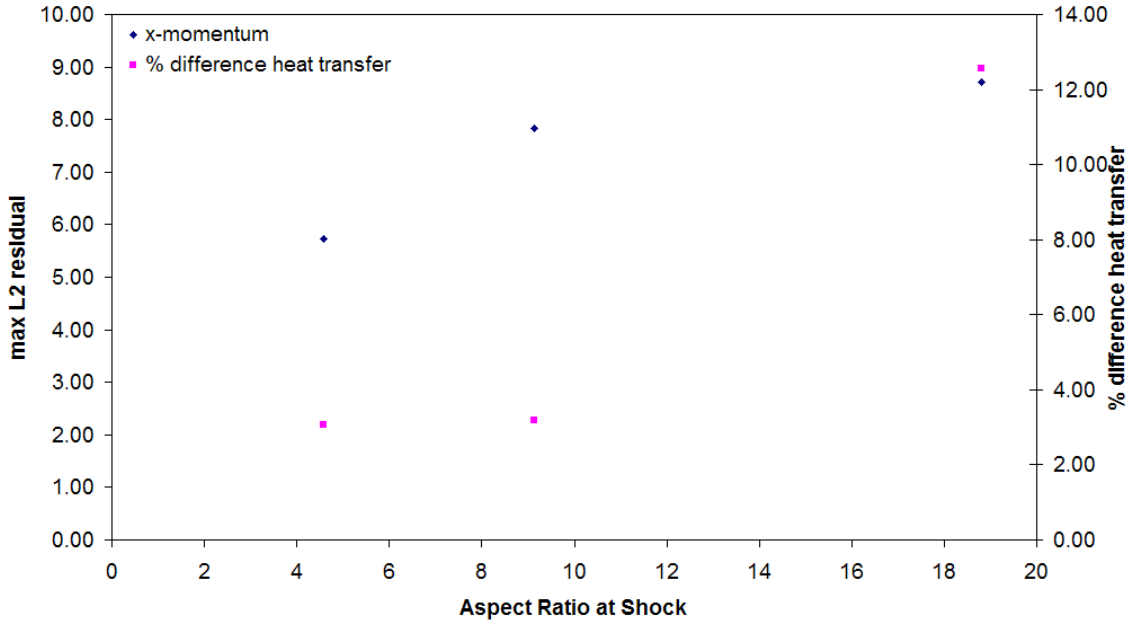

(a) Maximum L2 residuals of x-momentum.

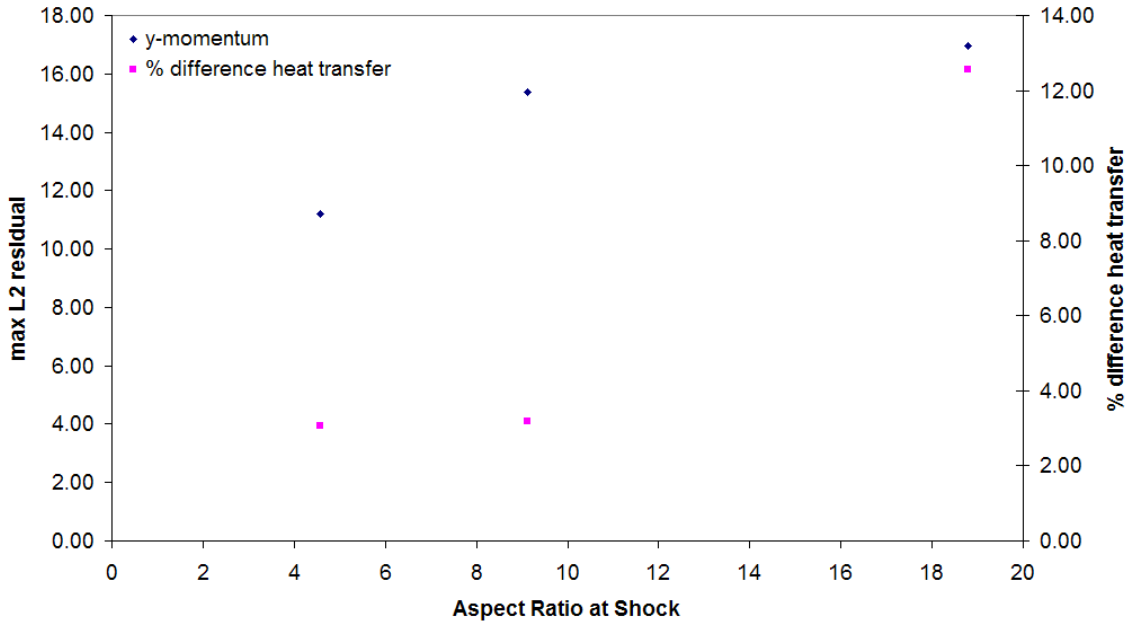

(b) Maximum L2 residuals of y-momentum.

Figure 6.16: Mach 16.34 flow for constant grid spacing in circumferential direction. Cell center not on stagnation streamline

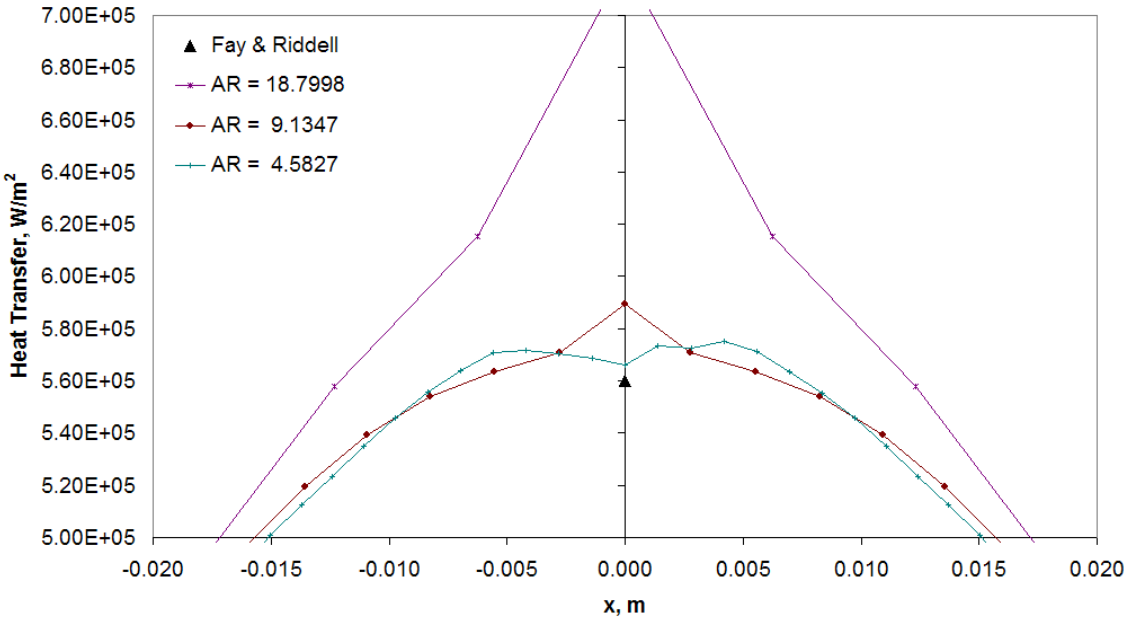

Figure 6.17: Mach 16.34 flow for constant grid spacing in circumferential direction. Cell center on stagnation streamline.

The results of this section indicate that there is a correlation between shock misalignment and poor heat transfer profile predictions. This correlation is not perfect; however, it is strong enough to indicate to the author that there is a connection between good heat transfer profiles and good grid-shock alignment. A possible reason for the imperfect correlation between the cause and effect is that another phenomenon affects the heat transfer predictions, the amount of viscous dissipation in the shock. Since shock viscous dissipation effects can not be completely eliminated or kept constant, they are present in the grid alignment results. This is possible explanation for the imperfect correlation.

6.6 Summary of Results

The carbuncle phenomenon is a numerical instability that affects the capturing of strong shocks when using a Riemann solver with low numerical dissipation. The carbuncle phenomenon manifests itself in the inability to compute uniform flow conditions downstream of a normal or nearly normal shock. For the carbuncle phenomenon to occur in a cell, several conditions must be met:

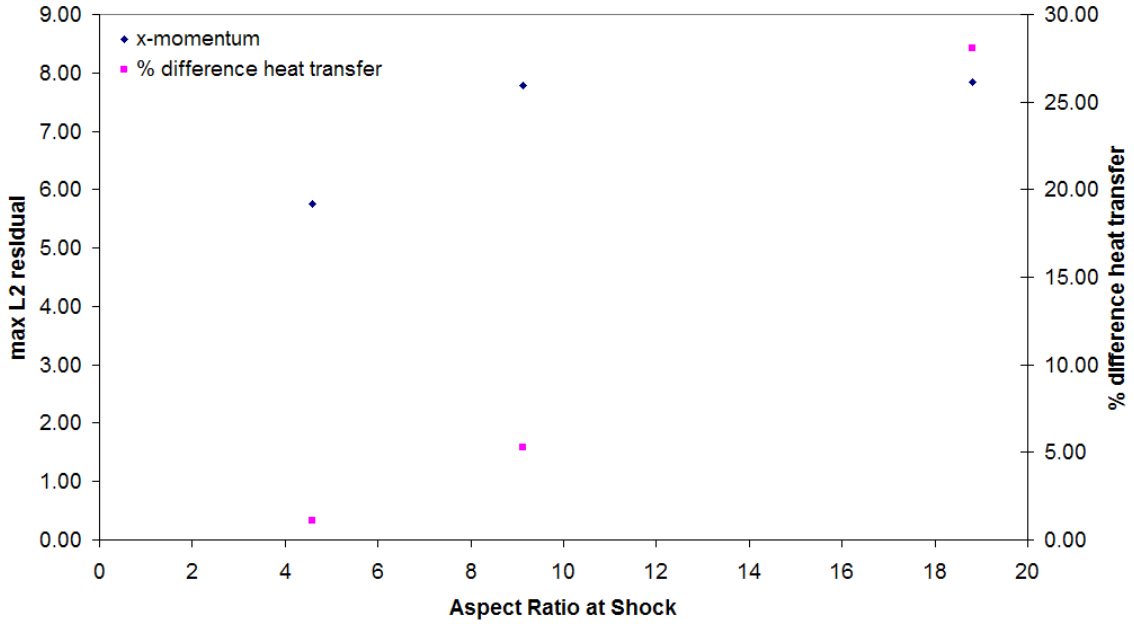

(a) Maximum L2 residuals of x-momentum.

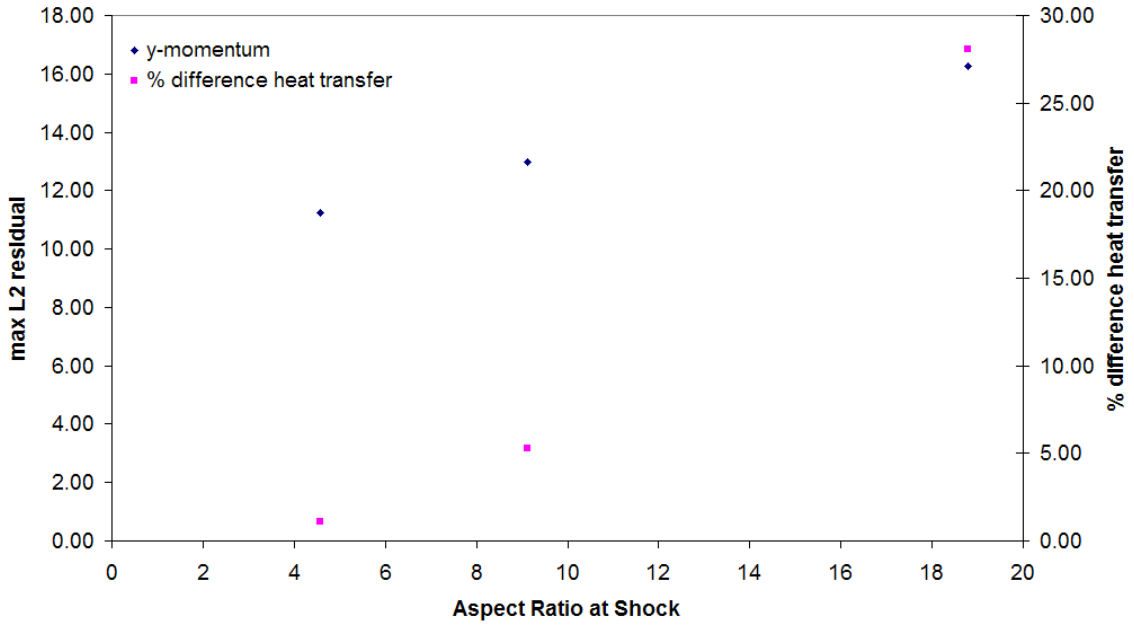

(b) Maximum L2 residuals of y-momentum.

Figure 6.18: Mach 16.34 flow for constant grid spacing in circumferential direction. Cell center on stagnation streamline.

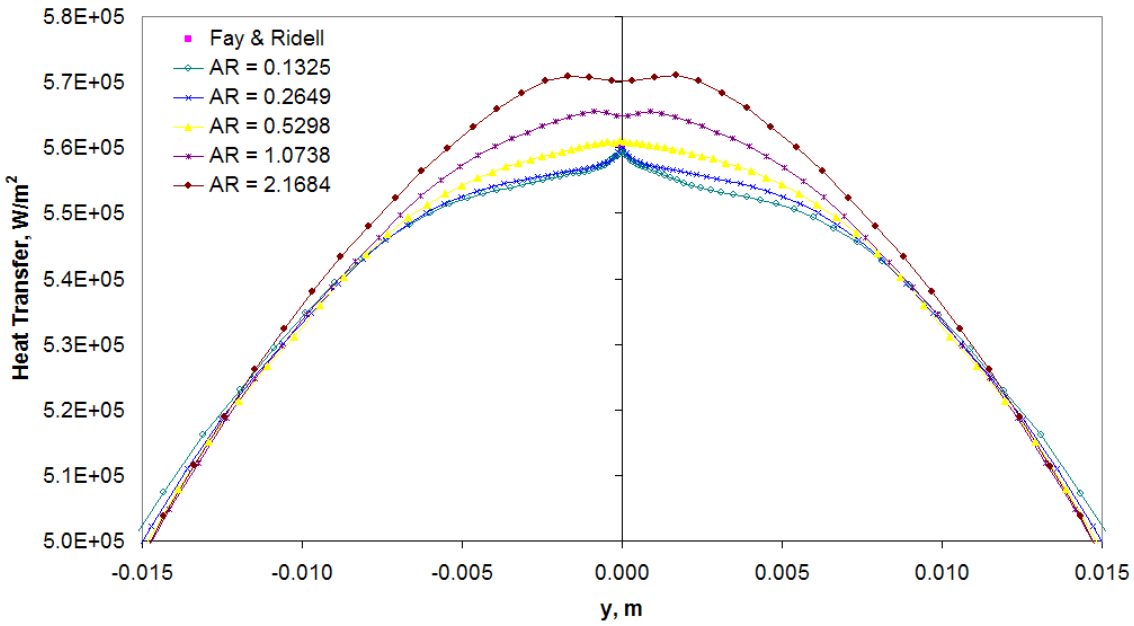

Figure 6.19: Mach 16.34 flow for grids with points clustered near the stagnation line with various aspect ratios.

1. The shock is normal or close to normal to a cell.
2. The computational cell is interior to the shock.
3. A flux function is used that includes contact waves.
4. The cell face perpendicular to the shock is aligned so that that the velocity normal to the cell face is zero or very close to zero. This leads to the contact wave speed being very close to zero.
5. The higher the pressure jump across the shock, the more likely the carbuncle phenomenon will occur.

The carbuncle phenomenon was studied in this chapter as having two possible causes. The first is the lack of numerical viscosity in the numerical routines used to model the hypersonic flow through a shock. The second is the effect of the alignment of the grid with the shock. The first of these possible causes of the carbuncle phenomenon is the improper amount of dissipation being added to the shock, which affects flow quantities downstream of the shock. The second is grid alignment which only affects second-order quantities like the heat transfer profile at the blunt body wall.

The hypothesis made in this chapter is that lack of the proper dissipation in the shock causes the carbuncle phenomenon and the nonalignment of the grids with the shock caused problems in the

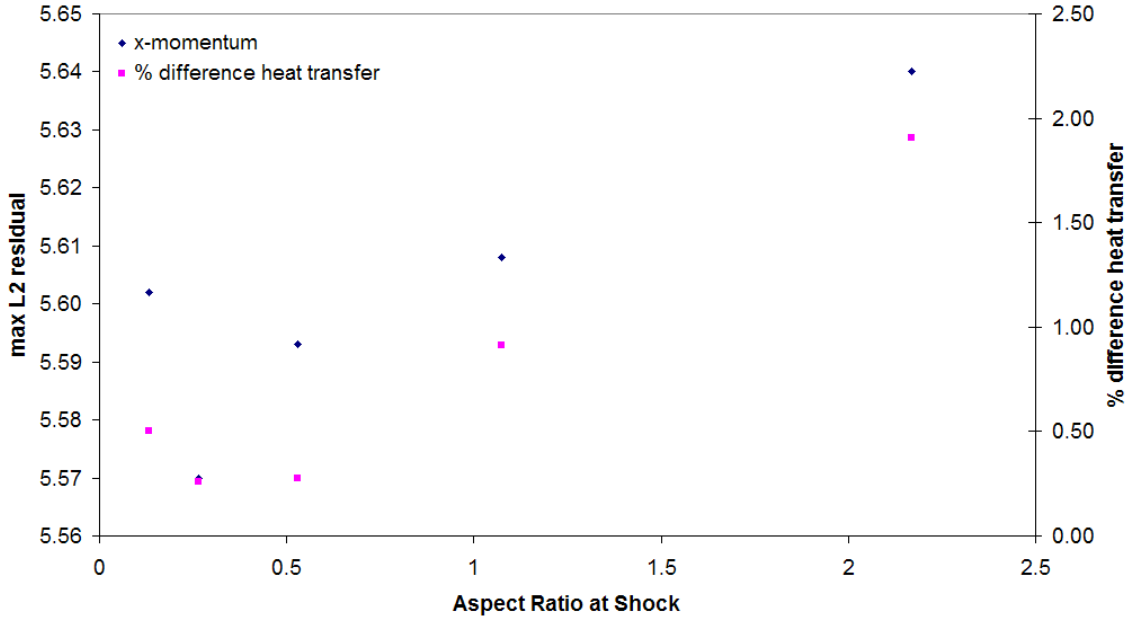

(a) Maximum L2 residuals of x-momentum.

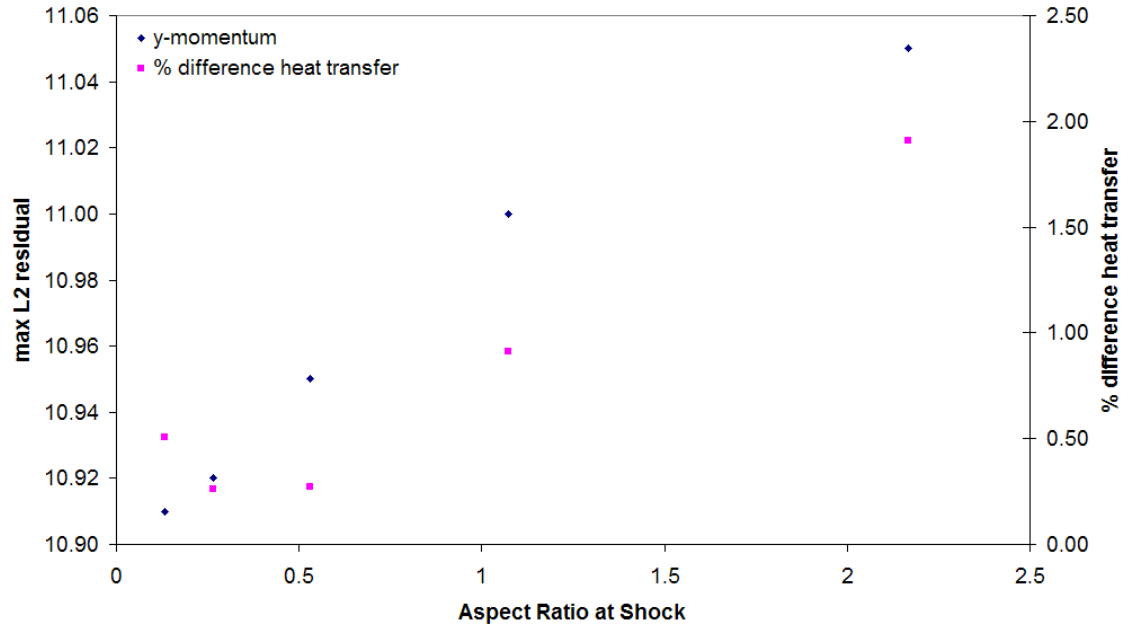

(b) Maximum L2 residuals of y-momentum.

Figure 6.20: Mach 16.34 flow for grids with points clustered near the stagnation line with various aspect ratios.

second order quantities. In addition, it was hypothesized that these are are two independent causes. It is believed that one can be eliminated and the other can still exist. Another reason for looking at these causes as being independent is the cure for each different. It would seem the cure for the lack of dissipation would be to apply the correct amount of dissipation to better mimic a physical shock. At present it is not known what is the correct amount. To fully cure the caruncle phenomenon it may be necessary to use a numerical method that calculates the inviscid and viscous fluxes in a coupled approach to better mimic the dissipation in a physical shock. This has been accomplished with some degree of success with the BGK and CESE methods that were mentioned in Chapter 2.

From the results of Quirk's case it was found that the carbuncle phenomenon has a threshold Mach number of slightly greater than 2. If the freestream Mach number is less than 2 the carbuncle phenomenon does not exist. As the Mach number increases above 2 the carbuncle phenomenon becomes more severe. It was also found that the machine precision used in the simulation can cause the carbuncle phenomenon. The machine precision used, changes the rate of growth of the carbuncle, but the asymptotic value is only slightly affected. Cell size does not effect the carbuncle phenomenon for Quirk's case. It is also seen from Quirk's case that the carbuncle phenomenon grows with the number of time steps the flow solver has performed. This is what you would expect if the carbuncle phenomenon was initiated by machine round-off error.

The results for the inviscid blunt body show that increasing the aspect ratio near the shock decrease the magnitude of the carbuncle phenomenon. The method of clustering grid points near the shock to increase the aspect ratio of the cells near the shock has the advantage that fewer grid points are required to obtain the desired aspect ratio. Using a grid with fewer grid points near the shock can greatly reduce the computational cost of a simulation. The main disadvantage of clustering grids points near the shock is that the steady-state location of the shock needs to be known in order to create the grid, or grid adaption must be applied.

It can be easily explained how increasing the aspect ratio of the cell decreases the effect of the carbuncle phenomenon. As the aspect ratio of the cells is increased the length of the cell faces

perpendicular to the shock become shorter, compared to the cell faces parallel to the shock. This means that more flux contribution is passing through the cell faces parallel to the shock, and less flux contribution is from the perpendicular cell faces. This decreases the flux contributions of the incorrectly calculated fluxes at the perpendicular cell faces.

The results of the inviscid blunt body grid study also show that increasing the angle of the cell face transverse to the shock decreases the effect of the carbuncle phenomenon. Increasing the angle of the cell face transverse to the shock, however, has less of an effect on the carbuncle phenomenon than increasing the aspect ratio. It was also shown that decreasing the cell size decreases the angle of the cell face perpendicular to the shock so that the effect of the carbuncle phenomenon increases. This is not a cell size effect, but a cell face angle effect.

The literature survey in Chapter 2 can help explain how changing the angle of the cell faces perpendicular to the shock can reduce the carbuncle phenomenon. When the cell face perpendicular to the shock is exactly 90° to the shock, the contact wave speed is zero. The carbuncle phenomenon occurs when the contact wave speed is zero or close to zero. Therefore angling the cell face at some angle other than exactly perpendicular to the shock increases the contact wave speed, so the carbuncle phenomenon is less likely to occur.

It was also shown that increasing the value of the dynamic viscosity does decrease the effect of the carbuncle phenomenon. The results show that around 6,000 times the dynamic viscosity calculated using the Sutherland correlation is required to start suppressing the carbuncle phenomenon. The reason that a such a large amount of physical viscosity is required to stabilize the shock is how the dissipation is distributed on the cell faces. For a mesh that is aligned with the shock a majority of the dissipation is applied to the cell faces that are parallel to the shock. It is the faces that are perpendicular to the shock that require additional dissipation to prevent the carbuncle phenomenon.

It was shown that using a blending parameter of $\alpha = 1.0$ produces the most accurate heat transfer profiles for blunt bodies. It also was concluded that using the HLL fluxes for the cell faces parallel to the shock instead of the van Leer fluxes produces more accurate heat transfer profiles.

The HLL+ and HLLC+ schemes produce results that are almost identical to that of the blended flux functions. This is due to the fact that the HLL+ and HLLC+ schemes both mimic the blended flux function by controlling the dissipation that is present in the cells. The HLL+ and HLLC+ produce fluxes near the shock that resemble the HLL scheme, and produce flux in the rest of the flowfield that resemble the HLLC scheme.

In conclusion grid studies on the carbuncle phenomenon show that adding numerical dissipation lessens the effect of the carbuncle phenomenon. This numerical dissipation can be obtained by changing the aspect ratio of the grids, the alignment of the grids, or increasing the blending parameter.

An other possible cause of the carbuncle phenomenon is the alignment of the grid with the shock. The grid-shock misalignment does not affect first-order quantities like density, temperature, and pressure, but affects second-order quantities like heat transfer. It is believed that misalignment of the mesh with the shock is still causing numerical errors for the inviscid cases, but the numerical errors are two small to be seen by first-order quantities.

For a measure of the degree the shock is misaligned from the mesh the maximum L2 momentum residuals near the shock are used. For cases where the shock is not well aligned with the mesh the shock may have difficulty finding a grid point to "settle" on. The shock moving back and forth between grid points can cause the momentum residuals to converge poorly for cells near the shock. The results for several case studies show that as the maximum L2 momentum residual increases, the departure of the stagnation point heat transfer from the theoretical value of Fay and Riddell (1958) increases. This shows that the more misaligned the shock is with the mesh, the poorer of the stagnation heat transfer is predicted. The results also show that the stagnation heat transfer profiles are worse when a grid is used with grid points on the stagnation streamline.

It would seem that the cure for grid misalignment with the shock is to align the grid with the shock. However, since one does not know the exact location or shape of the shock before the simulation is run, this is not an easy task. On top of this it appears that the carbuncle phenomenon

is quite sensitive to small misalignments between the grid and the shock.

7

Conclusions

7.1 Thermodynamic Properties of High Temperature Air in Chemical Equilibrium

The thermodynamic properties of air were found for temperatures up to 30,000 K and for a pressure range of 1x10^{-4} to 100 atm. A brief review of the various methods used to compute the chemical composition of air in chemical equilibrium were briefly reviewed. The CANTERA program[1] was used to determine the chemical composition and thermodynamic properties of the chemical equilibrium air. To determine chemical composition of the chemical equilibrium air, the CANTERA program uses the element potential method. The element potential methods required the thermodynamic properties of the individual species that could be present in chemical equilibrium air. There were 22 species of interest in this work, N_2, O_2, Ar,O, N, NO, N_2^+, O_2^+, NO^+, N^+, N^{+2}, N^{+3}, O^+, O^{+2}, O^{+3}, Ar^+, Ar^{+2},Ar^{+3}, N^-, O^-, O_2^- and e^-. A large majority of the thermodynamic data for the indivdual species were obtained from the Thermobuild NASA website[2]. The thermodynamic properties of the monoatomic species were not listed at higher temperatures. To determine the thermodynamic properties of the species at higher temperature the NASA code PAC99 [McBride

[1]The CANTERA documentation and code can be found on: URL http://cantera.org [Cited June 2007].
[2]URL: http://cea.grc.nasa.gov [Cited June 2007].

and Gordon 1992; Gordon and McBride 1999] was used, which uses partition function to determine the thermodynamic properties. A short description of how the element potential method determines the chemical equilibrium composition of the air is given. Once the gas composition is determined the thermodynamic properties of the gas mixture is obtained. The thermodynamic properties of interest were the constant pressure specific heat, specific internal energy, specific enthalpy, specific entropy, molecular weight ratio, equilibrium speed of sound, and the isentropic index.

It was found that the thermodynamic properties of this work compare well to the thermodynamic properties determined by other investigators [Boulos et al. 1994; Hillensrath and Klein 1965; Hansen 1959; Srinivasan et al. 1987a; Gupta et al. 1991]. In certain regions the effects of not including the higher ionized species can be seen. This is more pronounced at lower pressures. This work includes up to the third ionization stage. From these findings it can be deduced that the Debye correction and second virial correction are not critical for the range of pressures studied in this work. It is shown in the comparisons of the thermodynamic results that neglecting the trace species of Ar, Ar^{+}, Ar^{+2}, Ar^{+3}, O_2^{+}, N_2^{+}, O^{-}, and N^{-} does not significantly affect the results. If the desired temperature range is not too high, neglecting the triply and/or doubly ionized species gives good results. With good accuracy over a range of pressures and temperatures this data can be coupled with AVUS to perform accurate CFD calculations for high-speed flight simulations.

7.2 Adding Chemical Equilibrium to AVUS

Chemical equilibrium air thermodynamic and transport properties have been added to the CFD code AVUS. This provide AVUS with a greater range of applicability in the hypersonic flow regime. This new capability was added to AVUS by using the Tannehill curve fits of Srinivasan et al. (1987a and 1987b). The changes that were made to the AVUS code to include equilibrium air chemistry have been discussed. To validate that the equilibrium air chemistry was added to the AVUS code properly, the published results of several investigators were used. To verify the inviscid part of the

new AVUS code, results have been compared to the work of Prabhu et al. (1989) for a blunt body. This comparison shows excellent agreement. To verify the viscous part of the code, results have been compared to the work of Rosen (1991) using the CFL3D code for supersonic and hypersonic flat plate cases. Both of these flat plate cases show excellent agreement with the CFL3D code results. To see the effects of a strong shock for a high Mach number case, results were compared to the work of Tannehill (1990) for a Mach 25 hypersonic flow over a wedge and an axisymmetric cone. The AVUS results show good agreement to the work of Tannehill et al. To check the three-dimensional version of the equilibrium air AVUS code it was run in the three-dimensional, unstructured mode for the axisymmetric cone case. These results were compared to Tannehill et al.'s (1990) axisymmetric cone case. The comparisons were good indicating that the three-dimensional portion of the equilibrium air AVUS code is working properly.

7.3 Computationally Determining the Altitude-Velocity Plot

The third issue addressed in this work is the domain of applicability of the perfect gas model, the chemical equilibrium air model, the chemical nonequilibrium air model, and the thermo-chemical nonequilibrium air model. A computational study was carried out using AVUS to determine the regions of applicability of these air models for a blunt body at various velocities and altitudes. This type of altitude-velocity plot has already been produced by previous researchers, but the dividing lines between the different gas models were found using residence times. This work looks at temperature profiles of a blunt body in a high speed air flow to determine the dividing lines between the regions of applicability of the different air models. Unlike the previous works, this work provides specific error values for using a given model in a certain flight regime. It was found that the dividing lines between chemical equilibrium and chemical nonequilibrium have two dips in the curve that were not shown by previous researchers. These dips correspond to regions where O_2 and N_2 strongly dissociate. These results should be very beneficial to the CFD community.

7.4 Grid Study of Carbuncle Phenomenon

The carbuncle phenomenon is a numerical instability that affects the capturing of strong shocks when using a Riemann solver with low numerical dissipation. The carbuncle phenomenon manifests itself in the inability to compute uniform flow conditions downstream of a normal or nearly normal shock. Prior work has been done in this area to accurately capture strong shocks; and great progress has been made in reducing the effects of the carbuncle phenomenon. Even with these improvements the heat transfer profiles in the stagnation region still show some distortion from small upstream perturbations convected downstream to the wall. It has been determined that the grid quality in the region of the shock is a major factor in the inability of Riemann solvers to accurately capture the flow in the stagnation region. For this reason this work performs a grid study and makes recommendations as to what types of structured grids should be used to accurately capture strong shocks and predict heat transfer profiles at the body surface.

The carbuncle phenomenon was studied in this section as having two causes: the first is the lack of numerical viscosity in the numerical routines used to model hypersonic flows through a shock and second is the effect of the alignment of the grid with the shock. The first of these causes of the carbuncle phenomenon can affect all flow quantities downstream of the shock. The second cause only affects second-order quantities like the heat transfer profile at the blunt body wall.

The inviscid grid study shows that adding numerical viscosity lessens the effect of the carbuncle phenomenon. This numerical viscosity can be obtained by changing the aspect ratio of the grids, the alignment of the grids, or increasing the blending parameter.

The other possible cause of the carbuncle phenomenon is the alignment of the grid with the shock. The grid-shock misalignment does not affect first-order quantities like density, temperature, and pressure, but affects second-order quantities like heat transfer. It is believed that misalignment of the mesh with the shock is still causing numerical errors for the inviscid cases, but the numerical errors are two small to be seen by first-order quantities.

A reason for looking at these two causes of the carbuncle phenomenon as being independent is the cure for each is different. It would seem the cure for the lack of dissipation would be to apply the correct amount of dissipation in the shock. At present it is not known what is the correct amount. To fully cure the caruncle phenomenon it may be necessary to use a numerical method that calculates the inviscid and viscous fluxes in a coupled approach to better mimic the dissipation in a physical shock. This has been accomplished with the BGK and CESE methods that are mentioned in Chapter 2.

To cure the shock-grid misalignment problem the solution is to align the grid with the shock. This will take some work because the location of the shock is not known until the CFD problem is solved. On top of this it appears that the carbuncle phenomenon is quite sensitive to small misalignments between the grid and the shock. It is believed that the grid can be perfectly aligned with the shock and the carbuncle problem will still exist if the dissipation in the shock is not correct. Likewise, it is believed the carbuncle problem will still exist if the the correct amount of dissipation is added to the shock, but the grid is not correctly aligned with the shock.

For a measure of the degree the shock is misaligned from the mesh the maximum L2 momentum residuals near the shock are used. For cases where the shock is not well aligned with the mesh, the shock may have difficulty in finding a grid point to "settle" on. The shock moving back and forth between grid points can cause the momentum residuals to converge poorly for cells near the shock. The results from several case studies show that as the maximum L2 momentum residual increases, the departure of the stagnation point heat transfer from the theoretical value of Fay and Riddell (1958) increases. This shows that the more misaligned the shock is with the mesh the poorer the stagnation heat transfer results.

A

Transport Properties of High Temperature Air in Chemical Equilibrium

This appendix will focus on the aspect of computing the high temperature viscosity and thermal conductivity and showing how these properties tie into the Navier-Stokes equations. This work was originally written as a technical paper for the Physical Gas Dynamics (ME-590) class at the University of Dayton. The transport results were not extended to equilibrium air from the nitrogen gas results due to the decision to use the Tannehill curve fits of Srinivasan et al. (1987b) to provide the transport properties for AVUS.

For the sample calculations section a nitrogen gas was used so that only 5 species were included in the calculations, namely, N_2, N, N^+, N^{++}, and e^-. The focus of the results section is on the determination of the transport properties. The transport properties determined were the viscosity, translational thermal conductivity, internal thermal conductivity, and reactive thermal conductivity. The results are presented at pressures of 1 atm and $1x10^{-4}$ atm. All of the equations and results

of this chapter are presented in the centimeter-gram-second (CGS) unit system. This is due to the fact that using the CGS unit system gives simplified equations when performing calculations that deal with electric field effects.

Nomenclature

$A_{jm}(1)$	Sonine polynomial expansion coefficient, cm
$b_{jo}(1)$	Sonine polynomial expansion coefficient, s/cm^2
b_o	average close-impact parameter, cm
C_p	specific heat per mol, erg/mol-K
e	electron charge, 4.803x10^{-10} esu
d	diameter of colliding particles, Å
$D(f_i)$	left hand side of Boltzmann equation
$D_c(f_i)$	collision term of Boltzmann equation
D_{ij}	binary diffusion coefficient, cm^2/s
D_i^T	thermal diffusion coefficient, gm/cm-s
f_i	distribution function before collision
$f_i^{'}$	distribution function after collision
F	mean force on a particle, dyne
h	enthalpy per mole, erg/mol
k_b	Boltzmann constant, 1.38054x10^{-16} erg/K
m	species mass, gm/particle
M	molar species mass, gm/mol
n	number density, particles/cm^3
NE	number of elements in gas mixture
NS	number of species in gas mixture

P	pressure, atm
q	energy flux, erg/cm^2-s
R	universal gas constant, 8.3143x10^7 erg/mol-K
T	temperature, K
v	mean velocity, cm/s
V_{ij}	relative velocity before collision, cm/s
$V_{ij}^{'}$	relative velocity after collision, cm/s
$\overline{V}$	diffusion velocity, cm/s
x	mole fraction
Z	particle charge number

Greek

α	polarizability, Å
γ	ratio of specific heats
δ_{mn}	Kroeneker delta function
η	viscosity, gm/cm-s
λ_D	Debye length, cm
λ	thermal conductivity, erg/cm-s-K
μ_{ij}	molar reduced mass, gm/mol
ξ	inverse of collision frequency, s/collision
σ_{ij}	rigid sphere collision diameter, Å
$\Phi(r)$	interaction potential
$d\Omega$	differential solid angle
$\Omega_{ij}^{(ls)}$	collision integral, cm^3/s
$\Omega_{ij}^{(ls)^*}$	reduced collision integral, Å^2

Subscript-Superscipt

e	electron
f	frozen
h	heavy
i, j, k	species index
int	internal
r	reactive
tr	translational

A.1 Non-equilibrium Kinetic Theory and Collision Integrals

The diffusion, viscosity, thermal conductivity and electrical conductivity are related to fluxes present in a gas mixture. There are two types of diffusion present, the first type is mass diffusion which represents the transfer of mass from one region to another due to gradients in the concentration of a species. The other type of diffusion is thermal diffusion which accounts for diffusion of a species due to thermal gradients. Thermal diffusion is often called the Dufour effect. In most situations of engineering interest the Dufour effect is rather insignificant and thermal diffusion can be ignored [Anderson 1989]. Viscosity is the transport of momentum due to gradients in momentum. Thermal conductivity is the transport of thermal energy due to the presence of thermal gradients, chemical reactions, and the internal degrees of freedom in the gas. Electrical conductivity is the transport of the mass of electrons and ions due to gradients in the electric potential.

In order to accurately determine the transport coefficients of a high-temperature gas the collision integrals (also called transport cross-sections) of the different interactions of species must be known. The Boltzmann distribution can be expressed in terms of integrals defined as collision integrals.

There are several excellent references available that go through a rigorous derivation explaining how the collision integrals are related to the Boltzmann distribution and how to express the transport properties as functions of the collision integrals [Vincenti and Kruger 1965; Hirschfelder et al. 1954; Monochick et al. 1963].

In order to give the reader a better physical understanding of what the collision integrals and Sonine polynomials are, a brief review of how these terms are related to the Boltzmann distribution is given. A majority of the discussion of how the collision integrals are related to the Boltzmann distribution is taken from the following references: Hirschfelder et al. (1954) and Boulos et al. (1994). If NS different chemical species are considered, then the system can be described by NS different equations for the NS species. For a given particle of chemical species i the Boltzmann distribution is given as

$$D(f_i) = D_c(f_i) \tag{A.1}$$

with

$$D(\overrightarrow{f_i}) = \frac{\partial}{\partial t}\overrightarrow{f_i} + \overrightarrow{v_i}\left(\frac{\partial}{\partial x}\overrightarrow{f_i} + \frac{\partial}{\partial y}\overrightarrow{f_i} + \frac{\partial}{\partial z}\overrightarrow{f_i}\right) + \frac{\overrightarrow{F_i}}{m_i}\left(\frac{\partial}{\partial v_x}\overrightarrow{f_i} + \frac{\partial}{\partial v_y}\overrightarrow{f_i} + \frac{\partial}{\partial v_z}\overrightarrow{f_i}\right)$$

$$D_c(\overrightarrow{f_i}) = \sum_{j=1}^{NS}\int\int(f_i^{'}f_j^{'} - f_i f_j)V_{ij}\sigma_{ij}dv_j d\Omega.$$

The $D_c(\overrightarrow{f_i})$ term is the collision term that describes binary collisions between particles of type i and j. The $D(\overrightarrow{f_i})$ term describes how particles are distributed in position and velocity space. The $\overrightarrow{f_i}$ term is the distribution function, v_i the mean velocity of the particle, m_i is the atomic mass, and $\overrightarrow{F_i}$ is the mean force on a particle. The distribution function f is related to the colliding particles before the collisions and the distribution function $f^{'}$ is related to the colliding particles after the collision. V_{ij} is the relative velocity of chemical species i and j before a collision and $d\Omega$ is the differential solid angle. The term σ_{ij} is the rigid sphere diameter of particles of type i and j, which is calculated as

$$\sigma_{ij} = \pi\left[\frac{1}{2}(d_i + d_j)\right]^2 \tag{A.2}$$

where d_i and d_j are the diameters of the colliding particles.

The solution of these NS Boltzmann distributions gives NS distribution functions and allows us to calculate the mean values of the macroscopic properties and fluxes. A series solution of the Boltzmann equation can be obtained by introducing a perturbation parameter ξ in such a manner that the frequency of the collisions can be varied without affecting the relative number of collisions of a particular type [Boulos et al. 1994]. With this assumption the Boltzmann distribution can be written as

$$D(\overrightarrow{f_i}) = \frac{1}{\xi} D_c(\overrightarrow{f_i}) \tag{A.3}$$

where $1/\xi$ measures the frequency of collisions. If ξ is kept very small then collisions will occur very frequently and the gas will behave like a continuum in which local chemical equilibrium is maintained everywhere. The distribution function is then expanded in a series as follows:

$$f_i = f_i(0) + \xi f_i(1) + \xi^2 f_i(2) + \cdots \tag{A.4}$$

The first term $f_i(0)$ assumes that the right-hand side of the Boltzmann distribution is zero since no collisions occur. This corresponds to a Maxwellian distribution which can easily be solved. The higher order distribution function terms can be expressed as a perturbation function times the Maxwellian distribution. The perturbation function is linear in derivatives and the coefficients of these derivatives can be expanded into a finite series of Sonine polynomials. The final result is that transport properties are expressed in terms of complex quantities called bracket integrals which are themselves functions of the collision integrals. The collision integrals are functions of the interaction potentials characterizing collisions between different particles.

The solution of the transport coefficients of a high temperature gas depends on the solution of the collision integrals of all the different binary interactions between particles in the system. The collision integrals ,$\Omega_{ij}^{(l,s)}$, have the units of cubic centimeters per second and represent a thermally and orientationally averaged collision probability between two particles [Boulos et al. 1994].

There are many different types of intermolecular potential energy models that account for the attractive and repulsive forces that act on colliding particles. The collision integrals are often presented in terms of a reduced collision integral that is a ratio of the collision integral evaluated using a given potential energy model divided by the collision integral evaluated using the rigid sphere model. This ratio is multiplied by the rigid sphere cross section which has units of Angstroms (Å) to the give the reduced collision units of Angstroms,

$$\Omega_{ij}^{(l,s)^*} = \sigma_{ij}^2 \frac{\Omega_{ij}^{(l,s)}}{[\Omega_{ij}^{(l,s)}]_{rigid\ sphere}} \tag{A.5}$$

with

$$[\Omega_{ij}^{(l,s)}]_{rigid\ sphere} = \frac{\sqrt{\frac{2\mu_{ij}}{\pi k_b T}}}{\frac{1}{2}(s+1)!\left[1 - \frac{1}{2}\frac{1+(-1)^l}{1+l}\right]\pi\sigma_{ij}^2}$$

and

$$\mu_{ij} = \frac{m_i m_j}{m_i + m_j}.$$

For the above equations k_b is the Boltzmann constant and μ_{ij} is the reduced mass which has units of gm/particle. There are a number of different types of collision integrals that are used in finding the transport properties of a gas and the l and s specify which type of collision integral is being used.

There have been a large number of calculations for collision integrals for air in recent years [Capitelli et al. 2000; Selle and Riedel 2000; Murphy and Arundell 1994; Murphy 1995]. Since these calculations have already been performed and verified by checking results with other authors, it is more reliable to use the most recent collision integral data if it is available. It should be noted that the collision integral data is always being updated due to better potential energy models and more accurate fundamental data.

For most neutral-neutral, ion-neutral, and electron-neutral collisions there are collision integrals available in the literature. For collision pairs that do not occur very often such as N-N^{++} or N_2-N^+,

the polarizabilities model can be used to find the collision integrals. These equations in closed form are given by Capitelli et al (2000a),

$$\Omega^{(1,1)}(T) = 425.4Z\sqrt{\frac{\alpha}{T}} \tag{A.6}$$

$$\Omega^{(1,2)}(T) = 0.8333\Omega^{(1,1)}(T) \tag{A.7}$$

$$\Omega^{(1,3)}(T) = 0.7292\Omega^{(1,1)}(T) \tag{A.8}$$

$$\Omega^{(2,2)}(T) = 0.8710\Omega^{(1,1)}(T) \tag{A.9}$$

where $Z = 1$ for monocharged ions, $Z = 2$ for double charge ions, and $Z = -1$ for electron and negative ions and α is the polarizability. The values for polarizabilities of different neutral species are listed in McDaniel and Mason (1973) as: $N_2 = 1.76$ $\mathring{A}$, $O_2 = 1.60$ $\mathring{A}$, NO = 1.70 $\mathring{A}$, N = 1.13 $\mathring{A}$ and O = 0.77 $\mathring{A}$.

The collision integrals for ion-ion or ion-electron collisions are much larger than those involving neutral species. This is because charged particles have electrostatic intermolecular forces that influence the interactions between charged particles. These electrostatic forces are relatively long range compared to the intermolecular forces that occur with neutral species.

To compute the interactions between charged particles a screened Coulomb potential can be used which is written as

$$\Phi(r) = \left(\frac{e^2}{r}\right)\exp\left[\frac{-r}{\lambda_D}\right] \tag{A.10}$$

where λ_D is the Debye length and e is the electron charge. The Debye length is the average length where the Coulomb force acting between particles is effective. Since positive ions are surrounded by electrons this Coulomb force of a single ion is 'screened out' at a certain distance due to a large number of electrons shielding it. The distance where this occurs is the Debye length. For the

interaction between two different types of charged particles the Debye length is give as

$$\lambda_D = \left[\frac{k_b T}{4\pi(Z_i^2 n_i + Z_j^2 n_j)}\right] \tag{A.11}$$

where n_i is the number density of species i.

Collision integrals for charged particle interactions are found either in tabular form [Hahn et al. 1971] or approximated with a closed form solution [Liboff 1959]

$$\Omega^{(1,s)^*} = b_o^2 \frac{4}{s(s+1)}\left[\ln\Lambda - \frac{1}{2} - 1.154 + z(s)\right] \tag{A.12}$$

$$\Omega^{(2,s)^*} = b_o^2 \frac{12}{s(s+1)}\left[\ln\Lambda - 1 - 1.154 + z(s)\right] \tag{A.13}$$

where $\Lambda = 2d/b_o$ and b_o is the average close-impact parameter and $z(s)$ are defined below:

$$b_o = \frac{e^2}{2k_b T}, \qquad \text{and} \quad z(s) = \sum_{n=1}^{s-1} \frac{1}{n} \tag{A.14}$$

A.2 High Temperature Gas Viscosity

As stated earlier the viscosity of a multicomponent gas mixture can be obtained by solving the Boltzmann equation using the Sonine polynomial expansion. It has been shown by numerous authors that the mixture viscosity of a gas can be accurately represented by the first term of the Sonine polynomial expansion [Hirschfelder et al. 1954; Devoto 1966]. This is due to the rapid convergence of the Sonine polynomials.

Since the electrons have a much smaller mass than the neutral particles and ions, only the momentum of the electron is appreciably altered in an electron-neutral or electron-ion collision. This means that the speed of the heavy particles does not change appreciably and electron-heavy particle encounters are expected to have little effect on the distribution functions of the heavier species. This means that the heavy and electron transport coefficients can be considered separately.

Many of the above references also show that when the heavy particle and electron contributions to the viscosity are calculated that the electron contribution is rather insignificant [Devoto 1966].

There are numerous references that have reviews of how to compute the viscosity of a gas mixture [Gupta et al. 1991; Capitelli et al. 2000; Palmer and Wright 2003b; Bottin et al. 1999; Devoto 1966]. For this reason this appendix only covers the highlights of these papers. There are also many different ways of expressing the equations used to solve for various transport properties. In this paper all of the equations are written using the cgs unit system using mole fractions, reduced collision integrals, and properties on a per mole basis. Palmer and Wright (2003a) has a good review of how all the different formulations of the multicomponent viscosities are related.

Using this type of formulation the mixture viscosity can be expressed as

$$\eta(1) = \sum_{j=1}^{NS} x_j b_{jo}(1) \tag{A.15}$$

where $\eta(1)$ indicates this is a first order mixture viscosity, b_{jo} are the associated Sonine polynomial expansion coefficients, and x_j is the mole fractions of species j. The b_{jo}'s can be determined by solving the following system of linear equations,

$$\sum_{j=1}^{NS} H_{ij} b_{jo}(1) = x_i \qquad i = 1, 2, 3, \cdots, NS \tag{A.16}$$

where

$$H_{ij} = 52979 \frac{x_i}{\sqrt{T}} \sum_{k=1}^{NS} \frac{x_k \sqrt{\mu_{ik}}}{M_i} \left[\frac{5}{3} (\delta_{ij} - \delta_{jk}) \Omega_{ik}^{(1,1)^*} + \frac{M_k}{M_j} (\delta_i j + \delta_j k) \Omega_{(i,k)}^{(2,2)^*} \right]$$

and the M's are the molar mass of the species and δ_{mn} is the Kronecker delta function which is 1 if $m = n$ and 0 otherwise.

From the above formulation it can be seen that to compute the multicomponent viscosity a linear system of equations whose size is equal to the number species in the gas mixture must be solved. As the number of species in the gas mixture increases the cost of computing a result increases

rapidly. In most references it is cited that the system of equations is solved using Cramer's rule. The mixture viscosity is then found by the ratio of the determinant of an augmented H matrix over the determinant of the H matrix, where the augmented matrix includes an extra row and column containing the species mole fractions. Another technique to solve the system of equations is to use the standard pivoted Gaussian elimination routine. It is shown that Cramer's rule is less stable and prone to more numerical error than using pivoted Gaussian elimination and that Cramer's rule requires more CPU time for most cases [Palmer and Wright 2003b].

Solving the above system of NS equations gives the exact first-order approximation of the multicomponent mixture viscosity. Due to the computational time involved in solving this system of equations, various mixing rules have been developed that lower computational cost. These mixing rules make assumptions about the off-diagonal terms in the H matrix and assumptions in how the different collision integrals are related to form simple algebraic expressions to compute the mixture viscosity. Cowling et al. (1963) can be consulted as to the physical significance of the diagonal and off-diagonal elements of the H matrix.

The most commonly used mixture rules for the viscosity are the Wilke's Mixing Rule [Wilke 1950], the Armaly-Sutton Mixing Rule [Armaly and Sutton 1980], and the Gupta-Yos Mixing Rule [Gupta et al. 1991; Yos 1963]. It has been shown that if you are interested in mixture viscosities at high-temperatures where ionization is important, that all of the mixture rules should be avoided due to their lack of accuracy at high temperatures [Palmer and Wright 2003b]. This is due to the fact that the mixture rules make assumptions or ignore the off-diagonal terms of the H matrix in their formulations. Since the off-diagonal terms of the H matrix only become important at higher temperatures, where ionization is important, the mixing rules do not work as well in this range. If computational time is important and some sacrifice in the accuracy of the mixture viscosity at higher temperature is acceptable, then the Gupta-Yos mixture rule should be used. It should be noted that the Gupta-Yos mixture rule uses about half the computational time of the multicomponent method.

A.3 High Temperature Gas Thermal Conductivity

For computing the thermal conductivity of a gas mixture there are numerous references that have reviews [Gupta et al. 1991; Hirschfelder et al. 1954; Monochick et al. 1963; Capitelli et al. 2000; Palmer and Wright 2003a; Bottin et al. 1999; Devoto 1966; Yos 1963]. For this reason this appendix only covers the highlights of these papers. Again for the thermal conductivity all of the equations are written using the cgs unit system using mole fractions, reduced collision integrals, and properties on a per mole basis. Palmer and Wright (2003b) has a good review of how all the different formulations of the multicomponent thermal conductivity are related.

The general energy flux expression for a reacting, multicomponent gas mixture can be shown as

$$q = -\lambda_{fr}\frac{\partial T}{\partial r} + \sum_{i=1}^{NS} n_i h_i \overline{V_i} + \frac{k_b T}{n}\sum_{i}^{NS}\sum_{j}^{NS}\frac{n_j D_i^T}{m_i D_{ij}(1)}(\overline{V_i} - \overline{V_j}). \tag{A.17}$$

The first term in equation (A.17) represents the energy flux due to a temperature gradient. The second term represents the energy flux due to diffusion of all species at a point. The third term is the heat flux due thermal diffusion (also called the Dufour effect). As mentioned earlier the Dufour effect is insignificant for most engineering applications of interest and can be ignored. The h_i is the enthalpy per mole of species i, $\overline{V_i}$ is the diffusion velocity of species i, D_i^T is the thermal diffusion of species i coefficient which measures the diffusion of species i due to thermal gradients, and D_{ij} is the binary diffusion coefficient which will be discussed in more detail later.

The thermal conductivity in equation (A.17) consists of translational and internal components,

$$\lambda_{fr} = \lambda_{tr} + \lambda_{int}. \tag{A.18}$$

The translational thermal conductivity is due to the transfer of translational energy between colliding particles. The internal thermal conductivity is due to the transfer of energy between translational and internal degrees of freedom. Together, the translational and internal thermal conductivity are

referred to as the frozen thermal conductivity, because they are the only components that would exist in a non-reacting (frozen) mixture. Since electrons have a much smaller mass than the heavy particles the translational thermal conductivity can be divided into contributions from heavy particles (atoms, molecules, and ions) and from electrons,

$$\lambda_{tr} = \lambda_h + \lambda_e. \tag{A.19}$$

The second term on the right hand side of equation (A.17) accounts for the energy transfer due to ordinary diffusion. One of the primary sources of diffusion heat transfer is from chemical reactions. These chemical reactions lead to concentration gradients of species in the flow. Due to these concentration gradients the energy is conducted along these gradients by ordinary diffusion. For a finite-rate CFD application it is possible to evaluate these terms directly [Palmer and Wright 2003a]. If chemical equilibrium is considered this term can be manipulated to be expressed in terms of a temperature gradient [Anderson 1989; Gupta et al. 1991],

$$-\lambda_r \frac{\partial T}{\partial r} = \sum_{i=1}^{NS} n_i h_i \overline{V_i}. \tag{A.20}$$

The λ_r term is called the reactive thermal conductivity since it corresponds to heat transfer due to chemical reactions. A total equilibrium thermal conductivity, λ_{tot}, can be obtained by summing the contributions of the translational, internal, and reactive components,

$$\lambda_{tot} = \lambda_h + \lambda_e + \lambda_{int} + \lambda_r. \tag{A.21}$$

A general formulation for the translational thermal conductivity was first developed by Hirschfelder et al. (1954) . The most commonly used multicomponent formulations of the translational thermal conductivity are the first and second order approximations. Both of these methods involve the use of Sonine polynomials and solving a system of linear equations. The second-order approx-

imation is much more complicated and involves solving a system of linear equations that is twice the size of those solved using the first-order approximation. It is also shown in several references that the second-order approximation gives almost the same results as the first-order approximation [Palmer and Wright 2003a; Bottin et al. 1999]. For this reason only the first-order approximation of the multicomponent translational thermal conductivity is given.

The heavy particle translational thermal conductivity can be given as

$$\lambda_h(1) = \frac{5}{4} R \sum_{j=1}^{NS} x_j a_{j1}(1) \tag{A.22}$$

where R is the universal gas constant and $a_{j1}(1)$ is the first order Sonine polynomial expansion coefficient for translational thermal conductivity. The $a_{j1}(1)$ term can be determined by solving the following system of linear equations,

$$\sum_{j=1}^{NS} Q_{ij}^{11} a_{j1}(1) = x_i \tag{A.23}$$

where

$$\begin{aligned} Q_{ij}^{11} =& 8829.83 \frac{1}{M_i M_j \sqrt{T}} \sum_{k=1}^{NS} x_i x_k \mu_{ik}^{5/2} \\ & \left[(\delta_{ij} - \delta_{jk}) \cdot \left(\frac{15}{2} \left(\frac{M_j}{M_k} \right)^2 + \left(\frac{25}{4} \right) - 3B_{ik}^* \right) \Omega_{ik}^{(1,1)^*} + 4 \left(\delta_{ij} + \delta_{jk} \right) \frac{M_j}{M_k} \Omega_{ik}^{(2,2)^*} \right] \end{aligned} \tag{A.24}$$

with

$$B_{ik}^* = \frac{5\Omega_{ik}^{(1,2)^*} - 4\Omega_{ik}^{(1,3)^*}}{\Omega_{ik}^{(1,1)^*}}.$$

This system of equations can be solved by using the pivoted Gaussian elimination method.

The only mixture rule that gives good results for the translational thermal conductivity is the Gupta-Yos mixing rule [Gupta et al. 1991; Yos 1963]. The Gupta-Yos mixing rule avoids solving a system of linear equations by assuming that the off-diagonal elements are small relative to the

diagonal elements. The Gupta-Yos mixing rule was designed for gas mixtures that are neutral or weakly ionized. Several references have shown that the Gupta-Yos mixing rule can still be used where ionization is significant to get a good approximation of the total thermal conductivity [Palmer and Wright 2003a; Bottin et al. 1999]. This is because in the region where ionization is significant the translational thermal conductivity is relatively small compared to the electronic translational and reactive thermal conductivity.

The Gupta-Yos mixing rule is a first-order approximation of the translational thermal conductivity and can be given as

$$\lambda_{tr} = \frac{5}{4} R \sum_{i=1}^{NS} \frac{x_i}{Q_{ii}^{11}} \tag{A.25}$$

with

$$\begin{aligned} Q_{ii}^{11} &= \frac{12,487.27}{\sqrt{T}} \sum_{j=1}^{NS} \alpha_{ij} x_j \sqrt{2\mu_{ij}} \Omega_{ij}^{(2,2)^*} \\ \alpha_{ij} &= 1 + \frac{\left(1 - \frac{M_i}{M_j}\right)\left(0.45 - 2.54\frac{M_i}{M_j}\right)}{\left(1 + \frac{M_i}{M_j}\right)^2}. \end{aligned}$$

The electronic translational thermal conductivity is often calculated using a second-order or third-order approximation. The third-order approximation requires a much larger set of collision integrals and the improvement in accuracy compared to the second-order approximation is relatively small. For this reason only the second-order approximation is shown. Since the electronic translational thermal conductivity is the thermal conductivity for a single species, the second-order approximation reduces the complexity significantly. It turns out that for the electronic thermal conductivity a system of linear equations does not have to be solved since there is only one Sonine polynomial expansion coefficient [Capitelli et al. 2000]. The results are as follows:

$$\lambda_e(2) = \frac{5}{4} R \frac{x_e}{Q_{ee}^{11}} \tag{A.26}$$

with

$$Q_{ee}^{11} = \frac{8,829.83}{{M_e}^2\sqrt{T}} \sum_{k \neq e}^{NS} x_e x_k \mu_{ek}^{5/2} \left[\frac{25}{4} \Omega_{ek}^{(1,1)^*} - 15\Omega_{ek}^{(1,2)^*} + 12\Omega_{ek}^{(1,3)^*} \right].$$

The presence of internal degrees of freedom effects the energy flux possible. The exact expression for the coefficient of internal thermal conductivity depends upon the translational probabilities for the transfer of energy among the degrees of freedom of the molecules [Monochick et al. 1963]. If the assumption is made that the rate of transfer of energy is sufficiently fast, the internal energy is in an equilibrium distribution. With this assumption the equation for the internal thermal conductivity reduces to a single equation. It has been shown by many authors that this approximation works rather well for most gas mixtures [Hirschfelder et al. 1954; Bottin et al. 1999; Devoto 1966]. The expression for the internal thermal conductivity is

$$\lambda_{int} = 3.2036 \times 10^{-5} \sqrt{T} \sum_{i=1}^{NS} \frac{x_i C_{p,i}^{int}}{\sum_{j=1}^{NS} x_j \sqrt{2\mu_{ij}} \Omega_{ij}^{(1,1)^*}}. \tag{A.27}$$

In this equation $C_{p,i}^{int}$ is the internal specific heat on a per mole basis of species i. The internal specific heat can easily be calculated by subtracting the translational component of the specific heat out of the total specific heat,

$$C_{p,i}^{int} = C_{p,i} - \frac{5}{2}R. \tag{A.28}$$

The reactive thermal conductivity is often calculated using the formulas of Butler and Brokaw (1957). The Butler and Brokaw method is a rather rigorous approach and gives results that are in agreement with the fully rigorous method of Murphy (1995). Due to the complexity of these formulas the Butler and Brokaw method is not shown in this paper.

Another approach to calculate the reactive thermal conductivity is to use a mixture rule. Anderson (1989) and Gupta et al. (1991) show that the reactive thermal conductivity can be found by

some simple manipulations of the energy flux shown in equation (A.20). The final result is

$$\lambda_r = \frac{1}{R}\sum_{i=1}^{NS} n_i k_b D_{im} h_i \left|\frac{\partial c_i}{\partial T}\right| \tag{A.29}$$

with the h_i being the enthalpy on a per molar basis and c_i the mass fraction of species i. The mass fraction gradient can be calculated by numerically evaluating the value by the central difference formula

$$\frac{\partial c_i}{\partial T} \approx \frac{c_i(T+\triangle T) - c_i(T-\triangle T)}{2 \triangle T}. \tag{A.30}$$

The above formula can easily be calculated if the mass fractions are known at $T+\triangle T$ and $T-\triangle T$.

The D_{im} term is the multicomponent diffusion coefficient, which is related to the binary diffusion coefficients. The first-order approximation of the binary diffusion coefficients is given as

$$D_{ij}(1) = 0.002626\sqrt{\frac{T^3}{2\mu_{ij}}}\frac{1}{P\Omega_{ij}^{(1,1)^*}} \tag{A.31}$$

with P being the pressure given in atmospheres. The multicomponent diffusion is given by

$$D_{im} = \frac{1-x_i}{\sum_{j-1}^{NS}\frac{x_j}{D_{ij}}}. \tag{A.32}$$

It should be mentioned that using this mixture rule for the reactive thermal conductivity will often result in underestimating the reactive thermal conductivity when ionization becomes significant [Bottin et al. 1999]. Yos (1963) also presents another mixture rule for calculating the reactive thermal conductivity for an equilibrium gas mixture and this formulation also underestimates the reactive thermal conductivity.

A.4 Results

A FORTRAN program was written to compute the viscosity and thermal conductivity of a high-temperature gas mixture. The gas mixture evaluated was a five species nitrogen gas with the species of N_2, N, N^+, N^{+2}, and e^-. The temperature range of interest was from 400 - 20,000 K and pressures of 1 atm and 1x10^{-4} atm were calculated as shown in figures A.1 and A.2.

To compute the equilibrium composition and thermodynamic properties of the individual species the CANTERA program was used. CANTERA uses the element potential method to find the equilibrium composition. The sources for the thermodynamic properties of the individual species are given in Chapter 2.

To calculate the collision integrals the curve fits of Capitelli et al. (2000) were used for the neutral-neutral, neutral-ion, and neutral-electron collisions. For collision pairs that do not occur very often, N-N^{++} or N_2-N^+, the polarizabilities model of equation (A.9) was used. For the charged particle interactions the closed form solution of the Coulomb potential was used, equation (A.13).

The mixture viscosity is computed using the first-order multicomponent formulation of equation (A.15). The system of linear equations in equation (A.16) is solved by using the pivoted Gaussian elimination technique. In some cases if the mole fractions of a species were small enough, the species is removed from the system of equations so that the H matrix does not become singular.

The heavy particle translational thermal conductivity was computed using the Gupta-Yos mixing rules of equation (A.25). The first-order multicomponent formulation was also tried but the results were not on the same order of magnitude of translational thermal conductivities listed in other references. The second-order multicomponent formulation of equation (A.26) was used to calculate the electronic translational thermal conductivity. The internal thermal conductivity was calculated using equation (A.27). Finally the reactive thermal conductivity was computed using the mixture rules of Anderson (1989) and Gupta et al. (1991) (equations A.29-A.32). The mass fractions were numerically calculated by finding the equilibrium compositions at $T + \triangle T$ and $T - \triangle T$ using the

CANTERA program.

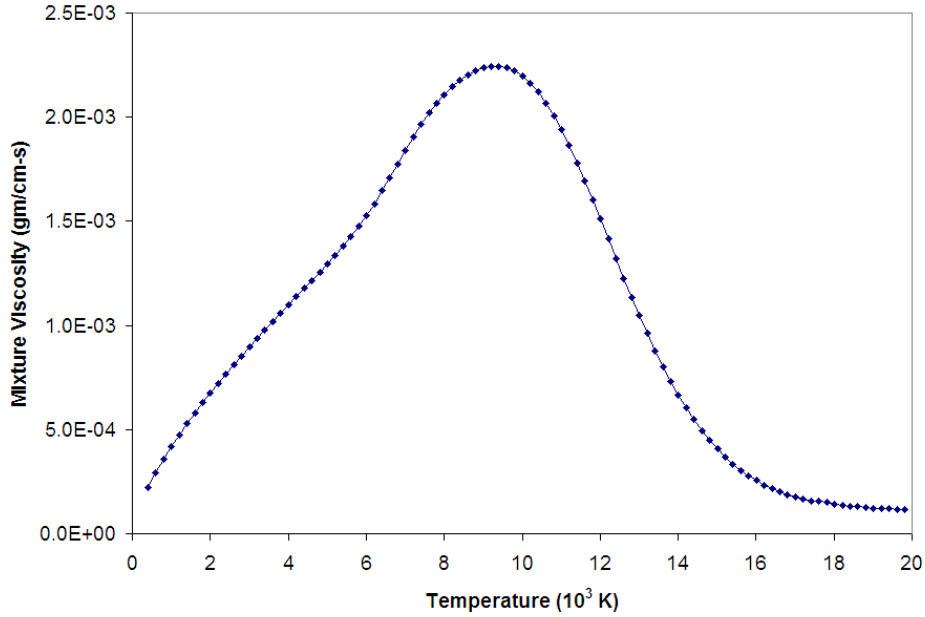

(a) Mixture viscosity.

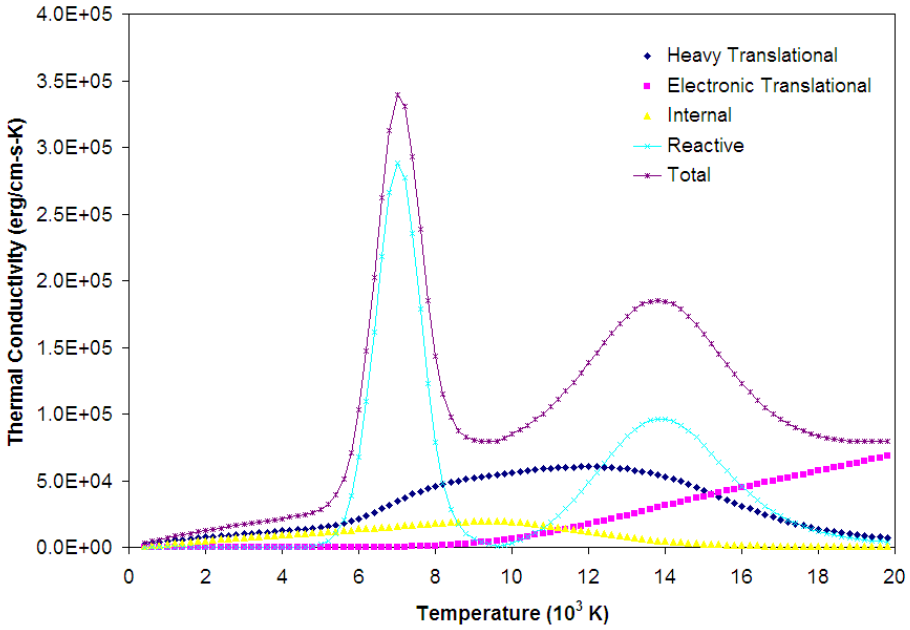

(b) Total thermal conductivity and components.

Figure A.1: Transport properties at 1 atm.

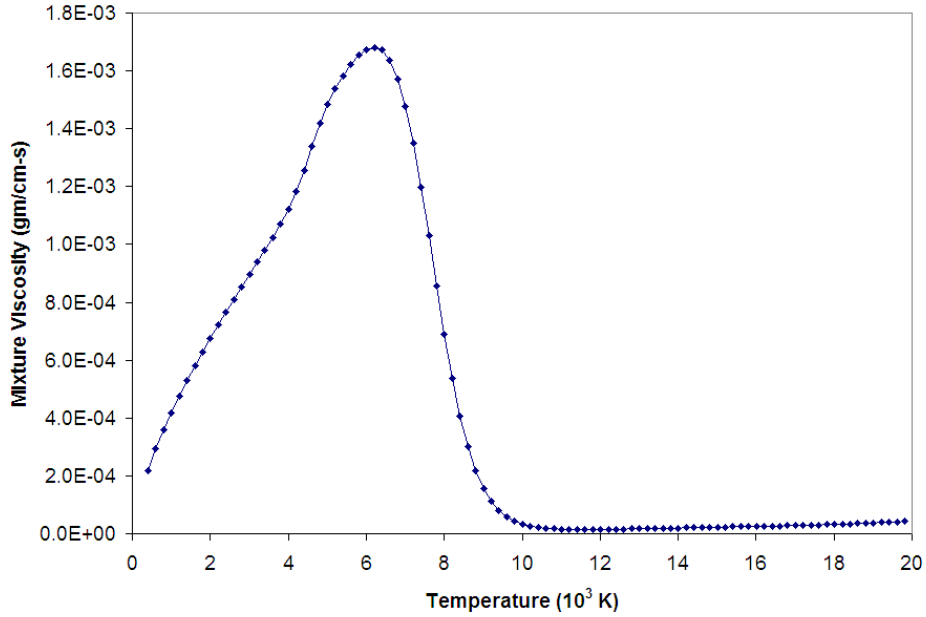

(a) Mixture viscosity.

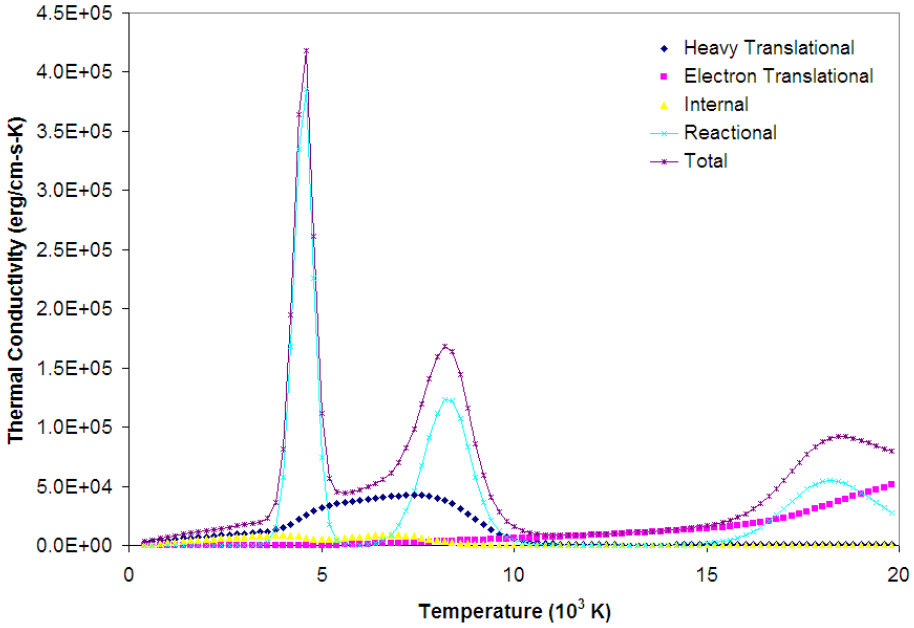

(b) Total thermal conductivity and components.

Figure A.2: Transport properties at 1×10^{-4} atm.

References

Amaladas, J. and Kamath, H. 1998. Accuracy and Assessment of Upwind Algorithms for Steady-State Computations. *Computers and Fluids 27,* 8, 941–962.

Anderson, J. 1989. *Hypersonic and High Temperature Gas Dynamics.* McGraw-Hill.

Armaly, B. and Sutton, L. 1980. Viscosity of Multicomponent Partially Ionized Gas Mixtures. AIAA paper 80-1495.

Bailey, H. 1967. Programs for Computing Equilibrium Thermodynamic Properties of Gases. Tech. Rep. NASA TN D-3921.

Barth, T. 1989. Some Notes on Shock Resoloving Flux Functions Part I: Stationary Characteristics. Tech. Rep. NASA TM-101087.

Batten, P., Clarke, N., Lambert, C., and Causon, D. 1997. On the Choice of Wave Speeds for the HLLC Riemann Solver. *SIAM Journal of Science and Statatistical Computing 18,* 6, 1553.

Bertin, J. 1994. *Hypersonic Aerothermodynamics.* AIAA Education Series.

Bhatnagar, P., Gross, E., and Krook, M. 1954. A Model for Collision Processes in Gases I: Small Amplitutude Processes in Charged and Neutral One-Compoment Systems. *Physics Review 94*, 511–525.

Bogdonoff, S. and Vas, I. 1959. Preliminary Investigations of Spiked Bodies at Supersonic Speeds. *Journal of Aerospace Science 26*, 584.

Bottin, B. 1997. *PEGASE 4.4 - Perfect Gas Equation For Arbitrary Mixtures at Low Pressure and High Temperature.* VKI Manual 47.

Bottin, B. 2000. Thermodynamic Properties of Arbitrary Perfect Gas Mixtures at Low Pressures and High Temperatures. *Progress in Aerospace Sciences 36*, 547–579.

Bottin, B., Abeele, D., Carbonaro, M., Degerez, G., and Sarma, G. 1999. Thermodynamic and Transport Properties for Inductive Plasma Modeling. *Journal of Thermophysics and Heat Transfer 13,* 3, 343–350.

Boulos, M., Fauchaus, F., and Pfender, E. 1994. *Thermal Plasmas: Fundamentals and Applications.* Wiley and Sons.

Butler, J. and Brokaw, R. 1957. Thermal Conductivity of Gas Mixtures in Chemical Equilibrium. *Journal of Chemical Physics 26,* 6, 1636–1643.

Cai, M., Yu, S., and Zhang, M. 2006. Theoretical and Numerical Solutions of Linear and Nonlinear Elastic Waves in a Thin Rod. AIAA paper 2006-4778.

Capitelli, M., Colonna, G., Giordano, D., Marraffa, L., Casavola, A., Minelli, P., Pagano, D., Pietanza, L., and Taccogna, F. 2004. High-Temperature Thermodynamic Properties of Mars-Atmosphere Components. AIAA paper 2004-2378.

Capitelli, M., Colonna, G., Gorse, C., and D'Angola, A. 2000. Transport Properties of High Temperature Air in Local Thermodynamic Equilibrium. *The European Physical Journal D 11*, 279–289.

Capitelli, M., Gorse, C., Longo, S., and Giordano, D. 2000. Collision Integrals of High-Temperature Air Species. *Journal of Thermophysics and Heat Transfer 14,* 2, 259–268.

Chang, C.-L. 2007. Three-Dimensional Navier-Stokes Calculations Using the Modified Space-Time CESE Method. AIAA paper 2007-5818.

Chang, S.-C. 1995. The Method of Space-Time Conservation Element and Solution Element - A New Approach for Solving the Navier-Stokes and Euler Equations. *Journal of Computational Physics 119*, 295–324.

Chang, S.-C., Wang, X., and Chow, C. 1999. The Space-Time Conservation Element and Solution Element Method: A New High-Resolution and Genuinly Multidimensional Paradigm for Solving Conservation Laws. *Journal of Computational Physics 156*, 89–136.

Chauvat, Y., Moschetta, J., and Gressier, J. 2005. Shock Wave Numerical Structure and the Carbuncle Phenomena. *International Journal for Numerical Methods in Fluids 47*, 903–909.

Colella, P. and Glaz, P. 1985. Efficient Solution Algorithms for the Riemann Problem for Real Gases. *Journal of Computational Physics 59*, 264–289.

Cowling, T., Gray, P., and Wright, P. 1963. The Physical Significance of Formulae for the Thermal Conductivity and Viscosity of Gas Mixtures. *Proceedings of the Royal Society of London, Series A: Mathematical and Physical Sciences A276*, 69–82.

Devoto, R. 1966. Transport Properties of Ionized Monatomic Gases. *Physics of Fluids 9,* 6, 1230–1240.

Donat, R. and Marquina, A. 1996. Capturing Shock Reflections: An Improved Flux Formula. *Journal of Computational Physics 125,* 1, 42–58.

Dumbser, M., Moschetta, J., and Gressier, J. 2004. A Matrix Stability Analysis of the Carbuncle Phenomenon. *Journal of Computational Physics 197*, 647–670.

Einfeldt, B. 1988. On Godunov-Type Methods for Gas Dynamics. *SIAM Journal of Numerical Analysis 25,* 2, 294–318.

Einfeldt, B., Munz, C., Roe, P., and Sjogreen, B. 1991. On Godunov-Type Methods near Low Densities. *Journal of Computational Physics 92*, 273–295.

Elling, V. 2005. A Possible Counterexample to Wellposedness of Entropy Solutions and To Godunov Scheme Convergence. Tech. Rep. Technical Report SCCM-03-05, Stanford University. http://front.math.ucdavis.edu/author/V.Elling.

Elling, V. 2006. Carbuncle as Self-Simliar Entropy Solutions. Tech. Rep. math.NA/0609666, NASA arXiv. http://front.math.ucdavis.edu/author/V.Elling.

Fay, J. and Riddell, F. 1958. Theory of Stagnation Point Heat Transfer in Dissociated Air. *Journal of Aeronautical Sciences 25,* 2.

Godunov, S. 1959. A Difference Scheme for Numerical Computation of Discontinuous Solution of Hydrodynamic Equations. *Sbornik Mathematics 47,* 271-306.

Goodwin, D. 2003. *Defining Phases and interfaces: CANTERA 1.5.* Division of Engineering and Applied Science, California Institute of Technology, CA.

Gordon, S. 1970. Complex chemical equilibrium calculations. In Kinetics and thermodynamics in high-temperature gases. Tech. Rep. NASA SP-239. pp. 1-15.

Gordon, S. and McBride, B. 1994. Computer Program for Calculation of Complex Chemical Equilibrium Compositions and Applications: I Analysis. Tech. Rep. NASA RP-1311.

Gordon, S. and McBride, B. 1999. Thermodynamic Data to 20,000 K for Monatomic Gases. Tech. Rep. NASA TP-1999-208523.

Gottlieb, J. and Groth, C. 1988. Assessment of Riemann Solvers for Unsteady One-Dimensional Inviscid Flows in Perfect Gases. *Journal of Computational Physics 78,* 2, 437–458.

Grossman, B. and Walters, R. 1987. An Analysis of Flux-Split Algorithms for Euler's Equations with Real Gases. AIAA paper 87-1117-CP.

Gupta, R., Lee, K., Thompson, R., and Yos, J. 1991. Calculation and Curve Fits of Thermodynamic and Transport Properties of Equilibrium Air to 30,000 K. Tech. Rep. NASA RP-1260.

Gupta, R., Yos, J., Thompson, R., and Lee, K. 1990. A Review of Reaction Rates and Thermodynamic Properties for an 11-Species Air Model for Chemical and Thermal Nonequilibrium Calculations to 30,000 K. Tech. Rep. NASA RP-1232.

Gurivich, L., Veyts, I., and Alcock, C. 1989. *Thermodynamic Properties of Individual Substances: Vol. 1.* Hemisphere Publishing Corp.

Hahn, H., Mason, E., and Smith, F. 1971. Quantum Transport Cross Sections for Ionized Gases. *Physics of Fluids 14,* 2, 278–287.

Hansen, C. 1959. Approximations for the Thermodynamic and Transport Properties of High-Temperature Air. Tech. Rep. NASA TR-R-50.

Harten, A. 1983. High Resolution Schemes for Hyperbolic Conservation Laws. *Journal of Computational Physics 49*, 357.

Harten, A., Lax, P., and van Leer, B. 1983. On Upwind Differencing and Godunov-Type Schemes for Hyperbolic Conservation Laws. *SIAM Review 25,* 1, 35–61.

Hayes, W. and Probstein, R. 1959. *Hypersonic Flow Theory.* Academic Press.

Hillensrath, J. and Klein, M. 1965. Tables of Thermodynamic Properties of Air in Chemical Equilibrium Including Second Virial Corrections from 1500 K to 15000 K. Tech. Rep. TR-65-58, Arnold Engineering Development Center.

Hirschfelder, J., Curtiss, C., and Bird, R. 1954. *Molecular Theory of Gases and Liquids.* Wiley and Sons, 441–610.

Holden, M. 1983. Studies of Boundary Layer Transition and Surface Roughness Effects in Hypersonic Flow. Tech. Rep. CALSPAN Report 6430-A-5.

Holden, M., Wieting, A., Moselle, J., and Glass, C. 1988. Studies of Aerothermal Loads Generated in Regions of Shock/Shock Interactions in Hypersonic Flow. AIAA paper 88-0477.

Hornung, H. and Lemieux, P. 2001. Shock Layer Instability Near the Newtonian Limit of Hypervelcity Flows. *Physics of Fluids 13,* 8, 2394–2402.

Hudson, D., Rajendran, N., Lee, R., and Dougherty, C. 2005. Computational Aerothermodynamics Program - Fifth Interim Report, Volume II: User's Manual Addendum - Reacting Gas Modeling Capability. Tech. Rep. AFRL Contract #F33615-02-C-3248.

Im, K., Yu, S., Kim, C., , Chang, S., and Jorgenson, P. 2002. Application of the CESE Method to Detonation with Realistic Finite-Rate Chemistry. AIAA paper 2002-1020.

Ismail, F. 2006. Toward a Reliable Prediction of Shocks in Hypersonic Flow: Resolving Carbuncles With Entropy and Vorticity Control. Ph.D. Thesis.

Kim, K., Kim, C., and Rho, O. 2001. Methods for the Accurate Computations of Hypersonic Flows I: AUSMPW+ Scheme. *Journal of Computational Physics 174*, 38–80.

Kim, S., Kim, C., Rho, O., and Hong, S. 2003. Cures for Shock Instability: Development of a Shock-Stable Roe Scheme. *Journal of Computational Physics 185*, 342–374.

Kitamura, K., Roe, P., and Ismail, F. 2007. An Evaluation of Euler Fluxes for Hypersonic Flow Computations. AIAA paper 2007-4465.

Korte, J. 1991. An Explicit Upwind Algorithm for Solving Parabolized Navier-Stokes Equations. Tech. Rep. NASA TP-3050.

Larrouturou, B. 1991. How to Preserve the Mass Fractions Postivity when Computing Compressible Multi-Compoment Flows. *Journal of Computational Physics 95,* 1, 59–84.

Lawrence, S., Tannehill, J., and Chaussee, D. 1986. An Upwind Algorithm for the Parabolized Navier-Stokes Equations. AIAA paper 86-1117.

Levque, R., Mihalas, D., Dorfi, E., and Müller, E. 1998. *Computational Methods for Astrophysical Flows.* Springer-Verlag, 111–118.

Liboff, R. 1959. Transport Coefficients Determined Using the Shielded Coulomb Potential. *Physics of Fluids 2,* 1, 40–44.

Lin, H. 1995. Dissipative Additions to Flux-Difference Splitting. *Journal of Computational Physics 117*, 20–27.

Liou, M. 1994. A Continuing Search for a Near-Perfect Numerical Flux Scheme. Tech. Rep. NASA TM-106524.

Liou, M. 2000. Mass Flux Schemes and Connections to Shock Instability. *Journal of Computational Physics 160*, 632–648.

Loh, C., Hultgren, L., Chang, S., and Jorgenson, P. 2000. Noise Computation of a Shock-Containing Supersonic Axisysmmetric Jet by the CE/SE Method. AIAA paper 2000-0475.

Loh, C. and Jorgenson, P. 2007. A Time-Accurate Upwind Unstructured Finite Volume Method for Compressible Flow with Cure of Pathological Behaviors. AIAA paper 2007-4463.

McBride, B. and Gordon, S. 1992. Computer Program for Calculating and Fitting Thermodynamic Functions. Tech. Rep. NASA RP-1271.

McBride, B., Zehe, M., and Gordon, S. 2002. NASA Glenn Coefficients for Calculating Thermodynamic properties of Individual Species. Tech. Rep. NASA TP-2002-211556.

Menter, F. 1993. Zonal Two Equation $k - \Omega$ Turbulence Models for Aerodynamic Flow. AIAA paper 93-2906.

Monochick, L., Yun, K., and Mason, E. 1963. Formal Kinetic Theory of Transport Phenomena in Polyatomic Gas Mixtures. *Journal of Chemical Physics 39,* 3, 654–669.

Moschetta, J. 2001. *Godunov Methods: Theory and Applications.* Kluwer Academic/Plenum Publishers, 623–629.

Murphy, A. 1995. Transport Coefficients of Air, Argon-Air, Nitrogen-Air and Oxygen-Air Plasmas. *Plasma Chemistry and Plasma Processing 15,* 2, 279–307.

Murphy, A. and Arundell, C. 1994. Transport Coefficients of Argon, Nitrogen, Oxygen, Argon-Nitrogen, and Argon-Oxygen Plasmas. *Plasma Chemistry and Plasma Processing 14,* 4, 451–490.

Palmer, G. and Wright, M. 2003a. A Comparison of Methods to Compute High-Temperature Gas Thermal Conductivity. AIAA paper 2003-3913.

Palmer, G. and Wright, M. 2003b. Comparison of Methods to Compute High-Temperature Gas Viscosity. *Journal of Thermophysics and Heat Transfer 17,* 2, 232–239.

Park, C. 1989a. Asseessment of Two-Temperature Kinetic Model for Dissociating and Weakly Ionizing Nitrogen. *Journal of Thermophysics and Heat Transfer 1,* 2, 8–16.

Park, C. 1989b. Asseessment of Two-Temperature Kinetic Model for Ionizing Air. *Journal of Thermophysics and Heat Transfer 13,* 3, 233–244.

Park, C. 1990. *Nonequilibrium Hypersonic Aerothermodynamics.* John Wiley and Sons.

Park, S. and Kwon, J. 2003. On the Dissipation Mechanism of Godunov-Type Schemes. *Journal of Computational Physics 188*, 524–542.

Peery, K. and Imlay, S. 1988. Blunt Body Flow Simulations. AIAA paper 88-2294.

Prabhu, R., Stewart, J., and Thareja, R. 1989. A Navier-Stokes Solver for High Speed Equilibrium Flows and Applications to Blunt Bodies. AIAA paper 89-0668. 27^{th} Aerospace Sciences Meeting.

Quirk, J. 1994. A Contribution to the Great Riemann Solver Debate. *International Journal of Numerical Methods in Fluids 18*, 555–574.

Reynolds, W. 1986. *The Element Potential Method for Equilibrium Analysis: Implementation of the Interactive Program STANJAN.* Department of Mechanical Engineering, Stanford University.

Riggins, D., Nelson, H., and Johnson, E. 1999. Blunt-body Wave Drag Reduction Using Focused Energy Deposition. *AIAA Journal 37,* 4, 460–467.

Robinet, J., Gressier, J., Casalis, G., and Moschetta, J. 2000. Shock Wave Instability and Carbuncle Phenomenon; Same Intrinsic Origin. *Journal of Fluid Mechanics 417*, 237–263.

Roe, P. 1981. Approximate Riemann Solvers, Parameter Vectors, and Difference Schemes. *Journal of Computational Physics 43*, 357.

Roe, P. 1988. A Survey of Upwind Differencing Techniques. In *Eleventh International Conference on Numerical Methods in Fluid Dynamics*, No. 323 in Lecture Notes in Physics ed. Springer-Verlag, 387–428.

Roe, P. 2005. Computational Fluid Dynamics - Retrospective and Prospective. *International Journal of Computational Fluid Dynamics 19,* 8, 581–594.

Roe, P., Nishikawa, H., Ismail, F., and Scalabrin, L. 2005. On Carbuncles and Other Excrescences. AIAA paper 2005-4872.

Roe, P. and Pike, J. 1984. Efficient Construction and Utilization of Approximate Riemann Solutions. In *Computing Methods in Applied Science and Engineering.* North Holland.

Rosen, B. 1991. Addition of Equilibrium Air to an Upwind Navier-Stokes Code and Other First Steps Toward a More Generalized Flow Solver. Tech. Rep. NASA TM-102616.

Selle, S. and Riedel, U. 2000. Transport Coefficients of Reacting Air at High Temperatures. AIAA paper 2000-0221.

Spalart, P. and Allmaras, S. 1992. A One-Equation Turbulence Model for Aerodynamic Flow. AIAA paper 92-0439.

Spalart, P., Jou, W., Strelelts, M., and Allmaras, S. 1997. Comments on the Feasibility of LES for Wings, and on a Hybrid RANS/LES Approach. In *Advances in DNS/LES, 1st AFOSR Int. Conf. On DNS/LES*. Greyden Press.

Srinivasan, S., Tannehill, J., and Weilmuenster, K. 1987a. Simplified Curve Fits for the Thermodynamic Properties of Equilibrium Air. Tech. Rep. NASA RP-1181.

Srinivasan, S., Tannehill, J., and Weilmuenster, K. 1987b. Simplified Curve Fits for the Transport Properties of Equilibrium Air. Tech. Rep. NASA CR-178411.

Steger, J. and Warming, R. 1981. Flux Vector Splitting of the Inviscid Gasdynamic Equations with Application to Finite Difference Methods. *Journal of Computational Physics 40,* 2, 263–293.

Strang, W. 2005. Progress Report for PRDA VAK-02-08. Cobalt Solutions, LLC.

Strang, W., Tomaro, R., and Grismer, M. 1999. The Defining Methods of Cobalt_{60} - A Parallel, Implicit, Unstructured Euler/Navier-Stokes Flow Solver. AIAA paper 99-0786.

Suzuki, Y. and van Leer, B. 2007. An Analysis of the Upwind Moment Scheme and Its Extensions to Systems of Nonlinear Hyperbolic-Relaxation Equations. AIAA paper 2007-4468.

Tannehill, J., Ievalts, J., Prabhu, D., Buelow, P., and Lawrence, S. 1990. Upwind Parabolized Navier-Stokes Code for Chemically Reacting Flow. *Journal of Thermophysics and Heat Transfer 4,* 2, 149–156.

Tomaro, R., Strang, W., and Sankar, L. 1997. An Implicit Algorithm for Solving Time Dependant Flows of Unstructured Grids. AIAA paper 97-0333.

Toro, E. 1999. *Riemann Solvers and Numerical Methods for Fluid Dynamics: A Practical Introduction*, 2nd ed. Springer-Verlag.

Toro, E., Spruce, M., and Speares, W. 1994. Restoration of the Contact Surface in the HLL-Riemann Solver. *Shock Waves 4*, 25.

VAN DYKE, M. 1982. *An Album of Fluid Motion Plate 272.* Parabolic Press.

VAN LEER, B. 1979. Towards the Ultimate Conservative Difference Scheme. V. A Second-Order Sequel to Godunov's Method. *Journal of Computational Physics 32,* 101-136.

VAN LEER, B. 1982. Flux-Vector Splitting for Euler Equations. Tech. Rep. ICASE Report 82-30.

VAN LEER, B., THOMAS, J., ROE, P., AND NEWSOME, R. 1987. A Comparision of Numerical Flux Formulas for the Euler and Navier-Stokes Equations. AIAA paper 1987-1104.

VINCENTI, W. AND KRUGER, C. 1965. *Introduction to Physical Gas Dynamics.* John Wiley and Sons.

WALDER, R. 1993. Some Aspects of the Computational Dynamics of Colliding Flows in Astrophysical Nebulae. Ph.D. Thesis, Astronomy Institute, ETH-Zurich, No. 10302.

WHITE, F. 1974. *Viscous Fluid Flow.* McGraw Hill, 28–33.

WILCOX, D. 1998. *Turbulence Modeling for CFD*, 2^{nd} ed. DCW Industries.

WILKE, C. 1950. A Viscosity Equation for Gas Mixtures. *Journal of Chemical Physics 18,* 4, 517–519.

XU, K. 1999. Does the Perfect Riemann Solver Exist? AIAA paper 99-3344.

XU, K. AND HU, J. 1998. Projection Dynamics in Godunov-Type Schemes. *Journal of Computational Physics 142*, 412–427.

XU, K., MAO, M., AND TANG, L. 2005. A Multidimensional Gas-Kinetic BGK Scheme for Hypersonic Viscous Flow. *Journal of Computational Physics 203*, 405–421.

YOS, J. 1963. Transport Properties of Nitrogen, Hydrogen, Oxygen, and Air to 30,000 K. Tech. Rep. TR AD-TM-63-7, Avco Corp.

Zhang, M., Yu, S., Lin, S., Chang, S., and Blankson, I. 2006. Solving the MHD Equations by the Space-Time Conservation Element and Solution Element Method. *Journal of Computational Physics 214,* 2, 599–617.